Magnetic Suspension and Vibration Control of Flexible Structures for Non-contact Processing

by

Ming-chih Weng

B.S., Mechanical Engineering, National Taiwan University (1991)

S.M., Massachusetts Institute of Technology (1995)

Submitted to the Department of Mechanical Engineering
in partial fulfillment of the requirements for the degree of

Doctor of Philosophy in Mechanical Engineering

at the

MASSACHUSETTS INSTITUTE OF TECHNOLOGY

February 2000

Author .....
Department of Mechanical Engineering
January 31, 2000

Certified by .....
David L. Trumper
Associate Professor of Mechanical Engineering
Thesis Supervisor

Accepted by .....
Ain A. Sonin
Chairman, Department Committee on Graduate Students

Magnetic Suspension and Vibration Control of Flexible Structures for Non-contact Processing

by

Ming-chih Weng

Submitted to the Department of Mechanical Engineering
on January 31, 2000, in partial fulfillment of the
requirements for the degree of
Doctor of Philosophy in Mechanical Engineering

Abstract

This thesis presents the design, analysis, and experimental testing of systems for non-contact suspension and control of flexible structures. Our particular focus is on the use of such suspensions in manufacturing processes which can be facilitated by the ability to control workpiece motion without contact. This can be of significant utility in processes such as coating, painting, heat treating, and web handling.

We develop a novel approach for the control of such non-contact suspensions through what we term *sensor averaging* and *actuator averaging*. The difficult stability and robustness problems imposed by the flexible dynamics of the workpiece can be overcome by taking a properly-weighted average of the outputs of a distributed array of N motion sensors (sensor averaging), and/or by applying a properly-weighted distributed array of M forces (actuator averaging) to the workpiece. The theory for these dual techniques is developed in detail in the thesis. These approaches are shown to be independent of the specific boundary conditions or the longitudinal dimensions of the workpiece. These approaches are thus generally applicable to a wide range of structural control problems.

We present both analytical and numerical analyses of the structural dynamics for typical flexible workpieces such as strings, beams, membranes, and plates. The analyses include axial translation of the workpiece.

We have experimentally demonstrated the utility of our theory by application in the successful magnetic suspension of a 3 m long, 6.35 mm diameter, 0.89 mm wall thickness steel tube with varying boundary conditions. This is a very challenging problem due to the extremely light damping of the modes (< 0.001 with free ends). The experiment uses a set of 8 sensors and 8 actuators to measure and control the motion of the tube in the two lateral degrees of freedom. We present the details of the developed electromagnetic actuators, position sensors, modeling of the structural dynamics, the relevant vibration control techniques, and develop the associated theory for choosing sensor and actuator locations. Our results experimentally confirm the value of our averaging techniques, and suggest the wide future application of these ideas in industrial processes which require non-contact handling of workpieces.

Thesis Supervisor: David L. Trumper
Title: Associate Professor of Mechanical Engineering

Acknowledgments

I would like to thank my thesis advisor Professor David L. Trumper for his guidance through these years. He brings me into the area of mechatronics, and enlightens me with his insight in control, machinery, and electromagnetic designs. He always keeps the highest standards towards research, and never compromises for defective solutions. I think he is the best advisor one can get, and I am proud to be one of his students. I would also like to thank my other thesis committee members. Professor Jeffrey H. Lang has a clear way of showing me how to solve complicated problems. Listening to him explaining electromagnetic theory is always enjoyable. Professor Samir Nayfeh has helped me with his great knowledge in structural dynamics. With his expertise in this field, he can interpret my work on vibration control better than I do.

This work is supported by the National Science Foundation under the grant award number DMI-9700973 on "Noncontact Processing of Fibers, Beams, Webs, and Plates."

I have been working with a group of intelligent minds in the Precision Motion Control Laboratory at MIT. It has been my pleasure working with them. I want to thank all of them for helping me during these years, and for being good friends to me. During this project, I worked together with Robin Ritter. Thanks for his excellent work, we are able to make this project successful. Xiaodong Lu joined this group last term, and is continuing this project to the next level. Steve Ludwick and Pradeep Subrahmanyan both excel on academic knowledge as well as hands-on experiences. I have always looked up to them since I joined this group. Mike Liebman has a great insight into physics, and I have always asked for his help whenever I was puzzled by the electromagnetic theory. I owe thanks to Katie Lilienkamp for her help on the dSPACE code. Joe Calzaretta has a brilliant mind open to all wild ideas. Marten Byl has been working with Joe on the diamond turning machine day after day since he joined this group. Marty Vona, Tsuyoshi Sato joined this group last term, and I hope they enjoy working in this group as I do. Dave Chargin, Paul Konkola,

Claudio Salvatore, Stephanie Gellar, Won-Jong Kim and Sai-Bun Wong are the other distinguished alumni from this lab whom I have worked with. Good luck to you all.

In the machining shop, I have great help from Mark Belanger, Gerry Wentworth, and Fred Cote. Maureen Lynch and David Rodriguera have helped all of us graduate students in the PMC lab on all matters. We are very lucky to have them. Thanks to Leslie Regan, she had reminded me the time to apply for the Ph.D. program, the qual exam, and the Ph.D. degree.

During this project, I had the chances to go to the IEEE CCA conference at Hawaii, the NASA ISMST-5 conference at Santa Barbara, and a seminar at U.C. Santa Barbara. I would like to thank Professor Carl Knospe from University of Virginia, and Professor Brad Paden and Professor Petar Kokotovitc from UCSB for their helpful comments on this research.

I would like to thank all members in R.O.C. Student Association at MIT. They have helped me since the first day I arrived Boston, and I have made many good friends there. I would like to thank R.O.C. Educational Bureau for financially supporting me for three years.

I would like to thank my family back in Taiwan for their support and understanding during my last 6.5 years at MIT. My mother So-Mei, father Fu-Lai, brother Yu-Ling, and sister Yu-Ping, they have always been supportive to me.

A special thank to Jane, who encouraged me to go for the Ph.D. degree. I never thought a serious guy like me can be crazy about someone until I met Jane. I want to thank her for always being thoughtful during these two years when we were apart by a few thousand miles. Finally, I am joining her at the sunny west coast.

For my parents, and

for Jane

獻給最敬愛的父母親

和佩貞

Contents

List of Figures

List of Tables

Chapter 1

Introduction

Many industrial operations are based upon the processing of an elongated element moving axially through successive functional stations. Examples include steel rolling, plastic film production, paper production, coating, and printing, and the coating and painting of materials such as plastic and metal. In such processes, it may be advantageous to handle the product without directly touching it. In this research, we focus on the development of suspension technology for such processes via magnetic and electrostatic forces. The developed technology can serve as the underpinnings for new classes of industrial processes heretofore unimagined.

The objectives of this research are threefold:

1. Establish general theory for electrostatic and magnetic suspensions applicable to non-contact processing.

2. Demonstrate utility of the developed theory by its application in a focused experiment on magnetic suspension of tubular beams.

3. Disseminate our ideas in detail to facilitate their adoption in a wide variety of processes.

This thesis presents the design, analysis, and experimental testing of systems for non-contact suspension and control of flexible structures. The main challenges we faced in this research include the designs of non-contact sensors and actuators, and

the attempt to robustly stabilize the lightly damped vibration modes of suspended structures via feedback control.

We develop a novel approach for the control of such non-contact suspensions through what we term *sensor averaging* and *actuator averaging*. Our results show that the difficult stability and robustness problems imposed by the flexible dynamics of the workpiece can be overcome by taking a properly-weighted average of the outputs of a distributed array of N motion sensors (sensor averaging) and/or by applying a properly-weighted distributed array of M forces (actuator averaging) to the workpiece. The theory for these dual techniques is developed in detail in the thesis. The advantages of this approach are shown to be independent of the specific boundary conditions or the longitudinal dimensions of the workpiece. These approaches are thus generally applicable to a wide range of structural control problems.

To support our work, we present analyses of the relevant structural dynamics for typical flexible workpieces such as strings, beams, membranes, and plates. The analyses include tension forces as well as continuous axial translation of the workpiece, and demonstrate the effect of the structural properties on the closed-loop control systems. Our models are based upon both analytical and finite-element techniques.

We have experimentally demonstrated the utility of our theory by application in the successful magnetic suspension of a 3 m long, 6.35 mm diameter, 0.89 mm wall thickness steel tube with free end conditions. This is a very challenging problem due to the extremely light damping ($\zeta < 0.001$) of the modes in the free-free condition. The experiment uses a set of 8 sensors and 8 actuators to measure and control the motion of the tube in the two lateral degrees of freedom.

In this thesis, we present the details of the developed electromagnetic actuators, position sensors, analytic and numerical modeling of the structural dynamics, the relevant vibration control techniques, and develop the associated theory for choosing sensor and actuator locations. Our results experimentally confirm the value of our averaging techniques, and suggest the wide future application of these ideas in industrial processes which require non-contact handling of workpieces.

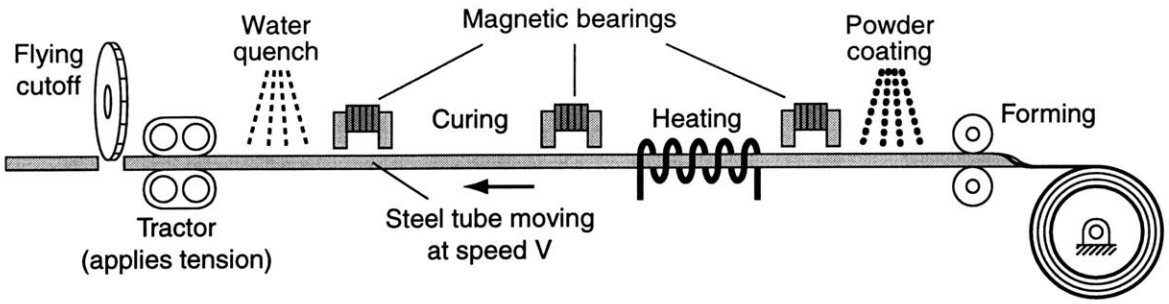

Figure 1-1: Non-contact coating process.

1.1 Motivations for Non-contact Processing of Flexible Structures

This project grew out of work at American Metal Handle (AMH), a small company that makes metal handles for brooms and mops[1]. Dr. Conrad Smith of AMH developed the idea of using a non-contact coating process in a continuous production line for painted metal handles, as illustrated in Figure 1-1. The idea is to use magnetic suspension stages to support a 47 m long steel tube moving at a speed of 1 m/s through multiple processing stages. The processing steps include:

1. Forming and seam-welding: Rollers wrap a steel sheet into a tube, and a seam-welding device welds the joint.

2. Powder coating: Electrostatic charged powder paint particles are adhered to the tube.

3. Induction heating: Heating the tube to about 600°F melts the coating powders and initiates the curing reaction.

4. Curing: Quartz tube heaters keep the melted paint warm for about 30 seconds until it cures.

5. Quenching: Water cools the cured paint, and a fly-cutter cuts the coated tubes into sections.

[1]American Metal Handle, Vulcan Dr., Birmingham, AL, U.S.A.

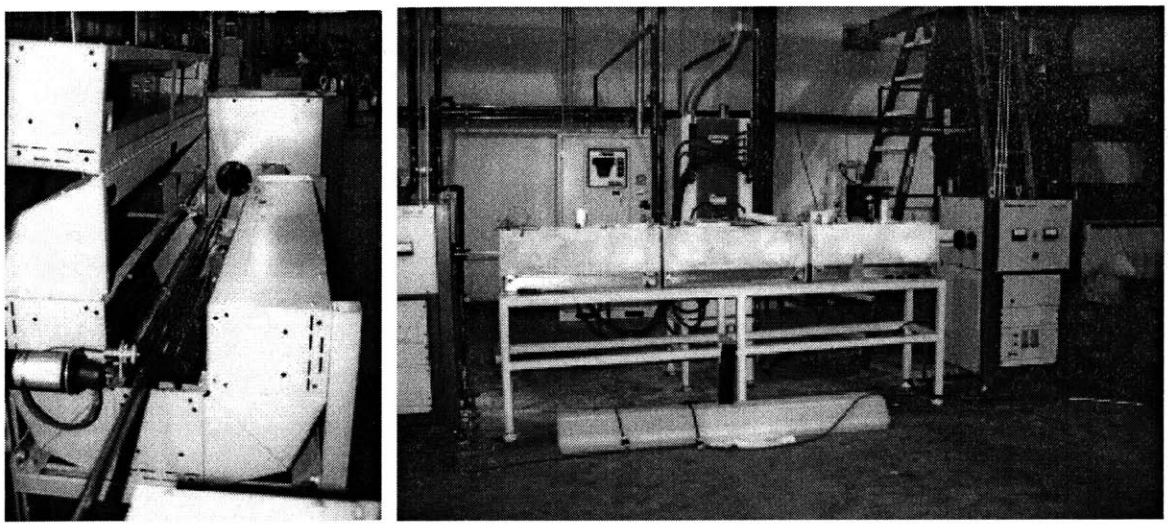

(a) (b)

Figure 1-2: Non-contact steel broom handle coating at AMH: (a)the tube passing through a quartz oven, and (b) the induction heating stage between 2 magnetic suspension stages.

6. Tractor for tension.

7. In the sections between the powder coat and the water bath, the tube is supported by magnetic suspension. There are 10 suspension stations total, with a spacing of $3 \sim 4$ m between stations.

8. Cutting: A flying cutter chops the coated tubes into sections.

The magnetic suspension of this flexible beam is very difficult due to the lightly-damped resonance modes, which have frequencies as low as 0.1 Hz. Professor Trumper consulted with this company on the design of the suspension stations and the PID controllers used to independently control each of the stations and thereby to stabilize this system. The system was stabilized with the extra help from the rollers at the boundaries and applied axial tension force. The rollers helped providing more damping to the system, and the tension force made the resonance frequencies higher. Figure 1-2 shows two photographs of this system.

With this work as a foundation and motivation, this thesis presents underlying theory and technologies for magnetic and electrostatic suspensions of flexible structures. Many industrial processes can benefit from such non-contact handling technology.

	1996	1997	1998	1999
JAN			Dimensionless analysis	1st committee meeting Solve PowerFET oscillation **2ft beam free-free stable**
FEB			Testing stage for sensors and actuators	Moving structure dynamics Solve sensor / sensor coupling Solve actuator / sensor feedthrough
MAR			1st dipole-quadrupole actuator	System identification Actuator linearization Sensor linearization
APR				Force/moment control (not good yet) Sensor interpolation Sensor averaging **10ft beam loose-bore stable**
MAY			FEM for beam dynamics	MIMO control / local control Peak envelop
JUN				Modify low-pass filters Passive damper (not good yet)
JUL		NSF grant starts	Beam controller design Power amp circuit 2D sensor	MIMO system identification Modal filter (not good yet) Actuator averaging **10ft beam free-free stable**
AUG			2nd dipole-quadrupole actuator **1.5ft beam hinge-free stable** Quad-U-core actuator	LQG (not robust) IEEE CCA conference
SEP		E-ferrite sensor Testing stage	PowerFET circuit	IEEE paper: sensor/actuator averaging NASA paper: beam suspension design
OCT	NSF proposal		Build hardware	2nd committee meeting Experiments: sensor/actuator averaging
NOV				Critical speed limit Eddy current model
DEC			Experiment setup complete FEM for plate dynamics	NASA ISMST-5 conference UCSB CCEC seminar 3rd committee meeting Thesis writing

Figure 1-3: Time line of project progress.

The major challenge of developing this technology is to achieve robustness and reliability for various manufacturing processes. Our goal is that the controlled system should be stable for systems with varying boundary conditions, varying structure lengths, and varying structure positions.

1.2 Project Review

This project started in July 1997; my progresses is summarized as a timeline in Figure 1-3. The successful suspension of tubes with different dimensions and boundary

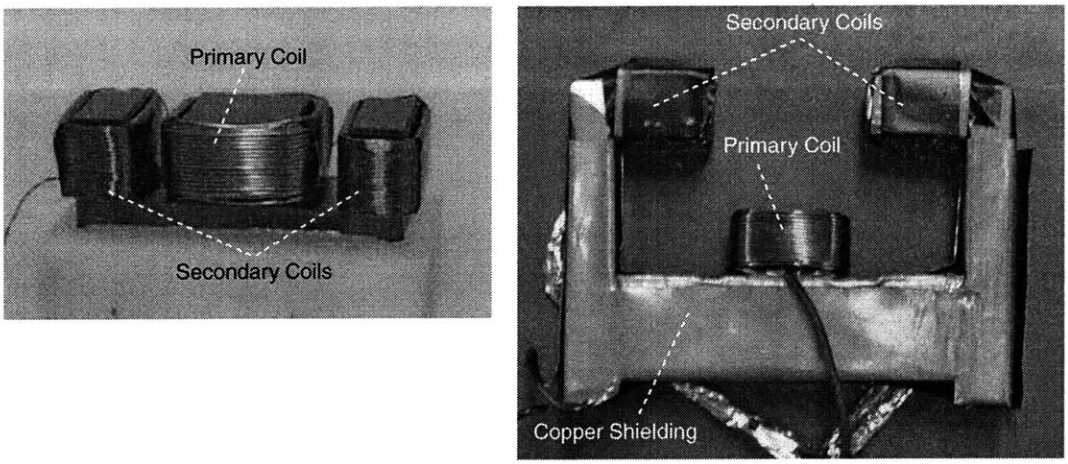

Figure 1-4: One-dimensional non-contact position sensor design: (a) a simple E-core, and (b) a modified E-core.

conditions are shown in bold print. The suspension of the 10 foot long beam with free-free boundary is the most challenging experiment I faced in this project. This was not stabilized until I developed both sensor averaging and actuator averaging methods. This project can be roughly separated into three major parts: sensor design, actuator design, and suspension experiments. The suspension experiments include the structural dynamic analyses, controller designs, and sensor/actuator positioning techniques. More details are described in the following sections.

1.2.1 Sensor Design for Tubular Beams

We chose to design inductive sensors for our tube magnetic suspension experiment because they are largely immune to the effects of a dusty environment such as in a coating process. Inductive sensors can also sense a large range of motion while the sensor itself can be very compact.

The evolution of our sensor designs is shown in Figure 1-4. We started developing a non-contact position sensor by using a simple ferrite E-core. This sensor acts as a differential transformer that senses position in the horizontal direction, as shown in Figure 1-4(a). A modified version of the one-dimensional position sensor is shown in Figure 1-4(b). In this refined version the output is less sensitive to motions in the

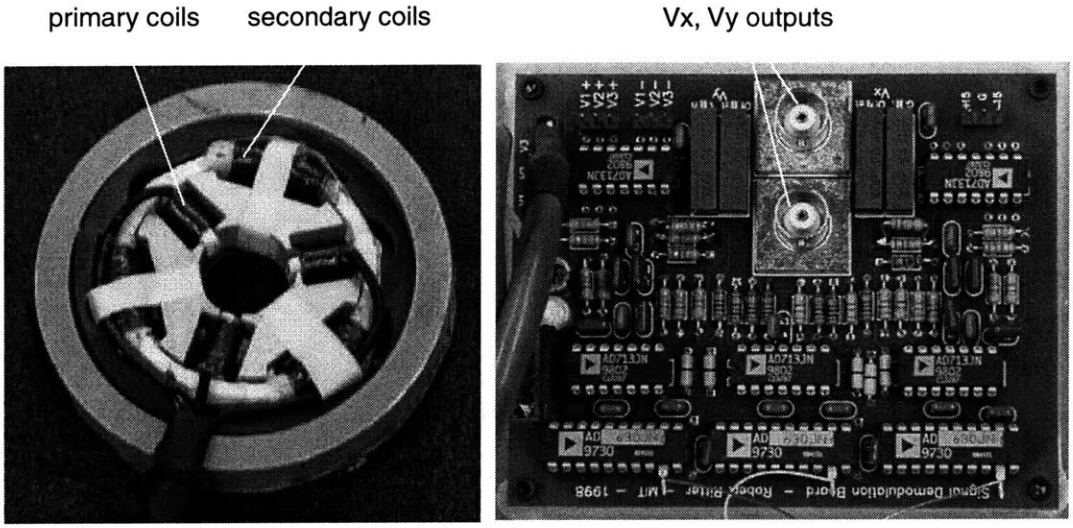

Figure 1-5: Two-dimensional non-contact position sensor design: sensor and demodulation circuit board.

vertical direction.

A two-dimensional position sensor was later designed by Robert Ritter [93] as part of his Master's thesis. The design is a compact two-dimensional differential transformer integrated with a demodulation circuit board, as shown in Figure 1-5. It has three primary coils that generate a rotating magnetic field; the outputs from three secondary coils are demodulated to determine the position of the tube.

1.2.2 Actuator Design for Tubular Beams

Our first actuator design used a dipole bias winding and two orthogonal quadrupole windings. Two versions of this type of actuator are shown in Figure 1-6. The first version is shown in Figure 1-6(a), it has the following flaws (mainly due to the lack of experience): (1) the wires cannot be tightly wound inside the slots, and (2) the wires are easily cut by the sharp edges of laminations and thus create a short circuit between the wires and the laminations, and (3) the force is much smaller than the ideal model. We modified the design, and built a much larger version as shown in Figure 1-6(b). This design is still based on the dipole-quadrupole field setup. This second version design shows excellent linear relations between current input and force

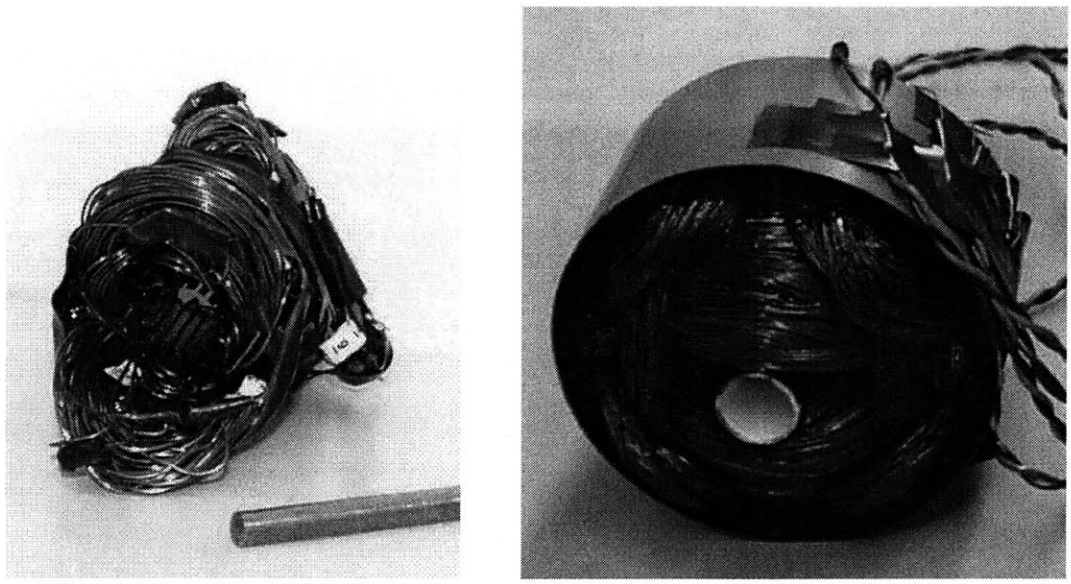

(a) (b)

Figure 1-6: Dipole-Quadrupole actuators: (a) a small version, and (b) a large version.

output as we inquired. However, once the tube approaches the outer portion of the actuator, it tends to be attracted to the pole tips. That is, we have not created a true dipole. Once the tube is stuck, it cannot be released from the pole tips unless we turn off the dipole field.

Due to the difficulties of building the dipole-quadrupole actuator and the sticking problem, we designed another type of actuator; which we have termed the Quad-U-Core actuators, as shown in Figure 1-7. They are easy to build, and the laminations can be assembled in the proper manner to eliminate eddy currents in the core, and thereby improve the bandwidth of the actuator. The first version is shown in Figure 1-7(a), and the experiment shows that the force saturates at a small current input (0.5 A). It is because that it has long legs which produce a large amount of fringing field, and it also has thin U-cores which saturate magnetically at a small current input. The second version is shown in Figure 1-7(b), it uses more laminations in the back iron to form thicker U cores, and has shorter legs to reduce fringing field. This actuator supplies sufficient force, and is being used in the final setup. Although the Quad-U-Core actuator is our final choice, it does have the following disadvantages: (1) the force/current relation is nonlinear, (2) forces in x and y directions are coupled,

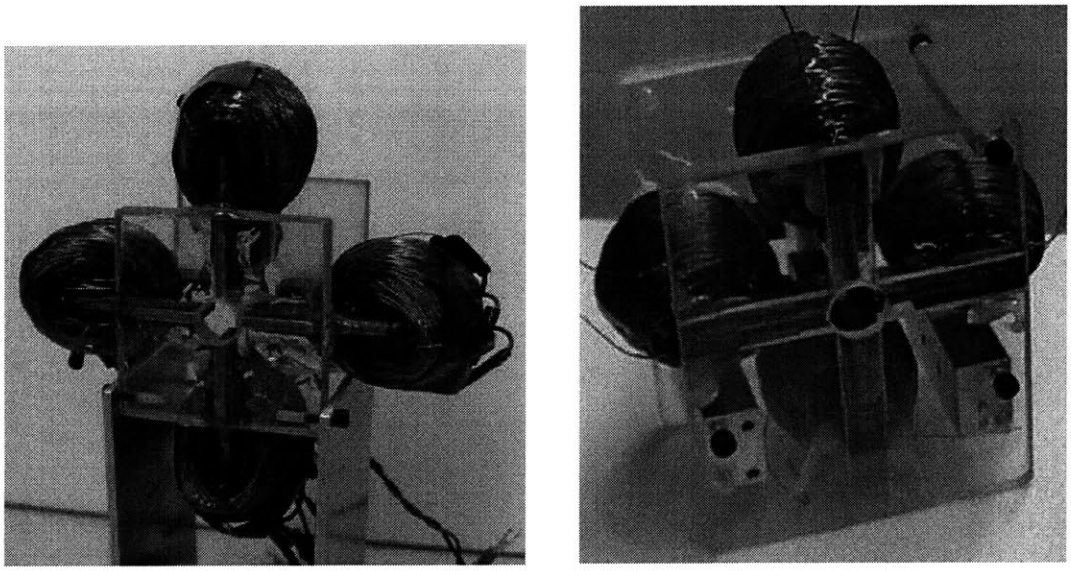

(a) (b)

Figure 1-7: Quad-U-Core actuators: (a) long and thin cores, and (b) short and thick cores.

and (3) it produces a larger magnetic field outside the actuator compared to Dipole-Quadrupole actuators. This large external field has caused problems with coupling to the inductive position sensor, especially when these are in close proximity.

In our experiment of tube suspension, we notice that the top electromagnet is driven by a current input of about 0.5 A, and the left and right electromagnets have an average current less than 0.1 A, and the bottom magnet is barely used. If we increase the weight of the tube, the top magnet can be easily overheated (a current of 1 A makes the electromagnet extremely hot). Hence it is advantageous to rotate the actuator by 45° and diversify the current to 2 electromagnets at the top. Recently, Xiaodong Lu in our lab has built this modified version of the Quad-U-Core actuators that are rotated 45°, so as to have maximum force at the $\pm x$ and $\pm y$ directions. They are shown in Figure 1-10 as the last 2 actuators at the right end.

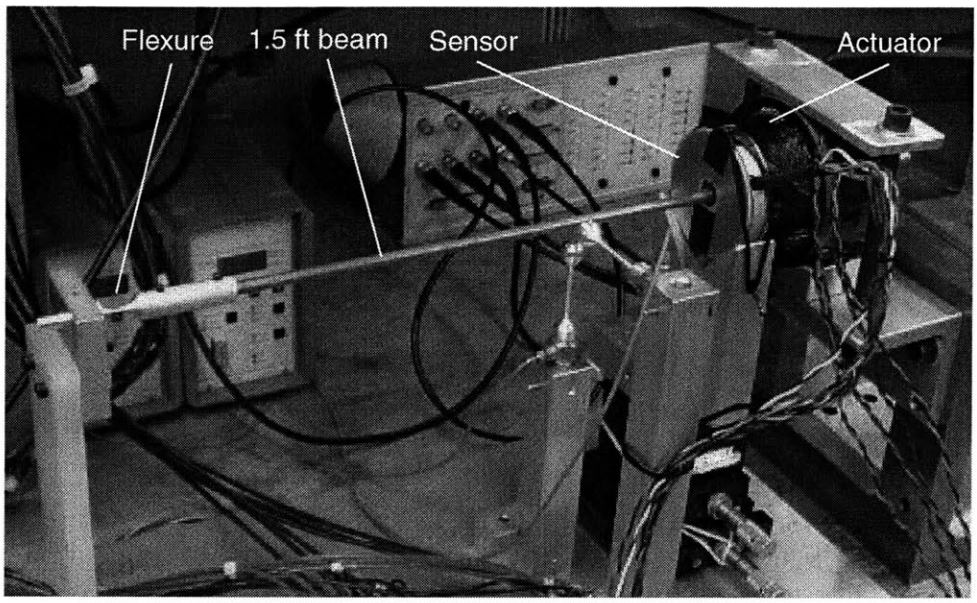

Figure 1-8: Magnetic suspension of a hinged-free beam with length $L = 1.5$ ft by using 1 sensor and 1 actuator.

1.2.3 1.5 Ft Beam Suspension Using One Sensor and One Actuator

The first stable suspension by using the 2-D inductive sensor, in conjunction with a Dipole-Quadrupole actuator is shown in Figure 1-8. The suspension supports one end of a 1.5 foot long steel tube. The other end of the tube is supported by the flexure hinge shown in the photo. The control bandwidth is well below the 1st vibration mode, that is, we only consider the rigid body modes in this setup.

1.2.4 2 Ft Beam Suspension Using Two Sensors and Two Actuators

The second stable suspension was accomplished by using two 2-D sensors, and two Quad-U-Core actuators to suspend a 2 foot long steel tube with free-free boundaries, as shown in Figure 1-9. The control is done by localized SISO control: each sensor/actuator pair is considered independently, and the sensor and actuator are considered to be collocated.

However, in this suspension, we start to realize the intriguing problem that we

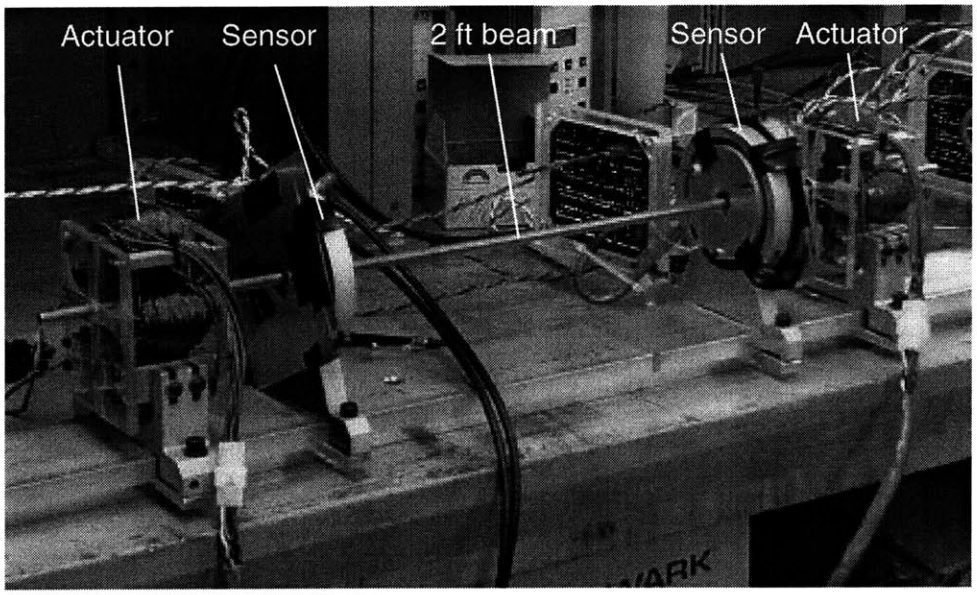

Figure 1-9: Magnetic suspension of a free-free beam with length $L = 2$ ft by using 2 sensors and 2 actuators.

are facing: the stability of the system depends on the vibration mode shape and the sensor/actuator positions. By moving the tube axially, the following situations happen:

1. The sensor and actuator are on the same side of the node of a vibration mode shape, the system is stable.

2. The sensor is right on the node of a vibration mode shape, the vibration mode is not observed, and the system is stable.

3. The actuator is right on the node of a vibration mode shape, the vibration is not controlled, and the system is stable.

4. The sensor and actuator are on the opposite sides of the node of a vibration mode shape, the system is unstable.

These results show that this stable suspension is not reliable enough. The system can be destabilized when we move the tube axially. The system becomes unstable because some vibration mode has a node between the assumed collocated sensor and actuator.

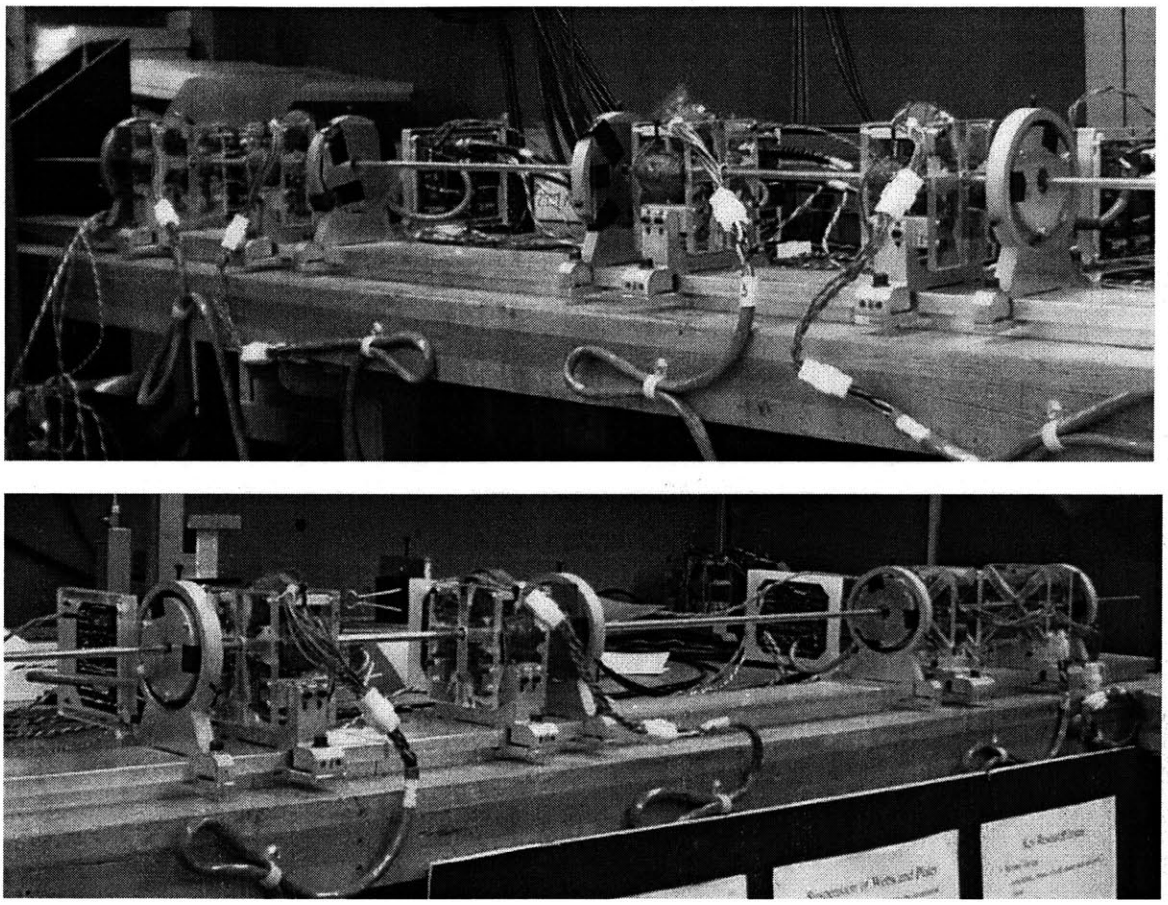

Figure 1-10: Magnetic suspension of a free-free beam with length $L = 10$ ft by using 8 sensors and 8 actuators. The top figure shows the left half of the setup, and the bottom figure shows the right half. The last 2 actuators on the right-most side are rotated by 45° with respect to the vertical, they were built by Xiaodong Lu.

1.2.5 10 Ft Beam Suspension Using Eight Sensors and Eight Actuators

The stable suspension of a 10 foot long beam with free-free boundaries is shown in Figure 1-10. The system is also stable for varying boundary conditions, including clamped, hinged, and free boundaries.

This suspension is the most challenging experimental problem that we encountered in this project. Because of the free-free boundaries, the damping ratio of the modes of the structure is less than 0.001. Because the 1st vibration mode is at about 3 Hz, and we require the control bandwidth up to 200 Hz, we need to add positive phase shift in the loop transfer function over the frequency range from 3 Hz to 200 Hz. This

requires some form of lead compensation, which also introduces the problem that the high-frequency modes are amplified.

After we developed the sensor averaging method, we were able to suspend the 10 foot long tube with loose-bore boundaries, which are holes slightly larger than the tube diameter. The collision between the tube and the loose fit bores provides sufficient damping to the system. The system always had limit cycles at very high frequencies such as 800 Hz, where we have no control bandwidth to stabilize it. The stabilization of such a free-free beam was made possible after we further developed the actuator averaging method.

1.2.6 Controller Design

In this thesis, we use a SISO lead compensator to control the system. We use this controller to add phase lead to the loop transfer function from 3 Hz to 200 Hz. At the same time, we do not want to amplify the gains too much at high frequencies. Therefore, we design a *slow roll-up lead compensator*, which has a form of:

$$H(s) = K_p \frac{(s+m)(s+4m)\cdots}{(s+2m)(s+8m)\cdots} \tag{1.1}$$

The Bode plot of this lead compensator is illustrated in Figure 1-11. Such a controller has an average phase lead of 30°, and a gain slope of 10 dB/decade. Besides this controller, I will also evaluate other model-based control methods later in Chapter 9.

1.2.7 Sensor/Actuator Positioning

In this project, we developed a novel sensor/actuator positioning method: *sensor averaging* and *actuator averaging*. By using 2 sensors set apart by $2d_s$, we average these 2 sensor measurements, and the resulting averaged output will have less observability on the resonance modes with wavelengths close to $4d_s$. Similarly, by using 2 actuators set apart by $2d_a$, we apply the same force to these 2 actuators, and the resonance modes with wavelengths close to $4d_a$ will be less controllable.

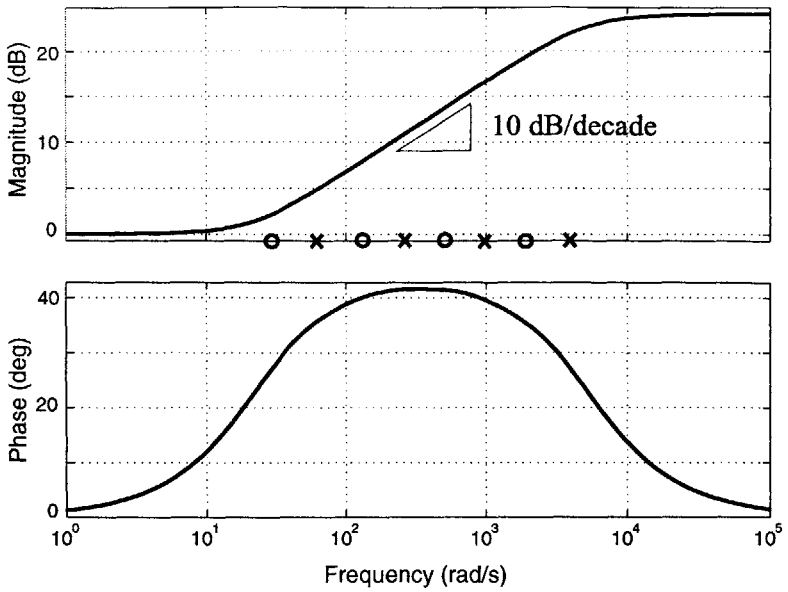

Figure 1-11: Bode plots of a slow-roll-up lead compensator.

To be more specific, if we assume modal shapes are dominated by sinusoidal waveforms, sensor/actuator averaging methods introduce the modal gain

$$\cos k_n d \tag{1.2}$$

for each resonance mode, where k_n is the wavenumber of the nth mode. In other words, the sensor averaging and actuator averaging methods will significantly attenuate the gains of vibration modes with $k_n d \approx \pi/2$, or equivalently with wavelength $4d$. The modal gain of $\cos k_n d$ can be easily related to frequency domain by the dispersion equations of the structures. Using an un-tensioned beam as an example, we have the beam dispersion equation:

$$\rho A \omega_n^2 = EI k_n^4, \tag{1.3}$$

where ρ is the mass density, A is the cross-sectional area, E is Young's modulus, I is the bending moment of inertia, and ω_n is the resonance frequency of the nth mode.

With the numerical parameters used in our experiment, we have the beam dispersion equation: $0.01\omega_n^2 = k_n^4$. To attenuate the resonance modes around 1000 rad/s,

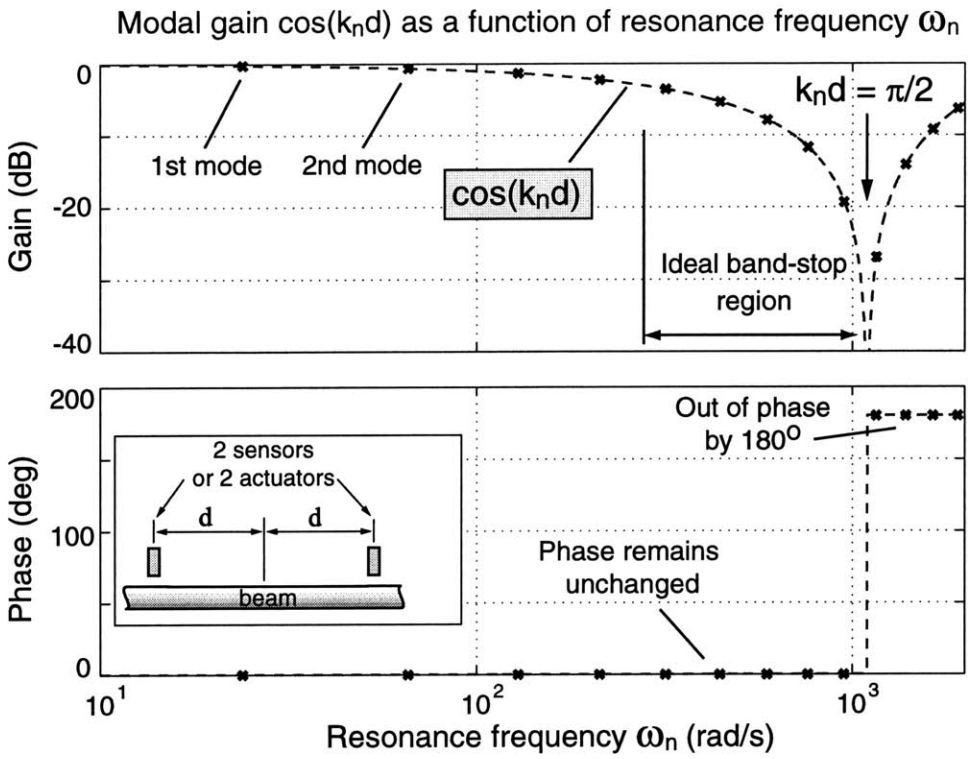

Figure 1-12: Modal gain and phase of each resonance mode by using sensor averaging or actuator averaging method. The broad notch attenuates several undesired resonance modes robustly.

we calculate the wavenumbers of these resonance modes; they are around 10 rad/m. Equivalently, the wavelengths of these modes are around 0.6 m. Hence we can simply place 2 sensors along the beam, each located $d_s = 15$ cm away from the center point. The resulting modal gain of $\cos k_n d$ is plotted as a function of resonance frequency ω_n in Figure 1-12. The modal gain $\cos k_n d$ creates a broad notch for resonance modes with $k_n d \approx \pi/2$. The phase is not affected before the notch, and becomes out of phase by 180° after the notch when $\cos k_n d$ becomes negative.

Furthermore, the resulting theoretical Bode Plots of the beam dynamics are shown in Figure 1-13, which shows that the resonance modes around 1000 rad/s are significantly attenuated, and no phase lag is introduced at lower frequencies.

To verify the proposed sensor/actuator averaging method, we did various experiments and measured the experimental Bode Plots. The details are shown in Chapter 6. The experimental Bode plots of 2-sensor averaging are shown in Figure 1-14. In

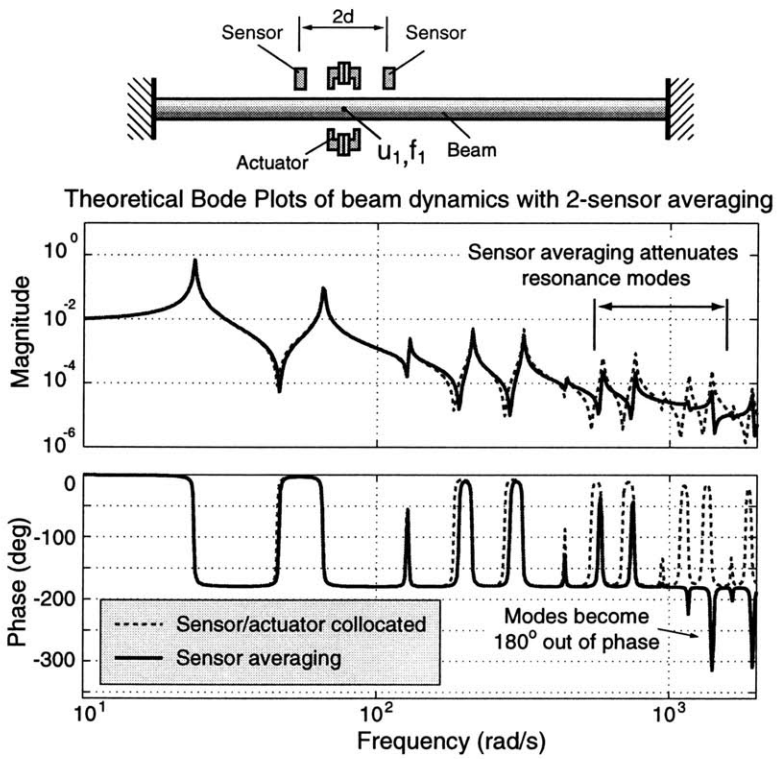

Figure 1-13: Theoretical Bode plots of the beam dynamics by using 2-sensor averaging, from force f(N) to averaged output u_{ave}(m). Undesired resonance modes are attenuated. Dashed line shows the beam dynamics with a collocated sensor/actuator pair for comparison.

this experiment, we use 2 sensors and 1 actuator to control a point along the beam. Dashed line shows the experiment with 2 sensors and 1 actuator located in close proximity and thus considered collocated. In this arrangement, the system is almost stable except a limit cycle vibration at 1100 rad/s. Solid line shows the experiment with 1 actuator in the middle and 2 sensors set apart by $2d = 30$ cm to perform sensor averaging. By this simple change, we stabilize the system and eliminate the limit cycle vibration. The experimental Bode plots shows the resonance modes around 1000 rad/s are attenuated, and no phase lag is introduced at lower frequencies, which agrees well with our theoretical Bode Plots in Figure 1-13.

This proposed sensor/actuator positioning method robustly attenuates the gains of the resonance modes without adversely affecting the phase. The curve of the broad notch $\cos k_n d$ shown in Figure 1-12 is simply a function of the properties of the beam element (ρ, A, E, and I) and the sensor/actuator distance d. The curve is not a

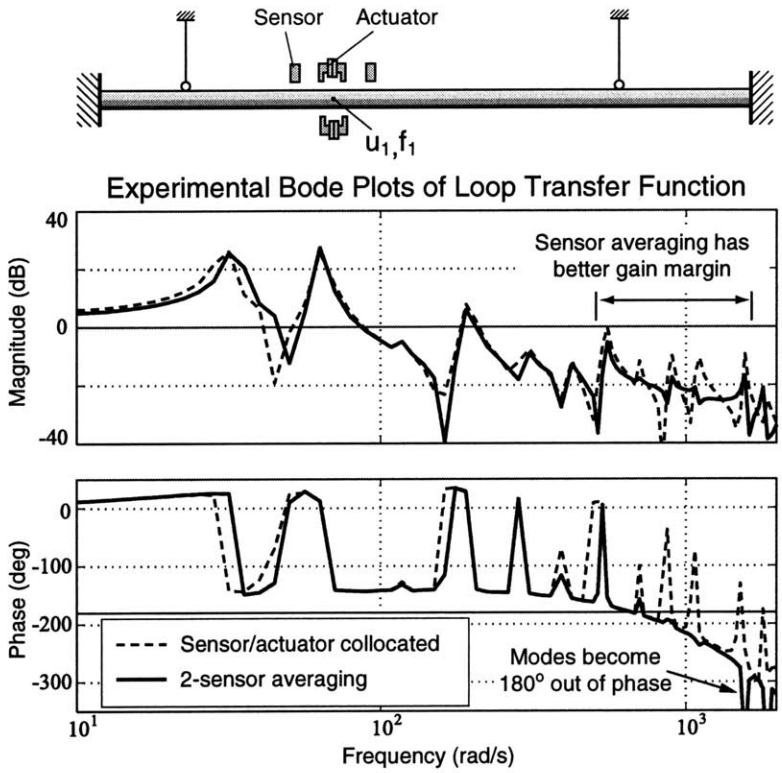

Figure 1-14: Experimental Bode plots of the loop transfer function by using 2-sensor averaging. Undesired resonance modes are attenuated. Dashed line shows the experiment using a collocated sensor/actuator pair for comparison.

function of boundary conditions, sensor/actuator positions, or structure dimensions. This averaging method is valid as long as the attenuated modes are dominated by sinusoidal waveforms. This property makes this method valuable for robust vibration control. We expect this method will have utility in many flexible structure and vibration control applications.

1.3 Summary of Contributions

This project has led to a very challenging task in the fields of magnetic suspension and non-contact vibration control. Magnetic suspension requires the knowledge of electromagnetic theories, electric circuit design, and feedback control. Non-contact vibration control requires knowledge of structural dynamics and feedback control. The lightly damped vibration modes of levitated structures make the controller design

extremely difficult, this is one of the reasons that most of the vibration control research focuses on model-based control approach. In this research, we developed a non-model-based control method, with the help of the new sensor/actuator positioning method, we are able to stabilize the system robustly even as the system varies, which is essential for various manufacturing processes.

I summarize the contributions of this project in two categories: basic theory level and practical level.

1.3.1 Contributions in Basic Theory Level

1. Developed integrated approaches for magnetic/electrostatic suspension and vibration control of flexible structures. In this thesis, I presents the details of the developed electromagnetic actuators, position sensors, analytic and numerical modeling of the structural dynamics, the relevant vibration control techniques, and develops the associated theory for choosing sensor and actuator locations.

2. Developed theory to guide the designs of sensors and actuators for magnetic suspension. Details are given in Chapter 8 and Chapter 7.

3. Developed the novel sensor averaging and actuator averaging method for robust vibration control. Details are given in Chapter 6.

4. Demonstrated the validation of the proposed ideas in a focused experiment on the magnetic suspension of tubular beams. Details are shown in Chapter 5 and Chapter 6.

1.3.2 Contributions in Practical Level

1. Generalized structural modeling using both analytic and numerical methods, including the dynamics of axially moving structures. In this project, we model the structural dynamics of beams, strings, plates, and membranes. We use the analytic results to develop an uncertainty envelope, controller design techniques, and the sensor/actuator positioning method. We also use the finite element

method as a convenient tool to model the structures within the Matlab software package.

2. Designed, built and tested different actuator designs for the magnetic suspension of tubular steel beams, including the power electronics design.

3. Designed, built and tested non-contact position sensor designs for the magnetic suspension of tubular steel beams, including the signal electronics and power electronics design.

4. Designed and evaluated different controllers for vibration control.

1.4 Thesis Overview

This chapter has broadly reviewed the objectives, results and contributions of this thesis. The details of the developed suspension technology will be discussed in the following chapters in more details as follows.

- Chapter 2 reviews relevant results in the literature.

- Chapter 3 describes principles for magnetic suspension and electrostatic suspension for different materials.

- Chapter 4 reviews the analytical modeling of flexible structures.

- Chapter 5 describes our experiment for magnetic suspension and vibration control of tubular beams. We demonstrate an integrated approach of design processes, including scaling, modeling, controller design, and system identification. An uncertainty envelope is derived to guide the controller design for structures with varying boundary conditions.

- Chapter 6 develops novel sensor/actuator positioning methods which we have termed *sensor averaging* and *actuator averaging*. This chapter includes theoretical derivations as well as experimental confirmation of our ideas.

- Chapter 7 develops the theory and evaluation of different designs of non-contact force actuators associated with our beam suspension experiment.
- Chapter 8 develops the design of non-contact position sensors associated with our beam suspension experiment.
- Chapter 9 reviews and evaluates model-based control methods theoretically, including LQG control, $\mathcal{H}_\infty$ control, μ analysis, and modal filters.
- Chapter 10 extends the analyses of structural dynamics to axially moving structures.
- Chapter 11 reviews the modeling of flexible structures using the finite element method for interested readers.
- Chapter 12 concludes this thesis and suggests future extensions to this project.

Chapter 2

Literature Review

This thesis covers multiple fields in electromagnetic systems, structural dynamics, and vibration control. I categorize my literature review into two parts: background studies and prior art. The background studies include fundamental theories underlying this thesis that are well developed, such as electromagnetic field analysis, structural dynamics, and control theories. Prior art are topics that are more advanced or still under research. These materials can be found mostly from journal papers or conference proceedings, such as electromagnetic suspensions and structural vibration control.

2.1 Background Studies

The fundamental theories underlying this thesis are well developed and can be learned from text books. The following are the books that I recommend to an interested reader.

2.1.1 Electromagnetic Theory

In this thesis, I only consider electroquasistatic (EQS) and magnetoquasistatic (MQS) systems. Electromagnetic dynamics (radiation) are not significant in this thesis. Purcell [91] introduces the theory of electricity and magnetism in physics. Haus [44] introduces fundamentals of the analysis of electric and magnetic fields. Woodson [110, 111]

and Fitzgerald [35] introduce electromagnetic machine design and analysis. Melcher [78] presents an in-depth treatment of continuum electromechanical systems.

2.1.2 Structural Dynamics

In this thesis, both analytical and numerical methods are used to model structural dynamics. Reismann [92, Chapter 6] and Timoshenko [100] analyze the static equations of a variety of structures and present the solutions for different boundary conditions. Meirovitch [75] and Benaroya [16] introduce fundamentals of structural vibration analysis, including natural responses, forced responses, and modal analysis. Bathe [9] introduces the numerical finite element method.

2.1.3 Control Theory

In this research, we focus on linear time-invariant controllers. The design of such controllers is presented in the following references. Franklin [36] introduces the fundamentals of feedback control theory. Roberge [94, Chapter 5] introduces feedback compensation in the content of analog circuit design. Franklin [37] introduces digital control theory and design methods. Multivariable control methods, such as LQG, $\mathcal{H}_\infty$ and μ-synthesis, can be found in Zhou [114, 113], the Control Handbook [66], or university class notes, such as MIT course Multivariable Control Systems [4]. Other control methods such as nonlinear control or adaptive control are not considered in this thesis.

2.2 Prior Art in Electromagnetic Suspensions

This thesis mainly focuses on magnetic suspension via the magnetization force. However, I will briefly introduce other principles of electromagnetic suspensions that are applicable for other materials which are candidates for non-contact processing. In the journal *Science*, Brandt [101] reviews possible suspension techniques, including aerodynamic, acoustic, optical, electric, magnetic, radio-frequency, and superconducting

levitation. Geary [40] covers different principles of electromagnetic suspensions and the technological development of such suspensions up to 1964.

2.2.1 History of Electromagnetic Suspension

Earnshaw [31] (1839) shows that for a free suspended point particle whose forces have an inverse square of distance relation, there is no stable equilibrium point. This result can also be interpreted as stating that in such a field, a local minimum of potential energy must be at the boundaries. Gravitational, electric and magnetic fields all belong to this category. Braunbek [18] (1939) derives a similar result, and also points out that for materials which have permittivity $\epsilon < \epsilon_0$ or permeability $\mu < \mu_0$, a stable equilibrium can be realized in a static electric or magnetic field respectively. In other words, if the material can be polarized or magnetized in the opposite direction of the field, it can produce a stable repulsive force. This is known as Earnshaw's theorem.

It turns out there are no materials with $\epsilon < \epsilon_0$, such that there is no stable suspension within a static electric field. On the other hand, lots of the materials are diamagnetic (μ slightly below μ_0), *e.g.* copper, water, and organic materials. Because of this property, it is possible to have stable suspension of such materials within a static magnetic field. For example, Geim [41] recently uses a static magnetic field to suspend a frog. Such a suspension is stable because water is mildly diamagnetic. Notice that if current is induced within the object to be suspended, it is considered dynamic, such as superconductive materials, and thus does not fall under the assumptions of Earnshaw's theorem.

For materials that are not diamagnetic or superconductive, they do not have a stable equilibrium point inside a static electric or magnetic field. However, they can have a "saddle" point inside a static field. In other words, they can be stable in one direction, and unstable in another direction. To create stable suspensions on such systems, we only need to stabilize the unstable directions. Geary [40] presents a variety of magnetic bearing designs that use combinations of permanent magnets to achieve stability in 5 degrees of freedom. The unstable direction can be stabilized by

feedback control[1].

Beams [14] (1946) magnetically suspended small solid steel balls in vacuum, and spun them up until they exploded by their own centrifugal forces at the order of ten million rpm. Dr. Beams has also developed many practical magnetic suspensions, such as a balance [13], high-speed rotating mirrors, ultracentrifuges [11], and concentric rotors [12]. Frazier [38] explored both electric and magnetic suspensions especially for the applications in gyroscopes developed at Draper Labs. This work presents a thorough treatment of tuned passive suspensions which were developed to center gyroscope floats in their fluid-filled housing.

2.2.2 Magnetic Suspension

The operating principles for magnetic suspensions can be divided into three main categories. Details on our use of this type of suspension are presented in Chapter 3.

1. Suspension by static field: stable repulsion forces, applicable to superconductors ($\sigma \to \infty$) and diamagnetics ($\mu < \mu_o$).

2. Suspension by alternating field: stable repulsion forces, applicable to conductors ($\sigma > 0$).

3. Suspension by controlling the magnetic field: unstable forces stabilized by tuning fields, applicable to ferromagnetic materials ($\mu \gg \mu_o$), paramagnetic materials ($\mu > \mu_o$), current-carrying objects and permanent magnets. Notice ferromagnetic materials lose their ferromagnetic properties above their Curie Temperatures (770°C for pure iron, and 358°C for pure Nickel [91]).

The application of magnetic suspensions used in wind tunnels can be found in Covert [25], Basmajian [8] and Stephens [99]. Such magnetic wind tunnels use the magnetization force to suspend an object, and use the required control current to estimate the aerodynamic force applied on the object. The application of magnetic

[1]Some magnetic bearing designs don't require a complete suspension, they can simply use mechanical bearings for the unstable directions.

suspensions used in high-speed trains can be found in Sinha [98] and Jayawant [50]. The application of magnetic suspensions used in precision engineering can be found in Trumper [102], which includes helpful rules for actuators and controllers design. Recent developments are presented at the International Symposium on Magnetic Suspension Technology [2] and at the International Symposium on Magnetic Bearings [1] conference series.

2.2.3 Magnetic Suspension of Flexible Structures

There are research done in Japan for the magnetic suspension of flexible structures for non-contact processing, which is very relevant to this thesis. Oshinoya [88] uses electromagnets to control a thin narrow plate deformation (36 cm by 4 cm by 0.3 cm) for hinged-hinged boundaries and hinged-free boundaries by using sub-optimal controllers. The thin plate is modeled as an Euler-Bernoulli beam, and the first 3 resonance modes are considered. Hayashiya [47, 46, 45] used electromagnets to suspend a thick rigid steel plate (50 cm by 10 cm by 2.2 cm) and a thin flexible steel plate (50 cm by 10 cm by 0.23 cm) without contact. The thick rigid plate can be suspended without problem. However, the suspension of the thin plate involves the stabilization of the resonance modes ,and is much difficult. The structural dynamics is measured experimentally. The thin plate was stabilized by placing 4 electromagnets on the 2nd vibration nodes, and 1 electromagnet on a 3rd vibration node, and by using a PID controller together with a notch filters.

In this thesis, we also aim to suspend the flexible beam without contact, and hence face similar problems that the high frequency modes tend to destabilize the system. We also face another challenge that we want to suspend the beam with varying boundary conditions, thus we cannot use model-based methods to stabilize the system, such as using notch filters, or placing sensors and actuators on the resonance nodes. In the end, we use a slow roll-up lead compensator, together with our developed sensor/actuator averaging method, and successfully suspend the structure without using model-based methods. The details will be discussed in Chapter 5 and Chapter 6.

2.2.4 Electrostatic Suspension

As mentioned earlier, because there are no electric analogs of superconductivity or diamagnetism, there can be no stable suspension in a static electric field. We thus need to control the electric field by active feedback control or a self-tuning circuit to stabilize an electrostatic suspension system. Electrostatic suspension is applicable to conductors ($\sigma > 0$) and dielectric materials ($\epsilon > \epsilon_o$). The advantages of using electric suspensions are that the response is fast, and the generated heat and magnetic field are much smaller compared to magnetic suspension. The disadvantage is that the force density is much lower than for magnetic suspension. The electrostatic force is limited by electric breakdown, which is about $1 \times 10^6 \sim 3 \times 10^6$ V/m in atmosphere, and $10^8 \sim 10^9$ V/m in high vacuum.

Possible arrangements of electrostatic suspension along with an estimation of the force limits will be discussed in Chapter 3. Due to the low force density of electrostatic suspension, there have not been many applications except that used in electric vacuum gyroscopes [84, 38] and micro-scale systems [58].

2.2.5 Electrostatic Suspensions of Plates

Recently, the electrostatic suspension of Silicon wafers and LCD glass plates have been of interest. Preliminary researches are done in University of Tokyo in Japan. In Jin [54, 53, 55], the suspension and propulsion of conductors and semiconductors are studied, where semiconductors are modeled as conductors. In Jeon [51, 52], the suspension and propulsion of dielectrics are studied, where dielectrics are modeled as resistors. In Chapter 3, I will modify the modeling of dielectrics to actual dielectric materials with resistance.

These papers introduce details of the experimental setups, and are good resources for our future studies on electrostatic suspensions. In these research, the structures are modeled as rigid bodies due to the low control bandwidth. The low control bandwidth may be the result of low electrostatic force density. The electrostatic suspension of flexible structures are not found in the literature.

2.3 Prior Art in Structural Dynamics and Vibration Control

This section reviews related work on modeling of moving structures and structural vibration control, including sensor/actuator positioning, modal control, and non-contact vibration control.

2.3.1 Modeling and Modal Analysis of Moving Structures

Although structural dynamics are well developed, the analysis of moving structures remains an area of active research. Mote [83] and Wickert [105] give general reviews of research on axially-moving materials. Most of earlier research on axially moving structures focused on free vibration and stability issues. In 1990, complex modal analysis was developed for axially moving structures, and decoupling of modal coordinates became possible.

In 1974, Meirovitch [73, 74] (1974) developed a modal analysis method for gyroscopic systems, in which objects vibrate while undergoing rotational relative motion. An example is an object attached to a spinning body by springs, and the vibration of the object will include the coriolis force ($2m\omega \times V$) and the centrifugal force (mV^2/R). In 1990, Wickert [106, 107] related the moving structure dynamics problem to gyroscopic systems, by introducing complex modal analysis in order to decouple the moving structure dynamics. The derived complex modal shapes (eigenfunctions) have orthogonal properties, hence we can decouple the dynamic equation into modal coordinates. Prior to this work, the analyses of moving structure responses were only done numerically.

Lee [64, 65] presents the energetics of second-order and fourth-order translating continua, including strings, tensioned pipes, beams, and fluid conveying pipes. Parker [90, 89] presents stability and critical speed criteria for axially moving continua, including strings supported by elastic foundation and beams. Lin [68] presents an analysis of axially moving plates.

Notice that a linear model of beam dynamics is only valid at subcritical speeds. Mote [82] derives a nonlinear model of an axially moving string, and shows that linear model will fail when moving speed approaches critical speed (wave speed). Wickert [104] uses a nonlinear model to describe moving beam dynamics and studies beam vibration above the critical speed. Sathyamoorthy [95, 96] reviews nonlinear plate vibrations research from 1979-1986.

2.3.2 Structural Vibration Control

There are many relevant references in the field of vibration control, especially for large space structures. Balas [7] reviews research on large space structure control theories. Most of the recent research work focuses on model-based controller design. Junkins [57] introduces the modeling of structures, reduced-order models, and model-based controller design. Fuller [39] reviews principles of modern active control techniques for structures. Meirovitch [76] presents an integrated approach to fundamental structural dynamics and control. Crawley [27] focuses on large space structure control, and introduces practical issues of modeling, control, distributed sensors and actuators (piezoelectric materials), and robust control techniques.

From these references, the common procedures for designing model-based controllers can be categorized into the following steps:

1. Modeling of structures: We first model the structural dynamics analytically or numerically. It is common to use numerical method such as Finite Element Method to model complicated structures. For the purpose of robust control, we include uncertainties in the model. To verify the accuracy of the model, it is always desirable to analyze the structural dynamics experimentally.

2. Modal analysis: For the purpose of controller design, we want to represent the model in state-space notation. We first decouple the dynamic equation into modal coordinates. Secondly, we truncate the higher order modes to reduce the model order. Finally, we assume a modal damping coefficient into each mode. Without damping, it is not possible to find a dynamic controller to stabilize a

structure. The damping coefficient is roughly $5 \times 10^{-4} \sim 4 \times 10^{-3}$ for steel [15].

3. Controller design: We can use model-based control techniques such as LQG control to design the controller based on the state-space model. Depends on the order of the model, the resulting controller design usually turns out to be a very high order controller, which will require a long calculation time in the computer. We can reduce the controller order by truncate less controllable or less unobservable modes.

4. Robust controller design: We can use different techniques to make the controller more robust to system uncertainties, such as $\mathcal{H}_\infty$ control, μ analysis, or Sensitivity Weighted LQG.

One specific approach to structural vibration control is the boundary control method. The basic idea is that for 2nd order vibrations, such as string transversal vibration or beam longitudinal vibration, we can derive a boundary condition to "match the impedance" of the structure, and make the vibration wave dissipated completely without any reflection [111, Chapter 9]. Chen [21] mathematically proves that Euler-Bernoulli beam energy decays exponentially by using damping control at boundaries (force or torque) and at intermediate points (force). In this paper, the control law is assumed static; no dynamics such as phase lag are modeled. Interestingly, for torque control at an intermediate point, the energy can not be proven to decay exponentially[2]. Morgül [80, 81] specifically includes dynamics in the boundary control law to a clamped-free beam and proved that the energy decays exponentially to zero. Applications of using boundary control can also be found in Wie [108] and Canbolat [20].

2.3.3 Sensor/Actuator Positioning

For experienced designers, the sensor/actuator locations for structural control can be qualitatively determined such that certain modes are controllable/observable, and

[2]Based on Professor Chen's reply to the me in 1999, in a personal communication, the problem of torque control at an intermediate point is still an open research issue.

certain modes are uncontrollable/unobservable. Recent research on sensor/actuator positioning tries to optimize this positioning rule quantitatively. These approaches first define the cost function, which is usually some combination of controllability gramians and observability gramians of certain modes. Secondly, standard optimization methods are used to determine the position of sensors and actuators such that the cost function is minimized (or maximized). Johnson [56] verifies the performance of such a method. Hać [43] illustrates this method for a simply supported beam and a rectangular plate. Yam [112] derives a sensor location synthesizing method in order to reduce the model order. Another example is to use specially-shaped distributed sensors and/or actuators to observe and/or control only certain modes. This approach is reviewed in the following section together with modal control.

2.3.4 Modal Control with Discrete Modal Filters and Distributed Sensors

Modal control plays an important role in structural vibration control. Engineers can analytically decouple the structural dynamics, and control only certain modes. The typical model-based control technique uses the following steps:

1. Sensor feedback: From single sensor or multiple sensors, the controller gets the feedback of the structure deformations.

2. Observer: The controller reconstructs modal coordinates by using observers. However, if the structure has an excited resonance mode that is not modeled, the observer will output estimated modal coordinates that are contaminated by this unmodeled mode, which is called observer spillover. Balas [6] uses comb filters to reduce the observer spillover. Meirovitch [72] uses discrete modal filters instead observers to avoid the observer spillover.

3. Modal Controller: Based on the estimated modal coordinates, the controller calculates the modal control force for each mode to be controlled.

4. Force output: Based on the model, the controller transforms modal forces into

real force for each actuator. However, if the structure has unmodeled resonance modes, the calculated forces can excite these modes, which is called control spillover.

The disadvantage of using this method is that the unmodeled dynamics causes observer spillover and control spillover. The observer spillover can destabilize the system, and the control spillover can excite unmodeled modes [6].

In order to effectively solve the observer spillover problem, Meirovitch [71, 72] develops the concept of discrete modal filters. This approach fits the measured displacements with modal shapes to obtain modal coordinates by simple algebra (no dynamic observer is involved). Due to the orthogonal properties of each mode, the unmodeled modal shapes will not contaminate the calculated modal coordinates, thus the observer spillover problem is solved. However, the disadvantage of using discrete modal filters is that we need a large number of sensors due to the following two reasons. First, with n sensors, we can only observe n modal coordinates at most. This is because we are simply solving algebra, and we can only solve n unknowns from n equations. Secondly, Fuller [39, Chapter 5] points out that this method needs to assume that those unmodeled modes have wavelengths larger than Nyquist wavelength (twice the sensor distance). In other words, if there are resonance modes with wavelengths shorter than twice the sensor distance, they will be aliased and can still contaminate the estimated coordinates.

In our experiment, we use 8 sensors and 8 actuators to suspend a tubular beam, thus the discrete modal filter method seems to be applicable to our system, as long as we do not change the system boundaries or beam positions. We did try to utilize it to control our system, however, the experiment was not successful. The reasons are believed to be that we do not have a straight beam, and we do not have identical sensors. Therefore, the 8 sensor outputs cannot be used to reconstruct the modal coordinates.

Another approach to modal control is the distributed sensors and actuators. The distributed actuators and sensors are made of sheets of shaped piezoelectric materials. While used as actuators, we apply voltage to the materials, they will deform in

certain direction. While used as sensors, we apply deformation to the materials, and they will output voltage. Bailey [5] develops a novel distributed piezoelectric-polymer actuator to control vibration modes of a cantilever beam. Clark [23] studies multiple distributed actuators for vibration control. The ideas of distributed actuators were then extended to distributed sensors. They are basically pieces of shaped piezoelectric materials adhered to the surface of the structure. The sensor outputs voltage as a function of the structure's curvature integrated over the area of the sensor. By designing the shape of the sensor, the output will have different weightings on the vibration modes. Miller [79] designs shaped distributed sensors on beams. Burke [19] analyzes distributed sensors on thin plates. Gu [42] designs shaped distributed sensors for plates to extract certain modal coordinates. Since distributed sensors are continuous, they do not have the aliasing problems as in discrete modal filters. However, Clark [22] points out that distributed sensors are very sensitive to placement errors. This study uses a distributed sensor to observe the 3rd mode on a simply supported beam, and intentionally misaligns the sensor by a 0.26% position error (1 mm misalignment on a 380 mm long beam), and shows that other modes can significantly contaminate the measured modal coordinate.

Most of the research of distributed sensors focuses on model-based modal sensing. Here the sensors are shaped to extract certain modal coordinates. Collins et al [24] focus on non-model-based distributed sensors; they design distributed sensors as spatial filters, and thus represent the closest prior art to our sensor averaging technique in the literature. In the beginning of this project, we did not mean to incorporate distributed sensors. Since we mainly focus on non-contact vibration control by position feedback and force output. However, after we developed sensor averaging and actuator averaging methods, and further extended the concept to continuous sensor/actuator averaging by using FIR windows, we actually meet the concept of distributed sensors.

The concepts of discrete modal filters and distributed sensors have one common property with sensor/actuator averaging: they are all spatial filters. Hence they have no phase lag problems as in temporal filters. The main differences are that

discrete modal filters and most of the distributed sensors are model-based filters, and sensor/actuator averaging method is a non-model-based filter. A main advantage of using sensor/actuator averaging method is the simplicity that we can use original sensors and actuators.

The comparison between discrete modal filters, distributed sensors and sensor / actuator averaging will further be discussed in Chapter 6. The application of using discrete modal filters in our experiment will be discussed in Chapter 9.

2.3.5 Non-contact Vibration Control

There are relatively few research efforts in the field of *non-contact* vibration control of flexible structures. Melcher [77] analyzes the problem of stabilizing a continuum electromechanical system with discrete spatial feedback control. Dressler [30] studies infinite continuum systems with discrete spatial and temporal feedback. Lang [61] develops control methods to stabilize an unstable wire mesh using electrostatic forces, and applies the results to the conceptual design of a 1 km diameter electrostatically figured satellite antenna made of a wire mesh. Ellis [33, 32] uses one sensor and one electromagnet to control the transverse vibration of thin circular saws, in the attempt to increase the transverse stiffness and damping without increasing the thickness of the saw blade. He encounters difficulties due to phase lag, actuator nonlinearities, and sensor/actuator noncollocation problems, which I also faced and attempted to solve in this thesis. Okada [85] used four electromagnets to control the vibration of a thin rotor shell, including independent PD control and modal control.

Chapter 3

Electromagnetic Theory and Suspension Technology

This chapter reviews the operating principles of electromagnetic suspensions which are relevant to our research. The purpose is to understand what materials we can suspend, and what principles we should use to suspend these materials. Furthermore, this chapter develops the maximum force density for each suspension principle. This information can be used to understand the physical limits of the looks and material dimensions that we can suspend.

3.1 Fundamental Electromagnetic Theory

In this section, we describe the fundamentals of electromagnetic theory, which are essential for the design of both actuators and sensors for electromagnetic suspensions. In the following subsections, I summarize the basic electromagnetic equations, and the method of calculating forces from a field distribution.

3.1.1 Summary of Fundamental Electromagnetic Theory

The fundamental theories of electromagnetics can be found in Haus [44], including Maxwell's Laws, solutions of Laplace Equations, magnetic circuit modeling, electric

Table 3.1: Variables used in electromagnetic analysis (SI units).

Variable	Unit	Description
ϵ_o	Farad/m	Permittivity of free space, $\epsilon_o = 8.854 \times 10^{-12}$
$\vec{E}$	Volt/m	Electric field intensity
$\vec{P}$	Coul/m^2	Polarization density
$\vec{D}$	Coul/m^2	Displacement flux density, $\vec{D} \equiv \epsilon_o \vec{E} + \vec{P}$
ρ_f	Coul/m^3	Free charge density
ρ_p	Coul/m^3	Polarization charge density
ρ_{total}	Coul/m^3	Total charge density, $\rho_{total} = \rho_f + \rho_p$
μ_o	Henry/m	Permeability of free space: $4\pi \times 10^{-7}$
$\vec{H}$	A/m	Magnetic field intensity
$\vec{M}$	A/m	Magnetization density
$\vec{B}$	Tesla or Weber/m^2	Magnetic flux density, $\vec{B} \equiv \mu_o(\vec{H} + \vec{M})$
ρ_m	Weber/m^3	Magnetization charge density
ϕ	Weber	Magnetic flux
λ	Weber	Magnetic flux linkage, $\lambda = N\phi$

polarization, and magnetization. More advanced topics can be found in the Woodson [110, 111] and Melcher [78] , including moving frames, Maxwell stress tensor, and magnetic diffusion.

The theories used in this thesis are summarized in the following tables. Table 3.1 shows the electromagnetic variables used in this thesis, and the SI unit associated with each variable.

Table 3.2 shows the Maxwell's Equations in both differential and integral forms. Table 3.3 shows the Maxwell's Equations and Maxwell stress tensor equations under the electroquasistatic (EQS) and magnetoquasistatic (MQS) limiting cases. In EQS systems, the time derivative of magnetic variables is negligible: $\partial \vec{B}/\partial t \approx 0$. On the other hand, in the MQS case, the time derivative of electric variables is negligible: $\partial \vec{D}/\partial t \approx 0$ and $\partial \rho_f/\partial t \approx 0$. As long as electromagnetic waves are not important, we can analyze electromagnetic components by either one of the EQS or MQS assumptions.

Table 3.2: Maxwell's Integral Laws and Differential Laws.

Name	Integral Law	Differential Law
Gauss' Law	$\oint_S \epsilon_o \vec{E} \cdot d\vec{a} = \int_V \rho_{total} dv$, or $\oint_S \vec{D} \cdot d\vec{a} = \int_V \rho_f dv$	$\nabla \cdot \epsilon_o \vec{E} = \rho_{total}$, or $\nabla \cdot \vec{D} = \rho_f$
Ampere's Law	$\oint_C \vec{H} \cdot d\vec{l} = \int_S \vec{J} \cdot d\vec{a} + \frac{d}{dt} \int_S \vec{D} \cdot d\vec{a}$	$\nabla \times \vec{H} = \vec{J} + \frac{\partial \vec{D}}{\partial t}$
Faraday's Law	$\oint_C \vec{E} \cdot d\vec{l} = -\frac{d}{dt} \int_S \vec{B} \cdot d\vec{a}$	$\nabla \times \vec{E} = -\frac{\partial \vec{B}}{\partial t}$
Magnetic Flux Continuity	$\oint_S \vec{B} \cdot d\vec{a} = 0$	$\nabla \cdot \vec{B} = 0$
Charge Conservation	$\oint_S \vec{J} \cdot d\vec{a} + \frac{d}{dt} \int_V \rho_f dv = 0$	$\nabla \cdot \vec{J} + \frac{\partial \rho_f}{\partial t} = 0$

Table 3.3: Maxwell's Differential Laws for EQS and MQS.

Name	EQS	MQS
Gauss' Law	$\nabla \cdot \epsilon_o \vec{E} = \rho_{total}$, or $\nabla \cdot \vec{D} = \rho_f$	$\nabla \cdot \epsilon_o \vec{E} = \rho_{total}$, or $\nabla \cdot \vec{D} = \rho_f$
Ampere's Law	$\nabla \times \vec{H} = \vec{J} + \frac{\partial \vec{D}}{\partial t}$	$\nabla \times \vec{H} = \vec{J}$
Faraday's Law	$\nabla \times \vec{E} = 0$	$\nabla \times \vec{E} = -\frac{\partial \vec{B}}{\partial t}$
Magnetic Flux Continuity	$\nabla \cdot \vec{B} = 0$	$\nabla \cdot \vec{B} = 0$
Charge Conservation	$\nabla \cdot \vec{J} + \frac{\partial \rho_f}{\partial t} = 0$	$\nabla \cdot \vec{J} = 0$
Maxwell Stress Tensor Force	$T_{ij} = \epsilon E_i E_j - \frac{1}{2}\delta_{ij}\epsilon E_k E_k$ $F_i = \int_V f_i dv = \oint_S T_{ij} n_j ds$	$T_{ij} = \mu H_i H_j - \frac{1}{2}\delta_{ij}\mu H_k H_k$ $F_i = \int_V f_i dv = \oint_S T_{ij} n_j ds$

Table 3.4: Polarization and Magnetization.

Polarization	
$\vec{D} \equiv \epsilon_o \vec{E} + \vec{P}$	$\vec{D}$:displacement flux density, $\vec{P}$:polarization density
$\vec{D} = \epsilon \vec{E}$	Linear polarization, ϵ: permittivity or dielectric constant
$\epsilon \equiv \epsilon_o(1 + \chi_e)$	χ_e: dielectric susceptibility (air:0.00059, paper:1.0)
$\nabla \cdot \vec{D} = \rho_f$	ρ_f: free charge density
$\nabla \cdot \epsilon_o \vec{E} = \rho_{total}$	ρ_{total}: total charge density
$\nabla \cdot \vec{P} = -\rho_p$	ρ_p: polarization charge density
$\vec{f} = (\vec{P} \cdot \nabla)\vec{E}$	Kelvin polarization force density
Magnetization	
$\vec{B} \equiv \mu_o(\vec{H} + \vec{M})$	$\vec{M}$:magnetization density
$\vec{B} = \mu \vec{H}$	Linear magnetization, μ:permeability
$\mu \equiv \mu_o(1 + \chi_m)$	χ_m: magnetic susceptibility (Silicon steel: 7×10^4)
$\nabla \cdot \vec{B} = 0$	Magnetic flux continuity
$\nabla \cdot \mu_o \vec{H} = \rho_m$	ρ_m: "virtual" magnetization charge density
$\nabla \cdot \mu_o \vec{M} = -\rho_m$	
$\vec{f} = (\mu_o \vec{M} \cdot \nabla)\vec{H}$	Kelvin magnetization force density

Table 3.4 shows the equations associated with electric polarization and magnetization. Notice the duality of these two sets of equations.

3.1.2 Force Estimation

We can solve for the force in a given field problem by first solving for the electromagnetic field, and then calculating the Maxwell stress tensor from the field distribution [111]. The force calculation will be demonstrated in Chapter 7 when we calculate the actuator forces.

In the stage of conceptual design, we need a tool to estimate the order of the suspension force. In the following, I introduce methods of estimating forces for different suspension principles. I categorize these methods into three simplified approaches: (1) a single dipole model, (2) volume force density, and (3) surface force density.

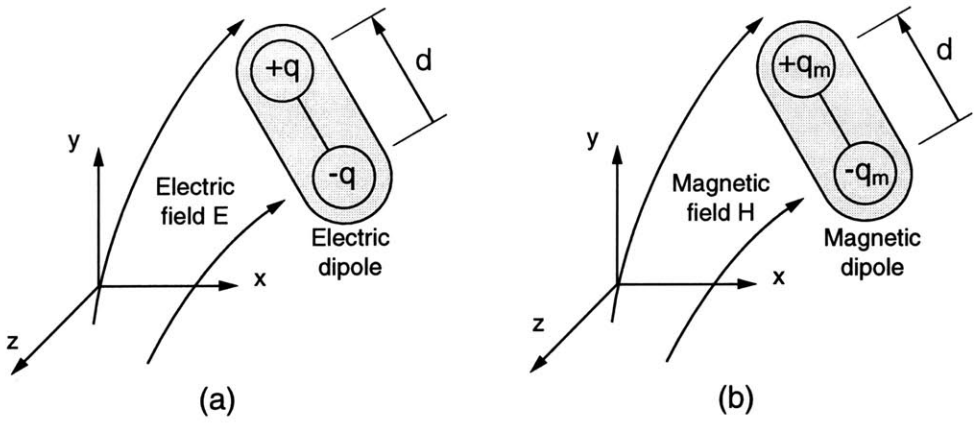

Figure 3-1: (a) Electric dipole $\vec{P} = q\vec{d}$, and (b) magnetic dipole $\mu_0\vec{M} = q_m\vec{d}$.

Single Dipole Model

For the suspension of magnetized or polarized materials, we can model the object by a single dipole, and calculate the force density by using the Kelvin force density.

A single dipole model is demonstrated in Figure 3-1: Figure 3-1(a) shows an electric dipole in an electric field, and Figure 3-1(b) shows a magnetic dipole in a magnetic field. The Kelvin force densities for these two cases are shown below [78, §3.6]:

1. Kelvin Polarization Force Density [N/m^3]:

$$\vec{F_v} = (\vec{P} \cdot \nabla)\vec{E}_a, \tag{3.1}$$

   where $\vec{E}_a$ is the applied electric field without the contribution of the dipole field.

2. Kelvin Magnetization Force Density [N/m^3]:

$$\vec{F_v} = (\mu_o\vec{M} \cdot \nabla)\vec{H}_a, \tag{3.2}$$

   where $\vec{H}_a$ is the applied magnetic field without the contribution of the dipole field.

These equations tell us that the force will be proportional to the polarization / magnetization intensity and the gradients of the field. Kelvin force density is easy to

visualize, and is thus easy to use in conceptual design. However, if we actually solve for the field distribution (E and H), it maybe difficult to distinguish which component is the applied field (E_a and H_a), and which component is the dipole field.

Volume Force Density

For the suspension of diamagnetic materials, paramagnetic materials, or dielectric materials, the field inside the materials is not negligible, we need to consider the volume force density. We calculate its volume force density, and then integrate along the whole volume to obtain the total force. For linear polarization and magnetization materials ($\vec{D} = \epsilon\vec{E}$ and $\vec{B} = \mu\vec{H}$), the force density is better represented by Korteweg-Helmholz force density [78, §3.7-3.8]. For incompressible materials, the force densities are:

1. Electrostatic volume force density [N/m^3]:

$$\vec{F}_v = \rho_f\vec{E} - \frac{1}{2}E^2\nabla\epsilon, \tag{3.3}$$

   which includes free-charge force density, and a polarization force density concentrated where there are permittivity gradients.

2. Magnetic volume force density [N/m^3]:

$$\vec{F}_v = \vec{J}_f \times \vec{B} - \frac{1}{2}H^2\nabla\mu, \tag{3.4}$$

   which includes Lorentz force density, and a magnetization force density concentrated where there are permeability gradients.

Notice that for uniform materials, the polarization and magnetization force is actually confined to interfaces where there are different electric or magnetic properties. To show the process of using this to calculate the force at the interface, we use a magnetic example as shown in Figure 3-2. In this problem, we assume $J_f = 0$, *i.e.*, no current is flowing. From Maxwell's Laws, we can derive the boundary conditions

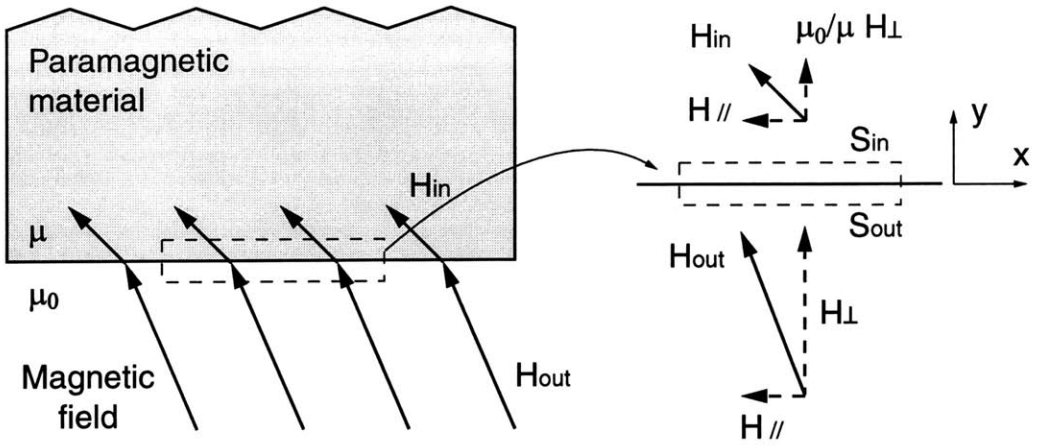

Figure 3-2: Magnetization force at the interface.

for magnetizable materials as:

$$\nabla \times \vec{H} = \vec{J} = 0 \Rightarrow (H_{out})_{\parallel} = (H_{in})_{\parallel}, \tag{3.5}$$

$$\nabla \cdot \vec{B} = 0 \Rightarrow (B_{out})_{\perp} = (B_{in})_{\perp}. \tag{3.6}$$

Further we use Maxwell stress tensor to calculate the forces at the interface. Using the control volume at the interface as shown in Figure 3-2, we have the shear force density F_x in N/m^2:

$$F_x = (T_{xy})_{in} - (T_{xy})_{out} = (\mu H_x H_y)_{in} - (\mu_0 H_x H_y)_{out} = 0 \tag{3.7}$$

And we have the normal force density F_y in N/m^2:

$$\begin{aligned} F_y &= (T_{yy})_{in} - (T_{yy})_{out} \\ &= \left(-\frac{1}{2}\mu H_x^2 + \frac{1}{2}\mu H_y^2\right)_{in} - \left(-\frac{1}{2}\mu_0 H_x^2 + \frac{1}{2}\mu_0 H_y^2\right)_{out} \\ &= \left(-\frac{1}{2}\mu H_{\parallel}^2 + \frac{\mu_0^2}{2\mu} H_{\perp}^2\right) - \left(-\frac{1}{2}\mu_0 H_{\parallel}^2 + \frac{1}{2}\mu_0 H_{\perp}^2\right) \\ &= \left(-\frac{1}{2}\mu H_{\parallel}^2 + \frac{1}{2\mu} B_{\perp}^2\right) - \left(-\frac{1}{2}\mu_0 H_{\parallel}^2 + \frac{1}{2\mu_0} B_{\perp}^2\right) \\ &= -\frac{1}{2}(\mu - \mu_0) H_{\parallel}^2 - \frac{1}{2}\left(\frac{1}{\mu_0} - \frac{1}{\mu}\right) B_{\perp}^2 \end{aligned} \tag{3.8}$$

This equation tells us that both a perpendicular field and a tangential field will attract a material with $\mu > \mu_0$, which is a reasonable result. I present this equation in such a way because $H_{\parallel}$ and $B_{\perp}$ are the same inside and outside the material, given that there are no surface currents.

Similarly, the polarization force can be calculated. We assume $\rho_f = 0$, *i.e.*, there are no free charge inside the material. From Maxwell's Laws, we can derive the boundary conditions for polarizable materials as:

$$\nabla \times \vec{E} = 0 \Rightarrow (E_{out})_{\parallel} = (E_{in})_{\parallel}, \tag{3.9}$$

$$\nabla \cdot \vec{D} = \rho_f = 0 \Rightarrow (D_{out})_{\perp} = (D_{in})_{\perp}. \tag{3.10}$$

We can calculate the polarization force density similar to calculating the magnetization force density.

Therefore, we summarize the polarization/magnetization force density at the interface in the following:

1. Polarization surface force density [N/m^2]:

$$F_s = \frac{1}{2}E_{\parallel}^2(\epsilon - \epsilon_0) + \frac{1}{2}D_{\perp}^2(\frac{1}{\epsilon_0} - \frac{1}{\epsilon}), \tag{3.11}$$

   where F_s is defined positive towards the outside of the object.

2. Magnetization surface force density [N/m^2]:

$$F_s = \frac{1}{2}H_{\parallel}^2(\mu - \mu_0) + \frac{1}{2}B_{\perp}^2(\frac{1}{\mu_0} - \frac{1}{\mu}), \tag{3.12}$$

   where F_s is defined positive towards the outside of the object.

Surface Force Density

When the magnetic/electric field inside the materials is negligible, we can further simplify the force calculation to surface force only. Such cases are like magnetic suspensions of ferromagnetic materials, perfect conductors, and moving conductors,

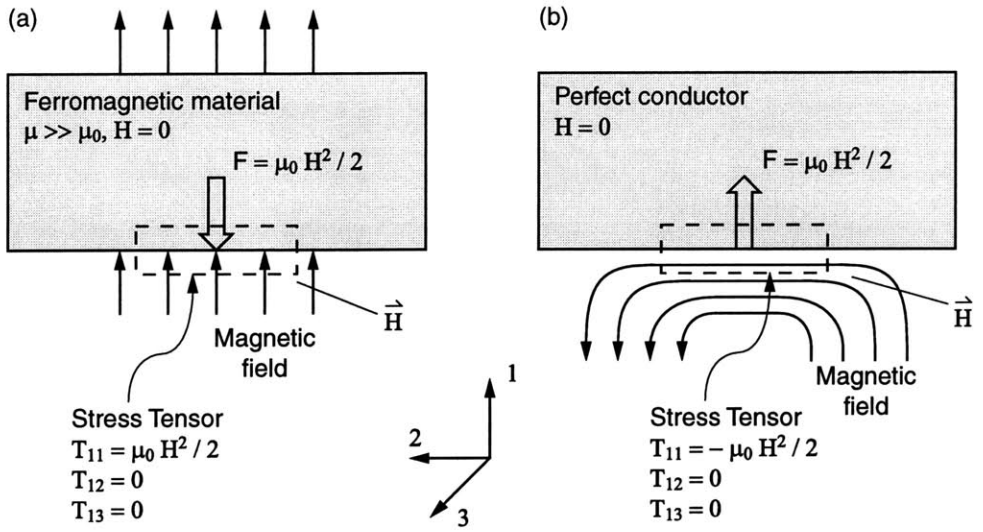

Figure 3-3: (a) Attractive force, and (b) repulsive force.

and electrostatic suspensions of conductors and semiconductors. We calculate the surface force density, and integrate along the surface to obtain the total force. We calculate the force density by using Maxwell stress tensor [111], as listed in Table 3.3.

We use a magnetic example as demonstrated in Figure 3-3: Figure3-3(a) shows an attractive force type, and Figure3-3(b) shows a repulsive force type. For the surface normal in the '1' direction, we calculate Maxwell stress tensor T_{1j}, and the force will be $\int T_{1j} n_j ds_1$. For the attractive force type, $|\vec{H}| = H_\perp = H$, the Maxwell stress tensor thus becomes $\mu_0 H^2/2$. For the repulsive force type, $|\vec{H}| = H_\parallel = H$, the Maxwell stress tensor becomes $-\mu_0 H^2/2$.

Similarly, the electrostatic force density can be calculated. Therefore, we can summarize both electrostatic and magnetic surface force densities in the following:

1. Electrostatic force density [N/m^2]:

$$F_s = \frac{1}{2}\epsilon_0 E^2. \tag{3.13}$$

Notice in Equation 3.11, if $\epsilon \gg \epsilon_0$, we will have $E_\parallel \to 0$, thus $F_s \approx D_\perp^2/(2\epsilon_0) = \epsilon_0 E_{out}^2/2$, which agrees with Equation 3.13.

2. Magnetic force density [N/m^2]:

$$F_s = \frac{1}{2}\mu_0 H^2, \tag{3.14}$$

Notice in Equation 3.11, if $\mu \gg \mu_0$, we will have $H_{\parallel} \to 0$, thus $F_s \approx B_{\perp}^2/(2\mu_0) = \mu_0 H_{out}^2/2$, which agrees with Equation 3.14.

3.1.3 Force Limit

These electromagnetic forces are usually limited by the following two factors:

1. Maximum magnetic flux density B_{max} due to magnetic saturation: In most cases, when we design a magnetic suspension, we use back-iron to guide the magnetic flux, *i.e.*, in steel or silicon iron laminations. These materials have magnetic saturation at $B \approx 1.5$ Tesla. After the magnetic saturation, the material has a relative permeability near μ_0 such that $\triangle B = \mu_0 \triangle H$. If we need higher magnetic flux density, the iron is no longer effective, and thus we will require a much greater coil current to drive this flux.

2. Maximum electric field intensity E_{max} due to electric discharge: When we apply electrostatic suspension, it will be limited by electric breakdown (spark). Discharge happens when $E \approx 1 \times 10^6 \sim 3 \times 10^6$ V/m in atmosphere, and $E \approx 10^8 \sim 10^9$ V/m in high vacuum.

Practically, the magnetic force of the actuators are often limited by the limited power dissipation too. We will discuss this issue when we design the actuators in Chapter 7. In this chapter, we will focus on the limit due to magnetic saturation.

3.2 Magnetic Suspension

This section describes the principles of magnetic suspension and their force density limits. In general, as long as the material is ferromagnetic ($\mu \gg \mu_o$), paramagnetic ($\mu > \mu_o$), diamagnetic ($\mu < \mu_o$), or conductive ($\sigma > 0$), it can be suspended by a

magnetic field. The principles of magnetic suspensions can be divided into three main categories, and the arrangements and maximum forces will be discussed in detail in the following sections.

1. Suspension by a static magnetic field: stable repulsion force, applicable to diamagnetic materials ($\mu < \mu_o$) and superconductors ($\sigma \rightarrow \infty$) .

2. Suspension by an alternating magnetic field: stable repulsion force, applicable to non-magnetic conductors ($\mu \approx \mu_o$ and $\sigma > 0$), such as aluminum or copper. The alternating magnetic field $\vec{B}$ induces eddy currents $\vec{J}$ inside the conductors, and the magnetic field is repelled and can only diffuse a certain skin depth in the conductive material.

3. Suspension by controlling the magnetic field via active feedback control or a self-tuning circuit. This method can stabilize an unstable force, and thus is applicable to ferromagnetic materials ($\mu \gg \mu_o$), paramagnetic materials ($\mu > \mu_o$), current-carrying objects and permanent magnets. Notice that ferromagnetic materials will lose their ferromagnetism above their Curie Temperatures (770°C for pure iron, and 358°C for pure Nickel [91]); this limits the temperature range for which this approach is applicable. Fortunately, when iron loses ferromagnetism at high temperatures, it is still conductive and can be suspended using an alternating magnetic field. Feedback control can also be used in the previous two open-loop systems to improve their performance.

3.2.1 Suspension by a Static Magnetic Field

Stable suspension by a static magnetic field is possible for diamagnetics ($\mu < \mu_o$) and superconductors ($\sigma \rightarrow \infty$). The operating principles are illustrated in Figure 3-4. These systems generate stable repulsion forces. Figure 3-4(a) shows the suspension of diamagnetic materials, such as organic materials ($\mu \approx 0.999991\mu_0$). Figure 3-4(b) shows the suspension of perfect conductors, which generate currents inside the material to keep the magnetic field outside the material, and the current inside the perfect conductor does not dissipate power nor decay with time.

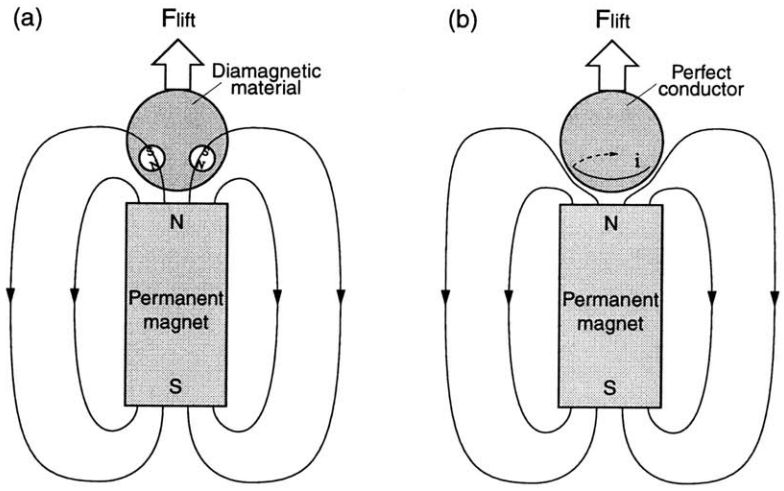

Figure 3-4: Stable suspension by a static magnetic field: (a) diamagnetic materials are magnetized in the opposite direction of the applied magnetic field and thus produce a repulsion force, and (b) perfect conductors have no magnetic field inside the material and thus create a suspension force.

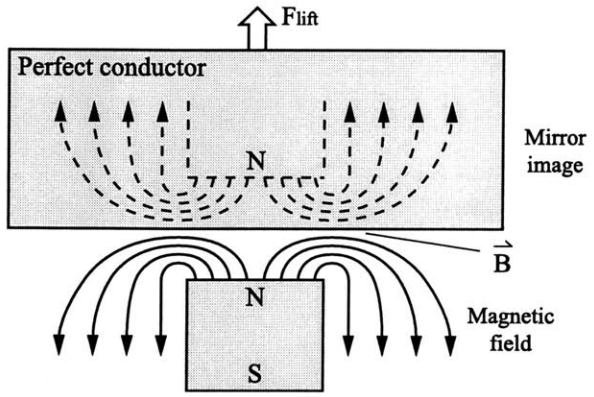

Figure 3-5: Force estimation of a perfect conductor in a static magnetic field.

Magnetic Force on Perfect Conductors

To calculate the magnetic force on the perfect conductor, we use an example as shown in Figure 3-5. The magnetic field from the permanent magnet cannot penetrate the prefect conductor, hence the magnetic field can be calculated by assuming a mirror image inside the perfect conductor. Assuming the magnetic flux density on the surface is calculated to be $\vec{B}$, as shown in the surface force model, the repulsion force density

will be

$$F_s = \frac{\mu_0 H^2}{2} = \frac{B^2}{2\mu_0}, \tag{3.15}$$

where F_s is the surface force density in $\mathrm{N/m^2}$. A normal limit to magnetic flux density is the saturation of the back iron of the actuator, $B_{max} \approx 1.5$ Tesla for steel. Hence we will have maximum surface force density of

$$F_{max} = \frac{B_{max}^2}{2\mu_0} = \frac{1.5^2}{2 \times 4\pi \times 10^{-7}} = 9 \times 10^5 \mathrm{N/m^2}. \tag{3.16}$$

Magnetic Force on Diamagnetic materials

Diamagnetic materials have $\vec{B} = \mu_0(\vec{H} + \vec{M})$, and linear diamagnetic materials have magnetization intensity $\vec{M} = \chi_m \vec{H}$. For example, organic materials have a magnetic susceptibility $\chi_m = -0.000009$. Because all diamagnetic materials have magnetic susceptibility $\chi_m \approx 0$, the diamagnetic materials have a negligible effect on the applied magnetic field. Hence we can use the single dipole model to predict the force.

The force density of a magnetic dipole inside a magnetic field can be calculated by the Kelvin magnetization force density:

$$\vec{F} = \mu_0(\vec{M} \cdot \nabla)\vec{H} = \mu_0(\chi_m \vec{H} \cdot \nabla)\vec{H} \Rightarrow |\vec{F}| = \frac{1}{2}\mu_0 \chi_m \nabla H^2, \tag{3.17}$$

where F is force density in $\mathrm{N/m^3}$, M is magnetization intensity in A/m, and H is magnetic field intensity in A/m.

Assume a simple geometry as in Figure 3-6, assume the diamagnetic material is a water drop which has $\chi_m = -0.000009$. We have radial magnetic field intensity

$$\vec{H} = H_r = H_i \frac{R_i^2}{r^2} \ \mathrm{N/m^3}, \tag{3.18}$$

where H_i is the magnetic field intensity at $r = R_i$. The magnetization force becomes

$$F_r = \frac{1}{2}\mu_0 \chi_m \frac{\partial}{\partial r} H_r^2 = -2\mu_0 \chi_m H_i^2 \frac{R_i^4}{r^5}. \tag{3.19}$$

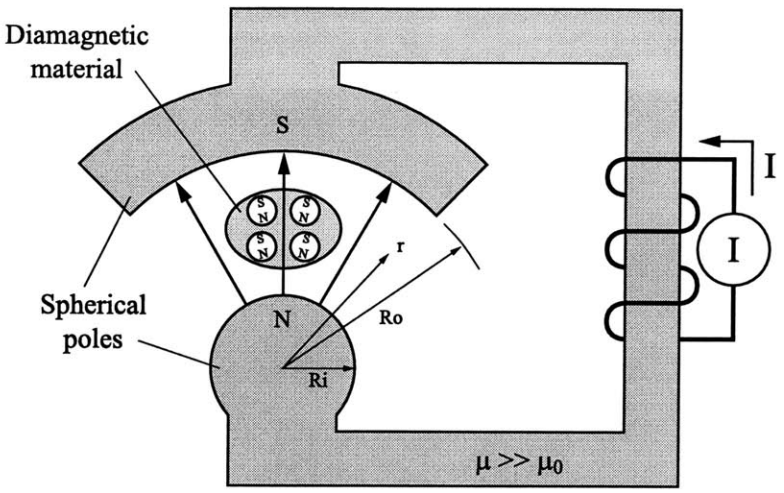

Figure 3-6: Force estimation of a diamagnetic material in a static magnetic field.

If we assume $B_{max} = 1.5$ Tesla, the resulting maximum force becomes:

$$F_{max} = -2\chi_m \frac{B_{max}^2}{\mu_0} \frac{R_i^4}{r^5} = 32 \frac{R_i^4}{r^5} \text{ N/m}^3 \tag{3.20}$$

$$\Rightarrow F_{max} = 32 \frac{1}{R_i} \text{ N/m}^3 \text{ when in contact } (\ r = R_i\ ), \tag{3.21}$$

which is a very small force. Since water has weight density of 1×10^4 N/m^3, we will need $R_i < 3$ mm to suspend a spherical water drop using normal magnetic materials.

However, larger bias fields B_{max} can be obtained via superconducting magnets or fluid-cooled magnets, and thereby suspend larger diamagnetic objects. Geim [41] uses fluid-cooled magnets to apply a static magnetic field with $B = 20$ Tesla, and successfully suspends a little frog.

3.2.2 Suspension by an Alternating Magnetic Field

Stable suspension by an alternating magnetic field is applicable to non-magnetic conductors ($\sigma > 0$), such as aluminum or copper. The operating principles are illustrated in Figure 3-7. Figure 3-7(a) shows an alternating magnetic field generated by an alternating current source. Figure 3-7(b) shows a constant magnetic field moving along a non-magnetic conductor. Both methods induce eddy-currents inside the conductors, and the magnetic field is repelled and can only diffuse a certain skin depth into the

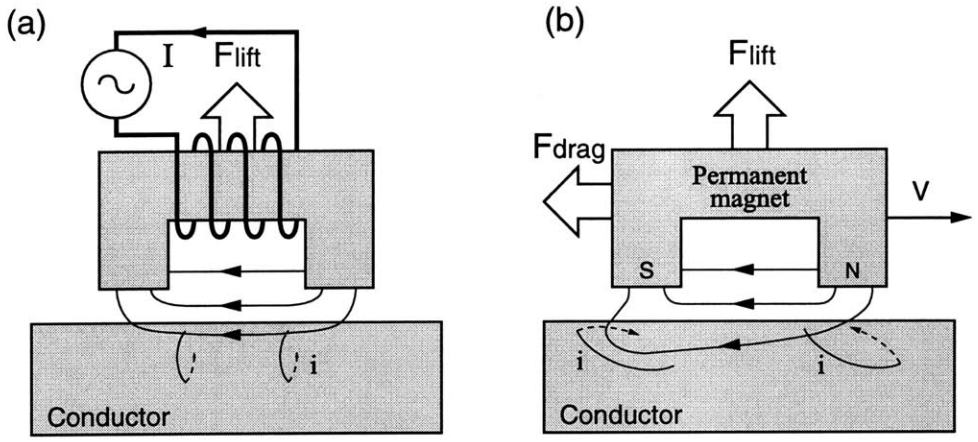

Figure 3-7: Stable suspension of conductive materials by an alternating magnetic field: (a) an alternating current source produces an alternating field, and induces eddy-currents inside the conductor, and (b) a moving field source creates a similar response.

conductor.

The calculation of the lifting force is similar to that of perfect conductors. To calculate the maximum force, we assume the field source is moving very fast or the excitation frequency is very high. Hence the diffusion skin depth is very small, and we can assume a mirror image inside the conductor and thereby analyze the field. Assuming the magnetic flux density on the surface is calculated to be $\vec{B}$, as shown before, the repulsion force density will be

$$F_s = \frac{\mu_0 H^2}{2} = \frac{B^2}{2\mu_0}, \tag{3.22}$$

where F_s is the surface force density in $\mathrm{N/m^2}$. Again, limited by the magnetic saturation of the back iron: ($B_{max} \approx 1.5$ Tesla for steel). We thus have a maximum surface force density of $F_{max} = 9 \times 10^5$ $\mathrm{N/m^2}$, which is significantly large compared to the weight of materials. For example, aluminum has weight density of 2.6×10^4 $\mathrm{N/m^3}$. If we could drive an alternating magnetic field of 1.5 Tesla at high frequencies, we can suspend a 35 m thick slab of aluminum.

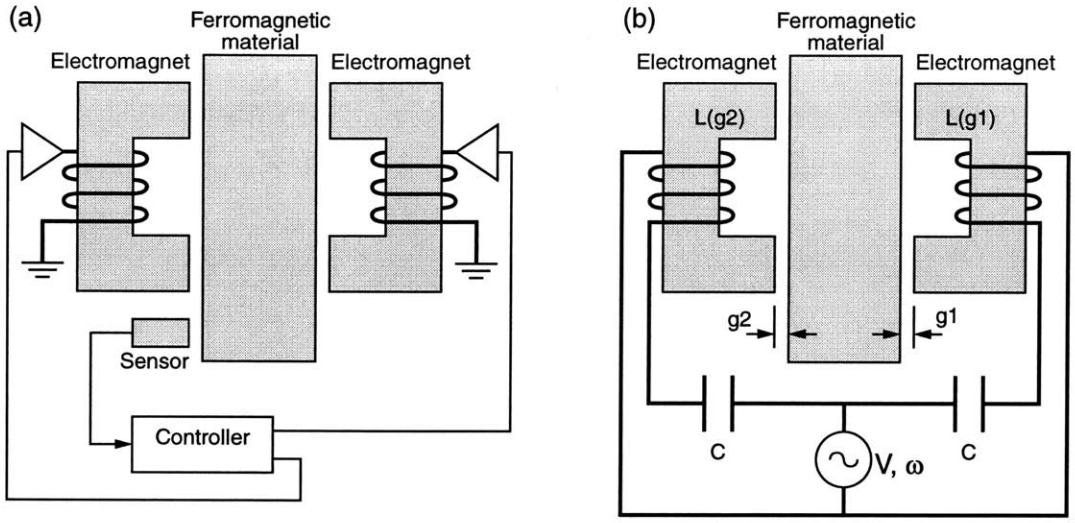

Figure 3-8: Stable suspension by controlled magnetic fields: (a) active feedback control, and (b) a self-tuning circuit.

3.2.3 Suspension by Controlled Magnetic Fields

The operating principles for this approach are illustrated in Figure 3-8. This method can be used in conjunction with the previous two open-loop systems to improve the performance. It can also be used to stabilize unstable electromagnetic forces, which is applicable to ferromagnetic materials ($\mu \gg \mu_o$), paramagnetic materials ($\mu > \mu_o$), current-carrying objects and permanent magnets. The controlled field can be obtained either from active feedback control or by a self-tuning circuit. Figure 3-8(a) uses active control to adjust the magnetic field according to the sensor feedback. One example of a self-tuning circuit design is shown in Figure 3-8(b). Here an electromagnet series with a capacitor is driven by an AC voltage. When the air gap increases, the inductance decreases, the current increases, and the attractive force increases with the current to stabilize the suspension.

Magnetic Force on Ferromagnetic Materials

For ferromagnetic materials, the magnetic field intensity H inside the material is negligible, and hence we can simply calculate the surface force. To calculate the limit of magnetization force, we use a simple example as shown in Figure 3-9. Magnetization

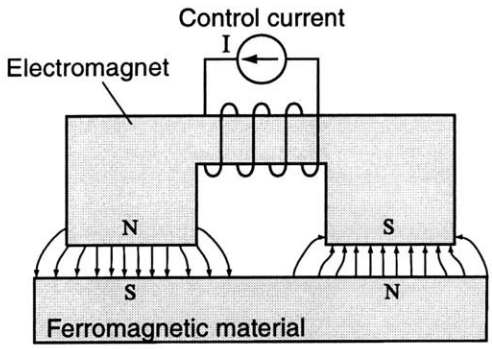

Figure 3-9: Estimation of magnetization force density on ferromagnetic materials.

force on ferromagnetic materials can be represented by

$$F_s = \frac{B^2}{2\mu_0}, \tag{3.23}$$

where F_s is the surface force density in N/m^2, B is the magnetic field between the gap in Tesla, and $\mu_0 = 4\pi \times 10^{-7}$ H/m is the permeability of the air gap. If we use the maximum magnetic field of B_{max}=1.5 Tesla due to saturation of actuator or the steel target, the maximum force density is $F_{max} \approx 9 \times 10^5$ N/m^2. For example, steel has a weight density of 7.8×10^4 N/m^3. If we can apply a magnetic field of 1.5 Tesla, we can suspend up to a 12 m thick slab of steel.

Magnetic Force on Current-carrying Conductors

The Lorentz force density on a current-carrying conductor is given by:

$$\vec{F_v} = \vec{J} \times \vec{B}, \tag{3.24}$$

where $\vec{F_v}$ is volume force density in N/m^3, $\vec{J}$ is current density in A/m^2, and $\vec{B}$ is the applied magnetic field in Tesla. If we assume a maximum current density of $J_{max} = 5 \times 10^6$ A/m^2 due to thermal dissipation limits, and a maximum magnetic field B_{max}=1.5 Tesla due to magnetic saturation of the actuator, we can obtain the maximum force density $F_{max} \approx 7.5 \times 10^6$ N/m^3. For example, aluminum has weight density of 2.6×10^4 N/m^3, which is much smaller than the maximum suspension force

density.

3.3 Electrostatic Suspension

This section describes the principles of electrostatic suspension and the limit of force density.

3.3.1 Principles of Electrostatic Suspension

There is no stable suspension in a static electric field since there are no materials with $\epsilon < \epsilon_0$. We thus need to control the electric field by active feedback control or by a self-tuning circuit to stabilize an electrostatic suspension system. The advantages of using electric suspension are that the response is fast, and the generated heat and magnetic field are much smaller as compared with a magnetic suspension. The disadvantage is that the force density is much lower than with magnetic suspensions. The electrostatic force is usually limited by electric breakdown at about $1 \times 10^6 \sim 3 \times 10^6$ V/m in atmosphere, and $10^8 \sim 10^9$ V/m in high vacuum.

Theoretically it is not possible to apply electromagnetic suspension on materials with conductivity $\sigma = 0$, permittivity $\epsilon = \epsilon_0$ and permeability $\mu = \mu_0$. However, most insulators still have a small conductivity, for example, ordinary glass has $\sigma \approx 10^{-12}$ mho/m, fused quartz has $\sigma < 10^{-17}$ mho/m. The material surface may also have a significant conductivity due to contamination. Hence it is still possible to accumulate electric charges on their surfaces, and suspend the object by feedback control, as was done by Jeon [51, 52] for the suspension of glass plates.

3.3.2 Electrostatic Suspension of Conductors and Semiconductors

The operating principles for controlled electrostatic suspensions are illustrated in Figure 3-10. Since the electric field inside the material is negligible, we can simply calculate the surface force.

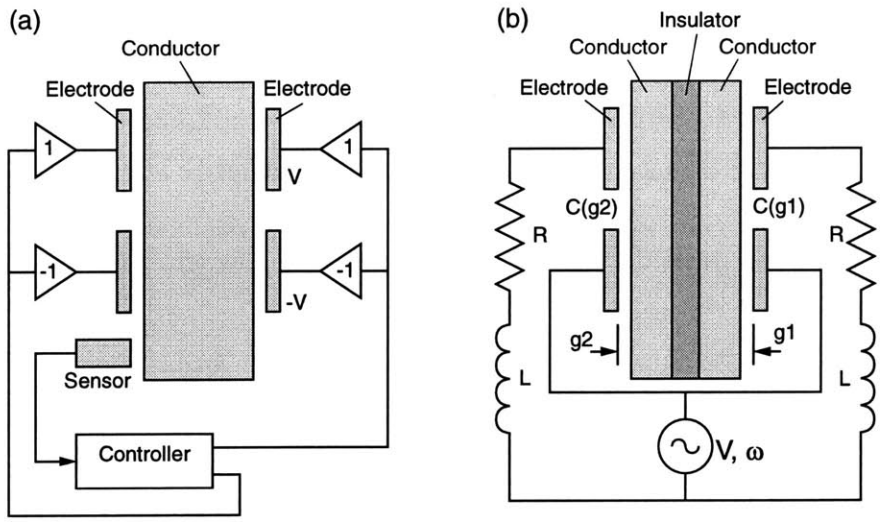

Figure 3-10: Stable suspension by controlled electric fields: (a) active feedback control, and (b) a self-tuning circuit.

To calculate the limit of electrostatic force, we use a simple example as shown in Figure 3-11. The electrostatic force density on a conductor can be represented by:

$$F_s = \frac{\epsilon_0 E^2}{2}, \tag{3.25}$$

where F_s is the surface force density in $\mathrm{N/m^2}$, E is the electric field between the gap in V/m, and $\epsilon_0 = 8.854 \times 10^{-12}$ F/m is the permittivity of the air gap. The limitation of electrostatic force is mainly due to the electric breakdown (spark), which is $E_{max} = 1 \times 10^6 \sim 3 \times 10^6$ V/m in atmosphere, and $E_{max} = 10^8 \sim 10^9$ V/m in high vacuum. Therefore, the maximum force density will be $F_{max} \approx 40$ $\mathrm{N/m^2}$ under atmosphere (if $E_{max} = 3 \times 10^6$ V/m), and $F_{max} \approx 4.4 \times 10^4$ $\mathrm{N/m^2}$ under high vacuum (if $E_{max} = 10^8$ V/m). This small force density in atmosphere limits the applications of electrostatic suspension. For example, a Silicon wafer has a weight of 17 $\mathrm{N/m^2}$, and therefore is just thin enough to be suspended by an electrostatic force in air. Another application of electrostatic forces is in Micro-electro-mechanical systems (MEMS), since a small force density is significant enough for these micro devices. Furthermore, if we count the thermal limit of magnetic actuators, the electrostatic force density in vacuum actually compete well with the magnetic force density.

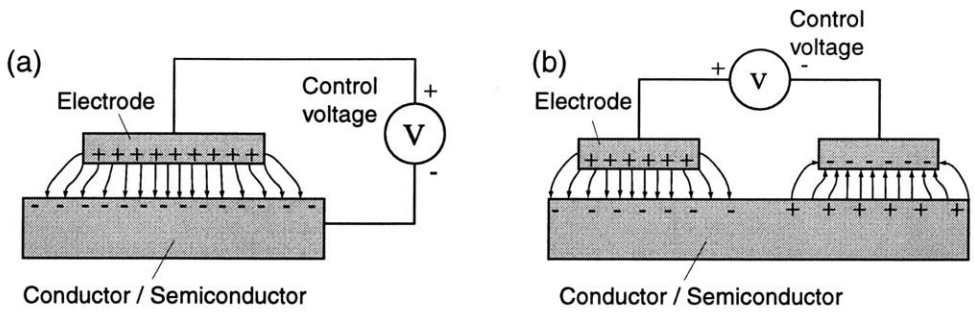

Figure 3-11: Estimation of electrostatic force density on conductors.

3.3.3 Electrostatic Suspension of Poor-conductive Dielectric Materials

To calculate the limit of electrostatic force on dielectrics, we use a simple example as in Figure 3-12. If we assume there are no free electrons, the system remains polarized as shown in Figure 3-12(a). However, most of dielectrics are poorly conductive, but are still conductive. The conductivity can be in the range of $\sigma = 10^{-12} \sim 10^{-17}$ mho/m. Even the humidity of air can contribute to the surface conductivity significantly. Hence there will be charge relaxation, which means free charges will slowly accumulate at the interface. The charge relaxation has a time constant of

$$\tau = \frac{\epsilon}{\sigma}, \tag{3.26}$$

where ϵ and σ are the dielectric constant and conductivity of the dielectric materials. After time $t \gg \tau$, the free charges will accumulate at the boundaries, as shown in Figure 3-12(b). Usually the dielectric constant ranges from ϵ_0(air), $2\epsilon_0$(paper) to $9\epsilon_0$(glass). The time constant can range from a few seconds to a few days, and can be significantly affected by air humidity. Therefore, we use 2 models to estimate the force of the electrostatic suspension of dielectric materials.

Electrostatic Force on Dielectric Materials by Polarization

The first model assumes the material is moving very fast, or the control voltage is alternating very fast, such that the charge relaxation is not significant. Thus the force

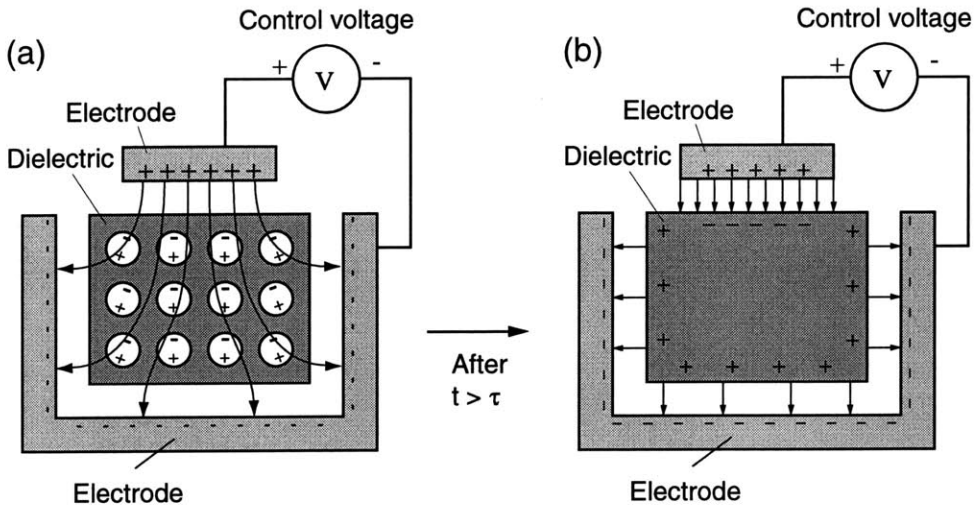

Figure 3-12: Electrostatic suspension model of dielectric materials: (a) within time constant, material is being polarized, and (b) after a few time constants, charges accumulate at the surface.

is dominated by the polarization force. Polarization force can be represented by:

$$\vec{F} = (\vec{P} \cdot \nabla)\vec{E} \Rightarrow |\vec{F}| = \frac{1}{2}\epsilon_0 \chi_e \nabla E^2, \tag{3.27}$$

where $\vec{E}$ is applied electric field, and χ_e is the dielectric susceptibility of the material.

We assume a simple geometry as in Figure 3-13, and assume that the dielectric is a piece of glass with $\chi_e = 5$, We have electric field

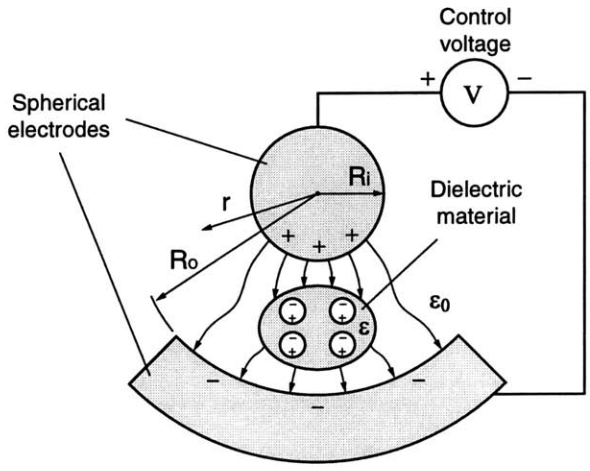

Figure 3-13: Estimation of electrostatic force density on dielectrics, assumed spherical electrodes and a small glass piece being suspended between the electrodes.

$$\vec{E} = E_r = E_i \frac{R_i^2}{r^2} \text{ N/m}^3, \tag{3.28}$$

where E_i is the electric field intensity at $r = R_i$. The polarization force becomes

$$F_r = \frac{1}{2}\epsilon_0 \chi_e \frac{\partial}{\partial r} E_r^2 = -2\epsilon_0 \chi_e E_i^2 \frac{R_i^4}{r^5}. \tag{3.29}$$

If we assume $E_{max} = 3$ kV/mm, the resulting maximum force becomes:

$$F_{max} = -2\chi_e \epsilon_0 E_{max}^2 \frac{R_i^4}{r^5} = -800 \frac{R_i^4}{r^5} \text{ N/m}^3 \tag{3.30}$$

$$\Rightarrow F_{max} = -800 \frac{1}{R_i} \text{ N/m}^3 \text{ when in contact } (\ r = R_i\ ), \tag{3.31}$$

which is a very small force. Since glass has a weight density of 3×10^4 N/m^3, we will need $R_i < 27$ mm to suspend a glass piece by this method.

Electrostatic Force on Dielectric Materials by Permanent Charges

The second model assumes the material is moving much slower than the charge relaxation speed, the force is dominated by the permanent charges on the surface. The nominal force will be

$$F_0 = \frac{\epsilon_0 E_0^2}{2}, \tag{3.32}$$

where F_0 is the surface force density in N/m^2, and E_0 is the nominal electric field intensity on the surface of the dielectric material in V/m. The charges accumulated on the surface can be calculated to be $\rho_s = \epsilon_0 E_0$ Coul/m^2. The dielectric material becomes like a object with permanent charges on its surface. Similar to the suspension of conductive materials, this nominal force density has a maximum of $F_{max} \approx 40$ N/m^2 under atmosphere, and $F_{max} \approx 4000$ N/m^2 under high vacuum.

If the control voltage produces extra electric field intensity $\triangle E$, the control force will be

$$\triangle F = \rho_s \triangle E = \epsilon_0 E_0 \triangle E, \tag{3.33}$$

where $\triangle F$ is the control surface force density in N/m^2.

3.4 Summary

In this chapter, we reviewed the operating principles and force limit of different types of electromagnetic suspensions. In general, magnetic suspensions has greater force density than electrostatic suspensions. Magnetic suspensions can be applied on ferromagnetic or conductive materials. Electrostatic suspensions can be applied on conductors or dielectric materials.

For materials that are considered non-magnetic, non-conductive, and non-dielectric, we can rely on the facts that the materials may be slightly paramagnetic ($\mu > \mu_0$), diamagnetic ($\mu < \mu_0$), conductive ($\sigma > 0$), or dielectric ($\epsilon > \epsilon_0$), and apply a strong field to produce enough force. For manufacturing processes, it may be more efficient by considering other suspension techniques, such as using compressed air to lift objects.

For the rest of this thesis, we will focus on magnetic suspension of ferromagnetic materials.

Chapter 4

Analysis of Structural Dynamics

In this chapter, we will explore the dynamics of four different structures: strings, beams, membranes, and plates. We will derive their governing equations and general solutions, and decouple the original equations into modal equations. We will consider slender structures only, and hence neglect the shear deformations in transverse direction. In this thesis, we will consider plates and membranes in rectangular shapes in Cartesian coordinate. For different shapes of plates or membranes, we need to use other coordinate systems or numerical methods to solve for the solutions. The dynamics of axially moving structures will be described in Chapter 10, and the analysis by numerical method will be discussed in Chapter 11. Related references are listed in Chapter 2.

4.1 Dynamics and Analysis of Beams

In this thesis, we use the Euler-Bernoulli beam model to describe dynamics of beams and strings. The dynamic equation can be derived by combining the beam elasticity and Newton's Second Law, $F = ma$. The free body diagram of a general beam element is shown in Figure 4-1.

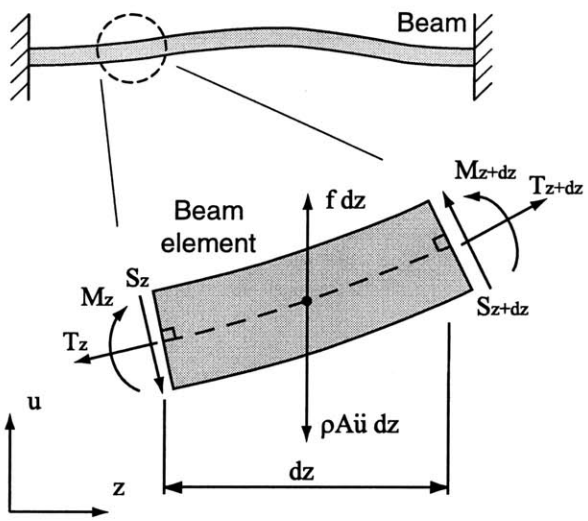

Figure 4-1: Free body diagram of a beam element.

4.1.1 Derivation of Beam Equation

To derive the beam equation, we can list the following three equations: force balance, torque balance, and the beam elasticity relation:

1. Force balance ($\sum$ Force $= ma$)

$$\underbrace{f}_{\substack{\text{external}\\\text{force}}} + \underbrace{\frac{\partial S}{\partial z}}_{\substack{\text{shear}\\\text{force}}} + \underbrace{\frac{\partial}{\partial z}\left(T\frac{\partial u}{\partial z}\right)}_{\substack{\text{tension}\\\text{force}}} = \underbrace{\rho A\frac{\partial^2 u}{\partial t^2}}_{\substack{\text{inertia}\\\text{force}}} . \tag{4.1}$$

2. Moment balance ($\sum$ Torque $= 0$):

$$S = -\frac{\partial M}{\partial z}. \tag{4.2}$$

3. Elasticity (derived in Appendix B):

$$M = EI\frac{\partial^2 u}{\partial z^2}. \tag{4.3}$$

In these equations, f is external transverse force density, S is transverse shear force, T is axial tension force, ρ is material density, A is cross-sectional area, u is

transverse deformation, z is axial axis, M is bending moment, E is Young's modulus, I is bending moment of inertia, and EI together is called beam's bending stiffness. Combining the previous three equations, we got the general beam equation:

$$f - \frac{\partial^2}{\partial z^2}(EI\frac{\partial^2 u}{\partial z^2}) + \frac{\partial}{\partial z}\left(T\frac{\partial u}{\partial z}\right) = \rho A\frac{\partial^2 u}{\partial t^2}. \tag{4.4}$$

Assuming constant T and constant EI, we can rewrite the governing equation to be:

$$\boxed{EI\frac{\partial^4 u}{\partial z^4} - T\frac{\partial^2 u}{\partial z^2} + \rho A\frac{\partial^2 u}{\partial t^2} = f}. \tag{4.5}$$

This is the governing equation for both beams and strings; in string analysis, the bending stiffness EI is neglected, and the fourth order model is reduced to a second order model.

4.1.2 Solution of Beam Equation with Tension

From Equation 4.5, assume homogeneous solution $u_h(z,t) = Ce^{j\omega t}e^{pz}$, the resulting beam dispersion equation becomes

$$EIp^4 - Tp^2 - \rho A\omega^2 = 0. \tag{4.6}$$

After solving p, the natural response of this beam equation can be represented by the superposition of all possible homogeneous solutions:

$$u(z,t) = \sum_{n=1}^{\infty} \xi_n(t)\phi_n(z), \tag{4.7}$$

where $\xi_n(t)$ is the nth modal coordinate, and $\phi_n(z)$ is the nth modal shape:

$$\phi_n(z) = C_{n1}\cos k_n z + C_{n2}\sin k_n z + C_{n3}\cosh\sigma_n z + C_{n4}\sinh\sigma_n z, \tag{4.8}$$

with

$$k_n = \sqrt{-\frac{T}{2EI} + \sqrt{\left(\frac{T}{2EI}\right)^2 + \frac{\rho A \omega_n^2}{EI}}}, \tag{4.9}$$

$$\sigma_n = \sqrt{\frac{T}{2EI} + \sqrt{\left(\frac{T}{2EI}\right)^2 + \frac{\rho A \omega_n^2}{EI}}}. \tag{4.10}$$

Where C_{n1} and C_{n2} represent sinusoidal waveforms with wavelength $2\pi/k_n$, and C_{n3} and C_{n4} represent evanescent waveforms, which decay exponentially with increasing distances from boundaries.

4.1.3 Solution to Beam Equation Without Tension

In our experimental setup, there is no axial tension T, the beam equation can be reduced to

$$EI\frac{\partial^4 u}{\partial z^4} + \rho A\frac{\partial^2 u}{\partial t^2} = f, \tag{4.11}$$

and the wavenumber-frequency relation can be reduced to

$$k_n = \sigma_n = \sqrt[4]{\frac{\rho A \omega_n^2}{EI}}. \tag{4.12}$$

The modal shapes become

$$\phi_n(z) = C_{n1}\cos k_n z + C_{n2}\sin k_n z + C_{n3}\cosh k_n z + C_{n4}\sinh k_n z, \tag{4.13}$$

Notice that the sinusoidal waves propagate at phase velocities:

$$v_n = \frac{\omega_n}{k_n} = \sqrt[4]{\frac{EI\omega_n^2}{\rho A}}. \tag{4.14}$$

It shows that the waveforms of different wavelengths will disperse at different speeds.

The solutions of natural responses can be obtained by solving wavenumbers k_n from the boundary conditions. The following are three common types of boundaries,

other boundary types can be derived similarly:

1. Free boundary:

$$\text{Moment: } \frac{\partial^2 u}{\partial z^2} = 0, \quad \text{Shear: } \frac{\partial^3 u}{\partial z^3} = 0$$

2. Hinged boundary:

$$\text{Deformation: } u = 0, \quad \text{Moment: } \frac{\partial^2 u}{\partial z^2} = 0$$

3. Clamped boundary:

$$\text{Deformation: } u = 0, \quad \text{Angle: } \frac{\partial u}{\partial z} = 0$$

We use a free-free beam of length L as an example. The general solution is:

$$u(z,t) = \sum_{n=1}^{\infty} \xi_n(t)(C_{n1}\cos k_n z + C_{n2}\sin k_n z + C_{n3}\cosh k_n z + C_{n4}\sinh k_n z), \quad (4.15)$$

and the boundary conditions are:

$$\left.\frac{\partial^2 u}{\partial z^2}\right|_{z=0} = \left.\frac{\partial^3 u}{\partial z^3}\right|_{z=0} = \left.\frac{\partial^2 u}{\partial z^2}\right|_{z=L} = \left.\frac{\partial^3 u}{\partial z^3}\right|_{z=L} = 0. \quad (4.16)$$

Combine Equation 4.15 and Equation 4.16, and we can get the resulting equations:

$$\begin{bmatrix} -k_n^2 & 0 & k_n^2 & 0 \\ 0 & -k_n^3 & 0 & k_n^3 \\ -k_n^2\cos k_n L & -k_n^2\sin k_n L & k_n^2\cosh k_n L & k_n^2\sinh k_n L \\ k_n^3\sin k_n L & -k_n^3\cos k_n L & k_n^3\sinh k_n L & k_n^3\cosh k_n L \end{bmatrix} \begin{bmatrix} C_{n1} \\ C_{n2} \\ C_{n3} \\ C_{n4} \end{bmatrix} = \begin{bmatrix} 0 \\ 0 \\ 0 \\ 0 \end{bmatrix} \quad (4.17)$$

For C_{ni} to be nontrivial, we set the determinant of the matrix to be zero: $|\triangle| = 0$, and the result becomes the following characteristic equation:

$$\boxed{\cos k_n L \cdot \cosh k_n L = 1}. \quad (4.18)$$

This equation determines the natural waveforms of the structure. (This characteristic equation happens to be the same as the one for clamped-clamped beam.) We further solve it and obtain

$$k_n L = 0,\ 4.74,\ 7.86,\ 11.00,\ \cdots, \infty$$

Various results for different structures and boundary conditions can be found in Blevins [17].

An alternative to solve for k_n is by using Phase-Closure Principle [70]. However, it does not offer advantages over solving the characteristic equations, and will not be used in this thesis.

4.1.4 Modal Analysis of Beams without Tension

The beam responses were discretized into different modes. By further prove that each mode is orthogonal to each other, we can decouple the partial differential equation of beams into ordinary differential equations of each mode. The detail proof of orthogonality is shown in Appendix C.

Here we rewrite the beam equation from Equation 4.11:

$$EI\frac{\partial^4 u}{\partial z^4} + \rho A\frac{\partial^2 u}{\partial t^2} = f.$$

The general solution is:

$$u(z,t) = \sum_{n=1}^{\infty} \xi_n(t)\phi_n(z), \tag{4.19}$$

where ξ_n is nth modal coordinate, and ϕ_n is nth modal shape. From the orthogonality properties of each mode as shown in Appendix C, we can decouple this partial differential equation to infinite number of ordinary differential equations:

$$M_n\frac{d^2\xi_n}{dt^2} + K_n\xi_n = N_n, \qquad \text{m=1, 2, 3, } \cdots \infty, \tag{4.20}$$

where M_n is nth modal mass, K_n is nth modal stiffness, and N_n is nth modal force. They are defined by:

$$M_n = \int_0^L \rho A \phi_n^2 dz, \tag{4.21}$$

$$K_n = \int_0^L EI\phi_n \frac{d^4\phi_n}{dz^4} dz = M_n \omega_n^2, \tag{4.22}$$

$$N_n = \int_0^L f\phi_n dz. \tag{4.23}$$

We can truncate the high frequency modes and only keep the first q modes:

$$\underbrace{\begin{bmatrix} M_1 & 0 & \cdots & 0 \\ 0 & M_2 & \cdots & 0 \\ \vdots & \vdots & \ddots & \vdots \\ 0 & 0 & \cdots & M_q \end{bmatrix}}_{M_\xi} \begin{bmatrix} \ddot{\xi}_1 \\ \ddot{\xi}_2 \\ \vdots \\ \ddot{\xi}_q \end{bmatrix} + \underbrace{\begin{bmatrix} M_1\omega_1^2 & 0 & \cdots & 0 \\ 0 & M_2\omega_2^2 & \cdots & 0 \\ \vdots & \vdots & \ddots & \vdots \\ 0 & 0 & \cdots & M_q\omega_q^2 \end{bmatrix}}_{K_\xi} \begin{bmatrix} \xi_1 \\ \xi_2 \\ \vdots \\ \xi_q \end{bmatrix} = \underbrace{\begin{bmatrix} N_1 \\ N_2 \\ \vdots \\ N_q \end{bmatrix}}_{N_\xi} \tag{4.24}$$

We can add modal damping (proportional damping) to each mode for the purpose of controller design. If there is no damping, no dynamic controller can possibly stabilize the system. By assuming modal damping, the equations are still decoupled and are thus easier to analyze. Assuming $D_n = 2\zeta_n\omega_n M_n$, where ζ_n is the damping coefficient of the nth mode. Hence we still have q decoupled equations:

$$\begin{aligned} & M_n\ddot{\xi}_n + D_n\dot{\xi}_n + K_n\xi_n = N_n \\ \text{or} \quad & M_n(\ddot{\xi}_n + 2\zeta_n\omega_n\dot{\xi}_n + \omega_n^2\xi_n) = N_n, \qquad \text{n=1, 2, 3, } \cdots q. \end{aligned} \tag{4.25}$$

We can further rewrite the new governing equations in the state-space notation,

$$\begin{bmatrix} \dot{\xi} \\ \ddot{\xi} \end{bmatrix} = \begin{bmatrix} 0 & I \\ -M_\xi^{-1}K_\xi & -M_\xi^{-1}D_\xi \end{bmatrix} \begin{bmatrix} \xi \\ \dot{\xi} \end{bmatrix} + \begin{bmatrix} 0 \\ -M_\xi^{-1} \end{bmatrix} N_\xi \tag{4.26}$$

Since the beam equation is decoupled, we can analyze each mode independently.

The frequency response of the nth mode can be represented as

$$\frac{\xi_n(s)}{N_n(s)} = \frac{1}{M_n(s^2 + 2\zeta_n\omega_n s + \omega_n^2)}, \tag{4.27}$$

Assuming that we have a point force at z_a: $f(z,t) = f(t)\delta(z - z_a)$, and a position feedback at z_s: $y(t) = u(z_s, t)$. To derive the frequency response from input f to output y, we first represent them in modal coordinates:

$$\begin{cases} y(t) = u(z_s,t) = \sum_{n=1}^{\infty} \xi_n(t)\phi_n(z_s) \\ f(z,t) = f(t)\delta(z - z_a) \Rightarrow N_n = \int_0^L f(z,t)\phi_n dz = f(t)\phi_n(z_a) \end{cases} \tag{4.28}$$

By combining these two equations with Equation 4.27, we have the transfer function:

$$\begin{aligned} y(s) &= \sum_{n=1}^{\infty} \frac{N_n(s)}{M_n(s^2 + 2\zeta_n\omega_n s + \omega_n^2)}\phi_n(z_s) \\ \Rightarrow \quad & \boxed{\frac{y(s)}{f(s)} = \sum_{n=1}^{\infty} \frac{\phi_n(z_s)\phi_n(z_a)}{M_n(s^2 + 2\zeta_n\omega_n s + \omega_n^2)}}. \end{aligned} \tag{4.29}$$

Notice that the modal shape at the sensor position z_s determines the modal observability $\phi_n(z_s)$, and the modal shape at the actuator position z_a determines the modal controllability $\phi_n(z_a)$ [27]. This formula plays a critical role when we derive the sensor/actuator positioning method. It represents the modal properties of sensor/actuator locations. It will be discussed later when we derive the sensor averaging and actuator averaging methods in Chapter 6.

4.1.5 Numerical Example of Beams without Tension

This section uses a free-free beam as a numerical example. We use one sensor and one actuator, and discuss the two cases of collocated sensor/actuator and non-collocated sensor/actuator.

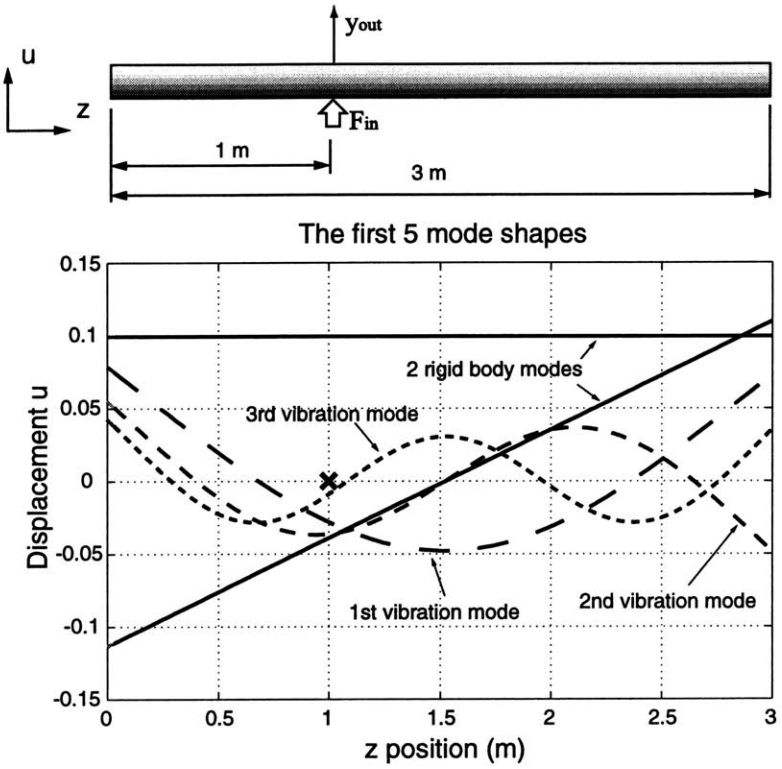

Figure 4-2: First 5 mode shapes of a free-free beam. The sensor and actuator are collocated. The sensor/actuator pair is near the node of the 3rd vibration mode.

Collocated Sensor/Actuator

We use a free-free beam and a pair of collocated sensor and actuator, as shown in Figure 4-2. It also shows the first 5 derived modal shapes, including 2 rigid body modes (translation and rotation), and 3 vibration modes. Notice that the sensor/actuator pair is near the node of the 3rd vibration mode.

Figure 4-3 shows the derived Bode Plots assuming modal damping ratio $\zeta_n = 0.005$. Notice the 3rd vibration mode is almost not observable/controllable, since the sensor/actuator pair is near its node.

This simple example demonstrated the difficulties of our control problem due to the lightly damped modes. Because the loop transfer function may have gain larger than 0 dB when the phase margin is below 180° at high frequencies, and the closed-loop system will be unstable.

Model-based control methods have been commonly used to solve this problem. The model can predict the resonance frequencies, and we can: (1) use notch filters to

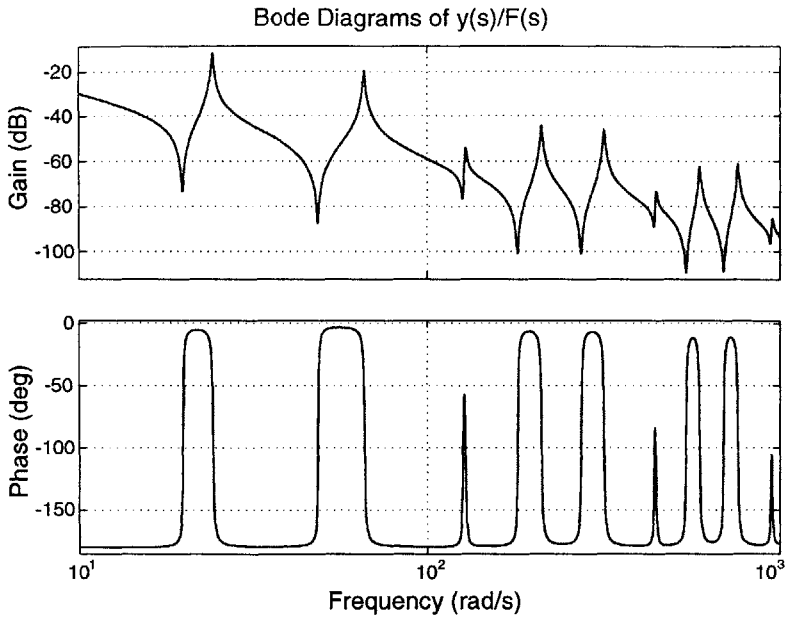

Figure 4-3: Bode Plots of a free-free beam. Notice the 3rd vibration mode is almost not observable/controllable.

avoid seeing or exciting the modes, or (2) place sensor/actuator pair near the nodes of the resonance modes to reduce the modal observability and controllability.

In this thesis, we are trying to control systems with varying boundary conditions, hence the model-based controller is not applicable. In this thesis, we developed a novel sensor/actuator averaging method to position sensors and actuators, which robustly attenuates these high frequency modes and solve this problem. It will be shown later in Chapter 6.

Non-collocated Sensor/Actuator

When the sensor and actuator are not located physically at the same position, it can make the closed-loop system unstable. It can be foreseen in Equation 4.29, when sensor and actuator are located at the opposite side of a node of a mode shape, $\phi_n(z_s)$ and $\phi_n(z_a)$ will have opposite signs. It will make the control effort 180^o out of phase.

Figure 4-4 shows the arrangement of sensor and actuator locations to a free-free beam. It also shows the first 5 modal shapes of the beam. Notice the node of the 3rd

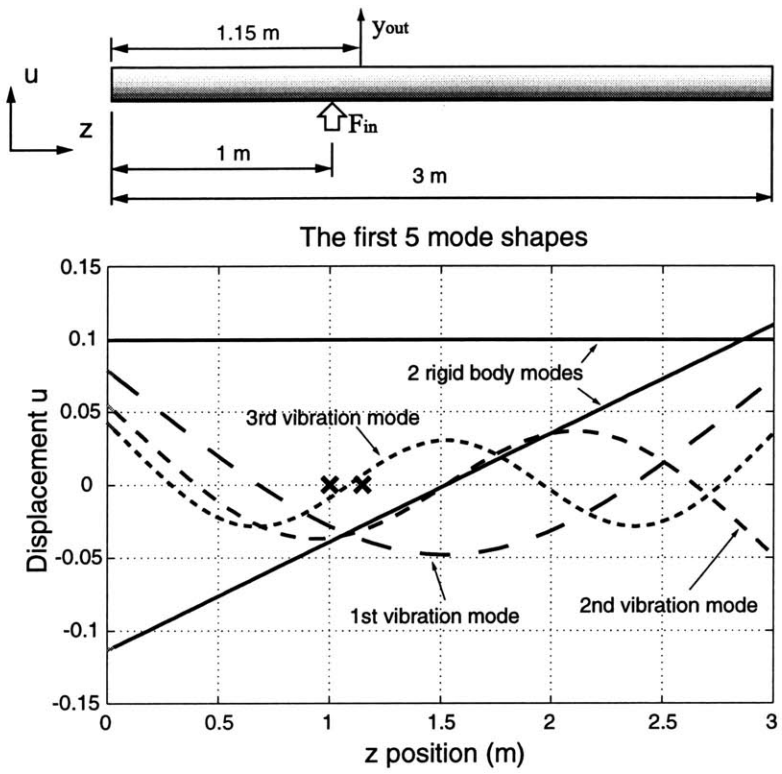

Figure 4-4: First 5 mode shapes of a free-free beam. The 3rd vibration mode has node between the sensor and the actuator.

vibration mode happens to fall in between the sensor and actuator. Figure 4-5 shows the derived Bode Plots assuming damping ratio $\zeta = 0.005$. Notice the 3rd, 6th and 9th resonance modes are out of phase by 180° because the sensor and actuator are at different sides of the nodes of these modal shapes.

This simple example demonstrated the difficulties of control due to non-collocated sensors and actuators. In model-based control, we can use observers or modal filters to estimate the modal coordinates and predict the real displacements at the actuators. In this thesis, we use non-model-based controller, and develop a novel sensor/actuator positioning method to eliminate this non-collocation problem.

4.2 Dynamics and Analysis of Strings

String element is similar to beam element, except that the bending stiffness of strings is negligible. Hence we use the beam equation, neglect bending stiffness EI, and

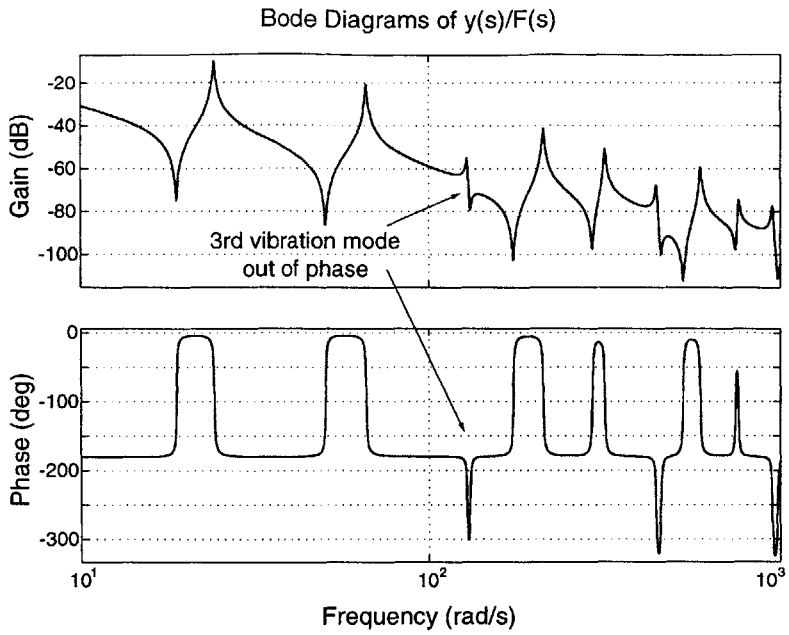

Figure 4-5: Bode Plots of a free-free beam. The sensor and actuator are non-collocated, which causes some resonance modes out of phase by 180°.

obtain the string equation:

$$-T\frac{\partial^2 u}{\partial z^2} + \rho A\frac{\partial^2 u}{\partial t^2} = f. \tag{4.30}$$

Similar to the procedures of solving beam equation, we obtain the nth modal shape of this string equation

$$\phi_n(z) = C_{n1}\cos k_n z + C_{n2}\sin k_n z. \tag{4.31}$$

It has only sinusoidal waveforms, and the the relation between wavenumber k_n and resonance frequency ω_n is represented by

$$k_n = \sqrt{\frac{\rho A}{T}}\omega_n. \tag{4.32}$$

The sinusoidal waves propagate at phase velocities:

$$v_n = \frac{\omega_n}{k_n} = \sqrt{\frac{T}{\rho A}}. \tag{4.33}$$

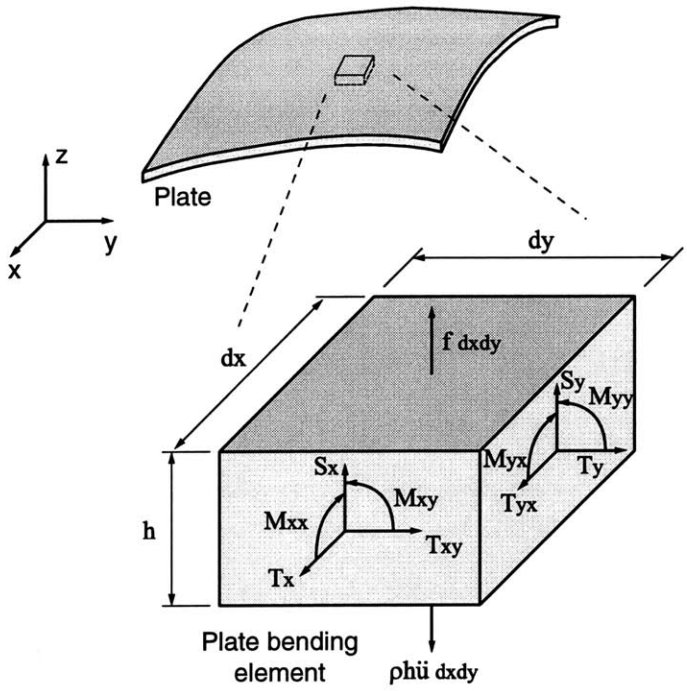

Figure 4-6: Free body diagram of a plate element.

It shows that all waveforms have the same propagating speed, and hence waves don't disperse. The speed of $\sqrt{T/(\rho A)}$ is well known as the transverse wave speed of strings. In Chapter 10, we will show that this speed is also the critical speed of axially moving strings.

The procedures of solving string dynamics and modal analysis are very similar to those of beams, and will not be repeated.

4.3 Dynamics and Analysis of Rectangular Plates

Similar to deriving beam dynamics, we can derive plate dynamics by introducing plate elasticity and force balance. The free-body diagram of a plate element is shown in Figure 4-6

To derive the plate dynamics, we list the following three relations: force balance, moment balance, and elasticity relations:

1. Force balance ($\sum$ Force $= ma$): notice that $T_{xy} = T_{yx}$

$$\underbrace{f}_{\text{external force}} + \underbrace{\left(\frac{\partial S_x}{\partial x} + \frac{\partial S_y}{\partial y}\right)}_{\text{shear force}} + \underbrace{\left(\frac{\partial}{\partial x}\left(T_x\frac{\partial u}{\partial x} + T_{xy}\frac{\partial u}{\partial y}\right) + \frac{\partial}{\partial y}\left(T_y\frac{\partial u}{\partial y} + T_{yx}\frac{\partial u}{\partial x}\right)\right)}_{\text{tension force}} = \underbrace{\rho h\frac{\partial^2 u}{\partial t^2}}_{\text{inertia force}} \quad (4.34)$$

2. Moment balance ($\sum$ Torque $= 0$): notice that $M_{xy} = M_{yx}$

$$\begin{bmatrix} S_x \\ S_y \end{bmatrix} = -\begin{bmatrix} \frac{\partial M_{xx}}{\partial x} + \frac{\partial M_{yx}}{\partial y} \\ \frac{\partial M_{xy}}{\partial x} + \frac{\partial M_{yy}}{\partial y} \end{bmatrix}. \quad (4.35)$$

3. Elasticity:

$$\begin{bmatrix} M_{xx} \\ M_{yy} \\ M_{xy} \end{bmatrix} = \frac{Eh^3}{12(1-\nu^2)}\begin{bmatrix} 1 & \nu & 0 \\ \nu & 1 & 0 \\ 0 & 0 & \frac{1-\nu}{2} \end{bmatrix}\begin{bmatrix} \frac{\partial^2 u}{\partial x^2} \\ \frac{\partial^2 u}{\partial y^2} \\ 2\frac{\partial^2 u}{\partial x \partial y} \end{bmatrix}. \quad (4.36)$$

In these equations, u is transverse deformation, f is external transverse force density, S is shear force, T is tension force, ρ is material density, h is plate thickness, E is Young's Modulus, , and ν is Poisson's Ratio of the material. Various materials' Young's modulus and Poisson's ratio are listed in Appendix A.

Combining all equations together, we can obtain a general plate bending equation. Here we assume that E, ν, T_x, T_y and T_{xy} are constant, and derive a simplified plate equation:

$$\boxed{D\left(\frac{\partial^4 u}{\partial x^4} + 2\frac{\partial^4 u}{\partial x^2 \partial y^2} + \frac{\partial^4 u}{\partial y^4}\right) - \left(T_x\frac{\partial^2 u}{\partial x^2} + T_y\frac{\partial^2 u}{\partial y^2} + 2T_{xy}\frac{\partial^2 u}{\partial x \partial y}\right) + \rho h\frac{\partial^2 u}{\partial t^2} = f}, \quad (4.37)$$

with defined plate rigidity D:

$$D \equiv \frac{Eh^3}{12(1-\nu^2)}. \tag{4.38}$$

4.3.1 Solution to Rectangular Plates with Uniform Tension

To solve the plate dynamics, we further simplify the problem to demonstrate the pattern of the solution. We assume constant tension force applied along all four edges: $T = T_x = T_y$ and $T_{xy} = 0$. The plate dynamics can then be modeled by

$$D(\frac{\partial^4 u}{\partial x^4} + 2\frac{\partial^4 u}{\partial x^2 \partial y^2} + \frac{\partial^4 u}{\partial y^4}) - T(\frac{\partial^2 u}{\partial x^2} + \frac{\partial^2 u}{\partial y^2}) + \rho h \frac{\partial^2 u}{\partial t^2} = f, \tag{4.39}$$

or equivalently

$$D\nabla^4 u - T\nabla^2 u + \rho h \frac{\partial^2 u}{\partial t^2} = f, \tag{4.40}$$

where ∇^4 is biharmonic operator. For rectangular plates, we assume homogeneous solution $u_h(x,y,t) = Ce^{j\omega t}e^{px}e^{qy}$, the resulting plate dispersion equation becomes

$$D(p^2+q^2)^2 - T(p^2+q^2) - \rho h\omega^2 = 0. \tag{4.41}$$

Similar to solving beam equation, we solve (p^2+q^2), and derive the nth modal shape $\phi_n(x,y)$

$$\begin{aligned} \phi_n(x,y) \;=\; & (C_{n1}\cos\alpha_n x + C_{n2}\sin\alpha_n x)(C_{n3}\cos\beta_n y + C_{n4}\sin\beta_n y) + \\ & (C_{n5}\cosh\alpha'_n x + C_{n6}\sinh\alpha'_n x)(C_{n7}\cosh\beta'_n y + C_{n8}\sinh\beta'_n y). \end{aligned} \tag{4.42}$$

with

$$k_n^2 = \alpha_n^2 + \beta_n^2 = -\frac{T}{2D} + \sqrt{\left(\frac{T}{2D}\right)^2 + \frac{\rho h\omega_n^2}{D}}, \tag{4.43}$$

$$\sigma_n^2 = \alpha_n'^2 + \beta_n'^2 = \frac{T}{2D} + \sqrt{\left(\frac{T}{2D}\right)^2 + \frac{\rho h\omega_n^2}{D}}. \tag{4.44}$$

Similar to beam element, plate dynamics include both sinusoidal and evanescent waveforms. Equation 4.43 shows the relation between wavenumber k_n and frequency ω_n, where α_n and β_n are wavenumber components in x and y directions respectively.

4.3.2 Solution to Rectangular Plates without Tension

For rectangular plates with negligible tension force T, the plate equation can be reduced to

$$D\nabla^4 u + \rho h \frac{\partial^2 u}{\partial t^2} = f, \tag{4.45}$$

and the wavenumber-frequency relation can be reduced to

$$k_n = \sigma_n = \sqrt[4]{\frac{\rho h \omega_n^2}{D}}. \tag{4.46}$$

The modal shapes become

$$\begin{aligned} \phi_n(x,y) &= (C_{n1}\cos\alpha_n x + C_{n2}\sin\alpha_n x)(C_{n3}\cos\beta_n y + C_{n4}\sin\beta_n y) + \\ &\quad (C_{n5}\cosh\alpha_n x + C_{n6}\sinh\alpha_n x)(C_{n7}\cosh\beta_n y + C_{n8}\sinh\beta_n y). \end{aligned} \tag{4.47}$$

At this moment, we can foresee the difficulties to decouple the plate equations. If we follow the same procedures as decoupling beam equation, we will have 8 boundary conditions to solve for the 8 unknown coefficients. At last we will have an 8 by 8 matrix, we will set the determinant to be zero and solve for the characteristic equation to get α_n and β_n. In this thesis, the analytical analysis is derived and used to design controller and sensor/actuator positioning method. As for solving the responses, I will use Finite Element Method instead.

4.4 Dynamics and Analysis of Rectangular Membranes

To solve the dynamics of rectangular membranes, we simplify the problem by assuming constant tension force applied along all four edges: $T = T_x = T_y$ and $T_{xy} = 0$. For membranes with tension in only one direction ($T_x = 0$ or $T_y = 0$), they can be considered as string elements. We obtain the membrane equation by neglecting plate rigidity D in Equation 4.37, and we have

$$-T\nabla^2 u + \rho h \frac{\partial^2 u}{\partial t^2} = f. \tag{4.48}$$

Similar to solving the plate equation, we obtain the nth modal shape:

$$\phi_n(x, y) = (C_{n1}\cos\alpha_n x + C_{n2}\sin\alpha_n x)(C_{n3}\cos\beta_n y + C_{n4}\sin\beta_n y). \tag{4.49}$$

The membrane dispersion equation becomes:

$$k_n^2 = \alpha_n^2 + \beta_n^2 = \frac{\rho h}{T}\omega_n^2. \tag{4.50}$$

4.5 Modeling of Passive Damping

For the purpose of being able to decouple the equations, the structures are usually assumed to have proportional damping (modal damping). This argument is applicable when damping is very small, hence the coupling can be regarded as being a second-order effect [75, pp.197]. The sources of passive damping are mainly contributed by boundaries (joints), material hysteresis, air drag, and electromagnetic force. We will prove that at higher frequencies, the air drag and electromagnetic force become insignificant compared to material hysteresis.

4.5.1 Material Hysteresis Damping

For our system, if the object has free-free boundaries, the main source of passive damping comes from the material hysteresis at the order of 10^{-3}. The seamless tube used in our experiment is measured to have loss factor of 0.002 at around 100 Hz[1]. When the object is attached to any boundaries, such as loose-bores, hinges, clamps, or even strings, the damping will be dominated by the boundaries. The energy of the structure can be transmitted through the boundaries and get dissipated. Especially the loose-contact boundaries will have a lot of relative motion when structures vibrate, and the friction will dominate the passive damping.

To model the material hysteresis damping, we can define a loss factor as the ratio of energy loss per cycle [29, 26]:

$$\eta = \frac{\triangle U}{2\pi U} = \frac{\text{(Energy dissipated per cycle)}}{2\pi\text{(Peak strain energy)}}, \tag{4.51}$$

and η can be measured experimentally. Lazan [62] presented a broad list of experimental loss factors for different materials at different temperatures and frequencies. Similarly, we can modify Young's modulus by using a complex modulus:

$$\hat{E} = E(1 + j\eta). \tag{4.52}$$

Using beam as an example, the governing equation can be rewritten as

$$\hat{E}I\frac{\partial^4 u}{\partial z^4} + \rho A\frac{\partial^2 u}{\partial t^2} = f. \tag{4.53}$$

The modal decomposition will be the same as before, and we have the system response

[1]If we had chosen a seam-welded tube for our experiment, the loss factor could be as high as 0.01 [15], and this project would had been much less challenging. We chose seamless tubes at the beginning in order to simplify this project since our designed LVDT sensor is sensitive to the location the seam-welded-joints.

as

$$\frac{u(s)}{f(s)} = \sum_{r=1}^{\infty} \frac{\phi_r(z_a)\phi_r(z_s)}{M_r(s^2 + \hat{\omega}_r^2)}, \tag{4.54}$$

where $\hat{\omega}_r^2 = \omega_r^2(1 + j\eta)$, hence we can rewrite it as

$$\frac{u(s)}{f(s)} = \sum_{r=1}^{\infty} \frac{\phi_r(z_a)\phi_r(z_s)}{M_r(s^2 + j\eta\omega_r^2 + \omega_r^2)}. \tag{4.55}$$

Near the resonance peak when $s \approx j\omega_r$, we have the loss factor η proportional to damping ratio ζ, and $\eta = 2\zeta$. Steel has a loss factor of $\eta \approx 0.001 \sim 0.008$. Loss factors of several different materials are shown in Appendix A. Generally aluminum has a smaller loss factor than steel. Fortunately, aluminum is non-magnetic and conductive, we can add passive damping to aluminum easily without touching it by applying a constant magnetic field.

If the loss factor is independent of frequencies, we can assume that modal damping of each mode is the same. However, loss factor is indeed a function of frequencies and temperatures. Lazan [62, Chapter 3] shows that some steel has its maximum loss factor around 10 Hz. In this project, we assume each mode has the same modal damping for simplicity. If the exact damping ratio is important, we can measure it experimentally. To measure the loss factor of a certain material, we can use a piece of string to hang the material freely. The attaching points can be arranged to be at the nodes of the first vibration mode to avoid extra energy dissipation through the string. Test the structure by hitting it with a hammer, and then observe the decay of the first mode vibration. To test the damping ratio at different frequencies, a simple way will be by using the same material with different lengths.

4.5.2 Air Drag Damping

For a material with loss factor smaller than 10^{-4}, the viscous damping from air may need to considered. To calculate the damping caused by air viscosity, we calculate the Reynold's number to determine the type of fluid flow.

Using the tubular beam in our experiment, for amplitude of 1mm, frequency of 1000 rad/s, the maximum velocity is 1 m/s. At this speed, we have Reynold's number

$$Re = \frac{\rho U D}{\mu} < \frac{1.2 \cdot 1 \cdot 0.006}{1.8 \times 10^{-5}} = 400, \tag{4.56}$$

where $\mu = 1.8 \times 10^{-5}$ kg/ms is the air dynamic viscosity, $U = 1$ m/s is the moving velocity, $\rho = 1.2$ kg/m^3 is the air density, and $D = 6$ mm is tube diameter. For this small Reynold's number, we can assume the drag is caused by viscosity [60, §20].

The drag on an infinity long cylinder cannot be solved easily. We can use three different approximation methods. One approximation is for cylinders with very small Reynold's number. The drag per unit length is

$$F = \frac{4\pi\mu U}{\log\left(\frac{7.4}{Re}\right)}. \tag{4.57}$$

This approximation apparently doesn't work for the case that Reynold's number is larger than 7.4, since it will give a negative drag force, which is wrong.

Another simple approximation is by using a model of sphere with radius R, the drag force is simply

$$F = 6\pi\mu R U. \tag{4.58}$$

A better but more complicated approximation can be solved by an ellipsoid model [59, §339]. The drag on an ellipsoid with radius R and length $2C$ can be found to be

$$F = 6\pi\mu U \frac{8}{3(A+B)}, \text{ with } \quad A = \int_0^\infty \frac{dk}{\triangle}, \quad B = R^2 \int_0^\infty \frac{dk}{(R^2+k)\triangle}, \quad \triangle = \sqrt{(R^2+k)^2(C^2+k)}. \tag{4.59}$$

For $R = 3$ mm and $C \gg R$, we can solve for the force per unit length:

$$\frac{F}{2C} \approx \pi\mu U = bU = 5 \times 10^{-5} U. \tag{4.60}$$

This approximation from ellipsoid model is roughly three times smaller than the that of sphere model, which is reasonable. This equation determined the damping coefficient $b = 5 \times 10^{-5}$ for the tube in our experiment.

In the following, I use modal analysis to find out the contribution of air drag to structural damping at different frequencies. By using our experimental setup as an example, assume the system is decoupled, we can derive natural frequency ω_n, modal mass M_n, modal stiffness K_n, and modal damping D_n from air drag:

$$\omega_n = \sqrt{\frac{EI}{\rho A}} \left(\frac{n\pi}{L}\right)^2 \approx 11n^2, \tag{4.61}$$

$$M_n = \int_0^L \rho A \phi_n^2 dz = \rho A \int_0^L \sin^2(\frac{z}{L} n\pi) dz = \frac{1}{2}\rho A L = 0.18, \tag{4.62}$$

$$K_n = M_n \omega_n^2 = 22n^4, \tag{4.63}$$

$$D_n = \int_0^L b\phi_n^2 dz = b \int_0^L \sin^2(\frac{z}{L} n\pi) dz = \frac{1}{2} bL = 7.5 \times 10^{-5}. \tag{4.64}$$

If we write a normal equation for the nth mode, we have

$$\begin{aligned} & M_n \ddot{\xi} + D_n \dot{\xi} + K_n \xi = N_n, \\ \text{or} \quad & M_n(\ddot{\xi} + 2\zeta_n \omega_n \dot{\xi} + \omega_n^2 \xi) = N_n \end{aligned} \tag{4.65}$$

In other words, the modal damping ratio ζ_n is

$$\zeta_n = \frac{D_n}{2M_n\omega_n} \approx \frac{2 \times 10^{-5}}{n^2}. \tag{4.66}$$

This result shows that the air drag may add damping to the structures at low frequencies. However, with the resonance frequency increases, the stiffness of structure increases such that the air damping becomes insignificant. Table 4.1 lists the numerical results of a hinged-hinged beam. The damping coefficient from the air drag is

Table 4.1: Properties of each resonance modes of a hinged-hinged beam. Each mode is considered an independent mass-spring system. Damping ratio ζ_n from air drag becomes negligible at high frequencies.

Mode	Frequency ω_n (rad/s)	Modal mass M_n (kg)	Modal stiffness K_n (N/m)	Modal damping D_n (Ns/m^2)	Modal damping ratio ζ_n
1	11	0.18	22	7.5×10^{-5}	2×10^{-5}
2	44	0.18	348	7.5×10^{-5}	5×10^{-6}
3	99	0.18	1764	7.5×10^{-5}	2×10^{-6}
4	176	0.18	5576	7.5×10^{-5}	1×10^{-6}
5	275	0.18	13612	7.5×10^{-5}	8×10^{-7}
6	396	0.18	28227	7.5×10^{-5}	5×10^{-7}
7	539	0.18	52294	7.5×10^{-5}	4×10^{-7}
⋮	⋮	⋮	⋮	⋮	⋮

shown to be negligible when resonance modes get higher.

4.6 Summary

Analytical analysis gives us understanding and insight about the structural dynamic behaviors. In this thesis, the structural uncertainty envelope, controller design, and sensor/actuator positioning method are derived from analytical analysis. Notice that we made the following assumptions when we derive the analytic model of structures

1. Consider small bending deformations only, and neglect transversal shear deformations.

2. Assume uniform material properties, dimensions, and tension forces.

3. Assume axially moving velocity is zero.

4. Assume linear elasticity.

5. Assume damping is small, and each mode can be decoupled.

Chapter 5

Experiments of Magnetic Suspension and Vibration Control of Levitated Beams

This project focused on the experiment of magnetic suspension of a slender tubular beam. In this chapter, I describe the design of experimental setup, the modeling of each component, and the results of the experiment. In our approach, we use multiple Single-Input-Single-Output (SISO) controllers. That is, each pair of sensors and actuators is controlled locally. In the next 2 chapters, I further describe the designs of the associated actuators and sensors for this experimental setup. In Chapter 6, I describe a novel sensor/actuator positioning method, which is a key to the successful suspension of the flexible structures in this thesis.

5.1 Experimental Setup

The experiment is designed to magnetically suspend a 3 m (10 ft) long steel tube, which has 6.35 mm (0.25 in) diameter and 0.9 mm (0.035 in) wall thickness. We use 8 non-contact position sensors and 8 non-contact force actuators to accomplish this suspension.

Figure 5-1 shows the experimental setup we developed in our laboratory, and Fig-

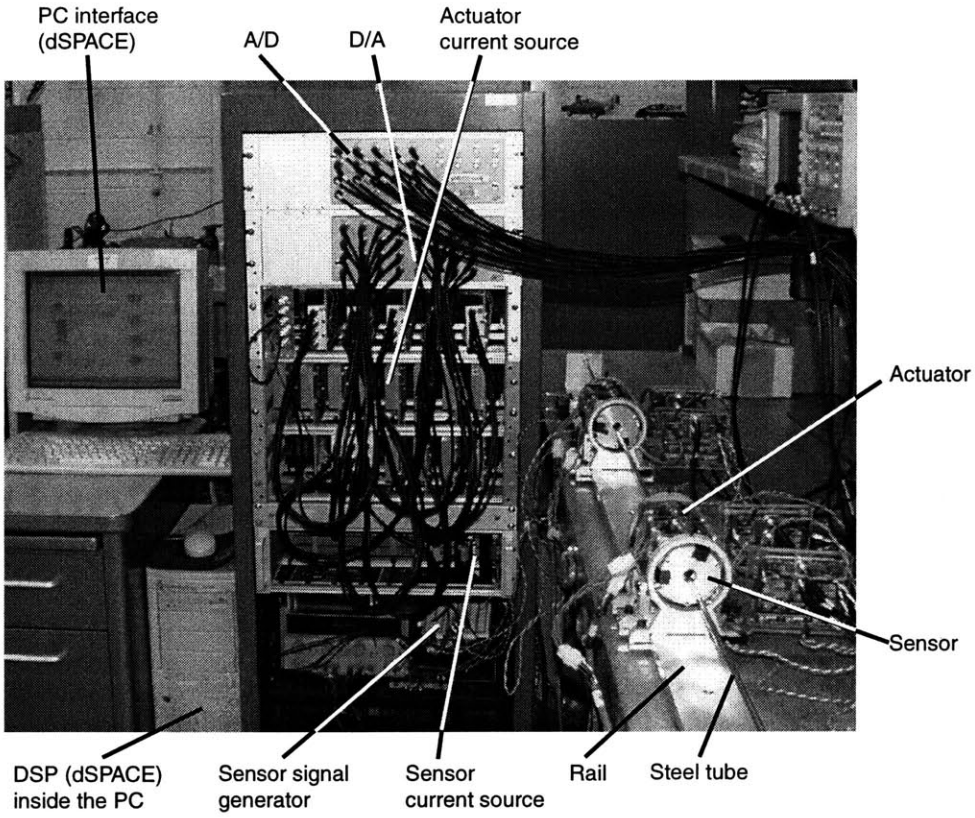

Figure 5-1: Tube suspension experimental setup

ure 5-2 shows the schematic design of the setup. The sensors detect the position of the tubular beam, and send the outputs to the DSP board via A/D converters. The DSP board does real-time sensor linearization and feedback control, and sends the control signals to the actuator current control boards via D/A converters. The actuators then apply the control forces to suspend the beam. The details of programming this DSP board are shown in Appendix D

The sensors and actuators can be moved freely along the 3 m long rail to study different sensor/actuator positioning methods. The designs of the sensor-stand and actuator-stand are shown in Figure 5-3. These stands are also designed to allow the sensors and actuators to be adjusted over ± 3 mm in the x and y directions, in order to compensate for any misalignment of the rail.

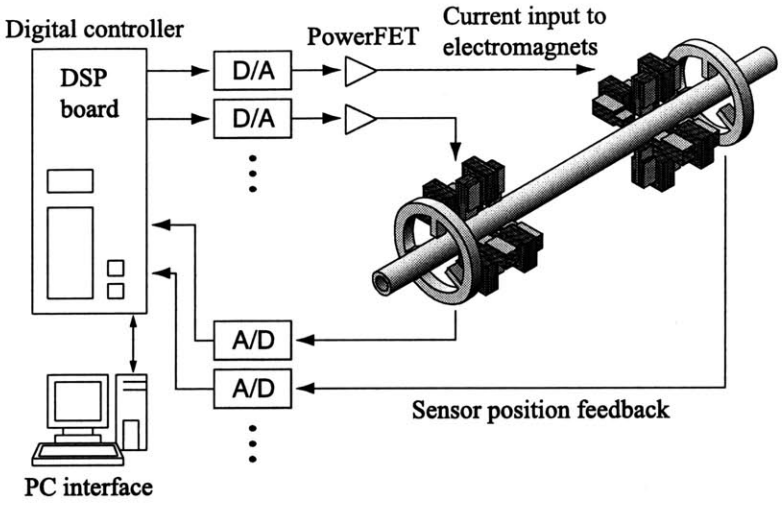

Figure 5-2: Schematic design of experimental setup for tube levitation.

5.2 Scaling of Experiment Design

In this section, we describe the design of dimensions for the scaled-down experiment. We will analyze the scaling of both structural dynamics and magnetic properties with respect to the original full-scale experiment at American Metal Handle.

5.2.1 Original Setup at AMH

This project germinated from ideas developed by Dr. Conrad Smith, founder of American Metal Handle, a company that produced metal handles for brooms and mops. They consulted with Professor Trumper on the magnetic suspension of the metal tubes for non-contact processing. The production line at American Metal Handle has a 47 m long seam-welded steel tube with 20 mm diameter and 0.36 mm thickness, which is suspended by 10 magnetic suspension stages.

5.2.2 Scaling of Beams

As discussed in previous chapters, for beams without tension, we have the dynamic equation:

$$EI\frac{\partial^4 u}{\partial z^4} + \rho A\frac{\partial^2 u}{\partial t^2} = f, \tag{5.1}$$

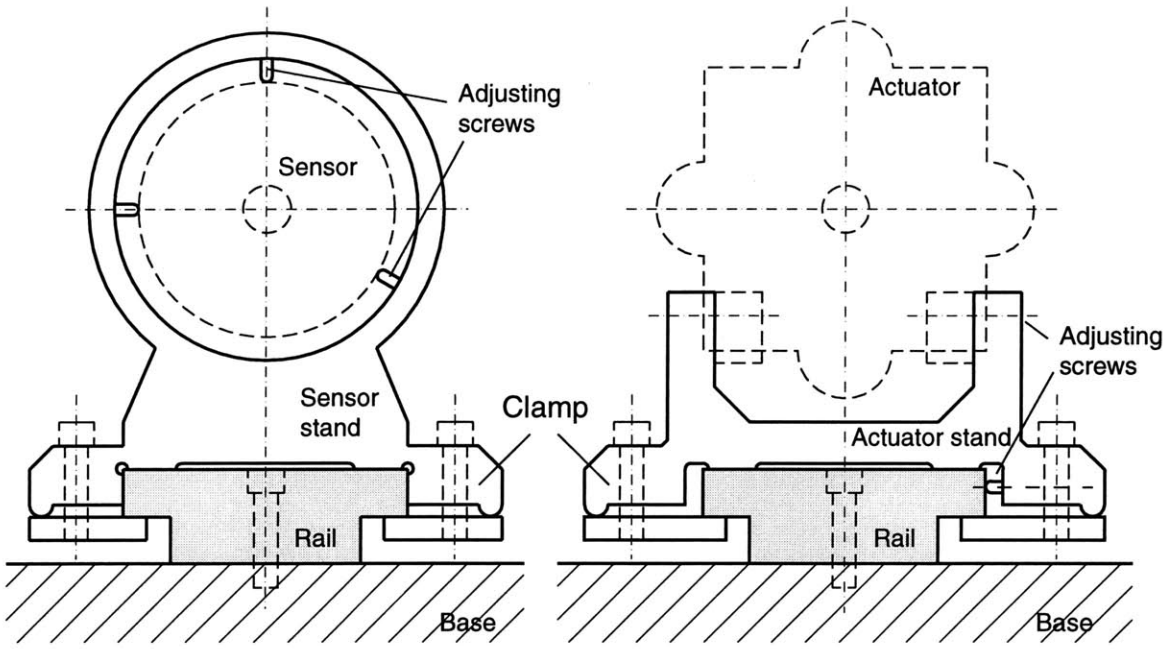

Figure 5-3: Stands for sensors and actuators: they allow sensors and actuators to be moved and clamped along the rail (z axis). The x and y positions can be fine adjusted by the adjusting screws.

where z is axial coordinate, u is transverse deflection, and f is external transverse force density. Assuming a homogeneous solution $u_h(z,t) = Ce^{j\omega t}e^{kz}$, the resulting beam dispersion equation becomes

$$EIk^4 - \rho A\omega^2 = 0. \tag{5.2}$$

If we use hinged-hinged boundaries for example, the beam with length L will have resonance modes with wavelengths of $2L$, L, $2L/3$, $\cdots$, $2L/n$. The corresponding wavenumbers k_n are π/L, $2\pi/L$, $3\pi/L$, $\cdots$, $n\pi/L$, where k_n is equal to 2π/wavelength.

For the purpose of our experiments, we designed our sensors and actuators with a bandwidth near 1 kHz, and we want to control the system vibration up to about 1000 rad/s. Therefore we designed our experiment such that there will be 10 vibration modes within 1000 rad/s. Our final experimental setup has $\rho A = 0.117$ kg/m, $EI = 11.68$ Nm^2, and a beam dispersion equation of $k_n^2 = 0.1\omega_n$. At 1000 rad/s, we have wavenumber $k_n = 10$ rad/m, which is around the 9th to 10th vibration modes.

For the original AMH setup, the tube has a bending stiffness of $EI = 212$ Nm^2,

and a mass distribution of $\rho A = 0.171$ kg/m, and the resulting dispersion equation is $k_n^2 = 0.028\omega_n$. At 100 rad/s, we have wavenumber $k_n = 1.67$ rad/m, which is near the 25th vibration modes. This tells us that in the real production line, if we only control the system to this low bandwidth, the dynamics of actuators, sensors, and sampling time are less problematic, but we need to have a controller with phase lead starting at a much lower frequency.

5.2.3 Scaling of Actuators

In Chapter 7, we derive that our actuator has a force function of

$$F(g, i) = 36\frac{i^2}{g^2}, \tag{5.3}$$

where F is force in N, i is input current in A, and g is air gap in mm. This nonlinear property is normal for an electromagnet, and cannot be scaled up and down linearly. That is the reason why electromagnets are usually designed case by case.

Details of the analyses of actuator field distribution and forces are given in Chapter 7. Using the Quad-U-core electromagnet as an example, assume that the back iron and the target both have permeability $\mu \gg \mu_o$, the applied force F from the 2 pole faces can be derived as:

$$F = \frac{\phi^2}{\mu_0 A_{pole}} = \frac{\mu_0 A_{pole}(Ni)^2}{4g^2}, \tag{5.4}$$

where $\mu_0 = 4\pi \times 10^{-7}$ H/m is permeability of air, N is number of turns of coil, i is current input, g is air gap, and A_{pole} is actuator pole face area.

The criteria to scale up and down the actuator size are based on the magnetic saturation and current limit:

1. Magnetic flux limit: The maximum magnetic flux density is $B_{max} = \phi/A_{mag} <$ 1.5 Tesla due to magnetic saturation of ferromagnetic materials, where A_{mag} is the minimum cross sectional area of ferromagnetic materials. In other words, the bottleneck along the magnetic flux path A_{mag} determines the maximum

force, which includes the path along actuator back iron and target steel.

2. Current density limit: The maximum current density is $J_{max} = Ni/A_{coil} < 5 \times 10^6$ A/m^2 due to limited heat transfer for air cool system, where A_{coil} is the cross sectional area of coil.

For example, if we want to obtain a maximum force of 2 N, we can decide the dimension of the actuator by the following 2 steps:

1. From magnetic saturation limit, assume that the minimum cross sectional area is the pole face, we have the force function as

$$F = \frac{\phi^2}{\mu_0 A_{pole}} = \frac{B_{max}^2 A_{pole}}{\mu_0} > 2. \tag{5.5}$$

With $B_{max} = 1.5$ Tesla, we have $A_{pole} > 1.1$ mm^2. Hence we need a minimum cross sectional area of 1.1 mm^2 for both the back iron and the target steel.

2. For an air gap of $g = 3$ mm, and a pole face area of $A_{pole} = 40$ mm^2, we have the force function as

$$F = \frac{\mu_0 A_{pole}(Ni)^2}{4g^2} = 1.2 \times 10^{-6}(Ni)^2 > 2, \tag{5.6}$$

hence we need $Ni > 1280$. From the current density limit of $Ni/A_{coil} < 5 \times 10^6$ A/m^2, we need a cross sectional area of the coil of $A_{coil} > 256$ mm^2.

In our design, we use 1200 turns of 26 gauge wire for each U-magnet.

5.3 Dynamics of Hardware

The designs of the actuators and sensors for this experimental setup are given in the following two chapters. Here I summarize the dynamics of actuators and sensors in the following subsections. I also include the dynamics of the time delay from the digital controller, which introduces a phase lag at high frequencies, and makes

the suspension control extremely difficult. These information will be included in the open-loop system dynamics to help us design the controllers.

5.3.1 Actuator Dynamics

The dynamics of Quad-U-Core actuators are discussed in Chapter 7. We summarize the properties in the following:

1. Force function: The actuator has the current-force relation:

$$f(g,i) = 36\frac{i_{act}^2}{g^2}, \tag{5.7}$$

   where f is force in N, i_{act} is actuator current in A, and g is air gap in mm.

2. Actuator dynamics: The actuator alone is modeled by a resistor (13 Ω), series with an inductor (0.13 H), and paralleled with a capacitor (10 nF).

3. Closed-loop dynamics: With the augmented damping resistor of 2 kΩ, the current command to actuator current output has a gain of 1 and two poles at 4.4 kHz with a damping ratio of 0.9. The transfer function is:

$$\frac{i_{act}}{i_{fet}} = \frac{(2.8\times10^4)^2}{s^2 + 2\times0.9\times2.8\times10^4 s + (2.8\times10^4)^2}. \tag{5.8}$$

4. Command filter: The 1st order low-pass filter has a dc gain of 0.1 and a pole at 28 kHz:

$$\frac{V_{out}}{V_{in}} = \frac{0.1\times1.79\times10^5}{s + 1.79\times10^5}. \tag{5.9}$$

5. Detachable 2nd order filter: The low-pass filter has a dc gain of 2.2 and two poles at 800 Hz with a damping ratio of 0.4:

$$\frac{V_{out}}{V_{in}} = \frac{2.2\times5000^2}{s^2 + 2\times0.4\times5000 s + 5000^2}. \tag{5.10}$$

These transfer functions together are the dynamics of our actuators. Notice that the detachable 2nd order filter is used to reduce sensor feedthrough induced by the actuator current. It is removed later when we suspend the 10 ft long beam with free-free boundaries in order to reduce the phase lag. Sensor feedthrough induced by the actuator current is no longer problematic since we use sensor/actuator averaging method, and hence the sensors and actuators do not need to be placed close to each other.

5.3.2 Sensor Dynamics

The sensor after linearization has the dynamics from the low-pass filters: two 2nd order filters and a twin-T notch filter:

1. Low-pass filter: We add two 2nd order low-pass filters to the sensor output, one filter has a dc gain of 2.2, two poles at 1 kHz with damping ratio 0.4, and the transfer function is:

$$\frac{V_{out}}{V_{in}} = \frac{2.2 \times 6060^2}{s^2 + 2 \times 0.4 \times 6060s + 6060^2}. \tag{5.11}$$

   The other filter has a dc gain of 1.7, two poles at 3.4 kHz with damping ratio 0.65, and the transfer function is:

$$\frac{V_{out}}{V_{in}} = \frac{1.7 \times 21300^2}{s^2 + 2 \times 0.65 \times 21300s + 21300^2}. \tag{5.12}$$

2. Twin-T notch filter: It has a dc gain of 1, a deep notch at 12kHz, and the transfer function is:

$$\frac{V_{out}}{V_{in}} = \frac{s^2 + 77000^2}{s^2 + 308000s + 77000^2}. \tag{5.13}$$

5.3.3 Time Delay by Digital Control

Our digital controller is fully loaded, and thus requires nearly the whole sample interval to compute the corresponding output. Thus the total time delay t_d of the digital controller can be approximated by the sum of the computational time t_c, and half of the sampling time t_s: $t_d = t_c + \frac{1}{2}t_s$. For the final setup of our system, we have computational time $t_c \approx 220$ μs, and sampling time $t_s = 250$ μs. Hence we can model the time delay in frequency domain by $G_d(s) = e^{-t_d s}$. It can be further approximated by Padé approximation (2nd order):

$$G_d(s) = \frac{1 - (t_d s/2) + (t_d^2 s^2/12)}{1 + (t_d s/2) + (t_d^2 s^2/12)}. \tag{5.14}$$

The main effect of the time delay to the system can be interpreted as phase lag at high frequencies. We have a sampling rate of 4 kHz, which is considered fast at this time[1]. However, if we take a look at the frequency domain at 1000 rad/s, which is our designed control bandwidth, a time delay of $t_d = 345$ μs causes $1000 \times 345 \times 10^{-6}$ rad phase lag, or equivalently, 20° phase lag. The phase lag due to time delay increases linearly with the frequency, which makes the stabilization of the high frequency vibrations extremely difficult.

5.3.4 System Open-Loop Dynamics

Combining the dynamics of the sensor, actuator, time delay, and the tubular beam, the open-loop dynamics is shown in Figure 5-4. The tubular beam is assumed to have free-free boundaries. Notice at 2000 rad/s, we have a phase lag of about 80°, in which the time delay of the digital control contributes 40°.

From Figure 5-4, we can see one of the difficulties of stabilize such a system: the significant phase lag at high frequencies. Furthermore, our goal is to stabilize the beam with varying boundary conditions, which makes the controller design even more challenging. In the following, I will introduce the modeling of the beam with

[1]Our state-of-art controller DSP board, A/D board, D/A board, and controller software costs about 20,000 US dollars.

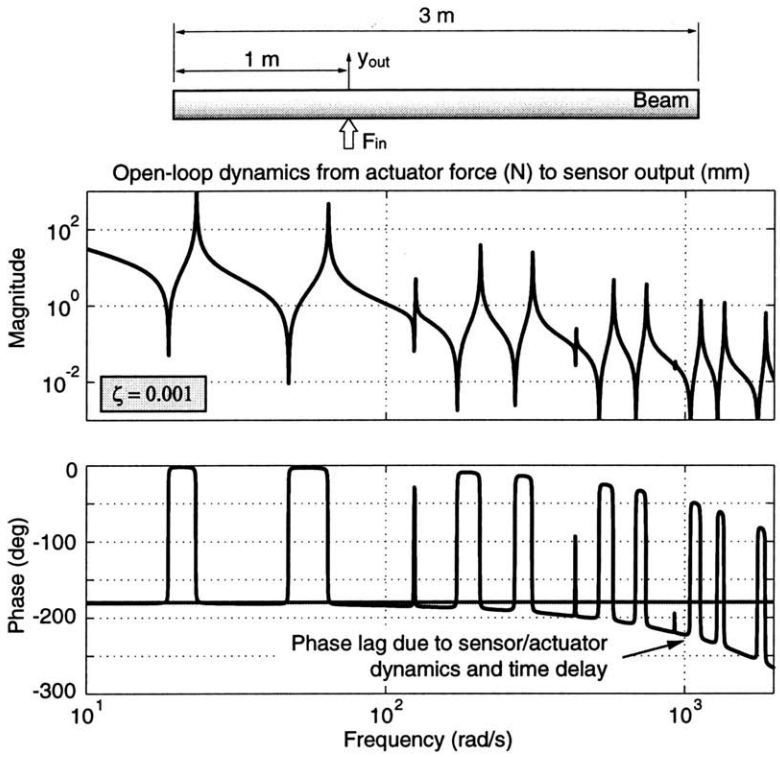

Figure 5-4: Open-loop dynamics from actuator force (N) to sensor output (mm), including dynamics of the free-free beam, sensor, actuator, and time delay.

varying boundary conditions, and then we can design our controller to stabilize the system.

5.4 Structural Dynamics with Uncertainties

In the previous section, we show the open-loop dynamics of the tubular beam with free-free boundaries, which is only one of the many typical cases of our system, hence it cannot be used directly to guide the controller design. Because in this project, our goal is to stabilize this tubular beam with varying boundary conditions and varying longitudinal lengths. We would like to find the uncertainty envelope that covers the dynamics of such system to guide the controller design. In this section, I derive the equation of the envelope that covers the resonance peaks in the Bode plot.

5.4.1 Envelope of Structure Resonance Peaks

As shown in Chapter 4, the modal analysis shows that the structural response can be represented by the superposition of each mode. For a beam structure, the transfer function from a point force f at $z = z_a$, to a position output y at $z = z_s$ can be shown as:

$$G(s) = \frac{y(s)}{f(s)} = \sum_{r=1}^{\infty} \frac{\phi_r(z_a)\phi_r(z_s)}{M_r(s^2 + 2\zeta_r\omega_r s + \omega_r^2)}, \tag{5.15}$$

where $\phi_r(z_a)$ is the amplitude of the modal shape at the actuator, and $\phi_r(z_s)$ is the amplitude of the modal shape at the sensor.

For each mode, the transfer function is

$$G(s) = \frac{\phi_r(z_a)\phi_r(z_s)}{M_r(s^2 + 2\zeta_r\omega_r s + \omega_r^2)}, \tag{5.16}$$

which has a resonance peak at

$$\omega = \omega_r\sqrt{1 - 2\zeta_r^2} \approx \omega_r \text{ for light damping,} \tag{5.17}$$

and the resonance peak has value of

$$\frac{\phi_r(z_a)\phi_r(z_s)}{2M_r\zeta_r\omega_r^2\sqrt{1-\zeta_r^2}} \approx \frac{\phi_r(z_a)\phi_r(z_s)}{2M_r\zeta_r\omega_r^2}. \tag{5.18}$$

We assume a sinusoidal modal shape, and normalize the modal shape such that the maximum amplitude is 1. Then the modal mass M_r can be calculated as

$$M_r = \int_0^L \rho A\phi_r^2 dz = \rho A\int_0^L \sin^2(\frac{z}{L}n\pi)dz = \frac{1}{2}\rho AL = \frac{1}{2}m, \tag{5.19}$$

where m is the total weight of the beam.

To derive the uncertainty envelope, we assume both modal controllability $\phi_r(z_a)$ and modal observability $\phi_r(z_s)$ to be 1, and the resulting resonance peak envelope

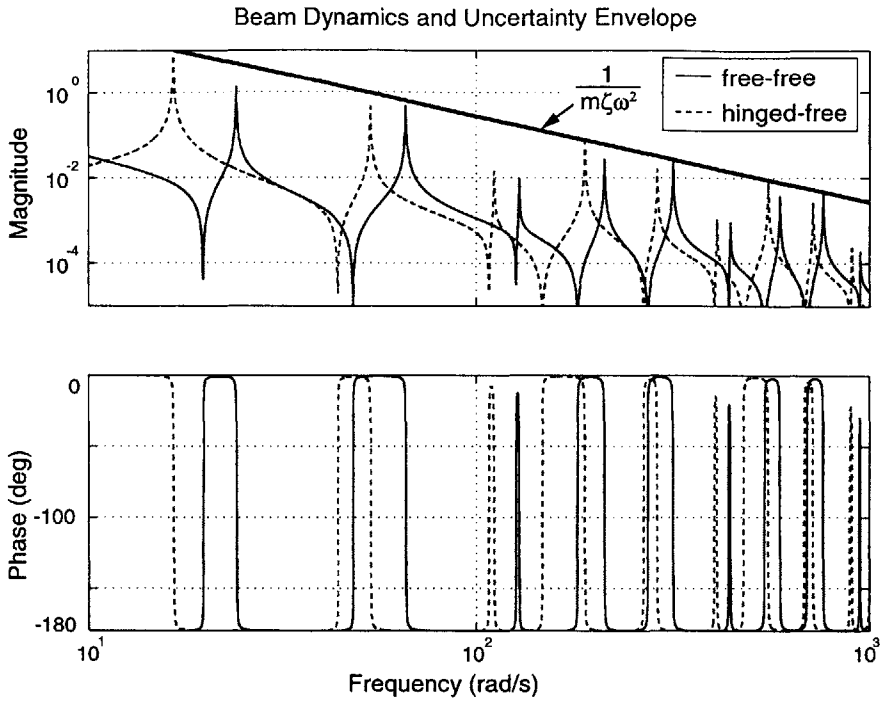

Figure 5-5: Beam dynamics and uncertainty envelope: both hinged-free beam and free-free beam are upper bounded by the envelope.

becomes

$$\boxed{G_{envelope}(\omega) = \frac{1}{m\zeta\omega^2}} \tag{5.20}$$

We use a beam example to demonstrate that the derived envelope is a conservative assumption. Figure 5-5 shows the Bode plots of a beam with damping ratio $\zeta = 0.001$ with hinged-free ends and free-free ends, and it also shows that the derived envelope covers the resonance peaks for either case. Our assumption of $\phi_r(z_s) = \phi_r(z_a) = 1$ assumes that each resonance peak is at its maximum. The peak envelope derived is actually the uncertainty that we want to cover in our applications. In other words, when the tube boundary conditions change, or the tube length changes, the resonance frequencies will change, however, the resonance peaks will remain below the derived envelope. This envelope is then very useful for design.

An important result from Equation 5.20 is that the designed suspension stiffness will be mainly limited by the beam's total mass m and damping ratio ζ. For the same

example of Figure 5-5, we assume the open-loop dynamics has a significant phase lag of about 40° at $\omega \approx 1000$ rad/s due to the dynamics of the sensor, actuator, and time delay. Thus we can design a controller such that the loop transfer function has a crossover at $\omega \approx 1000$ rad/s. Since the open-loop dynamics has a gain of $10^{-2.5}$ m/N at 1000 rad/s, we can immediately find the maximum controller gain at 1000 rad/s can not exceed $10^{2.5}$ N/m, or 316 N/m. Thus we can decide the order of the suspension stiffness quickly from the peak envelope.

5.4.2 Peak Envelope and System Stability

If we have a controller K, the loop transfer function of the peak envelope becomes $KG_{envelope}(\omega)$. Roughly speaking, the system will be unstable when the loop transfer function $KG_{envelope}(\omega)$ has phase below $-180°$, and the gain above 0 dB.

In fact, this criteria is conservative. To see this, we can plot the Nyquist plot of a resonance peak, and see if the resonance peak encircles the -1 point. For the nth resonance mode, we have the transfer function:

$$G_n(s) = \frac{1}{M_n(s^2 + 2\zeta_n\omega_n s + \omega_n^2)}. \tag{5.21}$$

We assume in the vicinity of a resonance mode, the transfer function is dominated by this mode. Thus the loop transfer function near this mode becomes $G_{loop}(s) = KG_n(s)$ It can be approximated as a circle in the Nyquist Plot. To prove that, we use the frequency ω around ω_n, and check the gain and phase of $G_{loop}(j\omega)$:

$$G_{loop}(j\omega) = \frac{K/M_n}{(\omega_n^2 - \omega^2) + j(2\zeta_n\omega_n\omega)}. \tag{5.22}$$

Suppose $\omega = \omega_n + \epsilon$, where ϵ is a small value compared to ω_n. The result becomes:

$$G_{loop}(j\omega) = \frac{K/M_n}{(-2\epsilon\omega_n - \epsilon^2) + j(2\zeta_n\omega_n^2 + 2\zeta_n\omega_n\epsilon)} \approx \frac{K}{M_n}\frac{(-\epsilon) + j(-\zeta_n\omega_n)}{2\omega_n\,(\epsilon^2 + \zeta_n^2\omega_n^2)}. \tag{5.23}$$

This result matches the equation for a circle in the complex plane that has the center

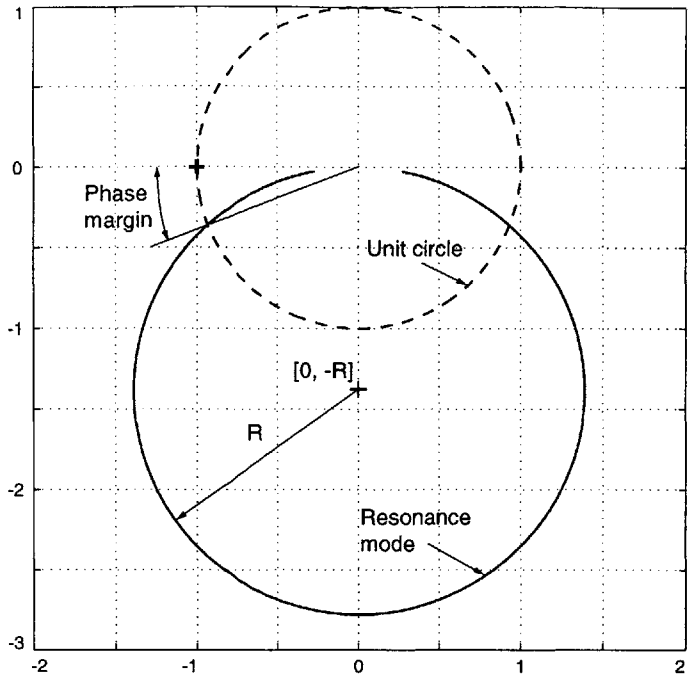

Figure 5-6: Nyquist Plot of a resonance mode.

at $[0, -R]$ and a radius R:

$$X^2 + (Y + R)^2 = R^2, \text{ with } R = \frac{K/M_n}{4\zeta_n \omega_n^2}, \tag{5.24}$$

where X is the real part, Y is the imaginary part, and R is the radius.

Assume $M_n = 0.18$, $\omega_n = 1000$, $\zeta_n = 0.001$, $K = 1000$, and hence $R = 1.39$. When we plot $KG_{loop}(j\omega)$ in the complex plane, we have a circle as shown in Figure 5-6. Notice that such a system has a phase margin of $\sin^{-1}\frac{1}{2R}$, which is 21° in this example.

Therefore we can obtain a less conservative criteria for stability using the peak envelope: the system will be unstable when the gain of $KG_{envelope}(\omega) > 0$ dB and the phase lag

$$\phi_{lag}(\omega) > \sin^{-1}\frac{1}{KG_{envelope}(\omega)}. \tag{5.25}$$

Notice that this is still an approximation, and is valid when the damping ratio is small and each resonance mode dominates its local frequency response. However,

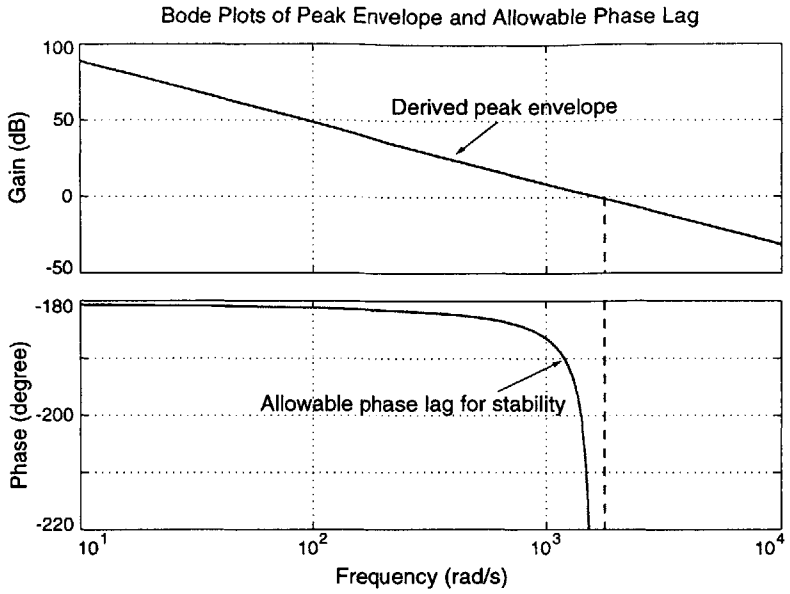

Figure 5-7: Bode Plots of the derived peak envelope and the allowable phase lag that the system remains stable.

this result is very useful for a first-level analysis of these types of loops. The Bode plot of this criteria is shown in Figure 5-7.

5.5 Controller Design

The controller needs to have the following functions:

1. Robustly stabilizes the system.

2. Damps the resonance modes within control bandwidth.

3. Provides enough dc stiffness to reject disturbances.

In this thesis, we design the controller using a SISO controller design method. We extend it to a MIMO controller by checking the loop transfer function of the SISO system multiplied by n times if we have n sensor/actuator pairs. In the following subsections, I will introduce the controller design, and justify the stability of the resulting MIMO controller.

5.5.1 SISO Controller Design and Analysis

Here we show the design of a SISO controller for one actuator/sensor pair. To achieve the robustness we need for non-contact processing, the beam dynamics will be replaced by the peak envelope as represented previously in this chapter. We represent the system open loop dynamics including the beam dynamics, actuator dynamics, sensor dynamics, and time delay. A typical bode plot of the system open loop dynamics is shown in Figure 5-4.

Notice that we cannot just have phase margin at the crossover frequency. We need to have phase margin at all of the resonance modes within the bandwidth to stabilize the system. This requires the addition of a lead compensator. However, we do not want to increase the high-frequency gain too much. Therefore, we have designed a *slow roll-up lead compensator*, which has the form

$$H(s) = K_p \frac{(s+m)(s+4m)\cdots}{(s+2m)(s+8m)\cdots}. \tag{5.26}$$

Such a controller will have a maximum phase lead of 45°, and have a gain slope of 10 dB/decade. A typical transfer function of the slow-roll-up lead compensator is shown in Figure 5-8.

For the beam example as shown in Figure 5-4, we design a slow-roll-up lead compensator of

$$H(s) = 4\frac{(s+30)(s+120)(s+400)}{(s+60)(s+240)(s+800)} \text{ N/mm}. \tag{5.27}$$

We add extra phase lead around the frequency of 800 rad/s to compensate for the significant phase lag of the open-loop dynamics. The resulting loop transfer function is shown in Figure 5-9. Notice that there will be high frequency resonance modes with gain higher than 0 dB if the damping ratio is this small, and these modes may destabilize the system if the phase margin is negative. In our work, this problem is solved by using a special sensor/actuator positioning method: *sensor averaging* and *actuator averaging*, which will be discussed in detail in Chapter 6.

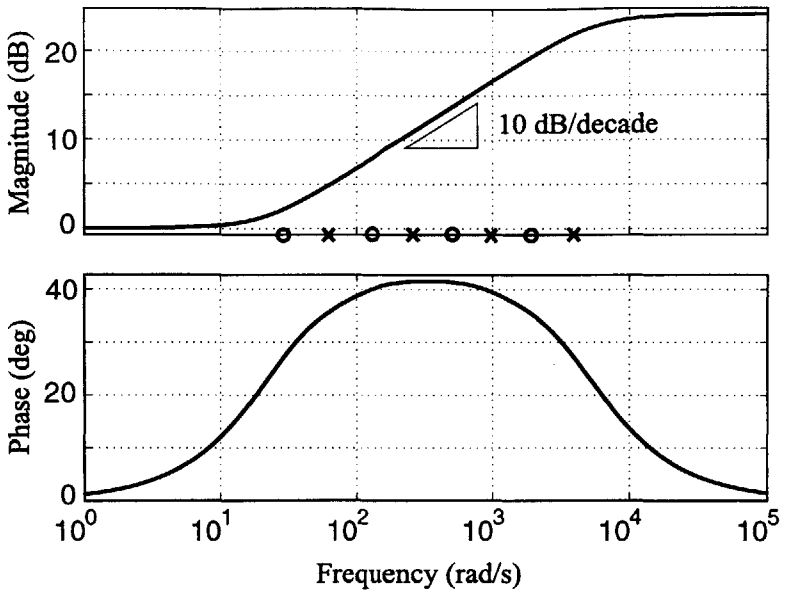

Figure 5-8: Bode Plots of a slow roll-up lead compensator, which has multiple zero-pole pairs distributed along the frequencies where we need phase lead. The compensator gives 10 dB/decade slope in gain, and an average phase lead of 30°.

Although we want to have a sufficient dc stiffness in our magnetic bearing, we do not want to use a lag compensator. For example, if the beam has the 1st resonance mode at 20 rad/s, we can design a lag compensator located at about 1/10 this resonance frequency. The lag compensator of

$$h(s) = \frac{(s+2)}{(s+1)} \tag{5.28}$$

can provide a 2 times larger dc stiffness. However, introducing such a slow dynamics into the system is not a good idea for our system. For example, if we have a displacement disturbance of +2 mm for a few seconds, once this disturbance is relieved, the tube will have a roughly −4 mm rebound, and could hit the magnetic bearings or sensors. Furthermore, the stability of the MIMO system by using a lag compensator for each sensor/actuator pair cannot be easily justified.

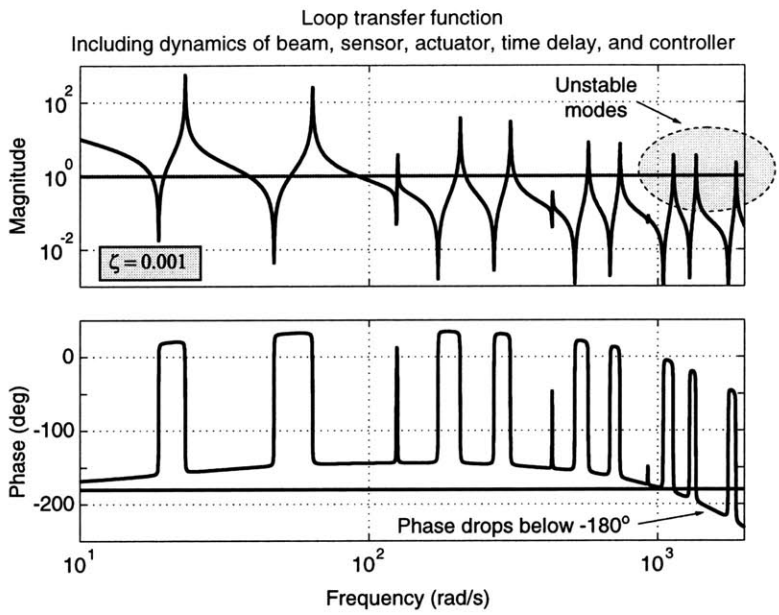

Figure 5-9: Loop transfer function of system dynamics, including the free-free beam, sensor, actuator, time delay, and controller. High frequency modes will be unstable since the gains are higher than 0 dB, and the phase margin is negative.

5.5.2 MIMO Controller Design and Analysis

For our system, we propose using a local controller on each sensor/actuator pair independently. To extend it to multiple sensor/actuator pairs, we can simply design the controller sequentially, and make sure the final closed-loop system is stable. A quick approximation is to modify the resonance peak envelop; for n-input-n-output system, we can simply multiply the peak envelop equation by n, and design the local controller $h(s)$ based on $n/(m\zeta\omega^2)$. In this section, I will justify this approximation method.

We demonstrate this approximation by considering a MIMO system shown in Figure 5-10, we have a plant $G(s)$ and a controller $H(s)$. The closed-loop transfer function is $G_{cl}(s) = y(s)/r(s) = (I + GH)^{-1}GH$. The closed-loop poles are determined the roots of $|I + GH| = 0$.

For a 2-input-2-output system, we have the open-loop dynamics:

$$\begin{bmatrix} y_1 \\ y_2 \end{bmatrix} = G(s) \begin{bmatrix} f_1 \\ f_2 \end{bmatrix} = \begin{bmatrix} g_{11}(s) & g_{12}(s) \\ g_{21}(s) & g_{22}(s) \end{bmatrix} \begin{bmatrix} f_1 \\ f_2 \end{bmatrix}, \tag{5.29}$$

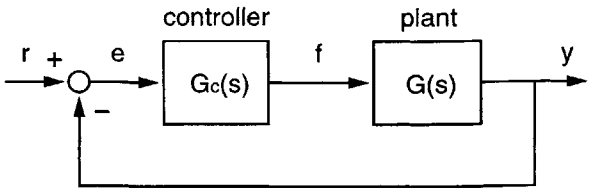

Figure 5-10: Block diagram of a MIMO system.

$$\text{where } g_{ij}(s) = \frac{y_j(s)}{f_i(s)} = \sum_{r=1}^{\infty} \frac{\phi_r(z_j)\phi_r(z_i)}{M_r(s^2 + 2\zeta_r\omega_r s + \omega_r^2)}. \tag{5.30}$$

Notice that g_{12} is equal to g_{21}. Using a local control method, we have the controller such that:

$$\begin{bmatrix} f_1 \\ f_2 \end{bmatrix} = H(s) \begin{bmatrix} e_1 \\ e_2 \end{bmatrix} = \begin{bmatrix} h(s) & 0 \\ 0 & h(s) \end{bmatrix} \begin{bmatrix} e_1 \\ e_2 \end{bmatrix}, \tag{5.31}$$

The determinant of $(I + GH)$ is

$$|I + GH| = \left| \begin{bmatrix} 1 + hg_{11} & hg_{12} \\ hg_{21} & 1 + hg_{22} \end{bmatrix} \right| = 1 + h(g_{11} + g_{22}) + h^2(g_{11}g_{22} - g_{12}^2). \tag{5.32}$$

The second order terms can be neglected when controller gain $h(s)$ is small, when g_{ij} is small, or when it is near resonance frequency since

$$g_{11}(j\omega_r)g_{22}(j\omega_r) \approx g_{12}^2(j\omega_r) \approx \left(\frac{\phi_r(z_1)\phi_r(z_2)}{m\zeta_r\omega_r^2}\right)^2. \tag{5.33}$$

Hence the determinant can be approximated by

$$|I + GH| \approx 1 + h(g_{11} + g_{22}) \tag{5.34}$$

when it is near resonance frequency or when it is at high frequencies. For a free-free beam example, the comparison of Equation 5.32 and Equation 5.34 is shown in Figure 5-11. We can see that at high frequencies, the real loop transfer function and the approximation is very close. Hence the stability of the closed-loop system can be predicted by this approximation.

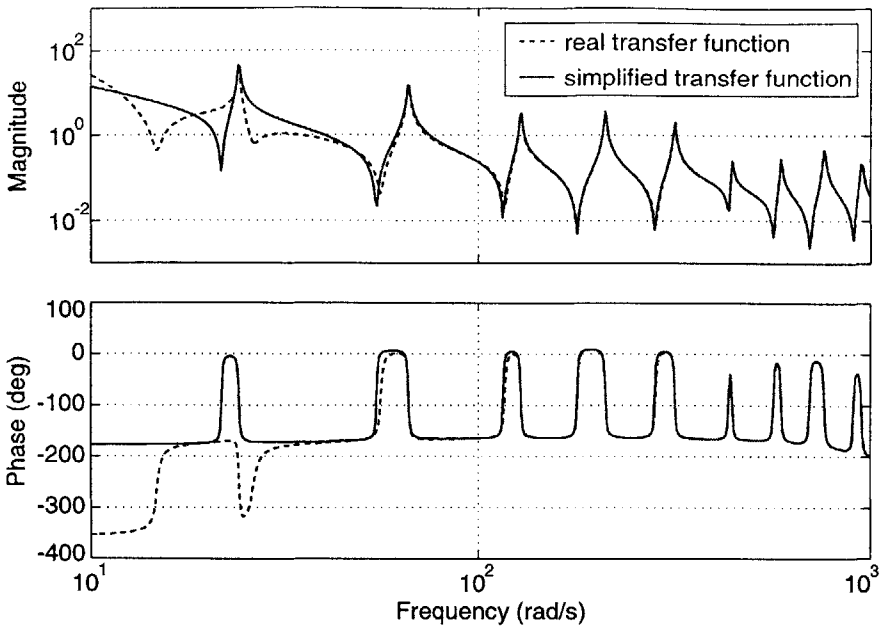

Figure 5-11: The Bode Plots show the loop transfer function of a free-free beam with 2 inputs and 2 outputs: the dashed line shows $h(g_{11}+g_{22})+h^2(g_{11}g_{22}-g_{12}^2)$, and the solid line shows $h(g_{11}+g_{22})$.

We can design the controller based on this approximation method, which has the following characteristics:

1. The approximation method simply sums up the loop transfer function of each sensor/actuator pair together. In terms of our derived peak envelope, we simply times it by n if we have n sensor/actuator pairs.

2. At high frequencies, the approximate loop transfer function is very close to the real loop transfer function.

3. At low frequencies, the approximation method differs from the real loop transfer function, However, since the controller at low frequencies can be considered as a good spring-damper, it will not destabilize the system. Notice that this simple argument will not be acceptable if we use a lag compensator at low frequencies.

4. This approximation method offers a quick way to estimate the controller design. The real closed-loop system can be easily verified by checking the closed-loop poles (roots of $|(I+GH)|=0$).

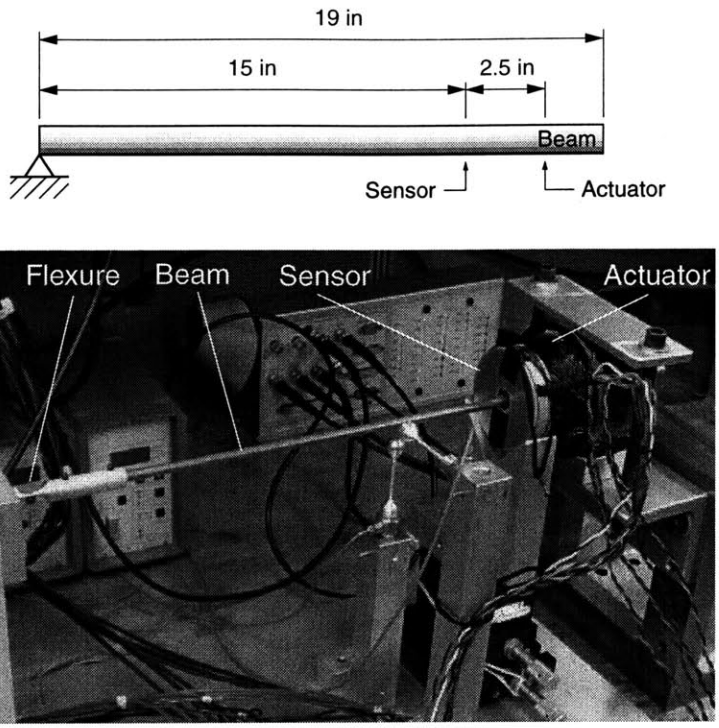

Figure 5-12: Suspension of a hinged-free beam with length L=1.5 ft by using 1 sensor and 1 dipole-quadrupole actuator.

5.6 Magnetic Suspension of Short Beams

We started our experimental efforts by testing the magnetic bearings on short beams with lengths of 1.5 ft and 2 ft. Short beams are easier to suspend since the vibration modes are at higher frequencies. In the control of short beams, we keep the bandwidth below the 1st vibration mode. We add damping to the rigid body mode, and make sure all the vibration modes have loop gains below 0 dB. When the vibration modes are excited, we add low-pass filters to reduce the gains of the vibration modes.

5.6.1 Suspension of a Short Hinged-Free Beam

We started the short beam suspension with hinged-free boundaries. The experimental setup is shown in Figure 5-12. The beam is 1.5 ft long, one end is supported by a flexure, and the other end is suspended by a magnetic bearing. We used the Dipole-Quadrupole actuator on this setup, since this was early in the project before we designed the Quad-U-Core actuators.

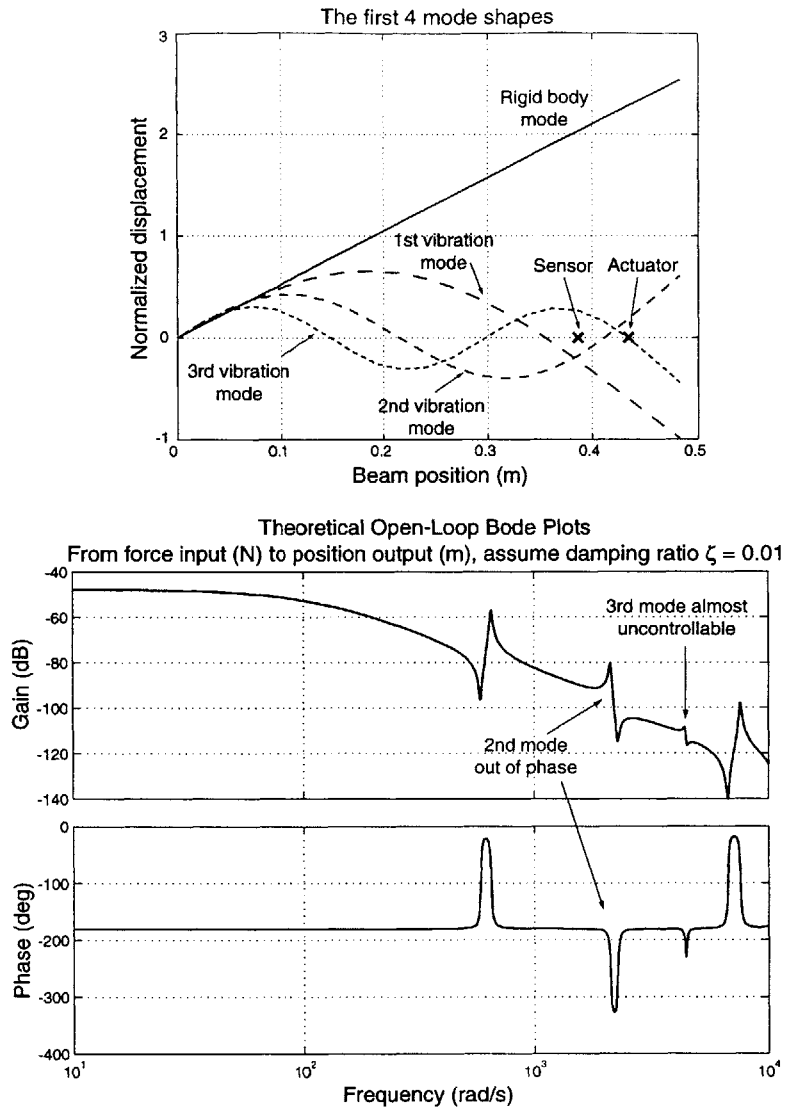

Figure 5-13: Modal shapes and open-loop Bode Plots of a hinged-free beam.

The modal shape for this beam and the associated open-loop Bode plot are shown in Figure 5-13. We design the controller such that the loop transfer function has a crossover around 150 rad/s. The controller is a simple lead compensator:

$$h(s) = 2\frac{s+50}{s+200} \text{ N/mm}, \tag{5.35}$$

which adds a phase lead around $50 \sim 200$ rad/s. We successfully stabilize it with a bandwidth below the 1st vibration mode.

The experimentally measured closed-loop Bode plot is shown in Figure 5-14. The

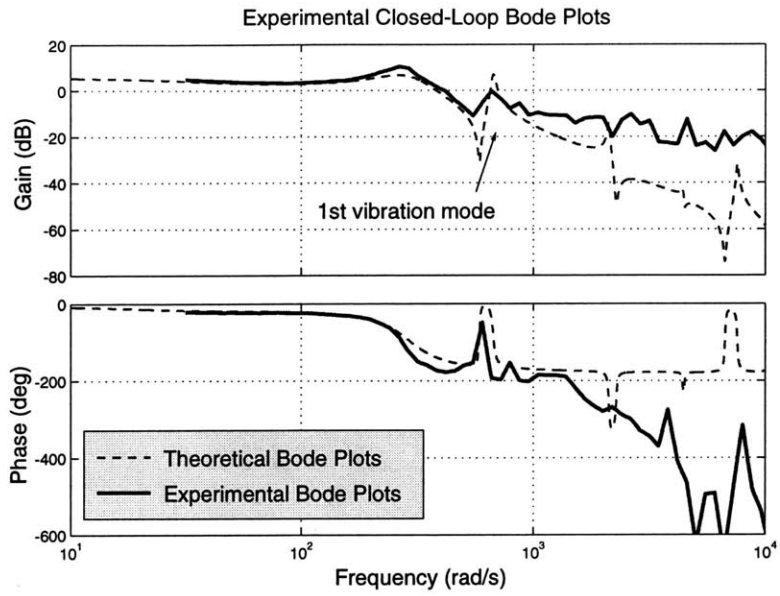

Figure 5-14: Experimental closed-loop Bode Plots of the suspension of a hinged-free beam. Dashed line shows theoretical Bode Plots for comparison, which neglects dynamics of actuator, sensor and time delay.

1st resonance mode is at around 100 Hz, and our closed-loop bandwidth is at around 25 Hz. These results show that we only control the rigid body mode of the short beam.

5.6.2 Suspension of a Short Free-Free Beam

In the second experiment, we use 2 Quad-U-Core actuators and 2 sensors to suspend a 2 ft long tube with free-free boundaries as shown in Figure 5-15. The purpose of this experiment is to test the new Quad-U-Core actuator design. In this experiment, we found the following problems:

1. Feedthrough from actuator to sensor: as described in Chapter 8, the main reasons are that the actuator has a fringing magnetic field in the axial direction, and that the actuator current controller has a resonance at 4 kHz.

2. Cross-coupling between sensors: due to the use of one current control board to drive all 8 sensors.

3. To use feedback linearization, we need accurate sensor feedback. The nonlinear

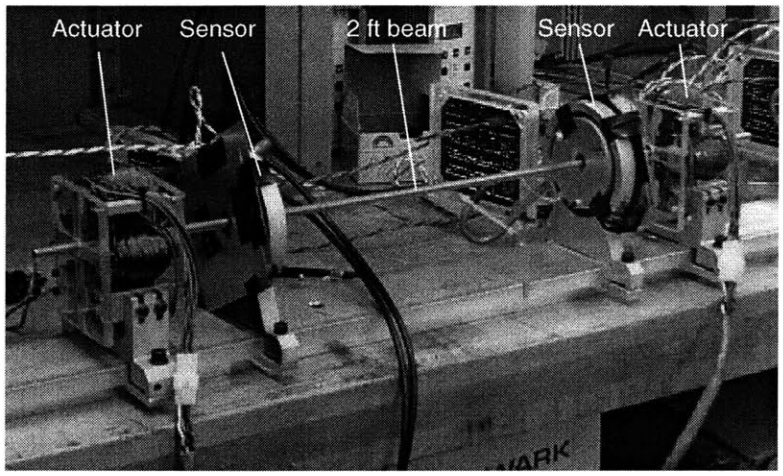

Figure 5-15: Suspension of a free-free beam with length L=2 ft by using 2 sensors and 2 Quad-U-Core actuators.

sensor output cannot provide accurate information.

4. When the tube has free-free boundaries, there is always some limit cycle resonance at high frequencies, such as 800 Hz, which is well above our control bandwidth.

5. Sensor/actuator non-collocation becomes problematic. The tube can be stable at one position, and becomes unstable when moved to the left or right by a few inches. The instability happens because the sensor and actuator move to the opposite sides of a vibration node, and the modal observability and controllability become out of phase.

After this experiment, I modified the circuit designs of sensors and actuators, as described in Chapter 8 and Chapter 7. The non-collocation and limit-cycle problems are solved later by the development of the sensor/actuator averaging methods, as will be described in Chapter 6.

5.7 Magnetic Suspension and Vibration Control of Long Beams

The final goal of our experiment is to robustly suspend the 10 ft long beam with varying boundary conditions. This is the most challenging task that we faced in this project. Especially when the tube is being suspended with free-free boundaries, the modal damping ratio is smaller than 0.001, which makes the control extremely difficult. After we developed the sensor/actuator averaging method, we successfully suspended the beam with varying boundary conditions, including free-free boundaries. Figure 5-16 shows the stable suspension of the 10 ft long beam with free-free boundaries.

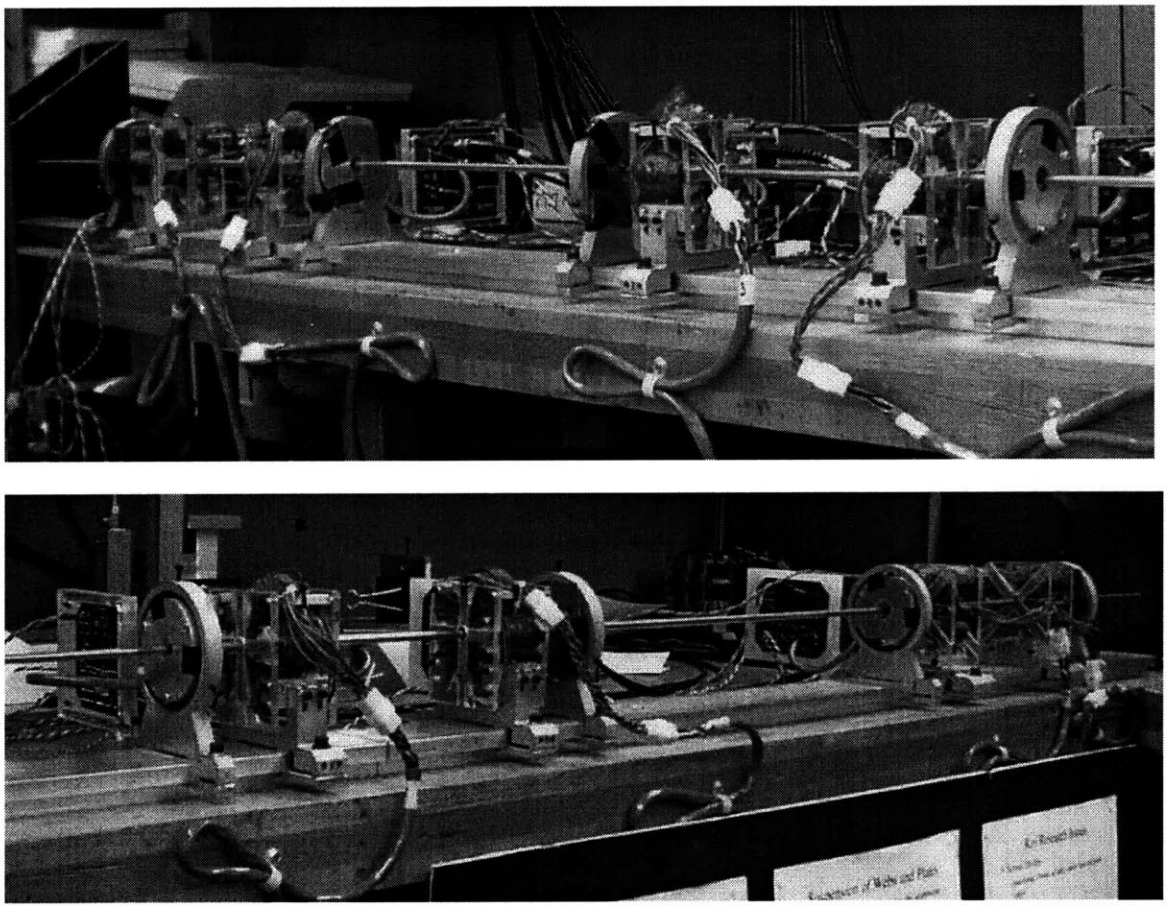

Figure 5-16: Suspension of a free-free beam with length L=10 ft by using 8 sensors and 8 quad-U-core actuators.

5.7.1 Suspension of Long Beams with Loose-Bore Ends

The first experiment of suspending the 10 ft long beam, we used 8 sensors and 8 actuators to control 8 points of the beam independently without sensor/actuator averaging. We applied the slow roll-up lead compensator, and could only stabilized the beam when it has loose-bore boundaries, which are supporting bores that are slightly larger than the tube. The loosely contacted boundaries provide enough damping to stabilize the system. However there were still high frequency vibration being excited as limit cycles. We could hear the collision between the tube and the loose bores. When the boundaries are set free, clamped, or hinged, the system goes unstable, because the energy can not be dissipated as much as by using loosely contacted boundaries.

We tried to lower the high frequency gains of the controller without loosing the dc stiffness, hence we applied a lag compensator. However, this attempt was never successful. The beam stuck to different poles of the actuators sequentially in a period of about 1 second, looked like a relay. For the rest of this experiment, I did not use a lag compensator.

5.7.2 Suspension of Long Beams with Free-Free Ends

The suspension of the free-free beam is extremely difficult since there is no contacted boundaries that can dissipate the vibration energy, hence the damping ratio is extremely low. In our attempt to suspend the free-free beam, we see the high frequency modes can be easily excited and destabilize the system. Hence we have tried to reduce the phase lag at high frequencies. We removed the actuator low-pass filters, and increased sensor filter bandwidth. By doing so, we reduce the phase lag, but allow the signals to be noisy. We minimized sampling time and calculation time. We designed the slow roll-up lead compensator to have only 15° phase lead across the vibration modes so as to reduce the high frequency gain increase associated with the compensator. After all these efforts, the system was still unstable. In operation, a resonance mode at 800 Hz built up in a few seconds and destabilized the system. We

were at a state that a slight touch by hand can add enough damping to stabilize the system.

We later came up with a special sensor/actuator positioning method that finally solves this problem. We use both sensor averaging and actuator averaging methods and finally stabilize the system. The levitated beam is robustly stable with varying boundary conditions. The details of sensor/actuator averaging method and the experimental results will be discussed in Chapter 6.

5.8 System Identification

To design the controller, it is important to understand the system dynamics. We can obtain the system dynamics by solving the analytic model, or by directly measuring it from the real system. Once we have the system open-loop dynamics, we can design and analyze our controller accordingly. In this section, I briefly describe how we experimentally identify the system dynamics, including identification of SISO systems and MIMO systems. For MIMO systems, the system transfer function needs to be obtained by solving matrix algebra.

In this thesis, I use the computer and DSP board to do on-line signal-analyzing to identify the system dynamics. I adopted the digital-signal-analyzer program developed by Lilienkamp [67] in our lab, and modified it for identifying MIMO systems. We use the swept sine method to measure the frequency response of the system for each sample frequency. The details of the program are shown in Appendix D.

5.8.1 Identification of SISO Systems

For SISO system, if the system is stable by itself, we can measure its open loop response directly, as shown in Figure 5-17(a).

However, if the system is neutral or unstable (such as our magnetic suspension system), we have to design a feedback controller to first stabilize the system, and then we can measure the system open-loop dynamics by measuring signals inside the loop, as shown in Figure 5-17(b). By introducing disturbance d, we have signals u_1

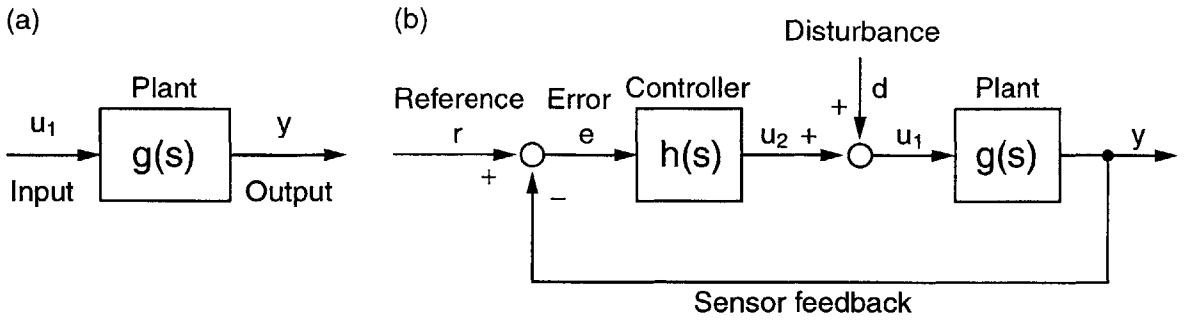

Figure 5-17: Block diagrams of SISO systems: (a) an open-loop system, and (b) a closed-loop system.

and u_2 excited. The transfer function can be shown as:

$$\frac{u_1}{d} = \frac{1}{1+hg}, \tag{5.36}$$

$$\frac{u_2}{d} = \frac{hg}{1+hg}, \tag{5.37}$$

where the order of $h(s)$ and $g(s)$ are interchangeable in multiplication since they are scalars. Hence the loop transfer function $h(s)g(s)$ can be obtained by directly calculating either one of these two equations, or by comparing u_1 and u_2 by

$$\frac{u_2}{u_1} = hg. \tag{5.38}$$

Equation 5.38 is more often used in analog analysis. By comparing u_1 and u_2 signals, it immediately shows the loop transfer functions. In digital analysis, all of these three equations can be used conveniently.

5.8.2 Identification of MIMO Systems

For MIMO system, the system identification involves matrix calculation, and cannot be simply obtained by comparing two signals. With the help of computer, we can identify MIMO systems by storing signals and solving matrix equation afterwards.

A stable open-loop system is shown in Figure 5-18(a), and the dynamics can be simply calculated from input u_1 and output y.

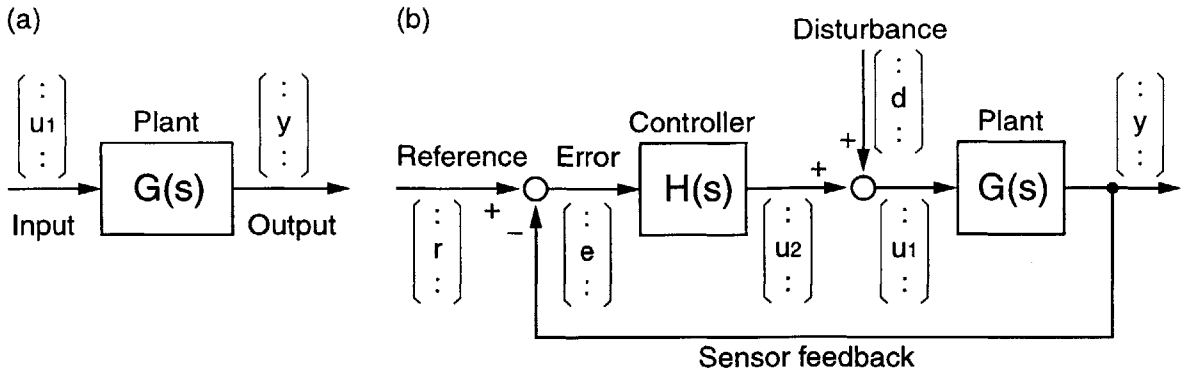

Figure 5-18: Block diagrams of MIMO systems: (a) an open-loop system, and (b) a closed-loop system.

For a neutral or an unstable open-loop system, we need to first stabilize the system, and then measure the open-loop dynamics by measuring signals inside the loop. With the system shown in Figure 5-18(b), the closed-loop transfer functions between the signals can be calculated by

$$\begin{aligned} & y = G(d + He) \\ \Rightarrow \quad & y = G(d + H(r - y)) \\ \Rightarrow \quad & (I + GH)y = Gd + GHr \\ \Rightarrow \quad & y = (I + GH)^{-1}Gd + (I + GH)^{-1}GHr. \end{aligned} \tag{5.39}$$

Notice the order of $G(s)$ and $H(s)$ are not interchangeable in multiplication since they are matrices. Our interest is to measure the open-loop transfer function matrix $G(s)$. It cannot be directly calculated from Equation 5.39. Instead, we can measure u_1 and u_2, which can be represented in the following equations:

$$\begin{aligned} & u_1 = d + He = d + H(r - Gu_1) \\ \Rightarrow \quad & (I + HG)u_1 = Hr + d \\ \Rightarrow \quad & u_1 = (I + HG)^{-1}Hr + (I + HG)^{-1}d, \end{aligned} \tag{5.40}$$

$$u_2 = H(r - y) = H(r - G(d + u_2))$$

$$\Rightarrow \quad (I + HG)u_2 = Hr - HGd$$

$$\Rightarrow \quad u_2 = (I + HG)^{-1}Hr - (I + HG)^{-1}HGd. \tag{5.41}$$

Since we know our controller $H(s)$, the transfer function matrix $G(s)$ can be easily calculated from Equation 5.40 from u_1 and d. Hence in this thesis, I assign $r = 0$, apply disturbance d, and measure u_1 and d to calculate $G(s)$ for each sample frequency by

$$u_1 = (I + HG)^{-1}d. \tag{5.42}$$

In the system identification code, we assign the disturbance d to be an identity matrix. Assume we have 3 inputs and 3 outputs, to calculate the 3×3 $G(s)$ matrix, we need to apply 3 different disturbances, and measure 3 outputs for each disturbances, as shown in Figure 5-19.

(1) At t_1, I apply the first disturbance: $d = [1\ 0\ 0]^T$, and the measured outputs are:

$$\begin{bmatrix} u_1(1) \\ u_1(2) \\ u_1(3) \end{bmatrix}_{t1} = \begin{bmatrix} a_{11} \\ a_{21} \\ a_{31} \end{bmatrix} = (I + HG)^{-1} \begin{bmatrix} d_1(1) \\ d_1(2) \\ d_1(3) \end{bmatrix}_{t1} = (I + HG)^{-1} \begin{bmatrix} 1 \\ 0 \\ 0 \end{bmatrix}. \tag{5.43}$$

(2) At t_2, I apply the second disturbance: $d = [0\ 1\ 0]^T$, and the measured outputs are:

$$\begin{bmatrix} u_1(1) \\ u_1(2) \\ u_1(3) \end{bmatrix}_{t2} = \begin{bmatrix} a_{12} \\ a_{22} \\ a_{32} \end{bmatrix} = (I + HG)^{-1} \begin{bmatrix} d_1(1) \\ d_1(2) \\ d_1(3) \end{bmatrix}_{t2} = (I + HG)^{-1} \begin{bmatrix} 0 \\ 1 \\ 0 \end{bmatrix} \tag{5.44}$$

(3) At t_3, I apply the third disturbance: $d = [0\ 0\ 1]^T$, and the measured outputs are:

$$\begin{bmatrix} u_1(1) \\ u_1(2) \\ u_1(3) \end{bmatrix}_{t3} = \begin{bmatrix} a_{13} \\ a_{23} \\ a_{33} \end{bmatrix} = (I + HG)^{-1} \begin{bmatrix} d_1(1) \\ d_1(2) \\ d_1(3) \end{bmatrix}_{t3} = (I + HG)^{-1} \begin{bmatrix} 0 \\ 0 \\ 1 \end{bmatrix}. \tag{5.45}$$

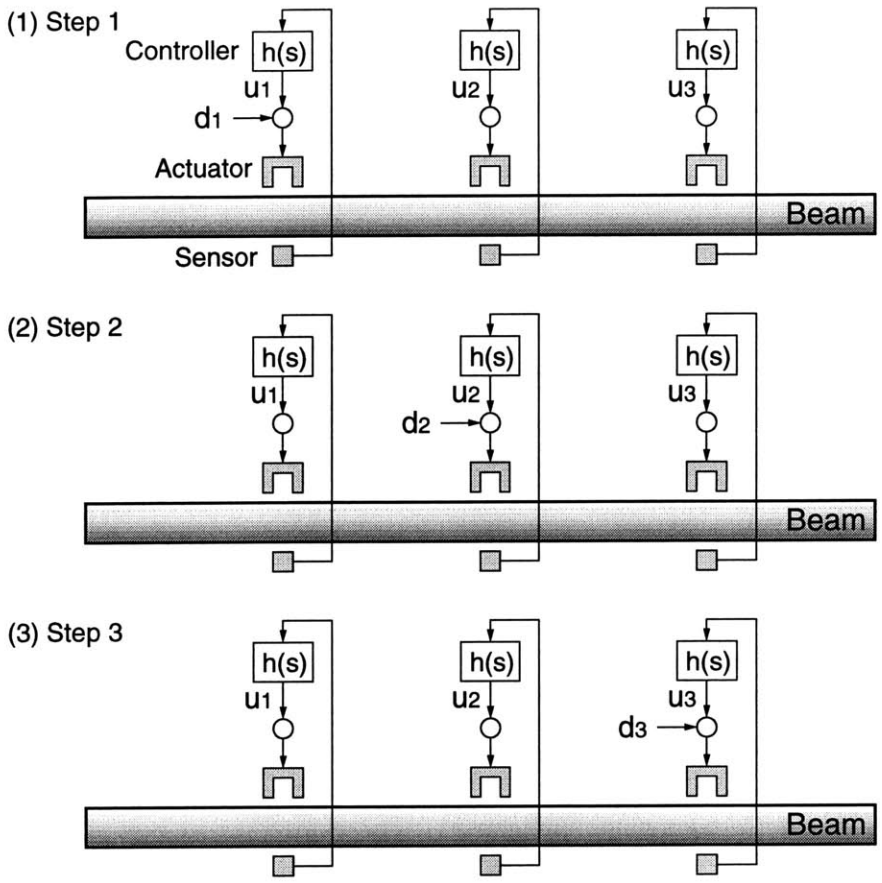

Figure 5-19: Identification of a 3-input-3-output system: (1) apply d_1, measure u_1, u_2, and u_3, (2) apply d_2, measure u_1, u_2, and u_3, and (3) apply d_3, measure u_1, u_2, and u_3.

(4) Combine the previous 3 equations, we have

$$A_{nn} = \begin{bmatrix} a_{11} & a_{12} & a_{13} \\ a_{21} & a_{22} & a_{23} \\ a_{31} & a_{32} & a_{33} \end{bmatrix} = (I + HG)^{-1} \begin{bmatrix} 1 & 0 & 0 \\ 0 & 1 & 0 \\ 0 & 0 & 1 \end{bmatrix}. \tag{5.46}$$

Thus we can recover the matrix of $G(s)$ by solving

$$G = H^{-1}(I - A_{nn}^{-1}). \tag{5.47}$$

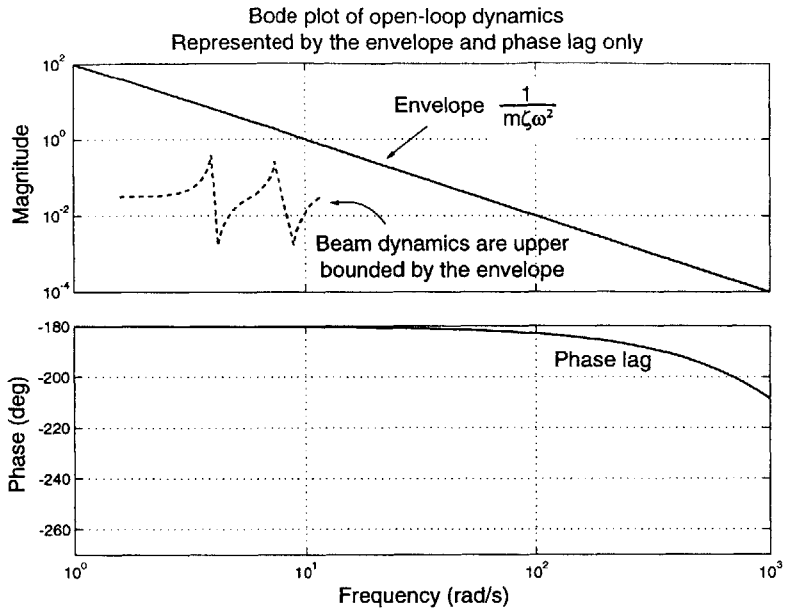

Figure 5-20: Open-loop Bode plot of the beam, which is represented by the peak envelope and phase lag.

5.9 Summary of Suspension Stage Design Method

In this chapter, we decompose the beam suspension systems design into a few simple steps. In the following, I will use a random example to show the simplicity of the proposed design method.

For example, suppose we have a beam with $EI = 200$ Nm^2, $\rho A = 0.2$ kg/m, total length $L = 10$ m, damping ratio $\zeta = 0.005$, and a time delay of 500 μs, which causes 30° phase lag around 1000 rad/s. We can design the suspension systems by the following steps:

1. **Peak envelope**: The equation of the peak envelope of this beam is $G_{envelope}(\omega) = 1/(m\zeta\omega^2) = 1/(2 \cdot 0.005 \cdot \omega^2) = 100/\omega^2$. The Bode plot of this envelope is shown in Figure 5-20, the phase lag is the result of the 500 μs time delay. At $\omega = 1000$ rad/s, the envelope has a gain of 1×10^{-4} m/N.

2. **Beam dispersion equation** ($EIk_n^4 = \rho A\omega_n^2$): For this example, we have $k_n^2 = 0.03\omega_n$. From beam equation, we know that the 1st vibration mode for simply supported boundaries has a wavelength of $2L = 20$ m (wavenumber $k_1 = 0.31$

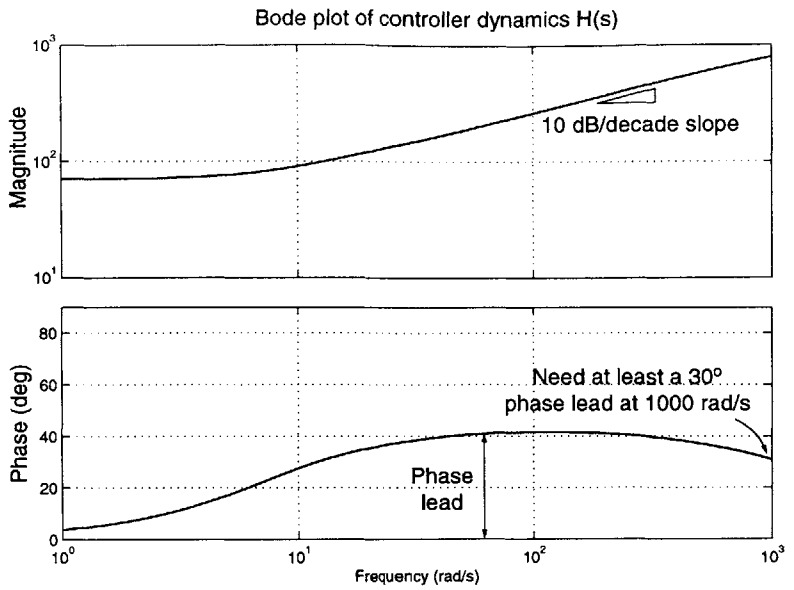

Figure 5-21: Bode plot of the slow roll-up lead compensator, which has a phase lead from 3 rad/s to 1000 rad/s .

rad/m), and has a resonance frequency of 3.3 rad/s. And the resonance mode near 1000 rad/s has wavenumber $k_n \approx 5.5$ rad/m (wavelength 1.1m).

3. **Controller**: We design a controller such that the cross over frequency of the loop transfer function with respect to the envelope to be around 1000 rad/s, where there is a 30° phase lag in the open-loop dynamics. We design a slow roll-up lead compensator with 10 dB/decade gain slope, that has roughly a 30° phase margin from 3 to 1000 rad/s (a lead compensator for 2.5 decade range). To make the loop gain to be 1 at 1000 rad/s, we choose a SISO controller gain to be 1×10^4 N/m at 1000 rad/s. If we actually use 8 independent sensor/actuator pairs to control the beam at 8 points, we should modify the envelope by 8 times, or divide the controller gain by 8. Hence we choose the controller to be

$$H(s) = 70\frac{16(s+10)(s+40)(s+160)(s+640)}{(s+20)(s+80)(s+320)(s+1280)}, \tag{5.48}$$

and the Bode plot of this controller is shown in Figure 5-21. This controller has a dc gain of 70 N/m, which is also the dc stiffness of each of the 8 magnetic bearings. The resulting loop transfer function is shown in Figure 5-22. In this

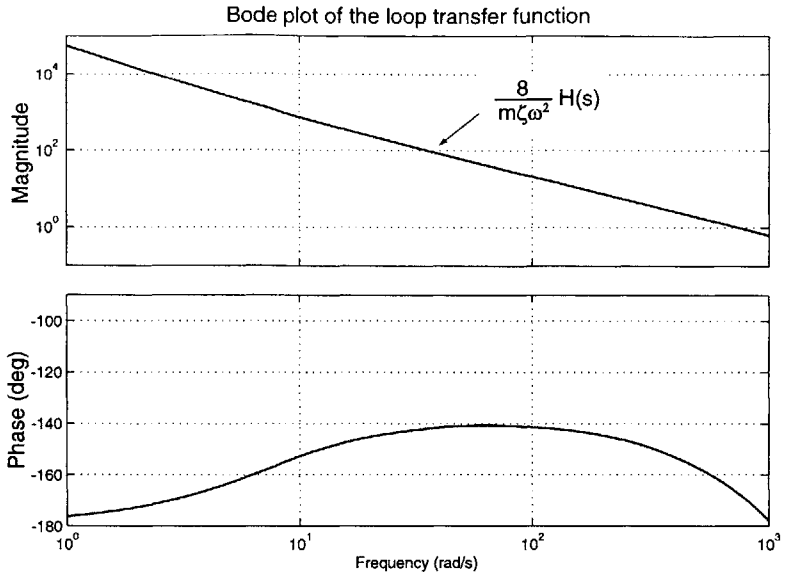

Figure 5-22: Bode plot of the loop transfer function.

Bode plot, when the gain is higher than 0 dB, the phase margin is positive, which shows the closed-loop system is stable.

4. **Sensor/actuator averaging**: The details of sensor averaging and actuator averaging methods will be introduced in Chapter 6. By using 2-sensor averaging, we place 2 sensors set apart by 55 cm and average the output, which will attenuate resonance modes with frequencies near 1000 rad/s (wavelengths near 110 cm). By using 2-actuator averaging, we place 2 actuators set apart by 50 cm, and apply the same force (1/2 the control force) to both actuators, that will attenuate resonance modes with frequencies near 1300 rad/s.

5. At last, we can fine tune the controller. With the help of sensor/actuator averaging, we can increase the proportional gain of the controller, hence increase the magnetic bearing stiffness. We can also fine tune the controller pole-zero locations to adjust for higher phase margin or lower gain slope.

This simple example shows the simplicity of our proposed design method for suspension systems. Given the information of the beam to be suspended, we can easily estimate the final suspension stiffness and positioning of the sensors and actuators.

Chapter 6

Sensor Averaging and Actuator Averaging Methods for Vibration Control

One of the key contributions of this thesis is the idea that the stability of the non-contact suspension of flexible objects can be significantly enhanced by the use of properly chosen weighted averages of sensing and actuation. We refer to this idea as *sensor averaging* when applied to measurements and *actuator averaging* when applied to control forces. The key idea of sensor averaging is to use a weighted average of the outputs of a distributed array of N motion sensors, and thus attenuates the observability of undesired resonance modes. On the other hand, with actuator averaging we apply a weighted distributed array of M forces , and thus reduce the controllability of undesired resonance modes. These approaches create spatial filters that robustly attenuate resonance modes without adversely affecting the phase. The advantages of these approaches are shown to be independent of the specific boundary conditions or longitudinal dimensions of the structure. The averaging also eliminate the sensor/actuator non-collocation problems. Theses approaches are thus applicable to a wide range of structural control problems, and can be used to deal with varying/unknown boundary conditions or varying/unknown structural lengths.

This chapter is organized as follows. To demonstrate the principles, I use the

vibration control of an untensioned beam to describe the concepts of sensor averaging and actuator averaging. Following this I demonstrate the effectiveness of sensor and actuator averaging in our experiments for magnetic suspension of tubular beams. Finally, I extend the theory of these averaging methods to more general tensioned structures, including beams, strings, plates, and membranes.

6.1 Introduction to Sensor Averaging and Actuator Averaging

The goal of this project is to robustly stabilize suspended flexible structures for non-contact manufacturing processes. The suspended objects may have varying boundary conditions, varying structure lengths, and varying structure positions. Moreover, the lightly-damped vibration modes make it extremely difficult to stabilize such systems. The challenges of controlling such systems is indicated in the Bode plot of Figure 6-1, where we can see the multiple crossings of unity gain and high-frequency phase lag typical of these suspensions. and time delay.

We stabilize the system resonance modes in two ways: (1) at low frequencies, we add damping (phase) to these modes by using a slow roll-up lead compensator, and (2) at high frequencies adding sensor and/or actuator averaging. Since we have significant phase lag and do not have the ability to damp these high-frequency modes, we use averaging to reduce the gains of these modes to below 0 dB.

By choosing a slow-roll-up lead compensator, we have the loop transfer function as shown in Figure 6-2, which has not included any sensor or actuator averaging. Figure 6-2 demonstrates the difficulties of stabilizing this flexible beam due to the lightly-damped resonance modes and the phase lag from the computational and sampling time-delay and from the sensor/actuator low-pass filters. The high frequency modes have loop gain higher than 0 dB and negative phase margin, and this will destabilize the system. This shows the difficulties we encountered before we developed the concept of sensor and actuator averaging.

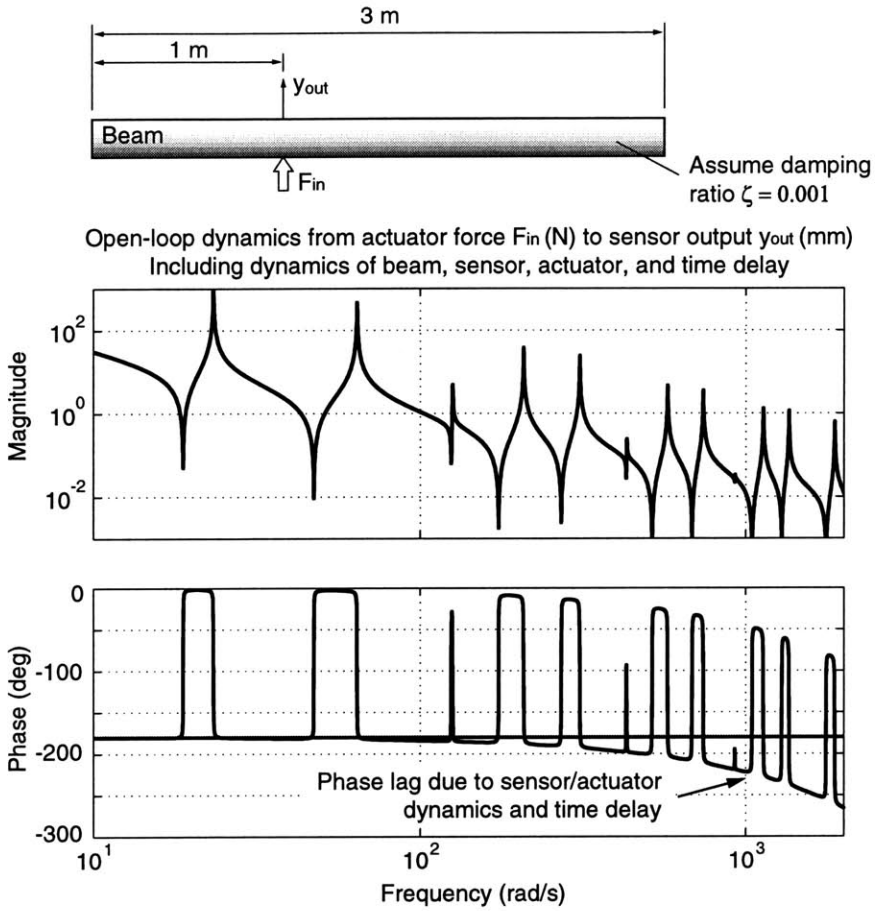

Figure 6-1: Plant dynamics from commanded actuator force F_{in} (N) to sensor output y_{out} (mm), including dynamics of the free-free beam, sensor, actuator, and time delay. Here we assume the modal damping ratio $\zeta = 0.001$.

The following methods are frequently considered to stabilize such systems:

1. Add a lead compensator to high frequencies: If we add phase lead to this high frequency range, the gain increase associated with the lead will amplify the gains of the modes at higher frequencies, and these higher frequency modes will destabilize the system.

2. Add a low-pass filter to high frequencies: If we add a low-pass filter to reduce the gains of these high frequency modes, we will lower the phase of the modes at lower frequencies, and these lower frequency modes will destabilize the system.

3. Reduce the controller proportional gain: This method is undesired since we cannot sacrifice the magnetic bearing stiffness.

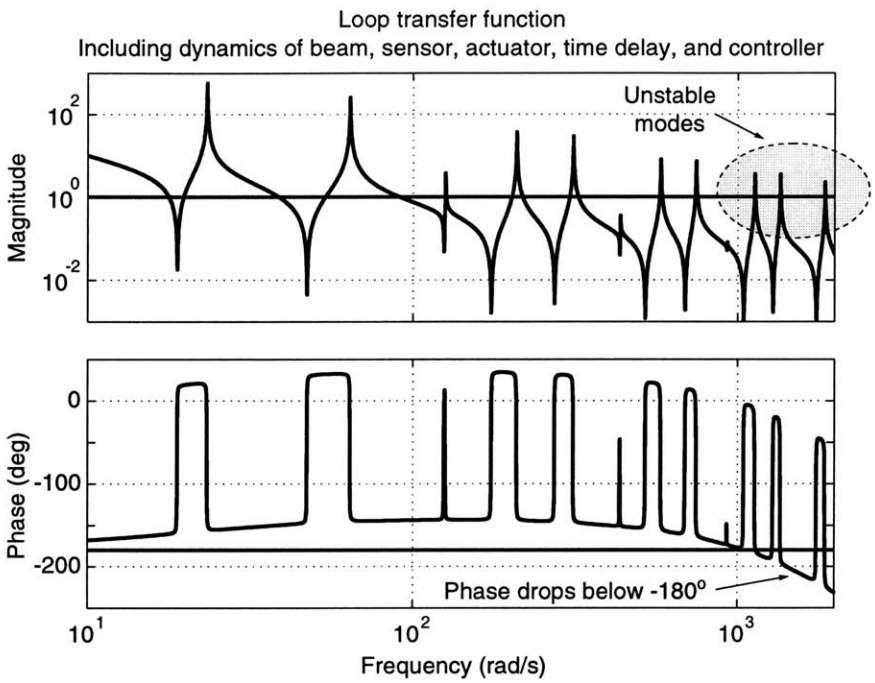

Figure 6-2: Suspension Loop transfer function, including the free-free beam, sensor, actuator, time delay, and controller. Note difficulty of stabilizing high frequency modes in the presence of the high frequency phase lag. This plot does not include any sensor or actuator averaging.

4. Design notch filters to exactly cancel the modes: This is essentially a model-based controller, which is sensitive to system uncertainties and changes. For example, a change of boundary conditions or structural lengths can easily destabilize such a controller.

5. Place sensors or actuators right on the nodes of the corresponding unstable modal shapes: This is also a model-based method, since it requires knowledge of the node locations and is thus sensitive to system uncertainties and changes. The varying boundary conditions make this approach not applicable.

In this project, we developed *sensor averaging* and *actuator averaging* methods to solve the stability problem. Both methods can robustly attenuate the gains of undesired resonance modes. These will later be shown as a new concept for a non-model-based modal-band-stop filter associated with non-contact suspensions. The basic arrangement of sensor averaging places two sensors set apart by a distance of $2d_s$, and uses the averaged measurement as a single output for feedback. Hence the

resonance modes with wavelengths close to $4d_s$ will have opposite deflections at the two sensors, and thus a low contribution to the averaged output. Actuator averaging is a dual to sensor averaging. Here, two actuators are spaced apart by a distance of $2d_a$, and we apply the same force to each actuator. Since the modes will be forced in opposite directions if their wavelength is close to $4d_a$, this results in a similar filtering effect. On this basis, we show that sensor/actuator averaging can reduce modal observability/controllability over a broad range of undesired resonance modes without adversely affecting the measurement or actuation phase. Another advantage of using these averaging methods is that they only depend on the properties of the structure element, and are independent of boundary conditions, structure lengths, or structure positions. Another advantage is that the averaging arrangement also eliminates possible sensor/actuator non-collocation problems. These advantages will be further discussed in the following sections.

6.2 Sensor Interpolation and Sensor Averaging

Before I start the derivation of sensor averaging, I would like to introduce how we came up with this idea. Before we developed the sensor averaging method, we had another idea of *sensor interpolation* to place sensors and actuators, which will be discussed in the following.

Our first approach to suspend the 10 ft long beam is by using 8 sensor/actuator pairs to control 8 points of the beam, each sensor/actuator pair consists one sensor and one actuator located in close proximity. However, it did not work out because of the problems with high-frequency modes elucidated in the previous section.

Our second approach is the idea of force/moment control; we try to control both linear and angular displacements of a point. This approach has the advantage that there is no hidden mode even when the sensor/actuator pair is located on a vibration node since we can observe the angular displacement on the node. In this approach, we place two actuators in between two sensors in close proximity as shown in Figure 6-3. With the two position sensors, we can sense both linear and angular displacements of

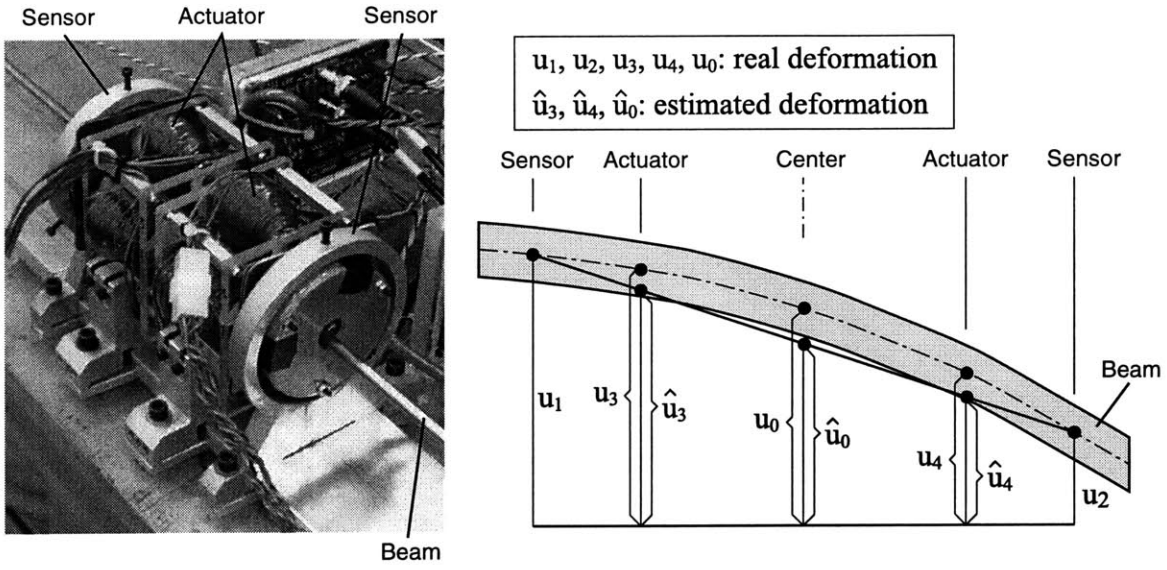

Figure 6-3: Sensor interpolation: measure u_1 and u_2, and calculate $\hat{u}_3$ and $\hat{u}_4$ by interpolation to estimate the real displacements of u_3 and u_4.

the mid-point, and with the two force actuators, we can apply both force and moment to the mid-point. We tried this approach, but it did not help on stabilizing the suspension. It does offer the advantage that every vibration mode is observable and controllable. However, what we need to stabilize our system is not to observe/control the hidden mode, but to attenuate the high frequency modes.

In this approach, we noticed that we can use the same sensor/actuator positioning method, and eliminate possible sensor/actuator non-collocation problems if we use sensor interpolation method. As shown in Figure 6-3, we measure sensor outputs u_1 and u_2, and calculate $\hat{u}_3$ and $\hat{u}_4$ by interpolation to estimate the real displacements u_3 and u_4 at the actuators. In result, sensors and actuators can be considered collocated and the non-collocation problems can be reduced.

However, our results show that the gain of the estimated displacement to the real displacement $\hat{u}/u$ depends on the sensor/actuator location along the beam. The only exception is when two actuators merge into one, in which case interpolation becomes averaging.

Averaging is a special case of interpolation, we place only one actuator at the mid-point between the two sensors. As shown in Figure 6-3, we average the sensor

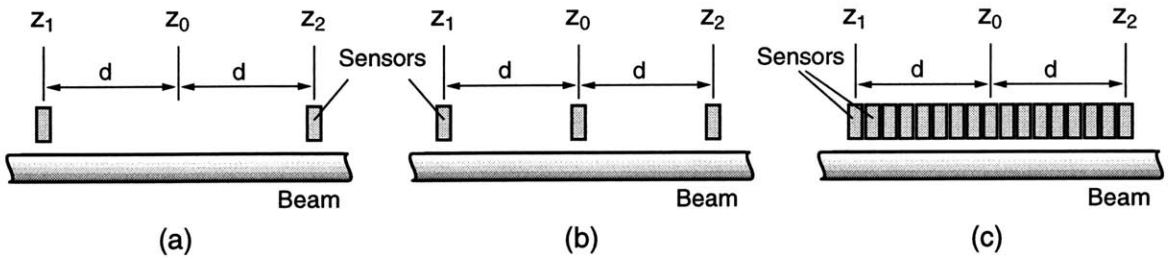

Figure 6-4: Sensor positioning arrangements for beams: (a) 2-sensor averaging, (b) 3-sensor averaging, and (c) continuous-sensor averaging.

outputs u_1 and u_2 to get $\hat{u}_0$ to predict the real displacement u_0 at the actuator. It has the property that the gain of the averaged displacement to the real displacement $\hat{u}_0/u_0$ is independent of the sensors/actuator location along the beam. Furthermore, we find that we can attenuate certain sinusoidal resonance modes by adjusting the sensor distance. With this discovery, we further study sensor averaging and its dual of actuator averaging in the following sections. We will show the derivation by using a beam example, and then extend it to other structures.

6.3 Sensor Averaging and Actuator Averaging for Beams without Tension

In this section, we explore the sensor averaging and actuator averaging methods for beams. We assume the beam has negligible tension force. We start with sensor averaging, and then show the dual properties of actuator averaging.

In sensor averaging, we use the average of multiple sensors' measurements to stand for a single point's displacement. Figure 6-4 shows the different arrangements of sensor locations that we will study in the following sections.

6.3.1 Summary of Dynamic Analysis of Beams without Tension

In this section, we briefly review the structural dynamics of slender beams without tension and axial velocity. As developed in Chapter 4, the beam equation can be

written as:

$$EI\frac{\partial^4 u}{\partial z^4} + \rho A\frac{\partial^2 u}{\partial t^2} = f, \tag{6.1}$$

where EI is bending stiffness, z is axial coordinate, u is transverse deflection, ρ is material density, A is cross-sectional area, and f is an external transverse force density. From Equation 6.1, assuming a homogeneous solution $u_h(z,t) = Ce^{j\omega t}e^{kz}$, the resulting beam dispersion equation becomes

$$EIk^4 - \rho A\omega^2 = 0. \tag{6.2}$$

The natural response of this beam equation can be represented by the superposition of all possible homogeneous solutions

$$\begin{aligned} u(z,t) &= \sum_{n=1}^{\infty} \xi_n(t)\phi_n(z) \\ &= \sum_{n=1}^{\infty} \xi_n(t)\left(C_{n1}\cos k_n z + C_{n2}\sin k_n z + C_{n3}\cosh k_n z + C_{n4}\sinh k_n z\right) \\ &\approx \sum_{n=1}^{\infty} \xi_n(t)\left(C_{n1}\cos k_n z + C_{n2}\sin k_n z\right), \\ &\quad (\text{ when } k_n \text{ is large, and } z \text{ is away from boundaries. }) \end{aligned} \tag{6.3}$$

with wavenumber k_n:

$$k_n = \sqrt[4]{\frac{\rho A\omega_n^2}{EI}}, \tag{6.4}$$

where ξ_n is the nth modal coordinate, ϕ_n is the nth modal shape, and ω_n is the resonance frequency. Here C_{n1} and C_{n2} represent sinusoidal waveforms with wavelengths $2\pi/k_n$, and C_{n3} and C_{n4} represent evanescent waveforms that decay exponentially with increasing distances from the boundaries. Notice that the evanescent waveforms have negligible effects far away from the boundaries especially at high frequencies where k_n becomes large. For example, the 9th modal shape for the beam in our

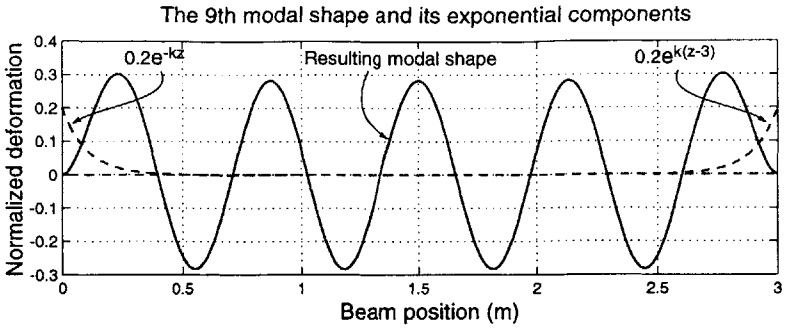

Figure 6-5: The 9th modal shape of a clamped-clamped beam. The exponential components are shown in dashed line, which have negligible effects away from the boundaries.

experiment with clamped-clamped ends is

$$\begin{aligned}\phi_9(z) &= -0.2\cos k_n z + 0.2\sin k_n z + \\ &\quad (0.2 + 2.184 \times 10^{-14})\cosh k_n z - (0.2 - 2.184 \times 10^{-14})\sinh k_n z \\ &= -0.2\cos k_9 z + 0.2\sin k_9 z + 0.2e^{k_9(z-3)} + 0.2e^{-k_9 z}. \end{aligned} \tag{6.5}$$

This modal shape is shown in Figure 6-5, and the exponential components are shown in dashed lines. It shows that the exponential components have negligible effects away from the boundaries.

We also derived the modal analysis of beam dynamics in Chapter 4. In summary, the system dynamics can be decoupled into ordinary differential equations for each mode. The frequency response of the nth mode of beam dynamics can be represented as

$$\frac{\xi_n(s)}{N_n(s)} = \frac{1}{M_n(s^2 + 2\zeta_n\omega_n s + \omega_n^2)}, \tag{6.6}$$

where N_n is modal force, M_n is modal mass, and ζ_n is modal damping ratio. If we have a point force input at z_a: $f(z,t) = f(t)\delta(z - z_a)$, and a position feedback at z_s: $y(t) = u(z_s, t)$, the frequency response from input f to output y becomes

$$\boxed{\frac{y(s)}{f(s)} = \sum_{n=1}^{\infty} \frac{\phi_n(z_s)\phi_n(z_a)}{M_n(s^2 + 2\zeta_n\omega_n s + \omega_n^2)}} \tag{6.7}$$

The modal shape at the sensor position z_s determines the modal observability $\phi_n(z_s)$, and the modal shape at the actuator position z_a determines the modal controllability $\phi_n(z_a)$ [4]. Equation 6.7 shows that the modal properties can be modified by sensor/actuator positioning. For example, if an actuator is placed on a node of the ith modal shape, such that modal controllability $\phi_i(z_a) = 0$, the gain of the 3rd mode will become zero. For another example, if an actuator and a sensor are placed on the opposite sides of a node of the jth modal shape, such that modal controllability $\phi_j(z_a) = -0.1$ and $\phi_j(z_s) = 0.1$, the modal gain becomes out of phase by 180°, which causes non-collocation problems in a feedback system based on these positions.

In the following, we discuss the averaging effects on beams with 2-sensor averaging, 3-sensor averaging, and with more general sensor weightings.

6.3.2 2-Sensor Averaging for Beams

As shown in Figure 6-4(a), we place two sensors set apart by a distance of $2d$, and predict the displacement of the center point at $z = z_0$. The real displacement at z_0 is:

$$u(z_o, t) = \sum_{n=1}^{\infty} \xi_n(t)\phi_n(z_0), \tag{6.8}$$

and the averaged output from 2 sensors at $z_1 = (z_o - d)$ and $z_2 = (z_o + d)$ is:

$$\begin{aligned}
\hat{u}(z_o, t) &= \frac{1}{2}(u(z_1, t) + u(z_2, t)) \\
&= \frac{1}{2}\sum_{n=1}^{\infty} \xi_n(t)[\phi_n(z_1) + \phi_n(z_2)] \\
&= \frac{1}{2}\sum_{n=1}^{\infty} \xi_n(t)[C_{n1}(\cos k_n z_1 + \cos k_n z_2) + C_{n2}(\sin k_n z_1 + \sin k_n z_2)] \\
&= \sum_{n=1}^{\infty} \xi_n(t)(C_{n1}\cos k_n z_o + C_{n2}\sin k_n z_o)\cos k_n d \\
&= \sum_{n=1}^{\infty} (\xi_n(t)\phi_n(z_o) \cdot \cos k_n d)\,.
\end{aligned} \tag{6.9}$$

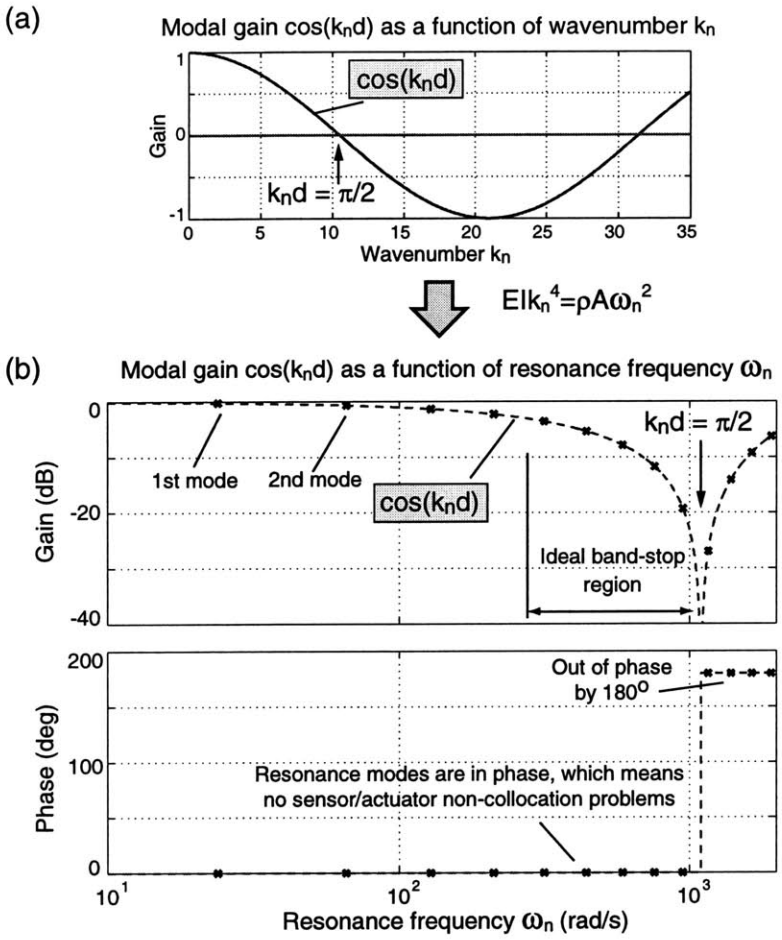

Figure 6-6: 2-Sensor averaging for beams: modal gain $\cos k_n d$ plotted as (a) a function of k_n, and (b) a function of ω_n.

Compare Equation6.8 and Equation 6.9, sensor averaging creates a modal-band-stop filter: each mode is multiplied by a gain of $\cos k_n d$. Replacing the wavenumber k_n by frequency ω_n from the beam dispersion equation, the modal gain $\cos k_n d$ becomes

$$\cos k_n d = \cos\left(\sqrt[4]{\frac{\rho A \omega_n^2}{EI}} d\right). \tag{6.10}$$

Using our experimental setup as an example, the tubular beam has $(\rho A)/(EI) = 0.01$. For a spacing $d = 0.15$ m, the result of Equation 6.10 is illustrated in Figure 6-6. If we plot the modal gain as a function of wavenumber k_n, it is simply a cosine function. The notch zero is located at $k_n d = \pi/2$ (wavelength = 4d). When we plot the modal gain as a function of resonance frequency ω_n, the resulting plot shows

that some resonance modes are attenuated near the notch zero at $\omega_n \approx 1000$ rad/s (wavelength = 60 cm). The phase stays unchanged before the notch, and flips by 180° after the notch when $\cos k_n d < 0$. The result shows a very promising potential: *if we can adjust the sensor distance* $2d$*, we can attenuate undesired resonance modes without adversely affecting the phase below the notch.* Furthermore, at frequencies below the cosine notch, all the resonance modes are in phase, which means there will be no sensor/actuator non-collocation problems for these modes.

To demonstrate this cosine effect on beam dynamics, I model the beam dynamics with an output $y(t) = \frac{1}{2}(u(z_1,t) + u(z_2,t))$ instead of $y(t) = u(z_0,t)$. In terms of state-space notation by $[A,B,C,D]$ matrices, I simply modify the C matrix to implement the sensor averaging. The resulting Bode Plots is shown in Figure 6-7, which is modeled by using the finite element method within the Matlab only for the purpose of convenience. The modal gain $\cos k_n d$ creates an ideal band-stop filter for the resonance modes over a broad range of frequencies without adversely affecting the phase. If we put the cosine notch at the frequency region where there will be unstable modes (gain > 0 dB, phase < −180°), this notch attenuates the resonance peaks without affecting the phase. Thereby we can increase the system gain margin and improves the stability-robustness.

6.3.3 Modal Analysis of Sensor Averaging

To further understand the behavior of sensor averaging, we can rewrite Equation 6.9 by modal analysis, and it becomes

$$\boxed{\frac{\hat{u}(s)}{f(s)} = \sum_{n=1}^{\infty}\left(\frac{\phi_n^2(z_o)}{M_n(s^2 + 2\zeta_n\omega_n s + \omega_n^2)} \cdot \cos k_n d\right)} \tag{6.11}$$

Equation 6.11 is indeed a non-model-based modal-band-stop filter. To demonstrate the effect of sensor averaging on resonance modes, we use an example of a system

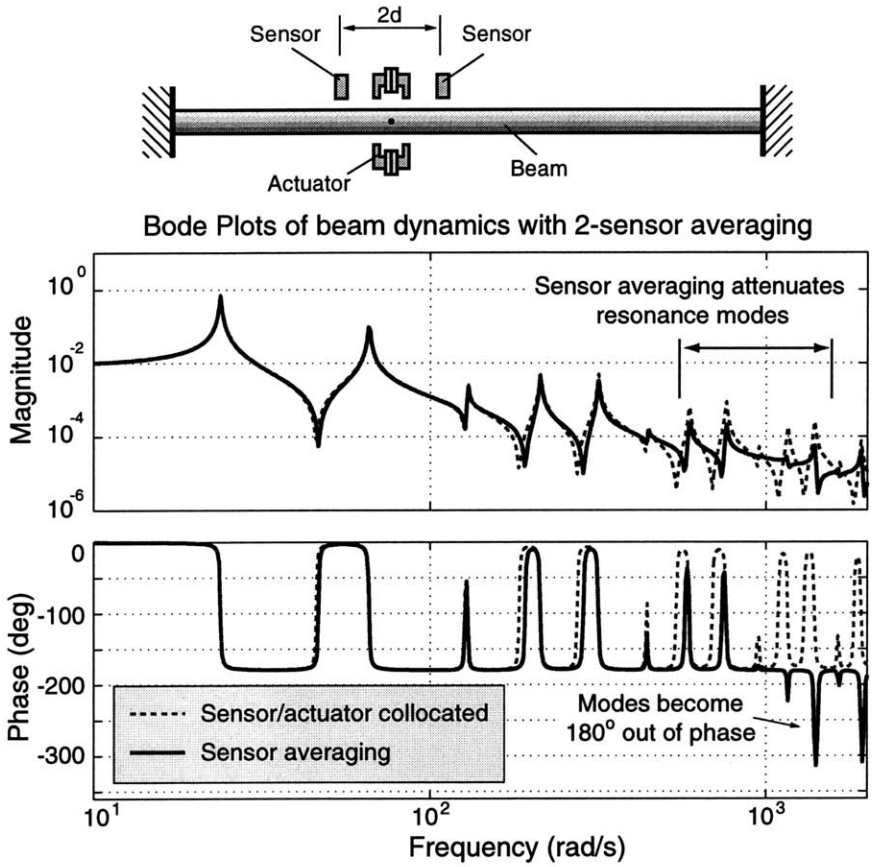

Figure 6-7: Theoretical beam model for 2-sensor averaging. Solid line shows a beam model with 2-sensor averaging ($d = 15$ cm). Note that a broad range of resonance modes are attenuated. Dashed line shows a beam model with collocated sensor and actuator ($d = 0$) for comparison.

with 3 resonance modes, The transfer function of this system is assumed to be:

$$\frac{y(s)}{f(s)} = \frac{1}{s^2 + 24^2} + \frac{K_2}{s^2 + 66^2} + \frac{1}{s^2 + 129^2}, \tag{6.12}$$

where the resonance frequencies are $\omega_1 = 24$ rad/s, $\omega_2 = 66$ rad/s, and $\omega_3 = 129$ rad/s. If the modal gain of the 2nd mode K_2 is equal to 1, we have the resulting frequency response as shown in Figure 6-8. The frequency response is simply the linear combination of each modal response.

If we can reduce the modal gain of the 2nd mode, assume K_2 is reduced to 0.1, we have the resulting frequency response as shown in Figure 6-9. The reduction of the modal gain makes the frequency response of the 2nd mode reduced by 10 times,

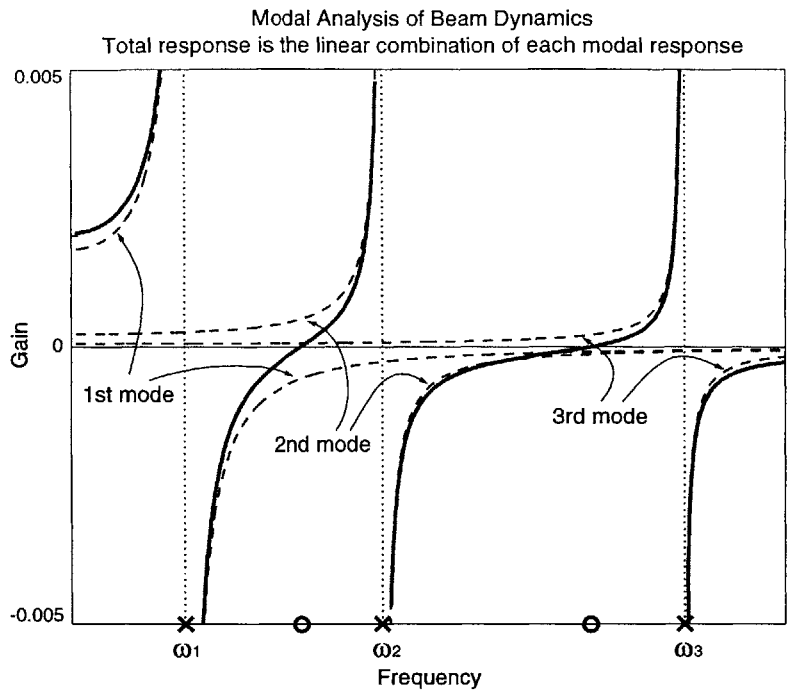

Figure 6-8: Modal analysis of beam dynamics: the total response is the linear combination of all modal responses. Note that the magnitude is plotted on a linear scale centered on zero.

and brings zero close to the pole robustly.

To demonstrate the dynamics in Bode plot, I add a modal damping of $\zeta = 0.001$ for each mode. Figure 6-8 and Figure 6-9 are put together for comparison in Figure 6-10 on Bode coordinates.

The reduction of modal gain is exactly what we are doing by using sensor averaging method. It robustly moves the system zeros to the poles of the resonance modes that we try to attenuate.

In comparison, if we use a notch filter to attenuate certain resonance mode, instead of moving the system zeros, it will add 2 extra zeros to that certain frequency to cancel to poles. When the system parameters change, and the resonance mode moves to another frequency, the notch filter can easily fail since the added zeros cannot cancel the poles anymore.

In summary, the sensor averaging method has the following properties: (assume 2 sensors are set apart by $2d$)

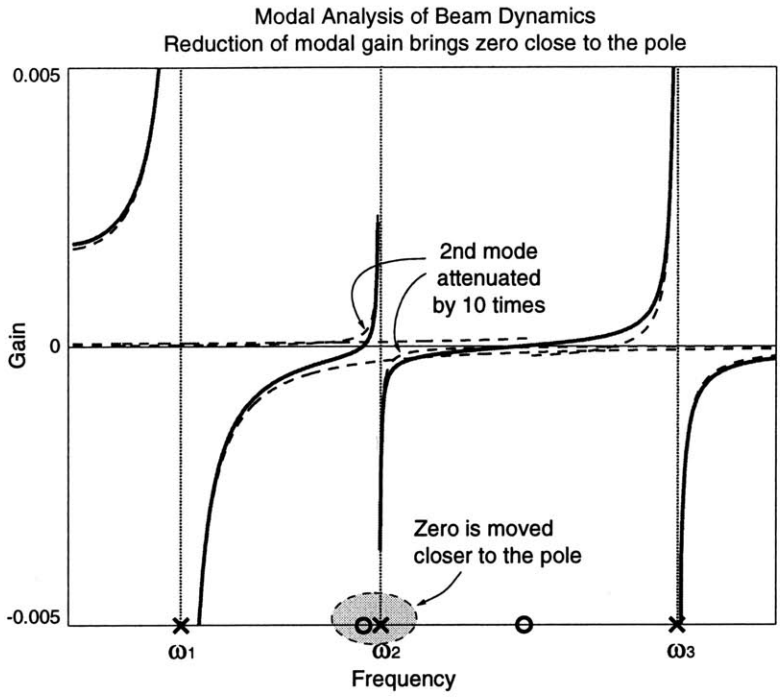

Figure 6-9: Modal analysis of beam dynamics: reduction of modal gain brings the zero close to the pole robustly, which can be caused by sensor averaging.

1. It makes a waveform with wavelength $4d$ unobservable.

2. It robustly attenuates the modal observability of waveforms with wavelengths close to $4d$.

3. It is independent of sensor pair location z_o.

4. It is independent of beam length and boundary conditions. When the beam length or boundary conditions change, natural frequencies ω_n change. In Figure 6-6, the curve of $\cos k_n d$ remains the same. So although the resonances move along the curve, those in the vicinity of the notch are still robustly attenuated.

5. Sensor averaging causes no phase lag because it is a spatial filter, not a temporal filter.

6. The 180° phase flip can be easily eliminated by a third sensor, or be reversed back by actuator averaging. Both will be discussed later in this Chapter.

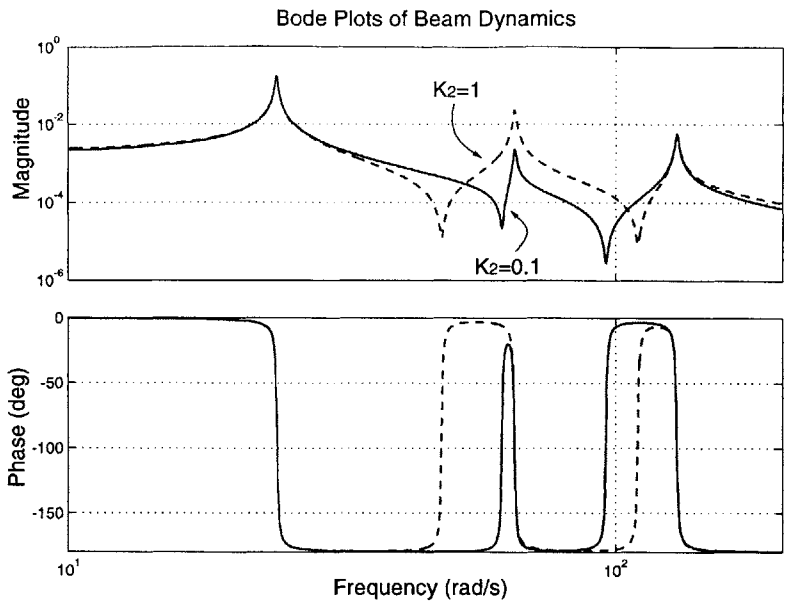

Figure 6-10: Bode plots beam dynamics. Dashed line shows the Bode plot of the original dynamics. Solid line shows the Bode plot of the dynamics if the 2nd mode is attenuated by 10 times.

6.3.4 3-Sensor Averaging for Beams

The sensor averaging method can be readily extended to more than 2 sensors. This section gives an example of using 3 sensors to obtain the cosine notch. Using 3 sensors has the advantage over 2 sensors that there is no phase reversal above the notch. By using 3 sensors as shown in Figure 6-4(b), and take the averaged measurement as

$$\hat{u}(z_o,t) = \frac{u(z_0,t)}{2} + \frac{u(z_1,t)+u(z_2,t)}{4} = \sum_{n=1}^{\infty}\left(\xi_n(t)\phi_n(z_o)\cdot\frac{1+\cos k_n d}{2}\right) \qquad (6.13)$$

Notice that the modal gain of $0.5(1+\cos k_n d)$ is always positive, and hence the 180° phase flip in 2-sensor averaging will not happen in 3-sensor averaging. Also notice that the notch zero is now located at $k_n d = \pi$. Again we use our experimental setup as an example, and choose $d = 0.30$ m to have the notch near 1000 rad/s. The result is illustrated in Figure 6-11. It shows the cosine notch as an ideal modal-band-stop filter while phase remains unchanged for all frequencies.

The FEM beam model with 3-sensor averaging is shown in Figure 6-12. The advantage of using 3 sensors is that phase remains unchanged for all frequencies, and

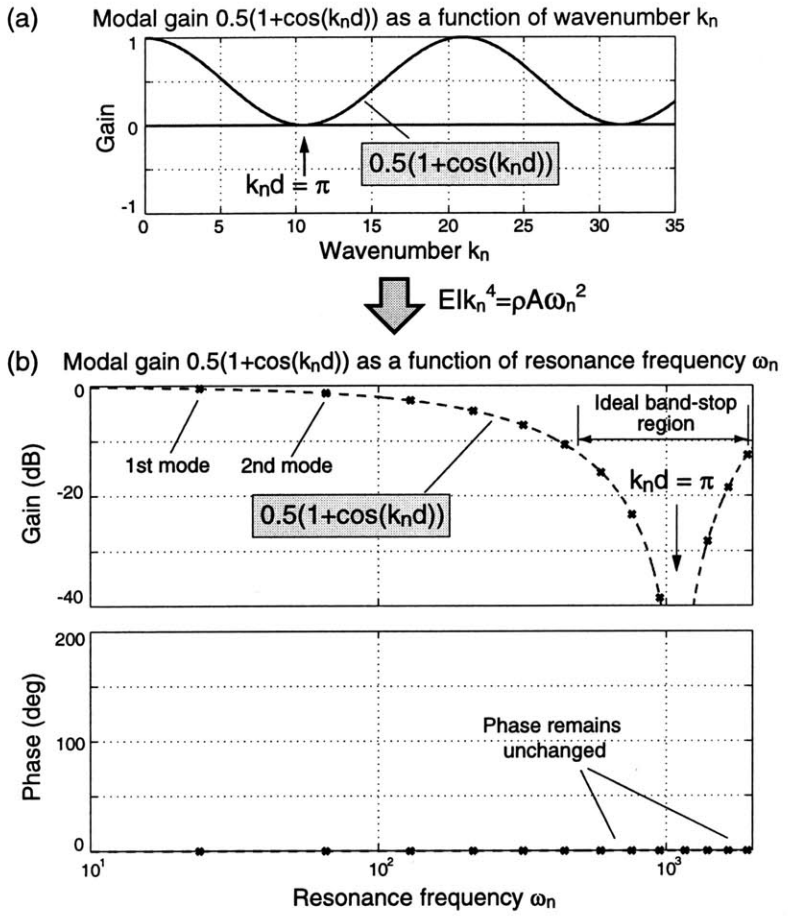

Figure 6-11: 3-Sensor averaging for beams: modal gain $0.5(1+\cos k_n d)$ plotted as (a) a function of k_n, and (b) a function of ω_n.

the notch is broader than 2-sensor averaging. The disadvantage is that the total sensor spacing $2d$ will be twice as long as for the two sensor case, if the notches are to be placed at the same frequency.

6.3.5 Continuous-Sensor Averaging for Beams

The logical extension of the sensor averaging at 2 or 3 points is to use more sensors. The limit is continuous position sensing as shown in Figure 6-4(c). From the previous derivation, we realize that sensor averaging is a spatial filter, and is a dual to a temporal filter. Therefore we can adopt the filter theory widely used for signal processing and apply it to sensor averaging. Oppenheim [87, Chapter 7] describes commonly used windows for FIR (Finite Impulse Response) filters, as shown in Appendix E.

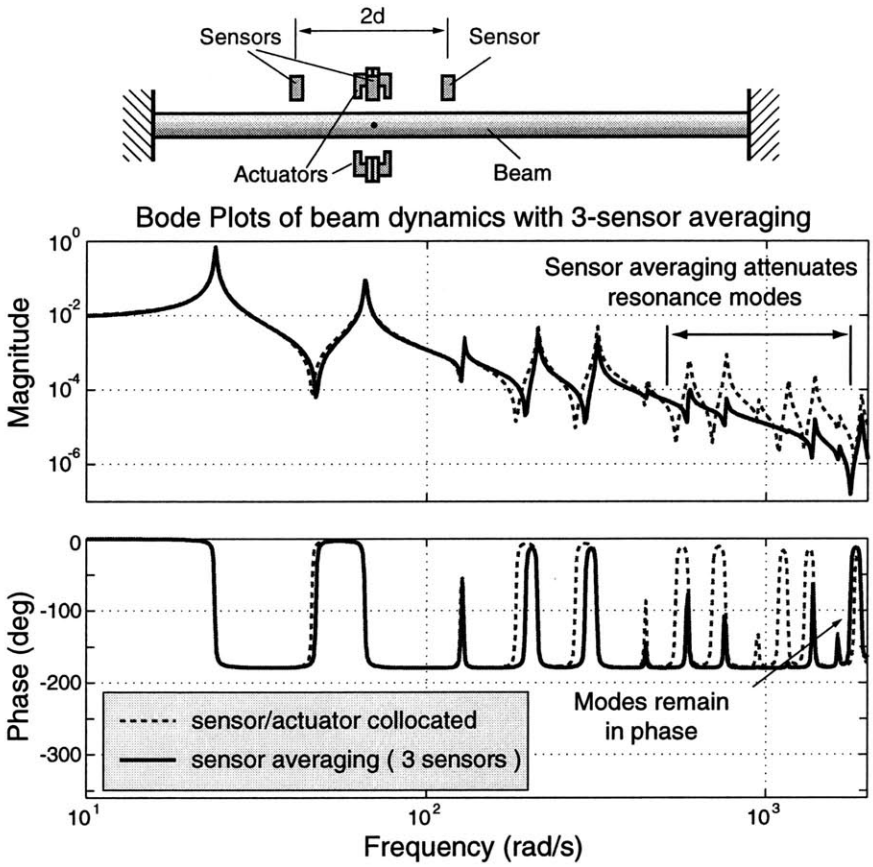

Figure 6-12: Theoretical beam model for 3-sensor averaging. Solid line shows a beam model with 3-sensor averaging ($d = 30$ cm), and a broader range of resonance modes are attenuated than by using 2-sensor averaging. Dashed line shows a beam model with collocated sensor and actuator ($d = 0$) for comparison.

In the following, we demonstrate the characteristics of continuous-sensor averaging using rectangular, triangular, and Blackman windows.

Rectangular Window

By using a rectangular window, we have the same weightings for all sensors. We assume that we have an infinite number of sensors placed within the length $2d$, the averaged output is chosen to be the integration of all sensor output:

$$\hat{u}(z_o, t) = \frac{1}{2d} \int_{z_1}^{z_2} u(z, t) dz = \sum_{n=1}^{\infty} \left(\xi_n(t) \phi_n(z_o) \cdot \frac{\sin k_n d}{k_n d} \right) \tag{6.14}$$

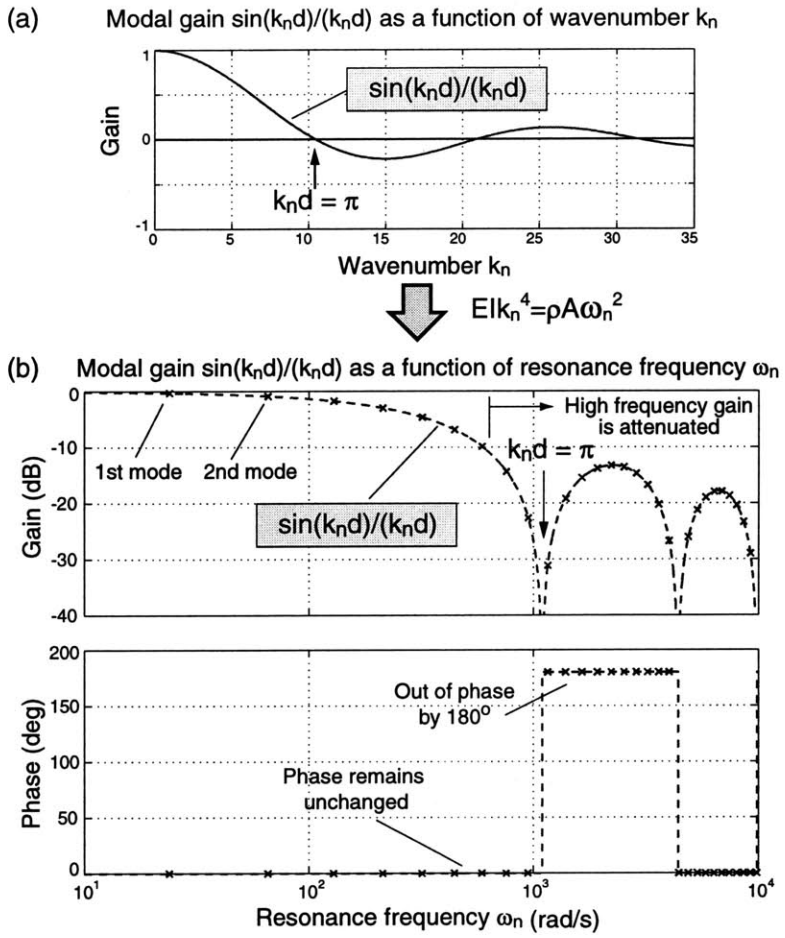

Figure 6-13: Sinc effect from continuous-sensor averaging for beams

The modal gain is a sinc function $(\sin k_n d)/(k_n d)$, which is illustrated in Figure 6-13 as a function of wavenumber k_n and resonance frequency ω_n. It has a notch zero at $k_n d = \pi$, and it has 180° phase flip after the notch zero. It also shows that the high frequency modes will be attenuated, which is the main advantage of using continuous-sensing.

Using our experimental setup as an example, instead of assuming an infinite number of sensors, I assume that we have 9 sensors over 60 cm span. The sensor weighting for each sensor is 0.1111. The resulting FEM beam model is shown in Figure 6-14. Notice that the modes become out of phase after the notch zero.

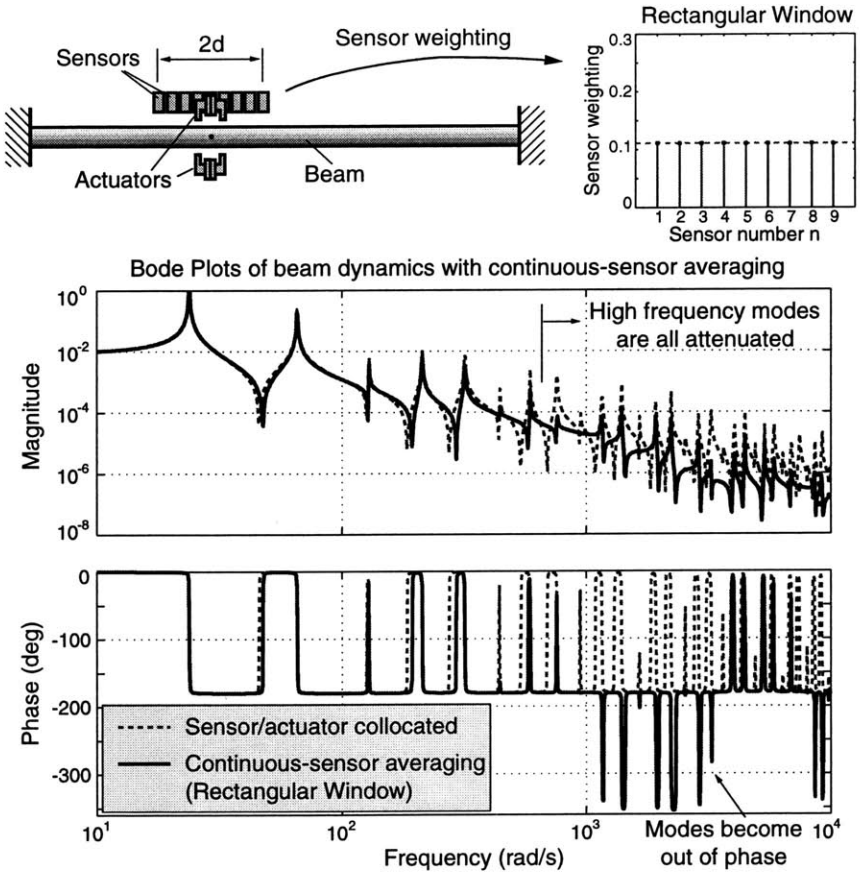

Figure 6-14: Theoretical beam model for 9-sensor averaging with a rectangular window. Solid line shows a beam model with 9-sensor averaging with a rectangular window ($d = 30$ cm), and resonance modes at high frequencies are all attenuated. Dashed line shows a beam model with collocated sensor and actuator ($d = 0$) for comparison.

Triangular Window (Bartlett Window)

A triangular window is known to have slightly wider mainlobe, and slightly lower sidelobes than a rectangular window. We will show that by using a triangular window, the main advantage is that the averaged output will have no phase change. The triangular window is simply defined by:

$$w[n] = \begin{cases} 2n/M & 0 \leq n \leq M/2 \\ 2 - 2n/M & M/2 < n \leq M \\ 0 & \text{otherwise} \end{cases} \tag{6.15}$$

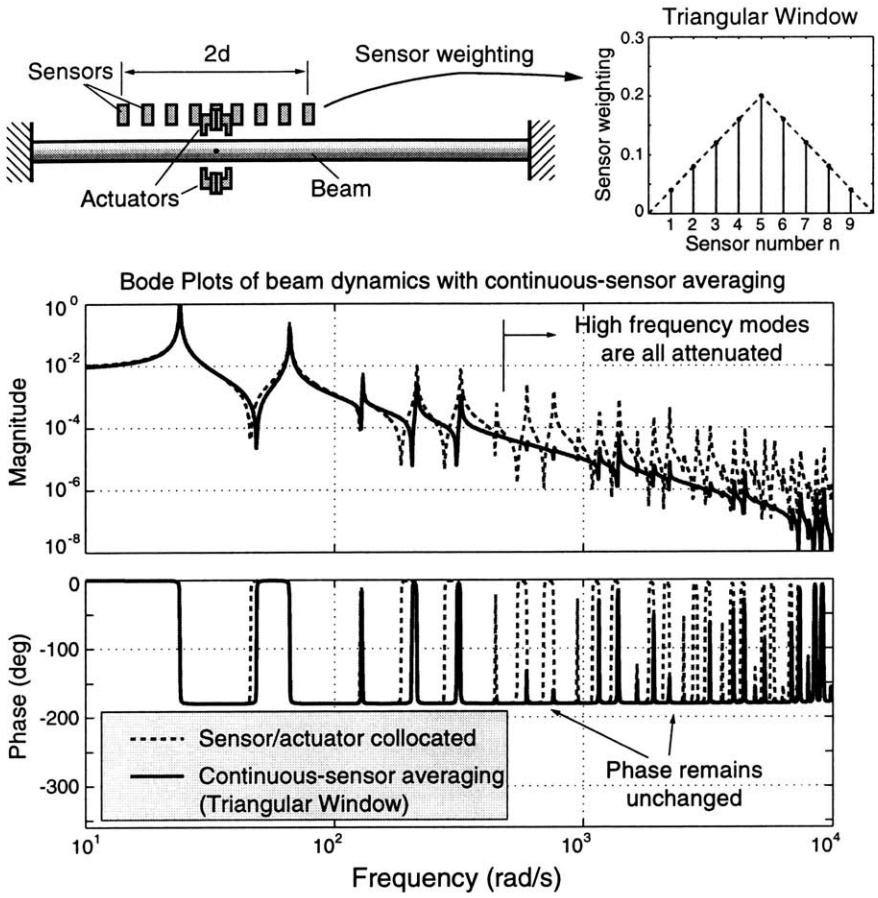

Figure 6-15: Theoretical beam model: 9-sensor averaging with a triangular window. Solid line shows a beam model with 9-sensor averaging with a triangular window ($d = 60$ cm), and phase remains unchanged. Dashed line shows a beam model with collocated sensor and actuator ($d = 0$) for comparison.

where M is the total number of sensors plus 1, and n is the nth sensor.

Using our experimental setup as a numerical example, we assume 9 sensors placed along a 120 cm span. The sensor weightings are: 0.04, 0.08, 0.12, 0.16, 0.20, 0.16, 0.12, 0.08, and 0.04. The resulting FEM beam model is shown in Figure 6-15. Notice that the phase remains unchanged.

Blackman Window

The Blackman window is known to have sidelobes lower than -60 dB. The tradeoff is that it has a wide mainlobe, hence we need a longer space to place sensors. The

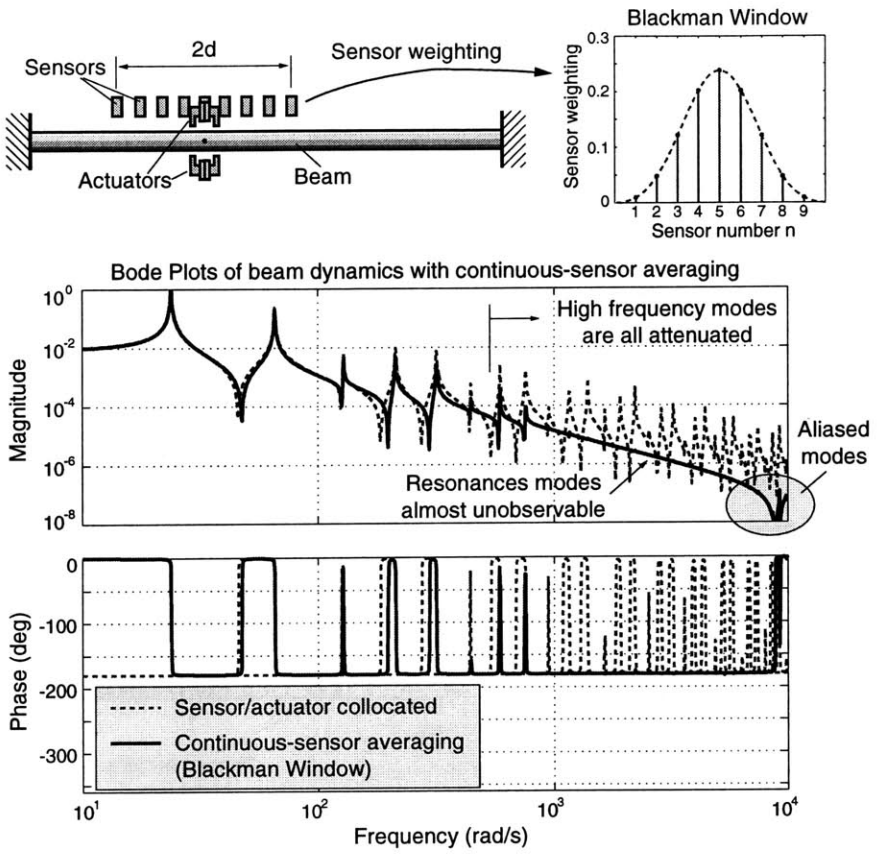

Figure 6-16: Theoretical beam model: 9-sensor averaging with a Blackman window. Solid line shows a beam model with 9-sensor averaging with a Blackman window ($d = 60$ cm), and resonance modes at high frequencies are almost unobservable. Dashed line shows a beam model with collocated sensor and actuator ($d = 0$) for comparison.

Blackman window is defined as:

$$w[n] = \begin{cases} 0.42 - 0.5\cos(2\pi n/M) + 0.08\cos(4\pi n/M) & 0 \leq n \leq M \\ 0 & \text{otherwise} \end{cases} \tag{6.16}$$

where M is the total number of sensors plus 1, and n is the nth sensor.

Using our experimental setup as an example, I place 9 sensors over 120 cm. The sensor weightings are: 0.0096, 0.0478, 0.1214, 0.2022, 0.2381, 0.2022, 0.1214, 0.0478, and 0.0096. The resulting FEM beam model is shown in Figure 6-16. It shows that the high frequency modes become almost unobservable. This can be interpreted that the mode shapes are mainly sinusoidal and orthogonal to the sinusoidal sen-

Table 6.1: Comparison of three FIR windows

Window	Phase change	High frequency modes	Window size
Rectangular	180°	slightly attenuated (> 0.2)	small
Triangular	unchanged	attenuated (< 0.1)	medium
Blackman	almost unchanged	almost unobservable	large

sor weighting, hence they become unobservable. Resonance modes at even higher frequencies start to appear, and can be interpreted that the wavelengths become so small that the waveforms are aliased through the 9 discrete sensors. If we could have an infinite number of sensors, theoretically all the high frequency modes will become unobservable. Another significant advantage of using a Blackman window is that the gain falls at a slope of -2, compared to the original dereverberated transfer function (backbone) of the original dynamics that falls at a slope of -1.5 [27].

Different windows for FIR filters have their own advantages and disadvantages. These are demonstrated in Appendix E, and are summarized in Table 6.1. A rectangular window has the notch zero at a lower frequency, therefore it needs a smaller space to place the sensors. However, after the notch zero, the high frequency modes are only slightly attenuated: the 1st sidelobe has a peak at -13 dB (gain = 0.22). A triangular window has the notch at a higher frequency, and hence needs a larger space to place the sensors. However it has the advantage that the phase does not change. A Blackman window has the notch at even higher frequency. The advantages of the Blackman window are that the phase remains almost unchanged, and the high frequency modes are almost unobservable.

At this point, the concept of continuous-sensor averaging meets the concept of the distributed sensors, which have been widely used for structural control. Distributed sensors are usually made of piezoelectric materials, and are attached on the surface of the structure. They output voltage as a function of the structure curvature integrated over the sensor surface area. Most of the research on distributed sensors focuses on model-based modal sensing. Here, the sensors are shaped to observe only the modes that are not orthogonal to the shape. Collins et al [24] focus on non-model-based

distributed sensors; they design distributed sensors shaped as a sinc function, and use them as spatial filters to attenuate high frequency modes. The sinc function is associated with an ideal low-pass response. These shaped sensors are designed from essentially the same perspective as our sensor averaging techniques, and thus represent the closest prior art in the literature. The application of distributed sensors and the comparison with sensor averaging method is described later in this Chapter.

6.3.6 Actuator Averaging for Beams without Tension

Actuator averaging is a dual to sensor averaging. Here, we use multiple actuators and apply the same force to each actuator. The resulting filtering effect is similar to sensor averaging. Actuator averaging attenuates the modal controllability, and sensor averaging attenuates the modal observability. Sensor averaging is easier to understand since it simply averages the vibration waveforms. Actuator averaging places actuators in a similar way such that certain resonance modes will not be excited, as can be interpreted from the concepts of modal forces.

If we place one actuator at $z = z_0$, and apply force f from the actuator, the resulting nth modal force can be calculated by:

$$N_n = \int_0^L f(z)\phi_n(z)dz = \int_0^L f\delta(z_0) \cdot \phi_n(z)dz = f\phi_n(z_0). \tag{6.17}$$

We then place two actuators set apart by $2d$, and apply the same control forces $f/2$ to each actuator. With actuators located at $z_1 = (z_o - d)$ and $z_2 = (z_o + d)$, the averaged modal force is given by

$$N_n = \int_0^L f(z)\phi_n(z)dz = \frac{1}{2}f(\phi_n(z_1) + \phi_n(z_2)) = f\phi_n(z_o) \cdot \cos k_n d. \tag{6.18}$$

Compare Equation 6.17 and Equation 6.18; actuator averaging creates a modal gain of $\cos k_n d$, just like the sensor averaging method.

Similar to 3-sensor averaging, by using 3 actuators, and assigning the force distribution as $f/4$ at $z = z_1$ and $z = z_2$, and $f/2$ at $z = z_o$, we can also create a cosine

notch filter without phase change.

Actuator averaging can also be readily used for strings, plates, and membranes, simply from its dual properties to the sensor averaging.

6.3.7 Combination of Sensor Averaging and Actuator Averaging

In the ideal case, sensor averaging and actuator averaging will be used together. The resulting modal gain is the multiplication of both averaging effects. For beams, using two sensors set apart by $2d_s$ and two actuators set apart by $2d_a$, the filter gain of each mode becomes $\cos k_n d_s \cdot \cos k_n d_a$. In other words, the frequency response shown in Equation 6.7 becomes

$$\frac{\hat{u}(s)}{f(s)} = \sum_{n=1}^{\infty} \left(\frac{\phi_n^2(z_o)}{M_n(s^2 + 2\zeta_n\omega_n s + \omega_n^2)} \cdot \cos k_n d_s \cdot \cos k_n d_a \right). \tag{6.19}$$

The distances d_s and d_a can be arranged to meet the system's requirement. If $d_s = d_a$, it creates a broader notch, and eliminates the 180° phase flip. If we set $d_s \neq d_a$, we can use two independent notches to attenuate two frequency regions.

6.4 Experimental Results of Sensor Averaging and Actuator Averaging

In this section, we show experimental results of magnetic suspension of a tubular beam. We will demonstrate that the experiments verify our proposed sensor averaging and actuator averaging methods.

6.4.1 Experimental Setup

As shown in Figure 6-17, we use eight sensors and eight actuators to suspend a steel tube. The details of the experimental setup, sensor dynamics, actuator dynamics,

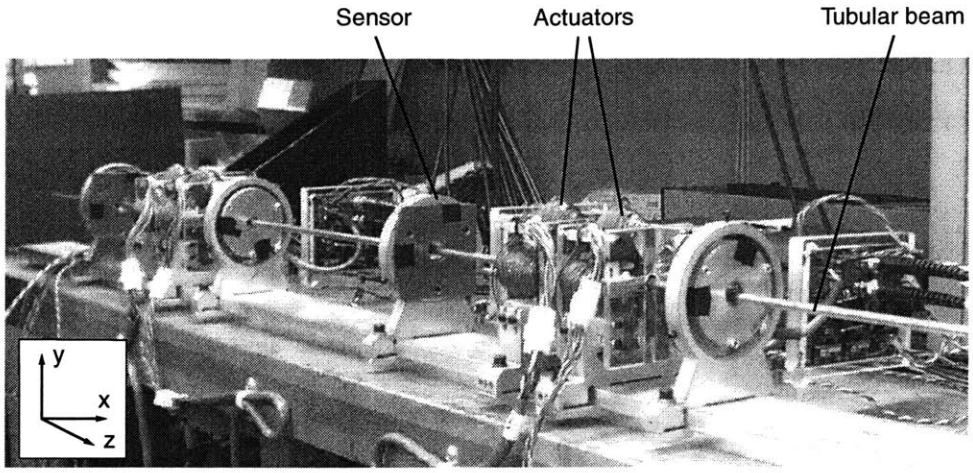

Figure 6-17: Experimental setup of tubular beam suspension.

and the controller design are shown in Chapter 5. In this chapter, we focus on the verification of sensor/actuator averaging methods.

6.4.2 Control with Nearly Collocated Sensor/Actuator

We clamp the beam at both ends, support the beam weight by two strings, and place one actuator between two sensors to control the beam at one point at $z = 1.12$ m. We place sensors and the actuator in close proximity (or more precisely, sensor averaging with notch zero at frequency higher than 5000 rad/s). We can thus regard a sensor and an actuator as both at $z = 1.12$ m. We use the controller

$$H(s) = 4000\frac{(s+30)(s+120)(s+400)^2}{(s+60)(s+240)(s+800)^2}, \tag{6.20}$$

which has a dc gain of 250 N/mm. We are almost able to stabilize the system locally, except there is a limit cycle vibration at 1100 rad/s. Figure 6-18 shows the experimental setup and the measured loop transfer function compared with our theoretical model. The loop has 30° phase margin for all vibration modes below 500 rad/s. The alternating pole-zero pattern shows that the modal controllability and modal observability have the same sign, which implies there is no non-collocation problem.

From the experimental Bode Plots, it seems that we do have positive gain margin

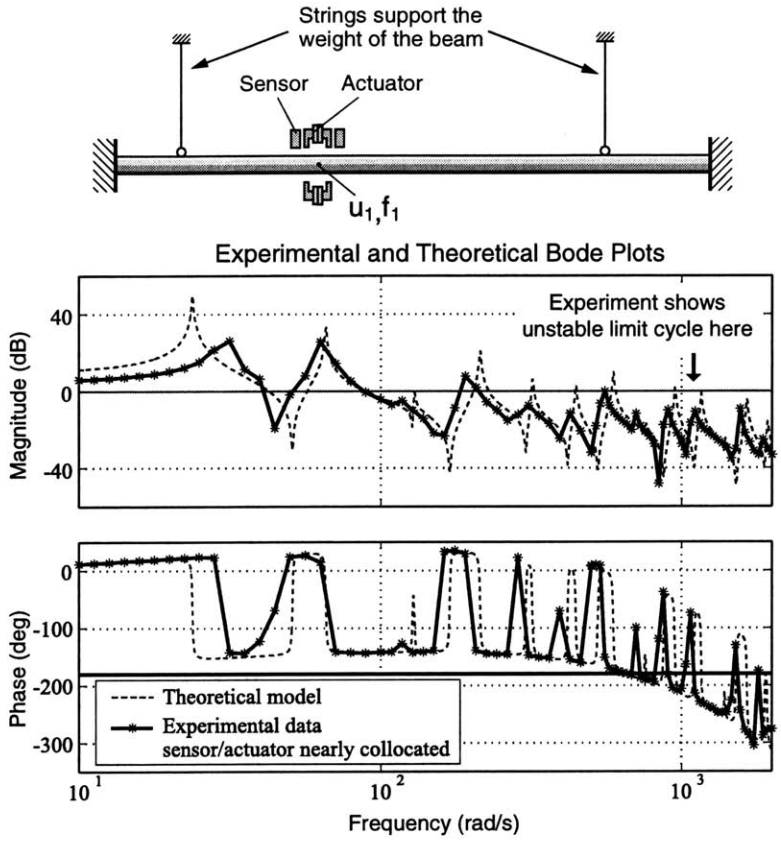

Figure 6-18: Experimental setup and Bode Plots of loop transfer function by using collocated sensor/actuator. Dashed line shows theoretical Bode Plots for comparison.

at 1100 rad/s, and cannot predict the limit cycle at that frequency. One possible reason is that we might not measure the resonance peaks accurately since we did not measure the frequency points fine enough. Another possibility is that the system is nonlinear, for example, the system damping from the boundaries may depend on the vibration amplitude.

6.4.3 Control with 2-Sensor Averaging

To avoid the limit cycle in the sensor interpolation experiment, we pull the sensors apart to implement sensor averaging. Specifically, the sensors are placed ± 0.15 m from the actuator at $z = 1.12$ m. We use the same controller as in the previous section. Figure 6-19 shows the experimental setup and the measured loop transfer function, and compared to the previous experiment in which sensor/actuator are

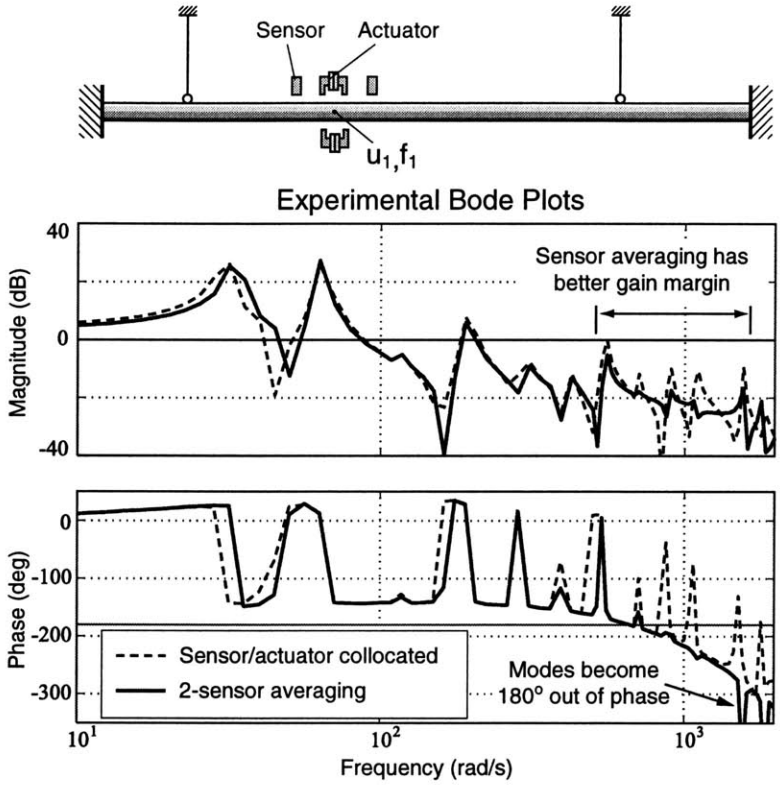

Figure 6-19: Experimental setup and Bode Plots of loop transfer function by using 2-sensor averaging. Dashed line shows the previous result of collocated sensor/actuator experiment for comparison.

nearly collocated. The sensor averaging shows the improvement of gain margin within frequency range from 700 rad/s to 1500 rad/s while the phase is below $-180°$. Thus we are able to stabilize the system and avoid the limit cycle. Notice the modal observability becomes 180° out of phase after the cosine notch zero as we expected.

To suspend the beam with free-free boundaries, we use 8 sensors and 4 actuators, apply the same sensor averaging method, and control the beam at 4 points. The system is stable with loosely clamped boundaries. However, when the beam is released to free-free boundaries, a 5000 rad/s vibration builds up and destabilizes the system in a few seconds. This frequency is much higher than our control bandwidth and the phase is significantly below $-180°$, and hence cannot be easily stabilized by conventional control methods. This problem was later solved by adding actuator averaging, as described in Section 6.4.6

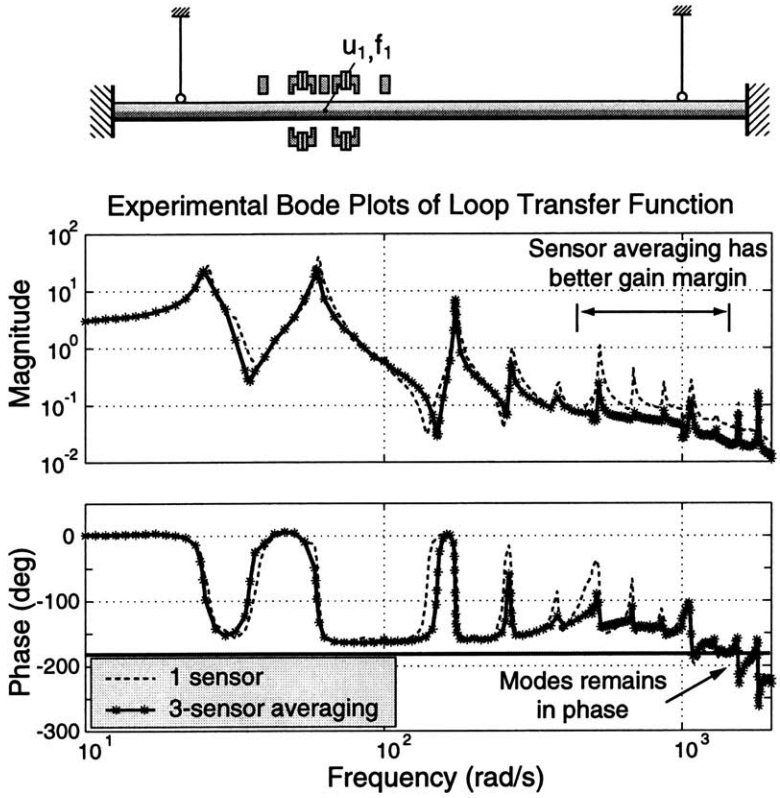

Figure 6-20: Experimental setup and Bode Plots of loop transfer function by using 3-sensor averaging. Notice that the phase remains unchanged. Dashed line is measured with 1 sensor for comparison.

6.4.4 Control with 3-Sensor Averaging

To verify the proposed idea of 3 sensor arrangement, we use 3 sensors and 2 actuators to implement this experiment. Specifically, the sensors are placed ± 0.15 m from each other and the center is at $z = 1.12$ m. The two actuators are placed closely to the sensor at the center.

The system low-pass filters and controller are different from the previous sections, since I did the experiments at much later time, and system has gone through some modifications. The new controller has the transfer function:

$$H(s) = 267 \frac{(s+80)(s+800)^2}{(s+120)(s^2+2\cdot 0.5\cdot 1200 s+1200^2)} \frac{(s+3000)^2}{(s+2000)^2}, \tag{6.21}$$

which has a dc gain of 180 N/mm. Figure 6-20 shows the experimental setup and the measured loop transfer function. It includes (1) 3-sensor averaging experiment,

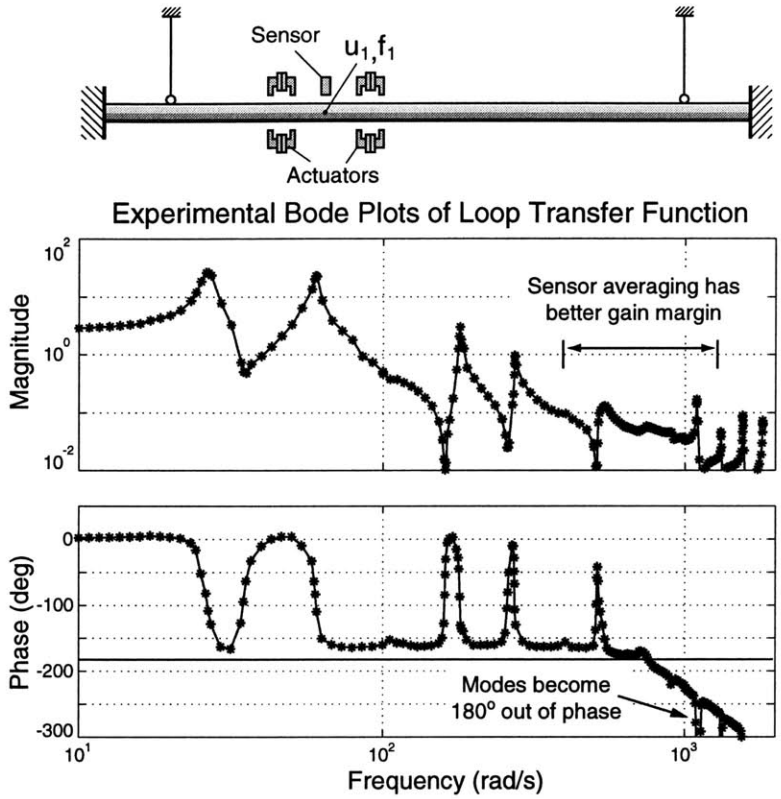

Figure 6-21: Experimental setup and Bode Plots of loop transfer function by using 2-actuator averaging.

and (2) 1 sensor experiment for comparison. Notice the modal observability stays in phase after the cosine notch zero.

6.4.5 Control with 2-Actuator Averaging

To verify the effectiveness of the proposed actuator averaging, we use 1 sensor and 2 actuators to implement this experiment. Specifically, the sensor is placed at $z = 1.12$ m, and the actuators are placed ± 0.17 m from the sensor. Figure 6-21 shows the experimental setup and the measured loop transfer function. Notice the similarity between this setup and sensor averaging.

6.4.6 Control with 2-Sensor Averaging and 2-Actuator Averaging

As shown in Section , our attempt to stabilize the free-free beam by using 2-sensor averaging was not successful. In this attempt, we used 8 sensors and 4 actuators to control the beam at 4 points independently. We have a positive phase margin in the loop transfer function up to about 120 Hz, and the sensor averaging is designed to attenuate resonance modes in the vicinity of 160 Hz. However, our results show an 800 Hz vibration builds up and destabilizes the system. The damping ratio of this free-free beam is later measured to be below 0.001, and the sensor averaging alone is not sufficient to attenuate the high frequency modes over such a broad frequency range.

To address this problem, we add actuator averaging along with sensor averaging to create a broader notch, which is basically the two cosine notches put side by side.

The experimental results show a stable result. The suspended tube is robustly stable when the boundary conditions varies, including simply-supported, clamped, and free boundaries. The experimental setup and measured Bode plots of $h(s)G_{22}(s)$ at the 2nd point is shown in Figure 6-22, where $h(s)$ is the controller transfer function, and $G_{22}(s)$ is the transfer function from the force input f_2 to the position output u_2.

Although this Bode plot is supposed to show the free-free beam dynamics, notice that the free-mass dynamics of $1/(ms^2)$ is not observed in Figure 6-22. This happens because we measure the dynamics of the beam in the horizontal direction, and the beam is controlled in the vertical direction at the same time. Thus the open-loop dynamics of the beam in the horizontal direction behaves like a pendulum instead of a free-mass. the natural frequency of this pendulum dynamics appears as a little bump at 20 rad/s in Figure 6-22.

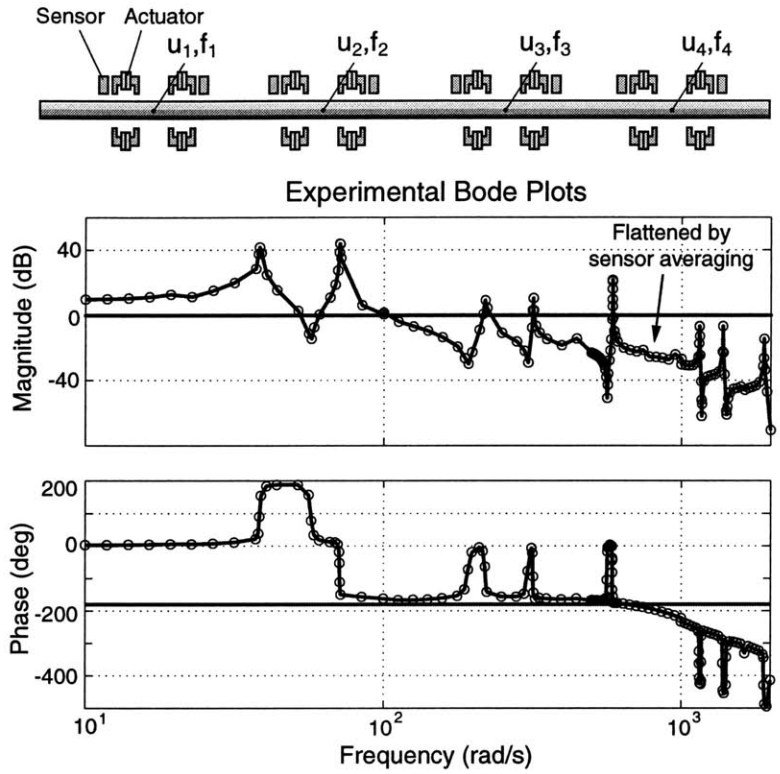

Figure 6-22: Experimental setup and Bode Plots of loop transfer function of the 2nd point. We use both sensor averaging and actuator averaging. The flattened region is the result from sensor averaging.

6.5 Sensor Averaging and Actuator Averaging on Beams and Strings with Tension

In this section, we extend sensor averaging and actuator averaging theoretically to beams and strings with tension. We will summarize their dynamic equations, dispersion equations, and general solutions. From the result, we can verify that sensor/actuator averaging is valid for these structures.

6.5.1 Summary of Dynamics of Beams with Tension

The beam equation with tension T can be shown to be

$$EI\frac{\partial^4 u}{\partial z^4} - T\frac{\partial^2 u}{\partial z^2} + \rho A\frac{\partial^2 u}{\partial t^2} = f, \tag{6.22}$$

where EI is bending stiffness, z is axial coordinate, u is transverse deflection, ρ is material density, A is cross-sectional area, and f is external transverse force density. Assuming a homogeneous solution $u_h(z,t) = Ce^{j\omega t}e^{pz}$, the resulting characteristic equation becomes

$$EIp^4 - Tp^2 - \rho A\omega^2 = 0. \tag{6.23}$$

The natural response is:

$$\begin{aligned} u(z,t) &= \sum_{n=1}^{\infty} \xi_n(t) \left(C_{n1}\cos k_n z + C_{n2}\sin k_n z + C_{n3}\cosh\sigma_n z + C_{n4}\sinh\sigma_n z\right) \\ &\approx \sum_{n=1}^{\infty} \xi_n(t) \left(C_{n1}\cos k_n z + C_{n2}\sin k_n z\right), \qquad (6.24) \\ &\quad (\text{ when } \sigma_n \text{ is large, and } z \text{ is away from boundaries. }) \end{aligned}$$

with

$$k_n = \sqrt{-\frac{T}{2EI} + \sqrt{\left(\frac{T}{2EI}\right)^2 + \frac{\rho A\omega_n^2}{EI}}}, \tag{6.25}$$

$$\sigma_n = \sqrt{\frac{T}{2EI} + \sqrt{\left(\frac{T}{2EI}\right)^2 + \frac{\rho A\omega_n^2}{EI}}}, \tag{6.26}$$

where $\xi_n(t)$ is the nth modal coordinate, $\phi_n(z)$ is the nth modal shape, C_{n1} and C_{n2} represent sinusoidal waveforms, and C_{n3} and C_{n4} represent evanescent waveforms. In general, tension helps the stabilization of the beam by increasing the resonance frequencies. Tension also makes σ_n increase, and thus make the system response more dominated by sinusoidal waveforms, which makes sensor/actuator averaging assumptions more valid.

6.5.2 Summary of Dynamics of Strings with Tension

To have interesting dynamics, a string must be subject to tension. The governing equation for a string under tension is

$$-T\frac{\partial^2 u}{\partial z^2} + \rho A\frac{\partial^2 u}{\partial t^2} = f, \tag{6.27}$$

where the nth modal shape is

$$\phi_n(z) = C_{n1}\cos k_n z + C_{n2}\sin k_n z. \tag{6.28}$$

A string has only sinusoidal waveforms. The relation between wavenumber k_n and resonance frequency ω_n is given by

$$k_n = \sqrt{\frac{\rho A\omega_n^2}{T}}. \tag{6.29}$$

Recall that in beam dynamics, we have to make the assumption that the evanescent waveforms are negligible at higher modes. However, in string dynamics, the response is pure sinusoidal, and thus do not need this assumption.

6.5.3 Sensor Averaging and Actuator Averaging on Beams and Strings

We combine the analysis of beam and string elements due to their similarities. Because we are focusing on the high frequency modes near the controlled-system bandwidth, the evanescent waveforms near the boundaries are less important. Therefore we assume the beam vibration is dominated by sinusoidal waveforms. We can represent the beam/string vibration by

$$u(z,t) = \sum_{n=1}^{\infty}\xi_n(t)\phi_n(z) = \sum_{n=1}^{\infty}\xi_n(t)(C_{n1}\cos k_n z + C_{n2}\sin k_n z). \tag{6.30}$$

This equation is exactly the same as what we derived for beams without tension.

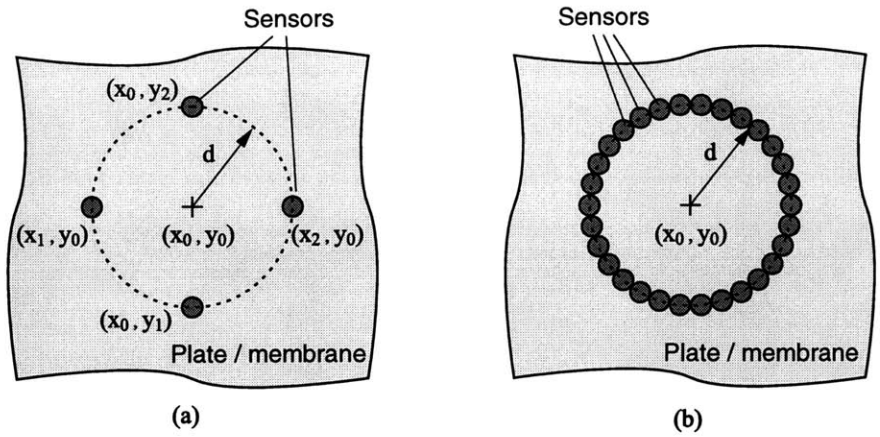

Figure 6-23: Sensor positioning arrangements for plates and membranes: (a) 4-sensor averaging, and (b) circular continuous-sensor averaging.

Therefore we conclude that sensor averaging and actuator averaging methods can be applied to beams and strings with tension, and the modal gain will still be $\cos k_n d$. The only differences are the relations between k_n and ω_n, as summarized in the following:

$$\text{Beams without tension} \qquad k_n = \sqrt[4]{\frac{\rho A \omega_n^2}{EI}}, \tag{6.31}$$

$$\text{Beams with tension} \qquad k_n = \sqrt{-\frac{T}{2EI} + \sqrt{\left(\frac{T}{2EI}\right)^2 + \frac{\rho A \omega_n^2}{EI}}}, \tag{6.32}$$

$$\text{Strings with tension} \qquad k_n = \sqrt{\frac{\rho A \omega_n^2}{T}}. \tag{6.33}$$

6.6 Sensor Averaging on Rectangular Plates and Rectangular Membranes with Uniform Tension

In this section, we extend sensor averaging and actuator averaging methods to vibration control of rectangular plates and rectangular membranes. We first summarize the dynamics of plates and membranes with uniform tension. Then we derive two different arrangements for sensor averaging: 4-sensor averaging and circular continuous-sensor averaging. Figure 6-23 shows these two arrangements of sensor locations. Of course,

other patterns may be of interest, depending upon the plate shape and intended use of the suspension. The two examples in Figure 6-23 suggest some of the possibilities.

6.6.1 Summary of Dynamics of Rectangular Plates with Uniform Tension

We consider plate element with constant plate rigidity D and constant tension force applied along all four edges: $T = T_x = T_y$. The plate dynamics can be modeled by

$$D\nabla^4 u - T\nabla^2 u + \rho h \frac{\partial^2 u}{\partial t^2} = f, \tag{6.34}$$

with

$$D = \frac{Eh^3}{12(1-\nu^2)}.$$

Here ∇^4 is the biharmonic operator, u is transverse deflection, f is an external transverse force density, E is Young's Modulus, h is plate thickness, and ν is Poisson's Ratio of the material. Assuming a homogeneous solution $u_h(x,y,t) = Ce^{j\omega t}e^{px}e^{qy}$, the resulting plate characteristic equation is

$$D(p^2+q^2)^2 - T(p^2+q^2) - \rho A\omega^2 = 0. \tag{6.35}$$

The nth modal shape is:

$$\begin{aligned}
\phi_n(x,y) &= (C_{n1}\cos\alpha_n x + C_{n2}\sin\alpha_n x)\cdot(C_{n3}\cos\beta_n y + C_{n4}\sin\beta_n y) + \\
&\quad (C_{n5}\cosh\alpha'_n x + C_{n6}\sinh\alpha'_n x)\cdot(C_{n7}\cosh\beta'_n y + C_{n8}\sinh\beta'_n y) \\
&\approx (C_{n1}\cos\alpha_n x + C_{n2}\sin\alpha_n x)\cdot(C_{n3}\cos\beta_n y + C_{n4}\sin\beta_n y), \qquad (6.36) \\
&\quad (\text{ when } \alpha'_n \text{ or } \beta'_n \text{ is large, and } x \text{ or } y \text{ are away from boundaries. })
\end{aligned}$$

with

$$k_n^2 = \alpha_n^2 + \beta_n^2 = -\frac{T}{2D} + \sqrt{\left(\frac{T}{2D}\right)^2 + \frac{\rho A\omega_n^2}{D}}, \tag{6.37}$$

$$\sigma_n^2 = \alpha_n'^2 + \beta_n'^2 = \frac{T}{2D} + \sqrt{\left(\frac{T}{2D}\right)^2 + \frac{\rho A \omega_n^2}{D}}. \tag{6.38}$$

Plate dynamics include both sinusoidal and evanescent waveforms. Equation 6.37 shows the relation between wavenumber k_n and frequency ω_n, where α_n and β_n are wavenumber components in x and y directions respectively.

6.6.2 Summary of Dynamics of Rectangular Membranes with Uniform Tension

In this paper, we consider membranes with constant tension force applied along all four edges, $T = T_x = T_y$. (For membranes with tension in only one direction, $T_x = 0$ or $T_y = 0$, they can be considered as string elements.) The membrane equation is:

$$-T\nabla^2 u + \rho h \frac{\partial^2 u}{\partial t^2} = f, \tag{6.39}$$

and the nth modal shape is:

$$\phi_n(x,y) = (C_{n1}\cos\alpha_n x + C_{n2}\sin\alpha_n x) \cdot (C_{n3}\cos\beta_n y + C_{n4}\sin\beta_n y). \tag{6.40}$$

The membrane dispersion equation is

$$k_n^2 = \alpha_n^2 + \beta_n^2 = \frac{\rho h}{T}\omega_n^2. \tag{6.41}$$

6.6.3 Sensor Averaging on Plates and Membranes with Uniform Tension

Similar to the argument for beam vibration, we assume that the plate vibration is dominated by sinusoidal waveforms, and combine the analysis of plate and membrane elements together. The plate/membrane vibration can be represented by

$$u(x,y,t) = \sum_{n=1}^{\infty} \xi_n(t)\phi_n(x,y)$$

$$= \sum_{n=1}^{\infty} \xi_n(t) \cdot (C_{n1}\cos\alpha_n x + C_{n2}\sin\alpha_n x) \cdot (C_{n3}\cos\beta_n y + C_{n4}\sin\beta_n y). \quad (6.42)$$

6.6.4 4-Sensor Averaging for Plates and Membranes

As shown in Figure 6-23(a), a simple way to use the averaging method is by placing 4 sensors to predict the deflection at the center. Assume the target point is at (x_o, y_o). The sensors are located at (x_1, y_o), (x_2, y_o), (x_o, y_1), and (x_o, y_2); the average output is chosen as

$$\begin{aligned}
\hat{u}(x_o, y_o, t) &= \frac{1}{4}[u(x_1, y_o, t) + u(x_2, y_o, t) + u(x_o, y_1, t) + u(x_o, y_2, t)] \\
&= \frac{1}{4}\sum_{n=1}^{\infty} \xi_n(t)[\phi_n(x_1, y_o) + \phi_n(x_2, y_o) + \phi_n(x_o, y_1) + \phi_n(x_o, y_2)] \\
&= \sum_{n=1}^{\infty} \left(\xi_n(t)\phi_n(x_o, y_o) \cdot \frac{\cos\alpha_n d + \cos\beta_n d}{2} \right). \quad (6.43)
\end{aligned}$$

The modal gain $(\cos\alpha_n d + \cos\beta_n d)/2$ is a function of wavenumber components α_n and β_n, but is not an independent function of wavenumber k_n. In other words, it is not an independent function of resonance frequency ω_n. Notice that it can still be used to attenuate the resonance modes that have waveforms such that $\alpha_n d \approx \frac{\pi}{2}$ and $\beta_n d \approx \frac{\pi}{2}$.

6.6.5 Circular Continuous-Sensor Averaging for Plates and Membranes

To obtain an averaged output that has a modal gain as a function of frequency ω_n, it is intuitive to choose a circular array of sensors with radius d around the center (x_o, y_o), as shown in Figure 6-23(b). The averaged output can be shown as

$$\begin{aligned}
\hat{u}(x_o, y_o, t) &= \frac{1}{2\pi}\int_0^{2\pi} \sum_{n=1}^{\infty} \xi_n(t)\phi_n(x_o + d\cos\theta, y_o + d\sin\theta)d\theta \\
&= \sum_{n=1}^{\infty} \xi_n(t)\phi_n(x_o, y_o)\frac{1}{2\pi}\int_0^{2\pi} \cos(k_n d\cos\theta)d\theta \\
&= \sum_{n=1}^{\infty} (\xi_n(t)\phi_n(x_o, y_o)g(k_n d)). \quad (6.44)
\end{aligned}$$

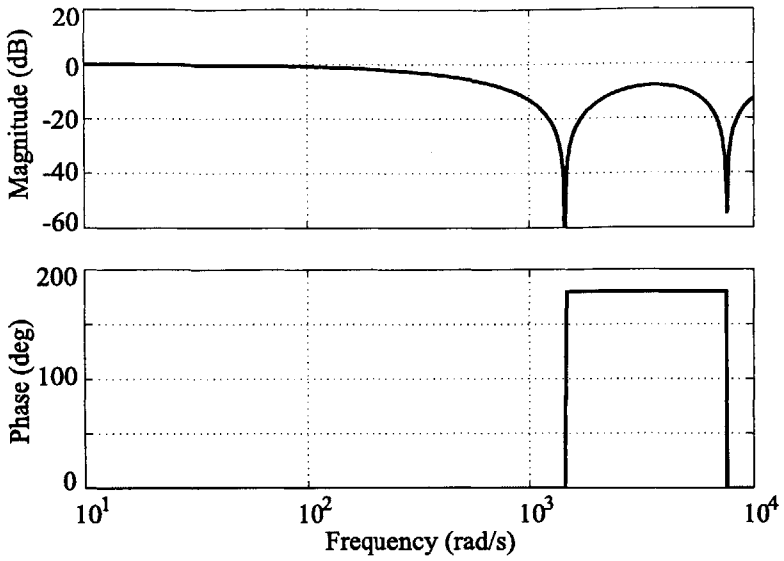

Figure 6-24: Modal gain of circular continuous-sensor averaging for rectangular plates.

The detail of this proof is shown in Appendix F. It shows that the circular averaged output has a modal gain as a function of wavenumber k_n, hence a function of resonance frequency ω_n. Using a plate as an example, the function $g(k_n d)$ is illustrated in Figure 6-24. The first notch zero falls at $k_n d \approx 2.4$. In reality, the circular continuous sensing may not be practical, but it can be approximated by multiple sensors in a circular arrangement.

6.7 Research on Discrete Modal Filters and Distributed Sensors

Two research topics relevant to the averaging method are Discrete Modal Filters [72] and Distributed Sensors [5, 63, 24]. References and primary introductions of these two methods are shown in Chapter 2. In this section, I summarize how they are applied to vibration control, and their comparison to sensor/actuator averaging method. The application of Discrete Modal Filters in our experiment will be further discussed in Chapter 9.

The concepts of discrete modal filters and distributed sensors have one common property with sensor/actuator averaging: they are all spatial filters. Hence they

have no phase lag problems as in temporal filters. The main differences are that discrete modal filters and most of the distributed sensors are designed as model-based modal filters; they are designed to extract modal coordinates. On the contrary, sensor/actuator averaging methods are non-model-based filters; they are designed to exclude the modal observability and modal controllability of certain modes.

Discrete modal filters are developed by Meirovitch [71, 72] to solve the observer spillover problem. Observer spillover happens when we use observers to estimate modal coordinates; if there are unmodeled modes, they can contaminate the estimated modal coordinates, and destabilize the system [6]. The approach of discrete modal filters fits the measured displacements with modal shapes to obtain modal coordinates by simple algebra (no dynamic observer is involved). Due to the orthogonal properties of each mode, the unmodeled modal shapes will not contaminate the calculated modal coordinates, and thus the observer spillover problem is solved. However, the disadvantage of using discrete modal filters is that we need a large number of sensors due to the following two reasons. First, with n sensors, we can only observe n modal coordinates at most. Secondly, if there are resonance modes with wavelengths shorter than twice the sensor distance, they will be aliased and can still contaminate the estimated coordinates [39, Chapter 5].

We use a beam example to demonstrate the concept of discrete modal filters. As shown in Figure 9-10, we use 8 sensors to detect the beam deformation. We can then match the 8 sensor outputs to 8 modal shapes, and therefore obtain 8 modal coordinates. To use discrete modal filters, we need to obtain the modal shapes in advance from the theoretical or experimental model.

The advantage of using a discrete modal filter is that it can avoid the observability spillover [6]. The disadvantages are: (1) It relies on the accuracy of the system model, and is sensitive to parametric uncertainties, and (2) Resonance modes with wavelengths smaller than twice the sensor distance will be aliased and contaminate the estimated modal coordinates. Furthermore, it is practically difficult to use this method in our system, because (1) The tubular beam in our experiment is not straight, and (2) The 8 sensors in our setup are not identical. Thus the 8 sensor outputs cannot

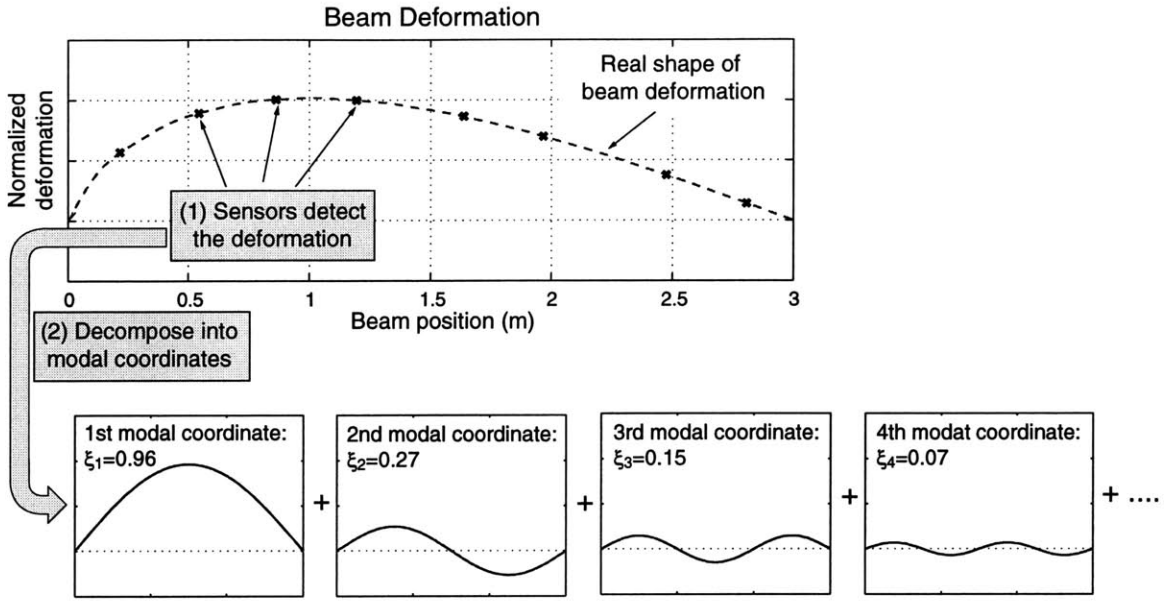

Figure 6-25: Discrete modal filters estimate the vibration modal coordinates of a simple supported beam.

properly represent the combination of the modal coordinates.

Another approach to estimate the modal coordinates is through distributed sensors. Distributed sensors are usually made of sheets of shaped piezoelectric materials and are bonded on the surface of the structure. The sensor outputs voltage as a function of the structure's curvature integrated over the area of the sensor. By designing the shape of the sensor, the output will have different weightings on the vibration modes. Since distributed sensors are continuous, they do not have the aliasing problems as in discrete modal filters. However, Clark [22] points out that distributed sensors are very sensitive to placement errors. This study [22] uses a distributed sensor to observe the 3rd mode on a simply supported beam, and intentionally misaligns the sensor by a 0.26% position error (1 mm misalignment on a 380 mm long beam). The paper shows that other modes can significantly contaminate the measured modal coordinate.

Similarly, we use a beam example to demonstrate the concept of distributed sensors, as shown in Figure 6-26. The sensor output is a voltage proportional to the

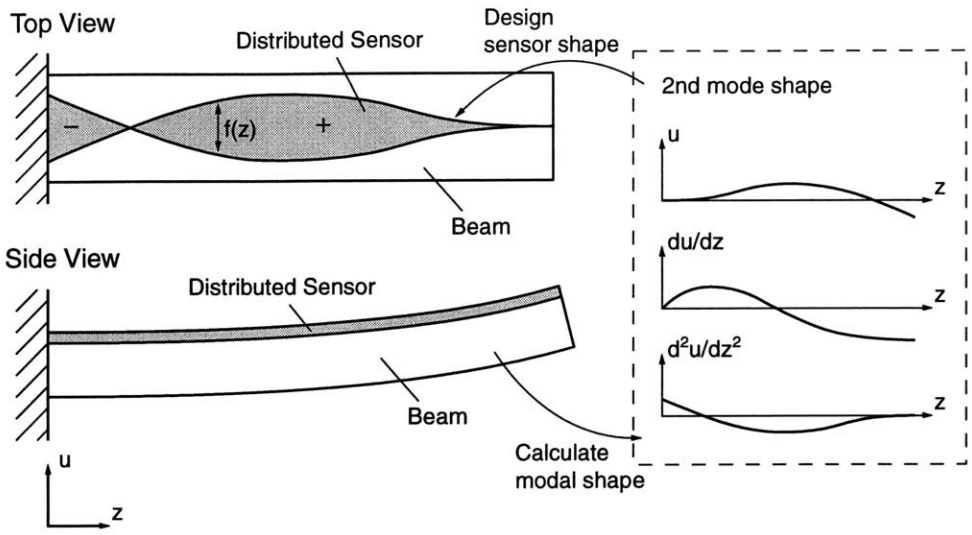

Figure 6-26: A distributed sensor for the 2nd vibration mode of a clamped-free beam. The sensor shape is designed to match the curvature of the 2nd modal shape.

structure curvature [79]:

$$V = -\frac{Q_0}{C}\int_0^L \frac{\partial^2 u}{\partial z^2}\cdot f(z)dz, \tag{6.45}$$

where V is output voltage, Q_0 is the sensor material's charge coefficient, C is a proportionality factor based on sensor dimension, $\partial^2 u/\partial z^2$ is the beam curvature, and $f(z)$ is the sensor distribution function. From this equation, we have the following observations:

1. The output is the integral of the structure curvature over the area of the sensor.

2. Rigid body modes cannot be observed since the curvature of rigid body modes is zero.

3. By choosing the sensor distribution function $f(z)$, all the modes that have curvature $\partial^2 u/\partial z^2$ orthogonal to $f(z)$ become unobservable.

In Figure 6-26, the sensor shape is designed to match the curvature of the 2nd modal shape. In turn, all the modes except the 2nd mode will be unobservable due to the orthogonality properties.

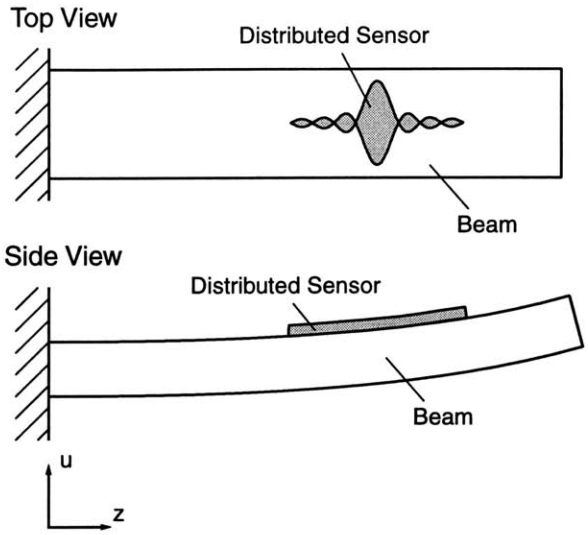

Figure 6-27: A distributed sensor works as a spatial filter, the shape of a sinc function can attenuate high frequency modes. This figure is adopted from the work of Collins et al [24].

Most of the research on distributed sensors focuses on model-based modal sensing; they design the sensor shapes to extract certain modal coordinates. Collins el al [24] focus on non-model-based distributed sensors, they use distributed sensors as spatial filters, which is the same concept as our continuous-sensor averaging. In this paper [24], they design a distributed sensor shaped as a sinc function as shown in Figure 6-27, and use it as a spatial filter that works as an low-pass modal filter.

In our experiment, we tried to use discrete modal filters in our experiment, but it was not successful. We will further discuss the application of discrete modal filters in our experiment in Chapter 9. On the other hand, we cannot possibly use distributed sensors since the beam itself is the product, and we are not able to touch the beam. However, the concept of distributed sensors is very similar to our continuous-sensor averaging method.

6.8 Conclusions

This Chapter presents the novel results of sensor averaging and actuator averaging method for vibration control of flexible elements. This method takes the advantage

that the relations between resonance frequencies and wavelengths depend on structural properties and can be calculated. Therefore we can place sensors and actuators based on wavelengths of undesired modes, and attenuate these resonance modes to improve the gain margin. Sensor averaging attenuates the modal observability, and actuator averaging attenuates the modal controllability. This averaging method is mathematically proved and experimentally verified. It creates band-stop filters for resonance modes without adversely affecting the phase. The resulting modal band-stop filter is independent of sensor/actuator pair locations, namely z_o for beams/strings and (x_o, y_o) for plates/membranes. It is also independent of structural lengths and boundary conditions. We summarize the properties of the fundamental 2-sensor averaging and 2-actuator averaging methods in the following:

1. In the derivation, we assume the modal shapes of the resonance modes are dominated by sinusoidal waveforms.

2. The modal gain of $\cos k_n d$ is only a function of the wavelengths of the resonance modes. The modal gain is independent of structure length and boundary conditions.

3. The modal gain is a function of sensor/actuator pair distance $2d$, and is independent of the sensor/actuator pair location.

4. Sensor/actuator averaging methods make the resonance mode with wavelength $4d$ not observable/controllable.

5. Sensor/actuator averaging methods robustly attenuate the modal observability/controllability of resonance modes with wavelengths close to $4d$.

6. Sensor/actuator averaging methods eliminate sensor/actuator non-collocation problems.

7. Sensor/actuator averaging methods cause no phase lag since they are spatial filters.

In our experiment of beam suspension, we simply choose the frequency where we want to attenuate the modal gain ($\omega_n = 1000$ rad/s), calculate the corresponding wavenumber k_n by the beam dispersion equation $k_n^2 = 0.1\omega_n$ ($k_n = 10$ rad/m), and then choose the averaging distance d such that $k_n d \approx \pi/2$ ($d = 15.7$ cm).

Notice in the analysis of averaging on rectangular plates and rectangular membranes, we assume uniform tension: $T_x = T_y$. For situations when T_x and T_y are different, the results need to be modified, and the circular continuous-sensor averaging will not be a pure function of resonance frequency ω_n as shown in Equation 6.44.

Although in this project we use frequency domain control for our application, this averaging method can be easily adopted in model-based control as well. Furthermore, for open-loop control, actuator averaging can be used to avoid exciting certain resonance modes.

For structures moving at significant speed (near critical speed), the sensor/actuator averaging still works on beams and plates, since the modal shapes of the high frequency modes are almost the same and are still dominated by sinusoidal waveforms. However, for strings and membranes, sensor/actuator averaging will not work because all the modal shapes change significantly when they are moving near critical speed. The verification of these results is shown in Chapter 10.

Chapter 7

Actuator Design for Magnetic Suspension of Tubular Beams

In this chapter, I describe the design and analysis of actuators for our experimental magnetic suspension of tubular beams. As shown in Figure 7-1, the main objective of the actuator designs is to provide magnetic forces F_x and F_y in the x and y directions respectively to control the tube motion, where F_y needs to be sufficient to support the tube weight. Furthermore, the actuators need to have large air gaps to leave room for the tube vibration, coatings, and other processes on the part. The part may also be at high temperature, and so we need space for thermal insulation.

For this experimental setup, I have developed two different actuators: a *Dipole-*

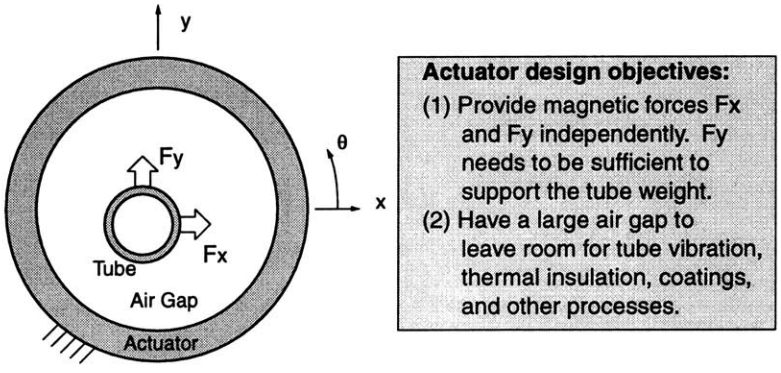

Figure 7-1: Actuator design objectives: (1) provide forces F_x and F_y, and (2) provide a large air gap.

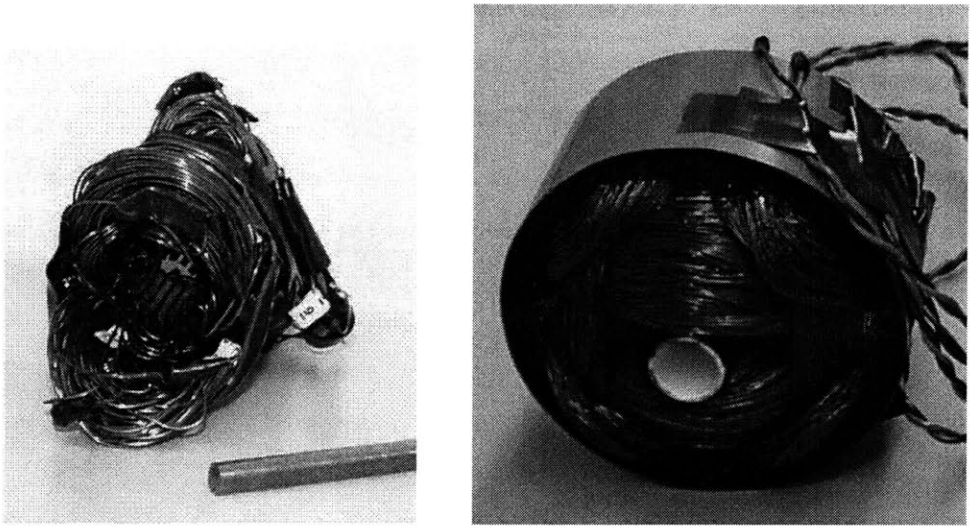

(a) (b)

Figure 7-2: Dipole-Quadrupole actuators: (a) a small version, and (b) a large version.

Quadrupole actuator and a *Quad-U-Core actuator*, as shown in Figure 7-2 and Figure 7-3. Both types of actuators are non-contact, electromagnetic force actuators capable of applying force in the two lateral dimensions. We tried both types of actuators in our experiment. The dipole-quadrupole actuator is a nice idea in theory, but it did not work out in practice. So we went with the quad-U-core actuators for our final experiment of the 10 ft long beam suspension. The following sections will include the actuator designs, magnetic field analysis, force analysis, and circuit designs.

At the end of this chapter, I further develop an eddy-current model for laminated actuators with small air gaps and a solid steel target. This is an extension for future development of similar actuators. We will show quantitatively that both actuators used in this project have large air gaps, and we can thus neglect the eddy-current effects.

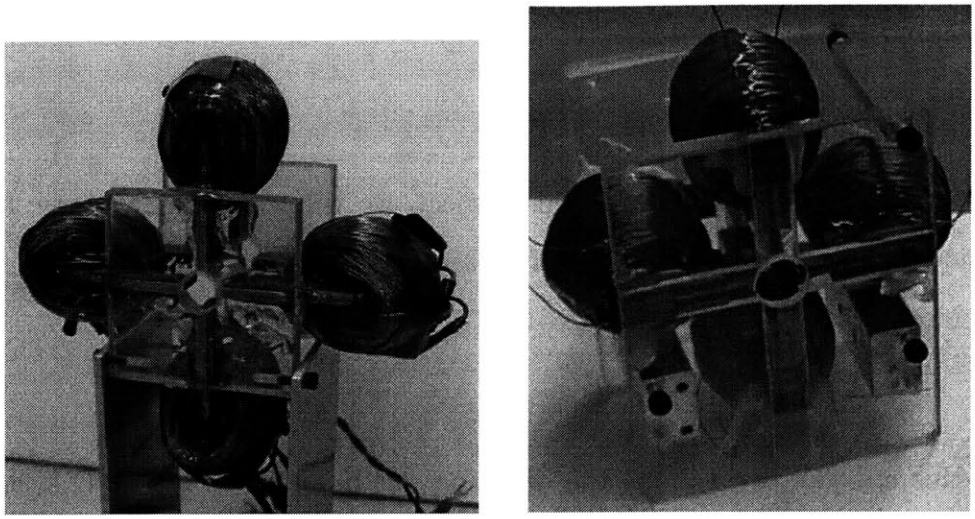

(a) (b)

Figure 7-3: Quad-U-Core actuators: (a) long and thin cores, and (b) short and thick cores.

7.1 Electromagnetic Theory for Calculating Actuator Forces

Before I introduce the conceptual designs of the actuators, I would like to briefly describe the methods that I use to predict the actuator forces. In this section, I include the calculation of the actuator electromagnetic field distribution. I also introduce a simplified magnetic circuit model, which can be used to guide the sensor and actuator designs.

7.1.1 Solutions of Laplace's Equation

The electromagnetic field distribution inside actuators can be solved from Laplace's Equation. For an EQS system, if there is no free charge in the control volume, we can define an electric scalar potential Φ, such that electric field is given by $\vec{E} = -\nabla\Phi$. In the control volume, the scalar potential satisfies Laplace's Equation $\nabla^2\Phi = 0$. Similarly, for an MQS system, if there is no electric current in the control volume, we can define a magnetic scalar potential Ψ, such that the magnetic field is given by $\vec{H} = -\nabla\Psi$. In the control volume, the scalar potential also satisfies Laplace's

Equation $\nabla^2\Psi = 0$.

In the analysis of actuators in this project, we will solve the magnetic Laplace's Equation in polar coordinates. For EQS systems and for other coordinate systems, it can be solved in a similar manner.

In this analysis, we assume the actuator can be modeled as a 2-D system, *i.e.*, that the fields are uniform along the z axis (perpendicular to paper). For a 2-D polar coordinate system, Laplace's Equation becomes:

$$\frac{1}{r}\frac{\partial}{\partial r}(r\frac{\partial \Psi}{\partial r} + \frac{1}{r^2}\frac{\partial^2 \Psi}{\partial \theta}) = 0. \tag{7.1}$$

Assuming that the solution is separable, it has the form of $\Psi(r,\theta) = R(r)F(\theta)$, and we obtain the following ordinary differential equations

$$\frac{d^2F}{d\theta^2} = -m^2F, \tag{7.2}$$

$$r\frac{d}{dr}(r\frac{dR}{dr}) = m^2R. \tag{7.3}$$

The general solutions are [44]:

(1) for $m = 0$

$$\Psi = a_1 + a_2\theta + a_3 \mathrm{ln}r + a_4\theta \cdot \mathrm{ln}r. \tag{7.4}$$

(2) for $m^2 \geq 0$ (azimuthal oscillating, radial exponential)

$$\Psi = b_1 r^m \mathrm{cos}m\theta + b_2 r^m \mathrm{sin}m\theta + b_3 r^{-m} \mathrm{cos}m\theta + b_4 r^{-m} \mathrm{sin}m\theta. \tag{7.5}$$

(3) for $m^2 \leq 0 (m \rightarrow jp)$ (radial oscillating, azimuthal exponential)

$$\Psi = c_1 e^{p\theta} \mathrm{cos}(p\mathrm{ln}r) + c_2 e^{-p\theta} \mathrm{cos}(p\mathrm{ln}r) + c_3 e^{p\theta} \mathrm{sin}(p\mathrm{ln}r) + c_4 e^{-p\theta} \mathrm{sin}(p\mathrm{ln}r). \tag{7.6}$$

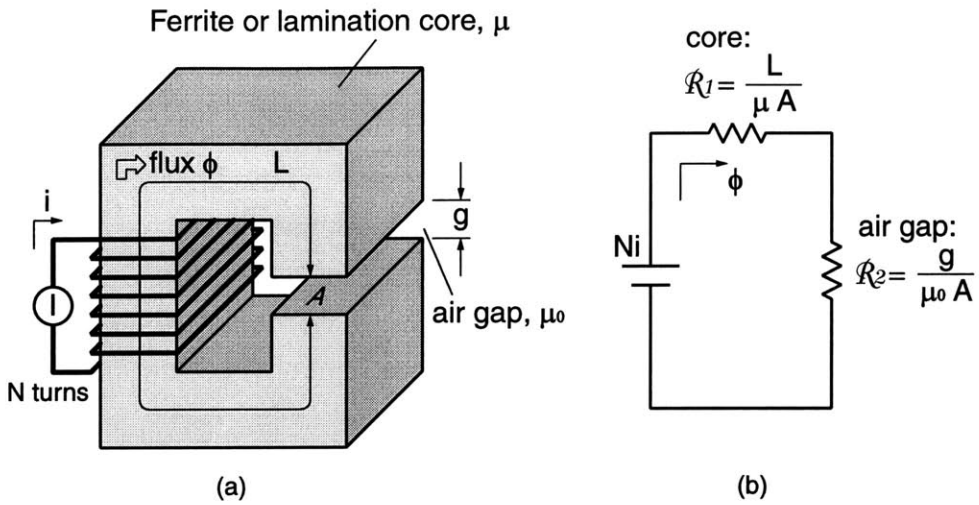

Figure 7-4: Magnetic circuit model (not including eddy-currents).

Also, the magnetic field intensity H can be obtained by

$$\vec{H} = -\nabla\Psi \Rightarrow [H_r, H_\theta] = \left[-\frac{\partial\Psi}{\partial r}, -\frac{1}{r}\frac{\partial\Psi}{\partial\theta}\right]. \tag{7.7}$$

7.1.2 A Magnetic Circuit Model without Eddy-Currents

To guide the design of actuators and sensors, we use a simplified magnetic circuit model. This approach is easier than solving Laplace's Equation, and can provide an accurate approximation to the performance of the design. A simple magnetic circuit model of constant cross-sectional area A is demonstrated in Figure 7-4. The analogy between an electric circuit and magnetic circuit is summarized in Table 7.1.

This magnetic circuit model includes materials with different permeabilities, but it does not include magnetic diffusion. In other words, if there are conductors in the system, and induced eddy-currents are not negligible, this model will not be acceptable. A magnetic circuit model including eddy-currents will be introduced later in this chapter.

Table 7.1: Analogy between electric circuits and magnetic circuits.

Electric circuit	**Magnetic circuit**
J: current density	B: magnetic flux density
I: current	ϕ: magnetic flux
E: electric field strength	H: magnetic field strength
V: voltage	$\mathcal{F} = NI$: magnetomotive force
σ: conductivity	μ: permeability
$R = L/(\sigma A)$: resistance	$\mathcal{R} = L/(\mu A)$: reluctance
$V = IR = El$	$Ni = \phi\mathcal{R} = Hl$

7.2 Design Considerations

During the design process of the electromagnetic actuators, we develop the following check list. They are very common issues that should be considered in actuator designs:

1. Maximum force: The maximum force that an electromagnetic actuator can apply is usually limited by magnetic saturation and input current limit, both are introduced in the following.

2. Magnetic saturation: Magnetic saturation limits the maximum magnetic flux density that the back iron and target steel remains effective. Steel and silicon iron have $B_{sat} \approx 1.5$ Tesla, and ferrite has $B_{sat} \approx 0.3$ Tesla. Fringing field may saturate the back iron easily when the air gap is large, hence it is preferable that actuators have short poles to reduce the fringing field, and thick back iron to prevent magnetic saturation.

3. Current limit: Air cooled systems have a typical current density limit of about 5×10^6 A/m^2 due to the limited heat transfer rate.

4. Air gap: Magnetic force in attractive-type suspension is approximately proportional to the inverse of air gap squared.

5. Current source: The power supply usually has its own voltage limit and current limit. A typical power supply that we use for the experiment has a 28 V output

and a 16 A current limit. The voltage limit determines the maximum current slewing rate.

6. Bandwidth: The actuator bandwidth can be limited by the current controller, magnetic diffusion, and low-pass filters in the circuit design.

7. Force functions of tube position and input current: We need to predict the force functions of $F_x(x, y, I_x, I_y)$ and $F_y(x, y, I_x, I_y)$, where F_x and F_y are forces in the x and y directions, x and y are the tube positions, and I_x and I_y are current inputs to control F_x and F_y. These functions may be nonlinear. For a more accurate modeling, we may further derive the forces as a function of magnetic hysteresis and magnetic diffusion. In this thesis, I include the eddy-current model to account for magnetic diffusion, and prove that our actuators have negligible eddy-currents effect due to the large air gaps. Magnetic hysteresis is a function of materials, and is neglected in this thesis.

8. Power efficiency: We may need to consider the power dissipation for the actuators, which include the power dissipation in coils and in power amplifiers. Our final experimental setup has an average of 25 W power dissipation for each actuator, including the actuator coil and power FET, which is reasonably low. In certain cases, if power dissipation needs to be minimized, we can use Pulse Width Modulation (PWM) method to drive the actuators, and the tradeoff is that the force output will be noisier.

9. Manufacturing: We need to consider the difficulties in fabricating actuators, including coil winding and the machining of laminations and ferrites.

7.3 Dipole-Quadrupole Actuator

The idea for using a Dipole-Quadrupole actuator originated with Professor Trumper. This actuator has one dipole field and two quadrupole fields: the dipole field is used to magnetize the suspended object, and the quadrupole fields are used to generate controlled forces in the x and y directions. The expected advantages of this

topology are: (1) the forces are controllable even when the object is magnetically saturated, (2) forces are linear to quadrupole current inputs, (3) forces are neutral to position change, and (4) it can be used for beams and strings. Although the Dipole-Quadrupole actuator is a nice idea in theory, the performance is not as ideal in practice. The main reason is that the presence of the tube is not negligible, hence the magnetic field distribution changes significantly with the tube motion. Our experimental results show that the forces are not neutral to tube position change, and the tube tends to stick to the pole tips.

The processes of fabricating a Dipole-Quadrupole actuator is shown in Figure 7-5. All the coil winding was done by hand. The steps are: (1) the arrangement of 12 laminated poles, (2) dipole coil winding[1], (3) y-quadrupole coil winding, (4) x-quadrupole coil winding, and (5) assembly of the outer laminated loop and epoxy bonding of the assembly[2].

7.3.1 Conceptual Design

As shown in Figure 7-6, the Dipole-Quadrupole actuator is driven by 3 field components: the dipole field, the x-direction quadrupole field, and the y-direction quadrupole field. In the conceptual design, we use surface current distribution on the inside surface of the actuator to predict the field distribution. In practice, the wires will take a lot of space, hence we fit varying turns of wires inside the actuator slots instead of on the surface to realize the sinusoidal field distribution. The field analyses of these three field patterns are given in detail in Appendix G. In the following I summarize the key results of the field analyses.

[1]Special care is needed to avoid short circuit between magnetic wires and lamination edges.

[2]Thermally conductive epoxy was ordered from Cast-Coat Inc., 354 West St., W. Bridgewater, MA 02379, (508) 587-4514.

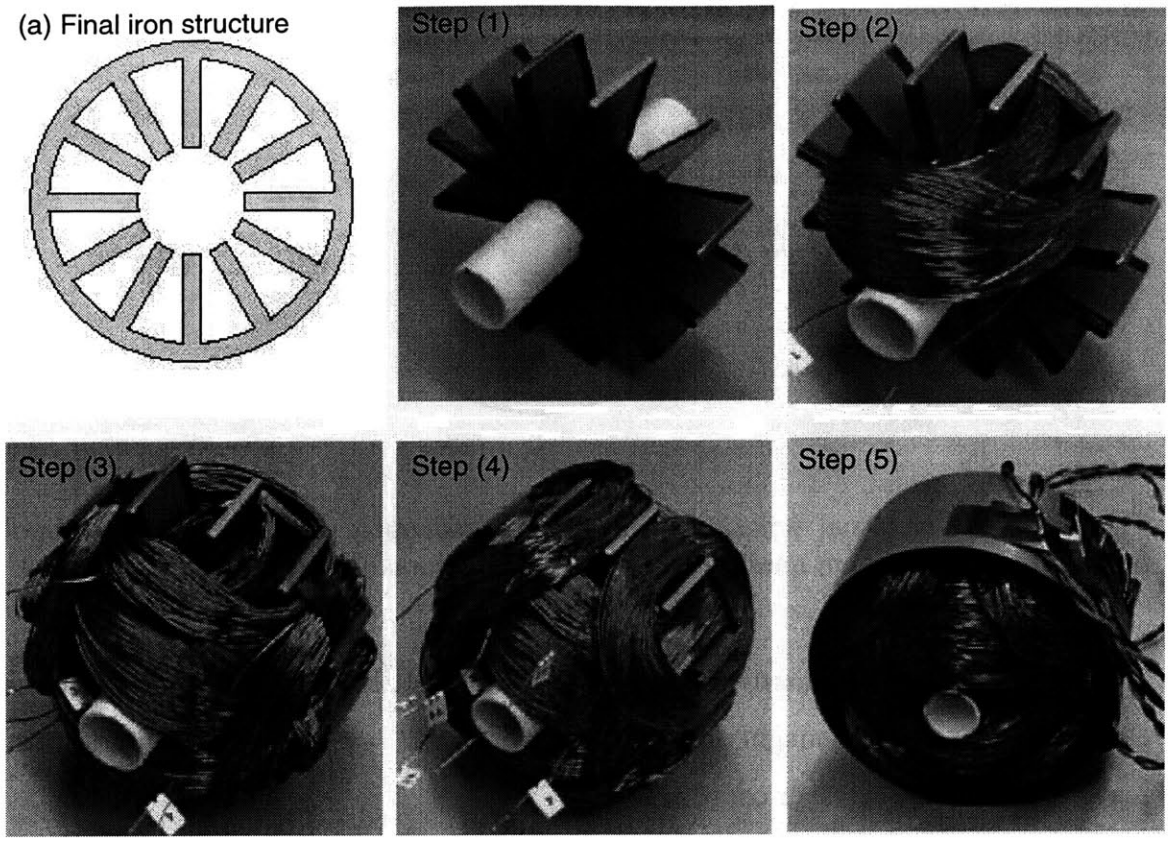

Figure 7-5: Processes of making a dipole-quadrupole actuator: (a) final iron structure, Step(1) 12 lamination poles, Step(2) dipole coil, Step(3) y quadrupole coil, Step(4) x quadrupole coil, Step(5) outer lamination loop and epoxy bonding.

Dipole Field: Uniform Field

As shown in Figure 7-6, the dipole field is driven by a z-directed surface current distribution of

$$J_{dipole}(\theta) = -J_o \cos\theta \tag{7.8}$$

at a radius R_0. After solving Laplace's Equation, we obtain the magnetic scalar potential due to the dipole as

$$\Psi = -J_o r \sin\theta. \tag{7.9}$$

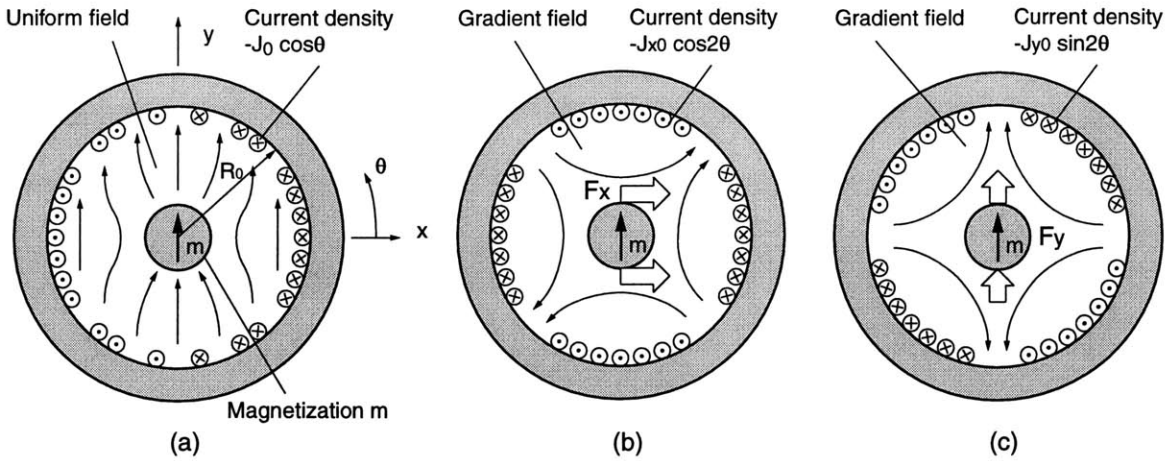

Figure 7-6: Conceptual function of a Dipole-Quadrupole actuator: (a) the dipole field, (b) the x-direction quadrupole field, and (c) the y-direction quadrupole field.

Notice that in the real hardware, we simply design the coil distribution such that the pole tips will have magnetic scalar potential as $\Psi = -J_o R_0 \sin\theta$. The resulting magnetic field in Cartesian coordinates is:

$$\vec{H} \;=\; [H_x, H_y] = [0, J_o]. \tag{7.10}$$

Thus we see that the dipole current generates a uniform magnetic field within the bore of the actuator.

In the hardware, we approximate the dipole current distribution by winding varying turns of coils into the 12 actuator slots. The designed coil distribution provides an approximately sinusoidal magnetic potential on the 12 poles, and thus realizes approximately a dipole field distribution.

X-Direction Quadrupole Field: Uniform Gradient Field

As shown in Figure 7-6, the x-direction quadrupole field is driven by the z-directed surface current distribution

$$J_x = -J_{xo}\cos 2\theta \tag{7.11}$$

at a radius of R_0. After solving Laplace's Equation, we obtain the magnetic scalar potential due to the x-quadrupole in Cartesian coordinates as

$$\Psi = \frac{1}{R_o} J_{xo} xy. \tag{7.12}$$

The resulting magnetic field in Cartesian coordinates becomes

$$\vec{H} = [H_x, H_y] = [\frac{J_{xo}}{R_o} y, \frac{J_{xo}}{R_o} x], \tag{7.13}$$

and the resulting gradients of the magnetic field are

$$\nabla H_x = [\frac{\partial H_x}{\partial x}, \frac{\partial H_x}{\partial y}] = [0, \frac{J_{xo}}{R_o}], \tag{7.14}$$

$$\nabla H_y = [\frac{\partial H_y}{\partial x}, \frac{\partial H_y}{\partial y}] = [\frac{J_{xo}}{R_o}, 0]. \tag{7.15}$$

The result shows that the x-quadrupole current generates a magnetic field with uniform gradients, and thereby will exert a uniform force on a dipole located in the field.

Y-Direction Quadrupole Field: Uniform Gradient Field

The y-direction quadrupole field is the same as x-direction quadrupole field rotated by 45°. The y-direction quadrupole field is driven by the current distribution:

$$J_y = -J_{yo} \sin 2\theta. \tag{7.16}$$

After solving Laplace's Equation, we obtain the magnetic scalar potential in Cartesian coordinate:

$$\Psi = \frac{1}{2R_o} J_{yo} (y^2 - x^2). \tag{7.17}$$

The resulting magnetic field in Cartesian coordinates is

$$\vec{H} = [H_x, H_y] = [-\frac{J_{yo}}{R_o}x, \frac{J_{yo}}{R_o}y]. \tag{7.18}$$

The resulting gradients of the magnetic field are

$$\nabla H_x = [\frac{\partial H_x}{\partial x}, \frac{\partial H_x}{\partial y}] = [-\frac{J_{yo}}{R_o}, 0], \tag{7.19}$$

$$\nabla H_y = [\frac{\partial H_y}{\partial x}, \frac{\partial H_y}{\partial y}] = [0, \frac{J_{yo}}{R_o}]. \tag{7.20}$$

The result shows that the y-quadrupole current generates a magnetic field with uniform gradients, and so creates a uniform force on a dipole located in the field.

Predicted Force Behavior

If we put a magnetized object with magnetization density $\vec{M}$ inside the cavity, the force density can be predicted by Kelvin magnetization force density:

$$f_x = (\mu_o \vec{M} \cdot \nabla) H_x = \mu_o (M_x \frac{\partial H_x}{\partial x} + M_y \frac{\partial H_x}{\partial y}), \tag{7.21}$$

$$f_y = (\mu_o \vec{M} \cdot \nabla) H_y = \mu_o (M_x \frac{\partial H_y}{\partial x} + M_y \frac{\partial H_y}{\partial y}), \tag{7.22}$$

where f_x and f_y are volume force densities in N/m^3. We make the following assumptions:

1. Assume that the radius of the tube is much smaller than the radius of the actuator bore, and the presence of the tube does not affect the dipole and quadrupole fields.

2. The dipole field applied by the actuator is much stronger than the quadrupole fields, and the tube is mainly magnetized by the dipole field only.

3. The dipole field applied by the actuator magnetizes the tube in the y direction with a magnetization density $\vec{M} = [0, M_y]$ A/m. From Haus [44], a cylinder with $\mu \gg \mu_0$ inside a uniform magnetic field with a field strength H A/m, the

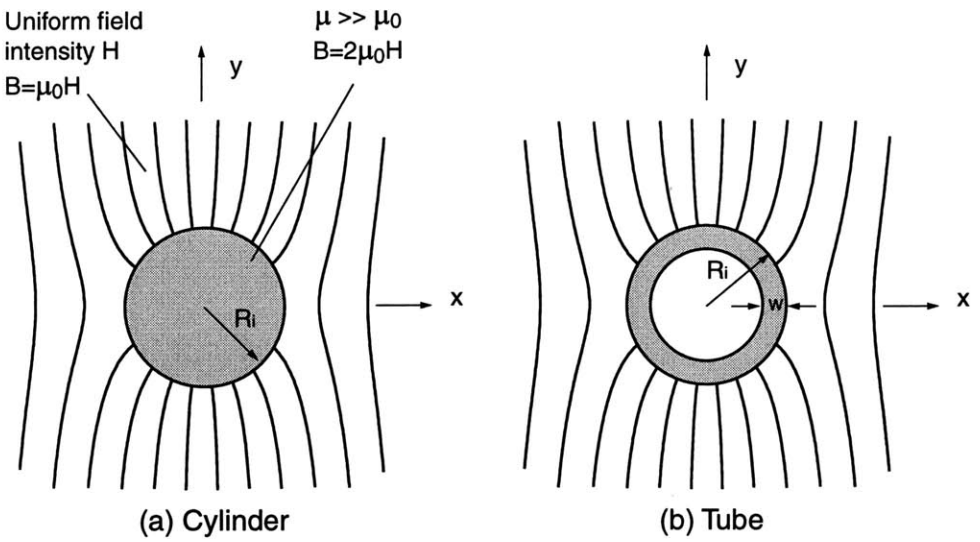

Figure 7-7: Magnetization of a tube inside a uniform field: (a) a cylinder is magnetized by a magnetization density of $M = 2H$, and (b) a tube has the same total magnetization strength.

magnetization density of the cylinder is $M = 2H$ A/m, as shown in Figure 7-7(a). A tube inside a uniform magnetic field has the same total magnetization strength as long as it is not saturated, as shown in Figure 7-7(b). Hence we can treat the tube as a cylinder when we calculate the field distribution and the forces. If the tube is saturated, we can modify the result, and assume that the magnetization density is determined by the ratio of wall thickness w to the radius R_i of the tube, such that $\vec{M} = [0, M_y] = [0, (B_{sat}/\mu_0) \times (w/R_i)]$.

Under these assumptions, we have the resulting forces:

$$F_x = \mu_o M_y \frac{\partial H_x}{\partial y} \pi R_i^2 = \frac{\mu_o}{R_0} M_y J_{xo} \pi R_i^2, \tag{7.23}$$

$$F_y = \mu_o M_y \frac{\partial H_y}{\partial y} \pi R_i^2 = \frac{\mu_o}{R_0} M_y J_{yo} \pi R_i^2, \tag{7.24}$$

where F_x and F_y are forces per unit length in N/m. The result shows that the actuator will have the following characteristics:

1. F_x and F_y are controlled by J_{xo} and J_{yo} independently.

2. F_x and F_y are decoupled.

3. F_x and F_y are independent of the position of the tube.

4. The actuator works even when the tube is saturated, which is a required characteristic for thin-wall tubes.

For the actuator shown in Figure 7-5, we have coil windings with 3 current inputs: I_0, I_x and I_y for dipole coil, x quadrupole coil and y quadrupole coil respectively. These current inputs relate to the current distribution by $J_0 \approx 9.3 \times 10^4 I_0$ A/m, $J_{x0} \approx 4.2 \times 10^4 I_x$ A/m, $J_{y0} \approx 4.8 \times 10^4 I_y$ A/m. For an actuator with 1" length and 0.5" inside diameter, and a tube with 0.25" diameter, the calculations above predict the forces as: $F_x = 1.24 I_0 I_x$ N, and $F_y = 1.42 I_0 I_y$ N. It will be shown later that this estimation is $3 \sim 4$ times smaller than the Matlab analysis and the experimental results. The reason is that the tube inside the actuator significantly reduces the magnetic reluctance, and hence increases the magnetic field, which was ignored in the idealized calculations above.

7.3.2 Matlab Analysis

In the previous analysis, we neglect the presence of the tube when we calculate the magnetic field distribution. However, in our final design, we have an actuator with 0.5" inside diameter and a tube with 0.25" diameter. The reluctance of the air is reduced by roughly a factor of 2, hence the presence of the tube is apparently not negligible. Therefore, I use numerical methods to solve for the magnetic field distribution of the actuator to account for the significant dimensions of the tube. I did this in the Matlab environment. The force is predicted as a function of the excitation currents and position of the tube. The details are given in Appendix H. In the following I only summarize the process and the result.

The Matlab model is shown in Figure 7-8. The magnetic scalar potential in the air gap is represented by Laplace's Equation:

$$\nabla^2 \Psi = 0.$$

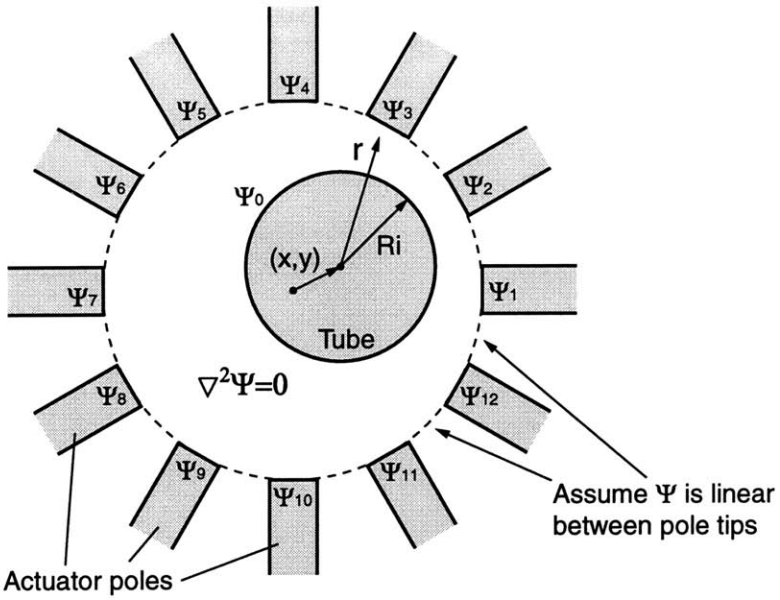

Figure 7-8: Matlab model of a Dipole-Quadrupole actuator for solving the magnetic field distribution.

I use the general solution of Laplace's Equation, and fit the boundary conditions of the given scalar potentials. The boundary conditions are:

1. Magnetic scalar potential Ψ_i of each pole tip is calculated from the current distribution.

2. Magnetic scalar potential between pole tips is assumed to be linear.

3. Scalar potential of the tube is a constant Ψ_o, *i.e.*, we assume the tube permeability is high.

4. The net magnetic flux going through the tube is zero:

$$\int_{\theta=0}^{2\pi} H_r d\theta = 0.$$

I use 360 point boundary conditions, and assume that the solution to be a combination

of 20 harmonics[3]:

$$\Psi = \Psi_o + \sum_{m=1}^{20} (C_{1m}\cos m\theta + C_{2m}\sin m\theta)\left(\left(\frac{r}{R_i}\right)^m - \left(\frac{r}{R_i}\right)^{-m}\right). \tag{7.25}$$

Under assumptions above, the field will be normal to the surface of the tube. The surface force distribution around the tube is thus

$$f = \frac{1}{2}\mu_o H_r^2, \tag{7.26}$$

directed normal to the tube surface at each point. An example of the resulting calculated force distribution is shown in Figure 7-9. The results of the numerical calculations can be approximated as:

$$F_x = 2.4I_x + 0.3x + 0.3xy, \tag{7.27}$$

$$F_y = 2.4I_y + 0.3y + 0.3xy, \tag{7.28}$$

where the dipole current is assumed to be 0.5 A, F_x and F_y are forces in N, I_x and I_y are the currents in the x-quadrupole and y-quadrupole respectively in A, and x and y are the tube positions in mm with respect to the centered condition.

7.3.3 Experimental Results

We design a testbed to measure the actuator forces as a function of current inputs and tube positions, the design is shown in Figure 7-10. We use an $X - Y$ stage to move the actuator in the 2 lateral directions relative to the fixed tube. The experimental results are shown in Figure 7-11 as compared with the theoretical analysis. The experimental results can be modeled as:

$$F_x = 1.5I_x + 0.2x, \tag{7.29}$$

$$F_y = 2I_y + 1.5y. \tag{7.30}$$

[3]For the Matlab code I wrote, the numerical solution becomes wrong when m is larger than 46. I did not further debug the code.

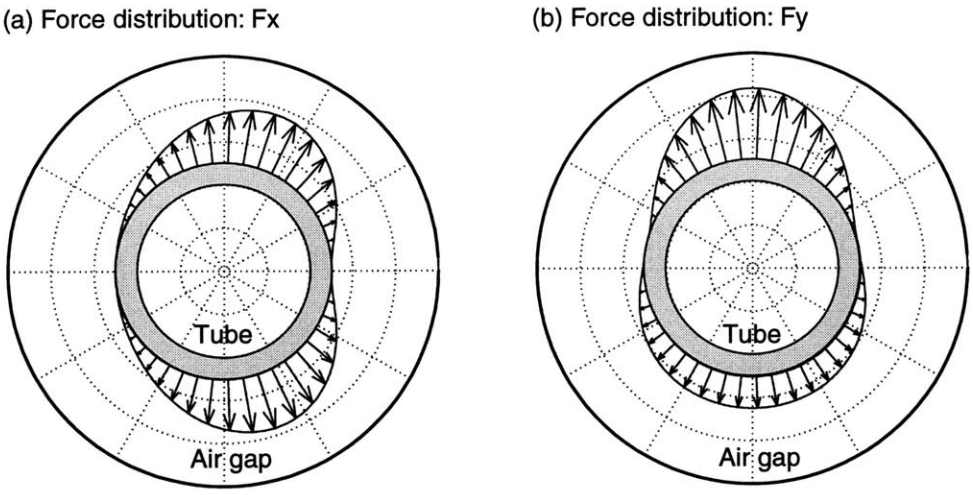

Figure 7-9: Force distribution of dipole-quadrupole actuators analyzed by using Matlab: (a) F_x with dipole current 0.5 A and x-quadrupole current $I_x = 0.5$ A, and (b) F_y with dipole current 0.5 A and y-quadrupole current $I_y = 0.5$ A.

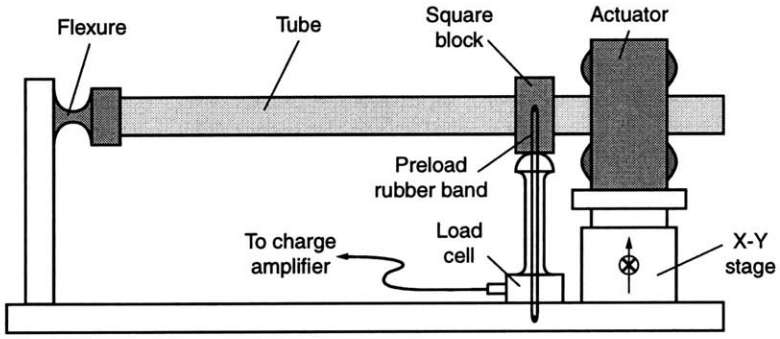

Figure 7-10: Testbed for measuring actuator forces as a function of current inputs and tube positions.

The experimental results show practical problems that were not considered at the conceptual design of this actuator:

- The actuator pole tips are close to each other, and can be magnetically saturated easily.
- The tube dimension is not negligible, and it thus significantly changes the magnetic field when it moves. The force is thus highly dependent on the tube position.
- When the tube is close to the pole, especially at the top and the bottom, it will

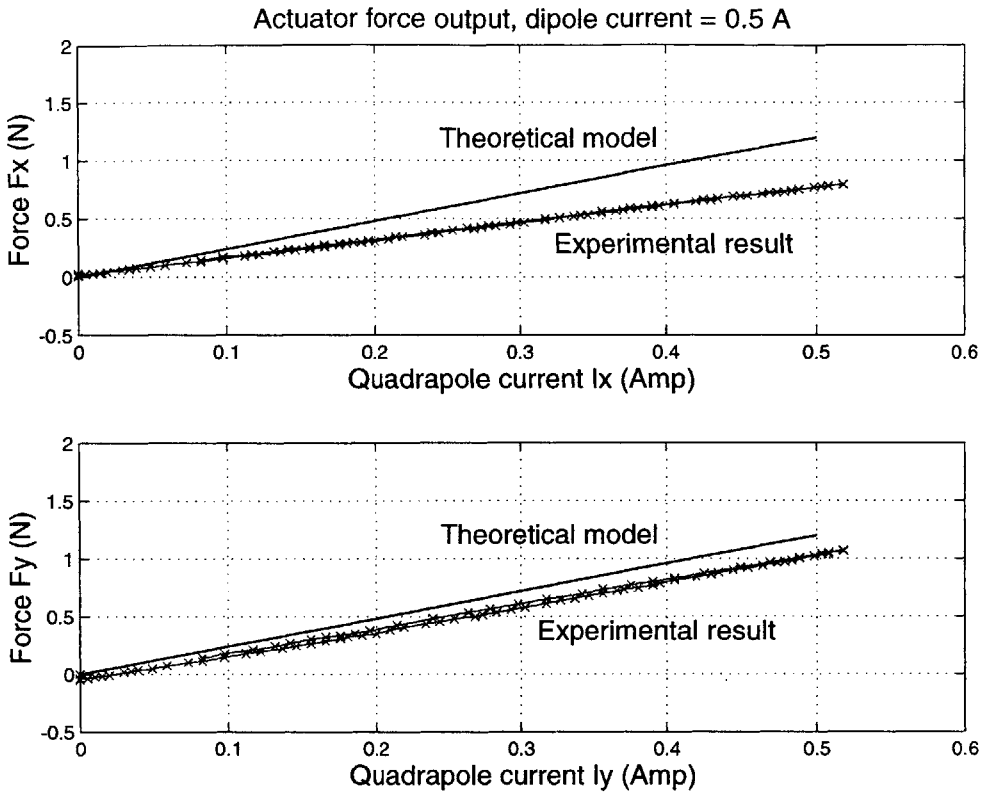

Figure 7-11: Experimental force function of the Dipole-Quadrupole actuators, compared with the Matlab analysis.

be attracted and stick to the poles, and cannot be removed unless we turn off the dipole field.

- The actuator has a maximum force of about 1 N due to thermal limit.

- It is troublesome to make such an actuator, the coil winding for the prototype took about 40 hours' work.

Due to these disadvantages, we only used it at the beginning of this project to suspend a 1.5 ft long beam with hinged-free ends. We then decided not to use this actuator for the final beam suspension experiment. However, such actuators still offer two promising applications: (1) suspension of thin-wall tubes, and (2) suspension of small-diameter strings. Furthermore, it has the advantages that the force f_x and f_y are decoupled, and are linear to input quadrupole currents.

7.4 Quad-U-Core Actuator

In this project, we decide to use a tube with a 0.25" diameter, and sensors and actuators with a 0.5" bore diameter. In this setup, the Dipole-Quadrupole actuator is not ideal since the presence of the tube is not negligible. Although it offers the linear current-force relations, it is not an attractive choice compared with its difficulties of fabrication. Hence I decide not give up using Dipole-Quadrupole actuators, and instead use typical electromagnets, and design the Quad-U-Core actuators as the actuators for our final experiment. The current-force relation is nonlinear for this type of actuators, but we can linearize it by using a biased current method or the feedback linearization method. The Quad-U-Core actuators are shown in Figure 7-3. Each U-shaped lamination is wound with 1200 turns of gauge 26 wires. The input current limit is set to be 1 A due to power dissipation limits, the input voltage is 28 V. Each electromagnet is measured to have a resistance of 13 Ω, and an inductance of 0.13 H. Hence from the 28 V power supply, the maximum available current is around 2 A, and the maximum current slewing rate on the inductance is about 0.2 A/ms.

Figure 7-3(a) shows the first version of this actuator; it has long and thin poles. From experiments, the force saturates at 0.5 N when the input current is 0.5 A. This is because the fringing magnetic field causes saturation in the back iron of the actuator. Figure 7-3(b) shows the second version of this actuator; it has shorter poles, and thicker cores.

7.4.1 Conceptual Design

Because of the difficulties of making the Dipole-Quadrupole actuator, the Quad-U-Core actuator is designed and used instead for the final experimental setup. The Quad-U-Core actuator simply consists of 4 U-core electromagnet, and each U-core is shown in Figure 7-12. The properties of the Quad-U-Core actuator are predicted by the magnetic circuit model shown here.

In designing the actuators, we want to obtain its force as a function of current and air gap $f(i, g)$. We also need to predict the maximum force, which is usually

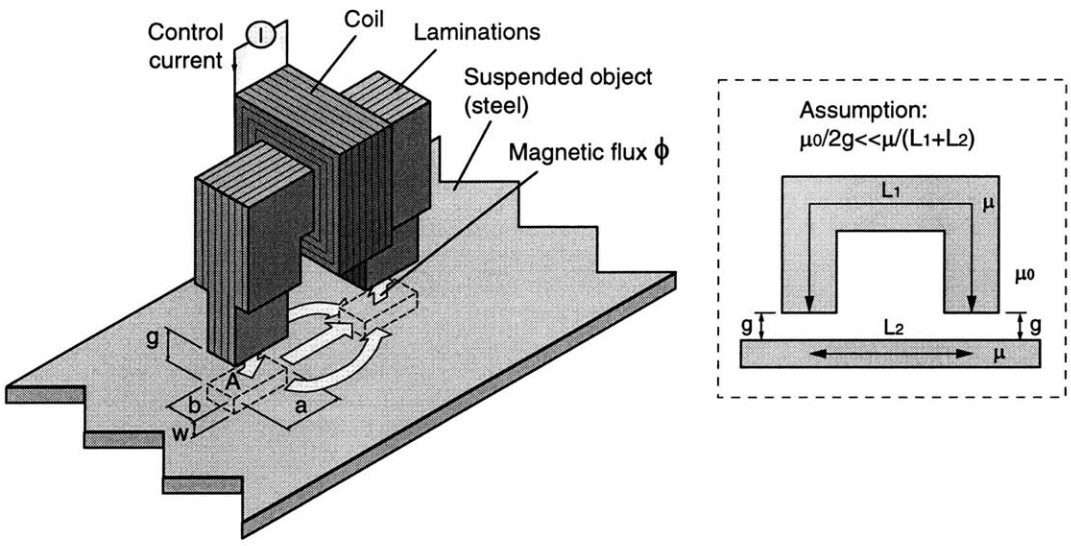

Figure 7-12: Conceptual design of a Quad-U-Core actuator.

limited by current limit due to heat transfer, and magnetic flux limit due to magnetic saturation.

In our experiment, we consider actuators with large air gaps. In this case, the eddy-current effect is negligible as shown later. As shown in Figure 7-12, we assume that the back iron and the target both have permeability such that $\mu_0/2g \ll \mu/(L_1 + L_2)$, the magnetic field in the air gap can then be obtained by

$$Ni = \mathcal{R}\phi = \frac{2g\phi}{\mu_o A} \Rightarrow H = \frac{Ni}{2g}, \qquad i < i_{max}. \tag{7.31}$$

The applied force F can then be derived as

$$F = 2A\frac{B^2}{2\mu_0} = \frac{\phi^2}{\mu_0 A}, \qquad \phi < \phi_{max}, \tag{7.32}$$

where $\mu_0 = 4\pi \times 10^{-7}$ H/m is permeability of free space, $N = 1200$ is the number of turns of coil, i is current input, and $A = 40$ mm^2 is the cross-sectional area of actuator pole face. With these numerical values, the resulting force function becomes

$$F(i, g) = 18\frac{i^2}{g^2}, \tag{7.33}$$

where F is force in N, i is current input in A, and g is air gap in mm. It will be shown

that this approximation is close to the Matlab analysis and the experimental result.

When designing the actuator, we estimate the maximum force output by considering current limit and magnetic saturation. The current intensity is mainly limited by heat transfer. For an air cooled system, $i_{max} \approx 5 \times 10^6 \times$(cross sectional area of one wire). Magnetic saturation can happen inside both the actuator and the suspended object. We follow the magnetic flux path in Figure 7-12 to find the bottleneck, the minimum cross sectional areas are A (the pole face area) and $2(a+b)W$ (the perimeter of the pole times the target steel thickness). Hence the maximum magnetic flux ϕ_{max} is approximately the minimum of $A \cdot (B_{sat})_{actuator}$, $A \cdot (B_{sat})_{target}$ and $(2a+2b)W \cdot (B_{sat})_{target}$. The saturating flux density B_{sat} is about 1.5 Tesla for Si-Fe laminations and for the target steel.

In our experimental setup, we have electromagnets wound by gauge 26 wires, which have a diameter of 0.016" (0.4 mm). Therefore, the maximum current input should be set at

$$i_{max} \approx 5 \times 10^6 \times \pi(2 \times 10^{-4})^2 = 0.6 \text{ (A)}. \tag{7.34}$$

In the real hardware, we have an operating point current running at $0.3 \sim 0.4$ A to support the weight of the beam. We set the maximum current in the software to 1 A for control purposes. However, if we run 1 A through the coil constantly for more than 1 minute, the coil becomes extremely hot. The maximum force due to current limit can be found to be

$$F_{max} = 18\frac{i_{max}^2}{g^2} = 18\frac{0.6^2}{3.2^2} = 0.6 \text{ (N)}. \tag{7.35}$$

The maximum force due to magnetic saturation can be found to be

$$F_{max} = 2A\frac{B_{max}^2}{2\mu_0} = 8 \times 10^{-5} \cdot \frac{1.5^2}{2\mu_0} = 72 \text{ (N)}. \tag{7.36}$$

It seems that the actuators should not have saturation problems. However, due to the large air gaps, the fringing field can saturate the back iron easily. That is why

we designed the actuators with thicker back iron as shown in Figure 7-12.

7.4.2 MATLAB Analysis

In an approach similar to that we used for the Dipole-Quadrupole actuator, in the Quad-U-Core actuator we can solve for the magnetic field in the air gap, and then solve for the force as function of current input and tube position. The details are shown in Appendix H. I summarize the result in the following.

We can assume that the solution of magnetic scalar potential as a combination of 20 harmonics[4]:

$$\Psi = C_0 \ln\frac{r}{R_i} + \sum_{m=1}^{20} (C_{1m}\cos m\theta + C_{2m}\sin m\theta)\left(\left(\frac{r}{R_i}\right)^m - \left(\frac{r}{R_i}\right)^{-m}\right). \tag{7.37}$$

Notice that the solution form is slightly different from that of the Dipole-Quadrupole actuators, that is because the boundary conditions are different. The resulting force is

$$F(i,g) = 34\frac{i^2}{g^2}, \tag{7.38}$$

where F is force in N, i is current in A, and g is air gap in mm.

7.4.3 Experimental Results

The experimental results show that the force is approximately

$$F(i,g) = 36\frac{i^2}{g^2}, \tag{7.39}$$

where F is force in N, i is current in A, and g is air gap in mm. As expected, the force is a nonlinear function of current and tube position. This result compares favorably with predictions from the Matlab analysis. In our test, the maximum continuous

[4]As in the analysis Dipole-Quadrupole actuators, my Matlab code starts to show errors when m is larger than 23.

current is around $0.7 \sim 0.8$ A, which limits the maximum force to $1.7 \sim 2.3$ N when the tube is centered and the air gap is 3.2 mm. Since the 10 ft long tube weighs 3.5 N, in order to lift the beam from the bottom of the actuator (air gap $g = 6.4$ mm), we need 8 actuators driven by a 0.7 A current to lift it. In practice, we set the maximum current to be 1 A for the control purpose. During suspension, the top magnet has an average input current of $0.3 \sim 0.4$ A.

7.4.4 Push-Pull Linearization versus Feedback Linearization

We can linearize the actuator output by two methods: push-pull linearization, and feedback linearization. We will show that push-pull linearization is not desirable because it makes control more difficult. We thus will use feedback linearization in our final setup.

The arrangement of push-pull linearization is shown in Figure 7-13. Here, the top magnet has input current $(i_0 + i)$ A with an air gap of $(g_0 - x)$ mm, and the bottom one has input current $(i_0 - i)$ A with an air gap of $(g_0 + x)$ mm, where i_0 is the constant bias current, and g_0 is the nominal air gap. The resulting force is the combination of the forces from these two electromagnets:

$$F = F_1 - F_2 = 36 \left[\frac{(i_0 + i)^2}{(g_0 - x)^2} - \frac{(i_0 - i)^2}{(g_0 + x)^2} \right], \tag{7.40}$$

which shows that the i^2 terms will be canceled. This function is plotted in Figure 7-13, we see that with 0.5 A bias current, the resulting force shows a linear relation to the input current i within the ± 0.5 A range.

In order to incorporate the actuator force function into the system dynamics, we further linearize this nonlinear equation with respect to input current i and displacement x by

$$\begin{aligned} F(i,x) &\approx F(0,0) + \frac{\partial F}{\partial i} i + \frac{\partial F}{\partial x} x \\ &= 36 \left[4 \frac{i_0}{g_0^2} i + 4 \frac{i_0^2}{g_0^3} x \right]. \end{aligned} \tag{7.41}$$

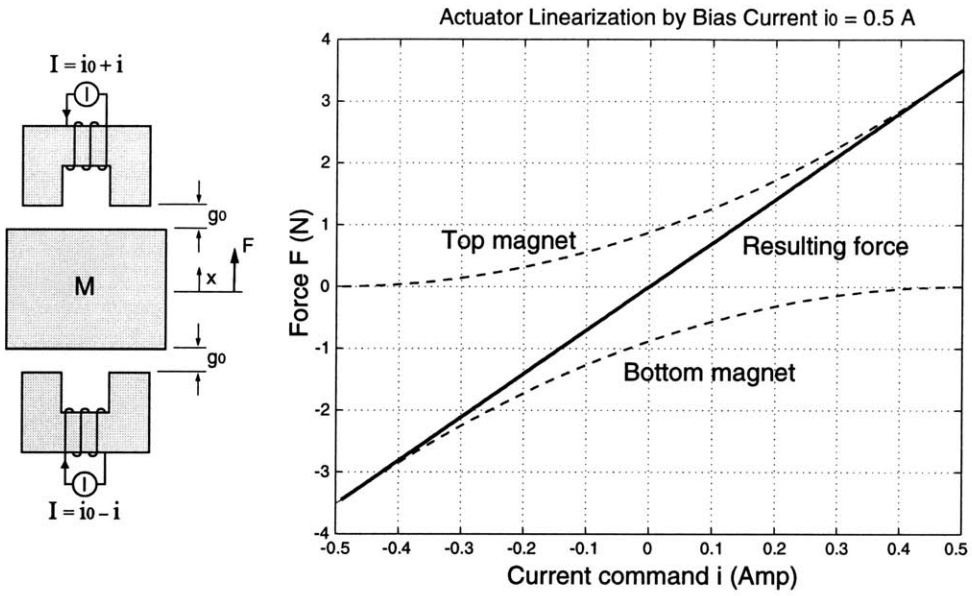

Figure 7-13: Actuator linearization by push-pull arrangements, assuming the actuator bias current is $i_o = 0.5$ A.

If we have a bias current of $i_0 = 0.5$ A, and a nominal gap of $g_0 = 3.2$ mm, the resulting force function becomes:

$$F(i, x) = K_i i + K_x x = 7.0i + 1.1x, \tag{7.42}$$

where F is force in N, i is current in A, and x is the displacement in mm.

As for statics, push-pull linearization seems to be a good solution to linearize the actuator output. However, if we look at the dynamics, we will find that the push-pull linearization makes the system difficult to control. The arrangement of the push-pull setup with a bias current is analogous to adding permanent magnets to both sides of the electromagnets. As shown in Figure 7-13, a free mass M with 2 biased electromagnets has dynamics: $M\ddot{x} = F = K_i i + K_x x$. Originally, the free mass has 2 poles at the origin. With the bias current, these two poles move to $\pm\sqrt{K_x/M}$, as shown in Figure 7-14. For our system, if we have $M = 0.35$ kg, and 8 actuators with a total $K_x = 8800$ N/m, the open loop poles will be moved from the origin to ± 160 rad/s. In order to stabilize these poles, the feedback control will need to have a proportional gain of at least 1100 N/m for each actuator.

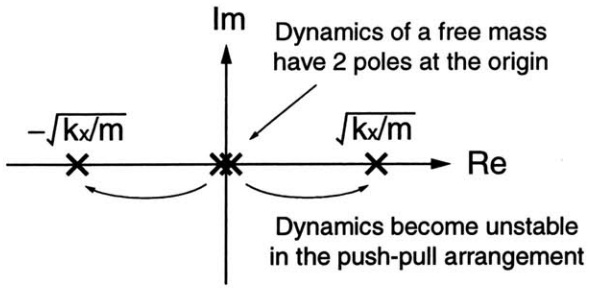

Figure 7-14: Instability caused by push-pull arrangements.

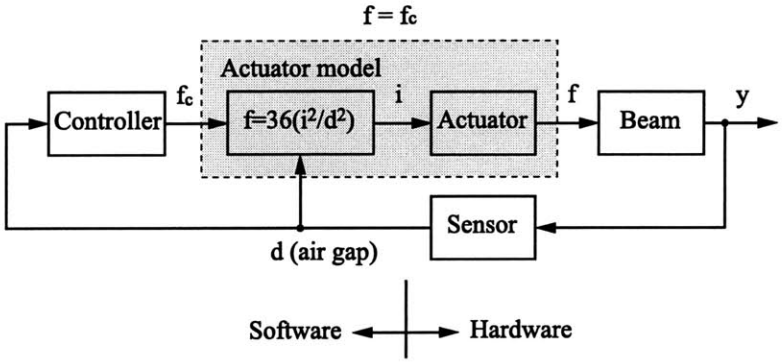

Figure 7-15: Block diagram of feedback linearization.

For this reason, we instead choose to use feedback linearization in our final experiment. The block diagram for feedback linearization is shown in Figure 7-15. For our actuator, we have $f = 36i^2/d^2$, where f is force in N, i is current in A, and d is air gap in mm. With the feedback of air gap d, from the control force command f_c, we can calculate the required current i by $i = d\sqrt{f_c}/6$ in the software. Hence we can avoid the nonlinearity in the actuator, and the resulting output force becomes follows the force command: $f = f_c$. By using this arrangement, the open loop poles stay at the origin.

7.5 Input Current Control

In this section, I include the circuit design of current source for the actuators. We use power amplifiers for Dipole-Quadrupole actuators since we need two-directional currents. We use power FET drives for Quad-U-Core actuators since we only need uni-directional currents.

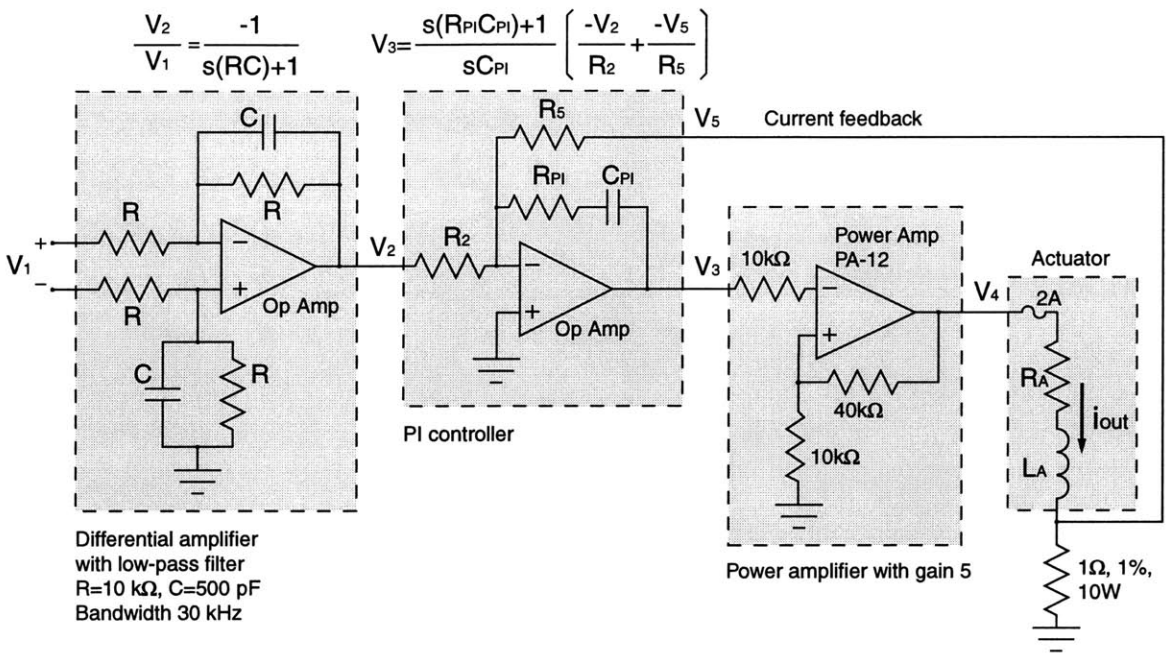

Figure 7-16: Current control circuit for Dipole-Quadrupole Actuators using power amplifier and PI controller.

7.5.1 Power Amplifier Circuit Design for Dipole-Quadrupole Actuators

The current control board for the Dipole-Quadrupole actuator is shown in Figure 7-16. This circuit is modified from a circuit design that has been widely used in our lab [109]. The circuit consists of a PI analog controller, a low-pass filter, PA-12 power amplifier, the load, and a 1 Ω current sense resistor. The same current control circuit is used to drive the primary coils of sensors.

The PI controller parameters are determined to properly tune the loop transfer function. We first model the actuator by a resistor R_A and an inductor L_A. From open-loop testing, the dipole coil has $R_A = 40\ \Omega$ and $L_A = 0.4$ H, and each quadrupole coil has $R_A = 20\ \Omega$ and $L_A = 0.07$ H. The low-pass filter is chosen to have $R = 10$ kΩ and $C = 500$ pF, and the bandwidth is 30 kHz. We design the PI controller such that the controlled current has a bandwidth of 1000 rad/s with 90° phase margin. The

resulting controllers are

$$G_{PI} = 500\frac{s+100}{s} \qquad \text{for dipole coil,} \tag{7.43}$$

$$G_{PI} = 100\frac{s+100}{s} \qquad \text{for quadrupole coils.} \tag{7.44}$$

7.5.2 Power FET Circuit Design for Quad-U-Core Actuators

For Quad-U-Core actuators, we only need uni-directional currents, hence we use power FET drives to control the current since they are cheaper than power amplifiers. The current control circuit for the Quad-U-Core actuators is shown in Figure 7-17. This circuit is modified from a design that has been widely used in our lab [69, ?, 3], the original circuit designs are shown in Appendix I. In the following, I will explain the functions of this circuit design. I will focus on the modifications that I made particularly for this project, including the damping resistor and the 2nd order low-pass filter.

In Figure 7-17, I separate the circuit into 6 subsystems:

1. Actuator: This can be simply modeled by a resistor R_A and an inductor L_A. However, when we drive the current by using power FET, there is a 4 kHz resonance in the actuator current i_{ACT}, although the power FET current i_{FET} is well controlled. Hence we model the actuator by a resistor R_A, an inductor L_A, and a capacitor C_A. This augmented model successfully predicts the current oscillation. However, we did not figure out exactly what sources introduce such a large capacitance (about 10 nF by this model), they can be the capacitance within the turns of the coil, between the coil and the lamination core, and/or between the power FET drain and the heat sink.

2. Damping resistor: A resistor is added to the circuit to damp the RLC circuit resonance in the actuator.

3. Detachable 2nd order low-pass filter: When the sensor and actuator are located close to each other, the magnetic field from the actuator causes feedthrough in

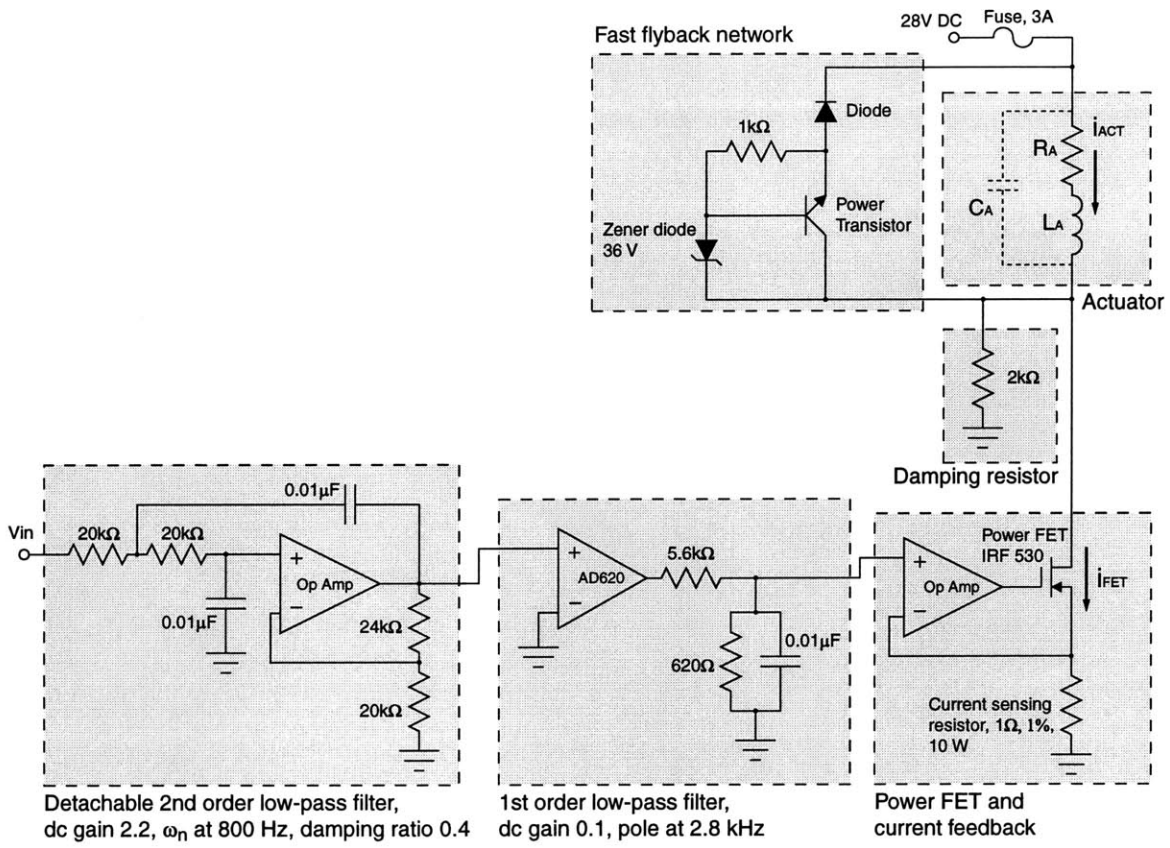

Figure 7-17: Current control circuit for Quad-U-Core actuators by using power FET.

the sensor outputs. By adding this 2nd order low-pass filter, we can reduce this feedthrough significantly. The tradeoff is that it causes extra phase lag to the actuator. To avoid this phase lag, the filter is usually removed when the sensors and actuators are not closely located.

4. 1st order low-pass filter: This part provides a low-pass filter to the current command. It is from the original design in Ludwick [69].

5. Power FET with current feedback: This is the key part of current control. Since we only need current in single direction, we chose power FET drives instead of power amplifiers since they are much cheaper.[5] The current feedback is sensed by the 1 Ω resistor. This feedback loop may need further modifications, since the local loop has a proportional gain of an order of 10^6 from the Op

[5]The power FET is about $1.00 each, and the PA-12 power amplifier is about $100.00 each.

Amp. Aggarwal [3] uses a lag compensator, and the circuit design is shown in Appendix I.

6. Fast fly-back network: It is from the original design in Olsen [86]. The purpose of fly-back circuit is to protect the circuit from excessive voltage when the system is suddenly turned off. However, a traditional diode-resistor fly-back circuit can lead to slow current negative slew rates and hence may reduce the actuator large-signal bandwidth. This design of the fast fly-back circuit can guarantee the current decrease at the rate of $di_{ACT}/dt = V_{Zener}/L_A$. In our design, we set V_{Zener} to about 37 V.

At the beginning, we modeled the actuator by a resistor (13 Ω) and an inductor (0.13 H). Hence we did not have the damping resister in the current control circuit. During suspension experiments, we put the sensors and actuators close to each other to avoid non-collocation problems. However, in this location, the magnetic field of the actuators causes significant feedthrough into the sensor outputs. As shown in Figure 7-18, when we apply a sinusoidal current command to the actuator using 10 ms steps, the current sensor (1 Ω resistor) voltage V_s shows nothing wrong. But the position sensor outputs become extremely noisy within ± 7 V while its operating range is ± 10 V.

To get a closer look, we measure the FET drain voltage V_d instead of source voltage V_s, and observe a lightly-damped resonance at 4 kHz as shown in Figure 7-19.

We successfully model this resonance by adding a capacitance of 10 nF into the actuator model as shown. The transfer function can be shown to be

$$\frac{i_{ACT}}{i_{FET}} = \frac{1}{(L_A C_A)s^2 + (R_A C_A)s + 1}. \tag{7.45}$$

The RLC circuit model has a resonance frequency of $1/\sqrt{L_A C_A}$. Hence we model the stray capacitance as about 10 nF, which is possibly due to the capacitance within the turns of the coil, between the coil and the lamination core, and/or between the power FET drain and the heat sink.

To avoid this resonance, we add a damping resistance R_d into the system, as shown

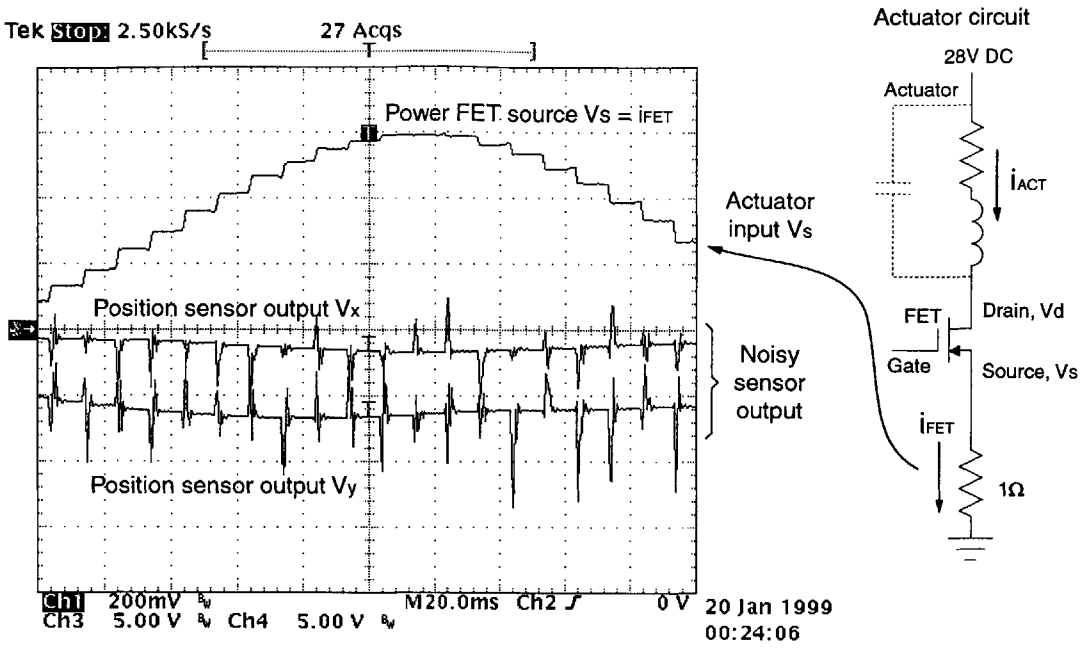

Figure 7-18: The steps on a computer-generated sinusoidal actuator current command (CH1) cause feedthrough into the position sensor outputs in both x and y (CH2 and CH3, respectively).

in Figure 7-17. With this addition, the system transfer function becomes

$$i_{ACT} = \frac{28}{R_A + R_d} + \frac{i_{FET}}{(L_A C_A)s^2 + (R_A C_A + \frac{L_A}{R_d})s + (1 + \frac{R_A}{R_d})}. \tag{7.46}$$

We choose $R_d = 2$ kΩ, such that the system has a bandwidth of 4.4 kHz with a damping ratio of 0.9. The disadvantage of using the damping resistor is that in steady state the actuator will have a bias current of 0.014 A, and the power dissipation from the damping resistor will be 0.4 W. This bias current may be eliminated by adding a series capacitor sufficiently big, such as a 10 μF, 200 V rating capacitor. For this project, we only use the damping resistor, and the damped output is shown in Figure 7-20. The actuator current no longer has the oscillation, and the sensor outputs are significantly improved.

After we solved the resonance in the actuator current, we still observe feedthrough in sensors that are caused by the actuator when the sensor and actuator are located next to each other. We then added an extra 2nd order low-pass filter to reduce

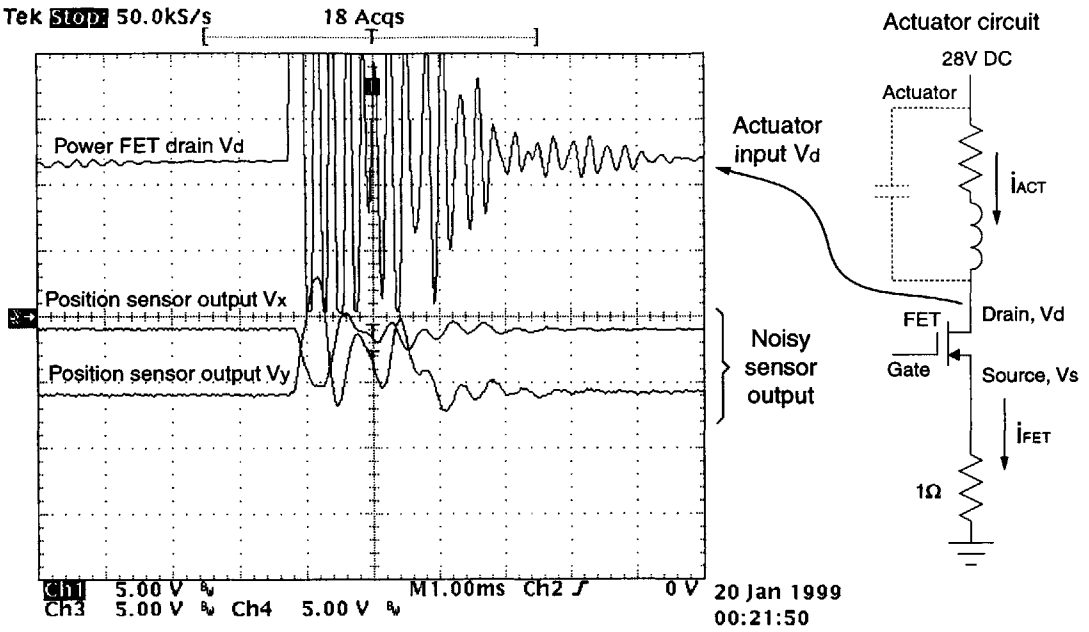

Figure 7-19: Resonance of actuator current causes feedthrough into position sensor outputs. The position sensors demodulate the feedthrough and result in noise with a different frequency from the actuator current oscillation.

this feedthrough. The reason is that we use inductive sensors by the principles of differential transformers. The sensor coils pick up the time derivative of the magnetic flux linkage $dN\phi/dt$, and the demodulation circuit cannot filter out the high frequency noise effectively. Therefore, a first-order filtered magnetic flux will still cause feedthrough in the sensor outputs. By adding this 2nd order low-pass filter, we reduced the feedthrough significantly. The tradeoff of adding this filter is that it causes extra phase lag to the actuator. The 2nd order low-pass filters are usually removed when sensors and actuators are not closely located.

In our final setup, we have:

1. Second order filter: $R = 20$ kΩ, $C = 0.01$ μF, $K = 2.2$, the low-pass filter has a dc gain of 2.2 and two poles at 800 Hz with a damping ratio of 0.4:

$$\frac{V_{out}}{V_{in}} = \frac{K}{(R^2C^2)s^2 + (3-K)RCs + 1} = \frac{2.2 \times 5000^2}{s^2 + 2 \times 0.4 \times 5000s + 5000^2}. \quad (7.47)$$

2. First order filter: $R_1 = 5.6$ kΩ, $R_2 = 620$ Ω, $C = 0.01$ μF, the low-pass filter

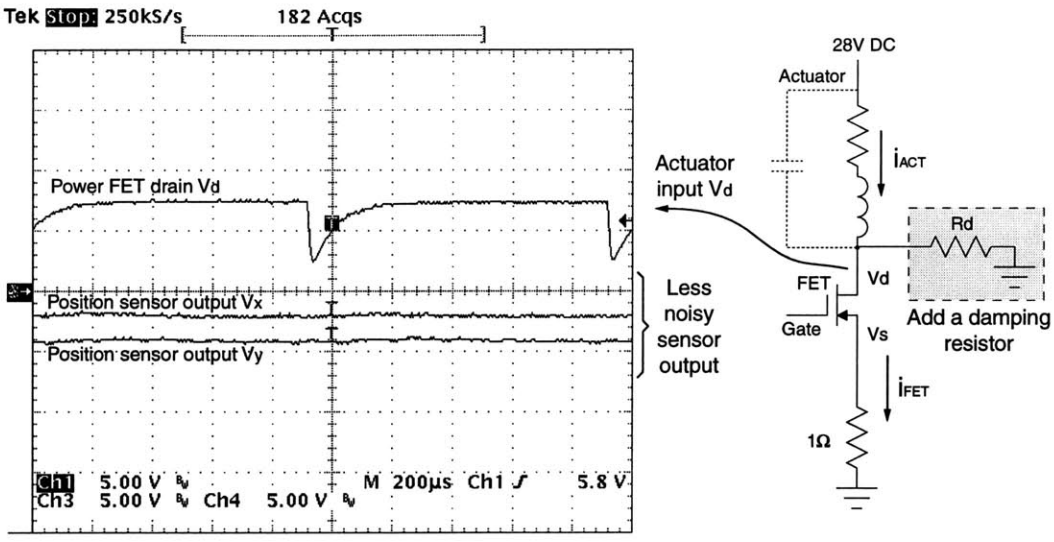

Figure 7-20: Actuator current is damped by the damping resistor R_d, and no longer cause feedthrough in the position sensors.

has a dc gain of 0.1 and a pole at 28 kHz:

$$\frac{V_{out}}{V_{in}} = \frac{R_2}{(R_1 R_2 C)s + (R_1 + R_2)} = \frac{0.1 \times 1.79 \times 10^5}{s + 1.79 \times 10^5}. \tag{7.48}$$

3. Damping resistor: $R_d = 2$ kΩ, the actuator has $R_A = 13\ \Omega$, $L_A = 0.13$ H, and $C_A = 10$ nF, the current command to current output has a dc gain of 1 and two poles at 4.4 kHz with a damping ratio of 0.9:

$$\begin{aligned} \frac{i_{ACT}}{i_{FET}} &= \frac{1}{(L_A C_A)s^2 + (R_A C_A + \frac{L_A}{R_d})s + (1 + \frac{R_A}{R_d})} \\ &= \frac{(2.8 \times 10^4)^2}{s^2 + 2 \times 0.9 \times 2.8 \times 10^4 s + (2.8 \times 10^4)^2}. \end{aligned} \tag{7.49}$$

We model the actuator dynamics by combining these transfer functions together. The eddy-currents in the actuator and target are ignored.

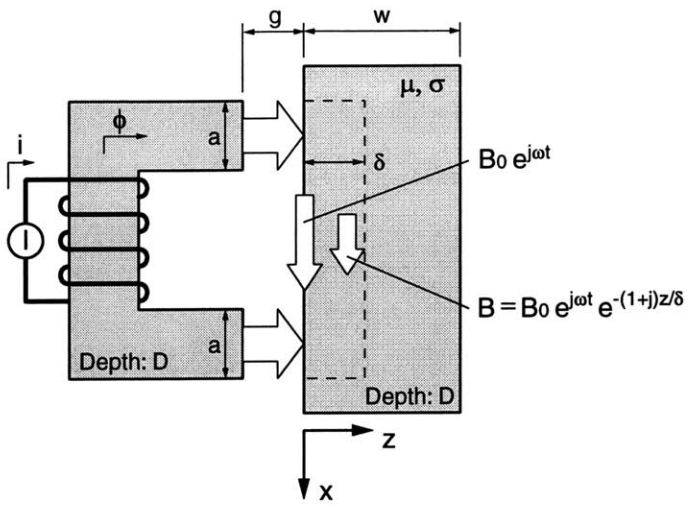

Figure 7-21: Model for computing the effects of magnetic diffusion in a conductive steel target. The model occupies a depth D into the paper

7.6 Eddy-Current Model

For magnetic bearings with small air gaps and a solid steel target, we need to consider the effects of eddy currents. The reason is because the reluctance of the air gap is small, and the eddy currents cause the reluctance of the suspended object to become significant relative to the gap reluctance. In the following, I solve the magnetic diffusion equations, and introduce a simplified magnetic circuit model including magnetic diffusion in a conductive target.

7.6.1 Magnetic Diffusion of Conductors

To include eddy-current effects, we start with the magnetic diffusion equation:

$$\nabla^2 \vec{B} = \mu\sigma \frac{\partial \vec{B}}{\partial t}. \tag{7.50}$$

A simple model of the magnetic circuit is shown in Figure 7-21. While applying an ac magnetic field $B = B_0 \cos\omega t = Re[B_0 e^{j\omega t}]$, the magnetic field diffuses into the material by a certain skin depth δ:

$$\delta = \sqrt{\frac{2}{\mu\sigma\omega}}. \tag{7.51}$$

The three variables here are permeability μ, conductivity σ, and the ac field frequency ω. The magnetic flux density inside the material is given by the solution of the one dimensional magnetic diffusion equation [111]

$$B = Re[B_0 e^{-z/\delta} e^{j(\omega t - z/\delta)}]. \tag{7.52}$$

We can integrate the magnetic flux density B through the material thickness W and multiply by D to obtain the total magnetic flux ϕ, assuming $\delta \ll W$:

$$\phi = \int_{z=0}^{W} BDdz = Re[B_0 e^{j\omega t} \frac{\delta D}{1+j}] = B_0 \delta D \frac{\sqrt{2}}{2} \cos(\omega t - 45^o), \tag{7.53}$$

where D is the width of magnetic flux path inside the target steel.

With the results from this 2-dimensional model in hand, we now move on to developing a model for our tube suspension. In our experimental setup, a 6.35 mm diameter tube is the steel target. We simplify the actuator by using a model as shown in Figure 7-22(a) and (b), which includes magnetic reluctance from the air gaps and the target steel. The air gaps are considered planar for simplicity. As shown in Figure 7-22(c), we have the magnetic circuit as:

$$Ni = \phi(\mathcal{R}_1 + \mathcal{R}_2 + \mathcal{R}_1), \tag{7.54}$$

where each component is given by

$$\phi\mathcal{R}_1 = H_1 g = \frac{\phi}{\mu_0 ab} g, \tag{7.55}$$

$$\phi\mathcal{R}_2 = H_2(c-a) = \frac{\phi(1+j)}{\mu D \delta}(c-a). \tag{7.56}$$

Here H_1 is the magnetic field intensity in the air gap, H_2 is the magnetic field intensity on the surface of the target steel, and ϕ is the total magnetic flux. Therefore we can rewrite the magnetic reluctance $\mathcal{R}$ for the magnetic circuit model as

$$\mathcal{R}_1 = \frac{g}{\mu_0 ab}, \tag{7.57}$$

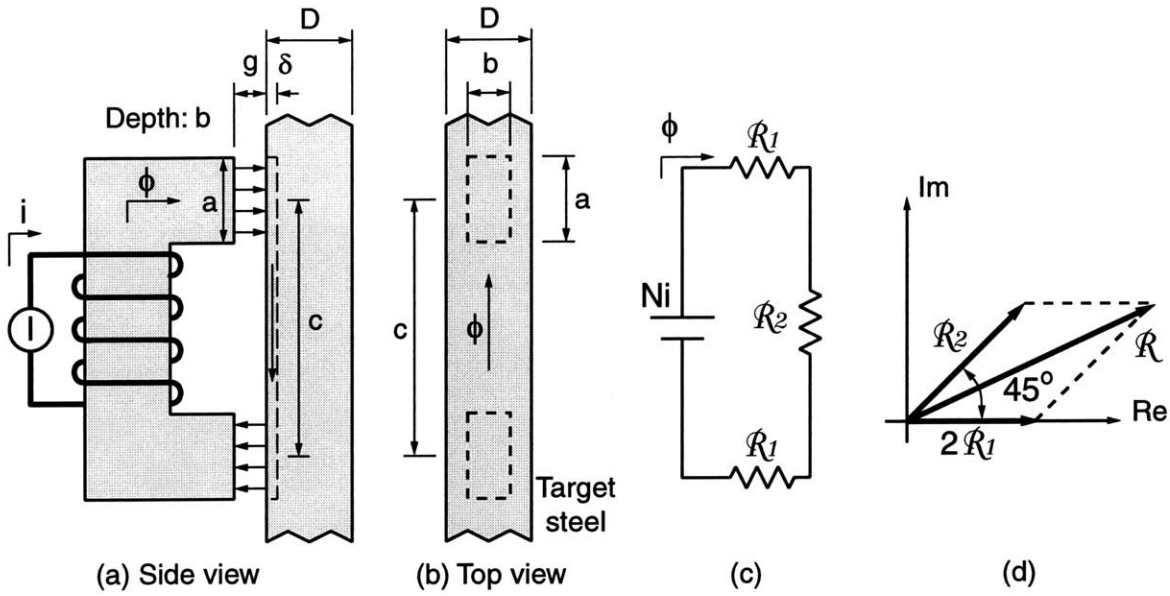

Figure 7-22: Actuator reluctance includes air gap reluctance and target steel reluctance with a 45° phase lag due to eddy-currents: (a) side view of the actuator model, (b) top view of the target steel, (c) magnetic circuit model, and (d) complex reluctance components.

$$\mathcal{R}_2 = \frac{(1+j)(c-a)}{\mu D \delta}, \quad \delta = \sqrt{\frac{2}{\mu\sigma\omega}} \ll W. \tag{7.58}$$

The combination of $\mathcal{R}_1$ and $\mathcal{R}_2$ is shown in Figure 7-22(d). This 45° phase lag matches qualitatively with results from the literature on magnetic bearings with small air gaps and a solid steel target [34].

To verify that we can ignore the eddy-currents for our experiment, we can compare the air reluctance and material reluctance over the bandwidth of the control loop, and thereby determine if eddy-currents are significant. The setup of our experiment has a required actuator bandwidth of close to 800 Hz, and the target steel has a skin depth of

$$\delta = \sqrt{\frac{2}{\mu\sigma\omega}} = \sqrt{\frac{2}{5000\mu_0 \cdot 7.5 \times 10^6 \cdot 1600\pi}} = 9 \times 10^{-5} \text{ m} = 0.09 \text{ mm} \tag{7.59}$$

at 800 Hz. Compared to the wall thickness of the tube $W = 0.9$ mm, the criteria of

$\delta \ll W$ is satisfied. Hence the resulting magnetic reluctance is:

$$2\mathcal{R}_1 = \frac{2g}{\mu_0 ab} = \frac{2 \cdot 3.2 \times 10^{-3}}{4\pi \times 10^{-7} \cdot 4 \times 10^{-5}} \approx 1.2 \times 10^8 \text{ [1/H]}, \tag{7.60}$$

$$\mathcal{R}_2 = \frac{(1+j)(c-a)}{\mu D \delta} = \frac{0.0254(1+j)}{5000\mu_0 \cdot 6.4 \times 10^{-3}\delta} \approx 1 \times 10^7 \text{ [1/H]}. \tag{7.61}$$

Since the reluctance from target steel is much smaller than that of air, we can conclude that the eddy-currents are negligible for our experiment.

7.6.2 Experiments on Eddy-Current Model

To further verify our eddy-current model, I did 2 simple experiments. In the first experiment, I use ferrite as the actuator core, and a solid steel slab as the target, with an air gap of 0.13 mm[6]. The air gap needs to be this small such that the air gap reluctance will be small relative to the reluctance from the target steel. In the second experiment, I replace the solid steel target by Silicon-iron laminations. The orientation of the laminations are designed to induce eddy currents, such that I can verify the eddy-current model[7]. Both experimental setups are shown in Figure 7-23, notice the laminations are oriented such that the large surface area is facing the actuator. The model is shown in Figure 7-24(a) and (b). We first calculate the reluctance from our eddy-current model, and then compare the results with the experimental results.

The calculation of reluctance is similar to that of the previous section, except that the target steel has a larger surface area. In order to integrate the surface and calculate the reluctance, I assume the pole face has a radius of r as shown in Figure 7-24(b). The reluctance of the target steel between two pole faces becomes:

$$\phi\mathcal{R}_2 = \int_{x_1}^{x_2} H dx = \frac{1}{\mu}\int_r^{c-r} \left(\frac{\phi(1+j)}{2\pi x \delta} + \frac{\phi(1+j)}{2\pi(c-x)\delta} \right) dx$$

[6] 0.13mm is the thickness of a piece of paper.

[7] In magnetic bearings, if laminations are used as targets, they will be oriented to avoid eddy currents. Here I am doing the opposite for experimental purposes.

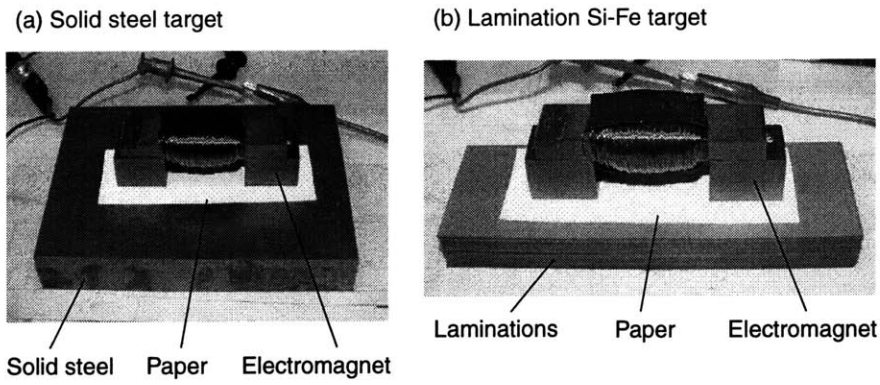

Figure 7-23: Experiments of testing target steel reluctance: (a) a solid steel slab as the target, and (b) Silicon-iron laminations as the target.

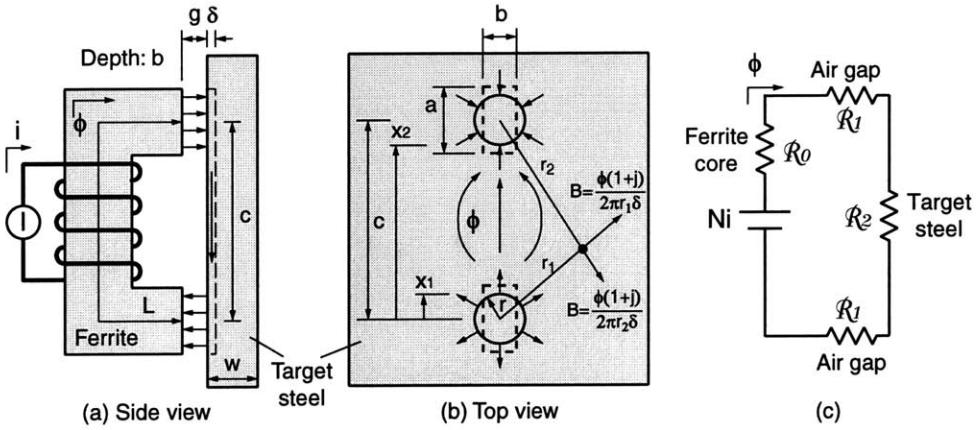

Figure 7-24: Actuator reluctance includes air gap reluctance and steel reluctance: (a) side view of the actuator model, (b) top view of the target steel, and (c) magnetic circuit model.

$$= \frac{\phi(1+j)}{\pi\mu\delta}\ln\frac{c-r}{r}, \tag{7.62}$$

where H is the magnetic field intensity on the surface of the target steel, and ϕ is the total magnetic flux. Therefore we can rewrite the magnetic reluctance $\mathcal{R}$ for magnetic circuit model by

$$\mathcal{R}_0 = \frac{L}{\mu_{\text{ferrite}}ab} = 1\times 10^5\ [1/\text{H}] \quad \text{for the ferrite core,} \tag{7.63}$$

$$\mathcal{R}_1 = \frac{g}{\mu_0 ab} = 4\times 10^5\ [1/\text{H}] \quad \text{for the air gap,} \tag{7.64}$$

$$\mathcal{R}_2 = \frac{1+j}{\pi\mu\delta}\ln\frac{c-r}{r} = 1.3\times 10^4(1+j)\sqrt{\omega}\ [1/\text{H}], \quad \text{for the steel target} \tag{7.65}$$

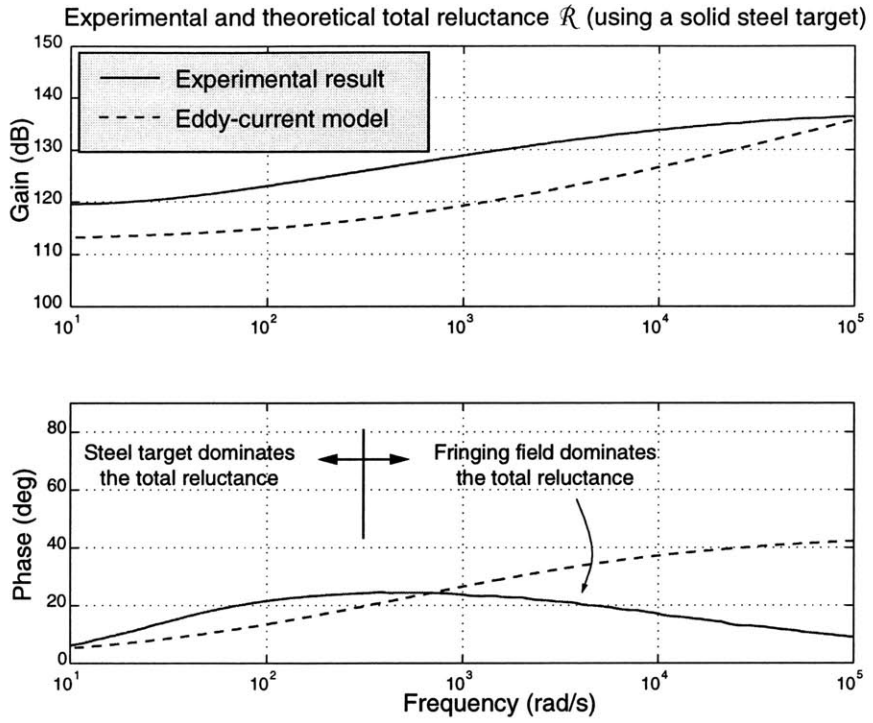

Figure 7-25: Experimental Bode Plots of total reluctance $\mathcal{R}$ by using a solid steel target, the effects of eddy-currents cannot be clearly observed due to the fringing field.

$$= 3 \times 10^3(1+j)\sqrt{\omega}\ [1/\mathrm{H}], \quad \text{for the Si-Fe target.} \quad (7.66)$$

, where $\delta = \sqrt{2/(\mu\sigma\omega)} \ll W$.

In the experiments, we measure the voltage V and the current i of the electric circuit. From the relation $V = i(R + j\omega L_i)$, since the circuit resistance R is given, we can thus calculate the system inductance L_i. From the relations $L_i i = N\phi$ and $\mathcal{R} = Ni/\phi$, the resulting reluctance can be calculated by $\mathcal{R} = N^2/L_i$, where $N = 500$ is the turns of the coil.

The first experimental result of using a solid steel target is shown in Figure 7-25. it shows the measured total reluctance as a function of the frequency compared with theoretical calculation. The reluctance does increase with frequency as we expect it. However, we find that the 45° phase shift is not very obvious at high frequencies, which we believe is due to the effects of the fringing field.

As shown in Figure 7-26, the fringing field of the actuator does not contribute to

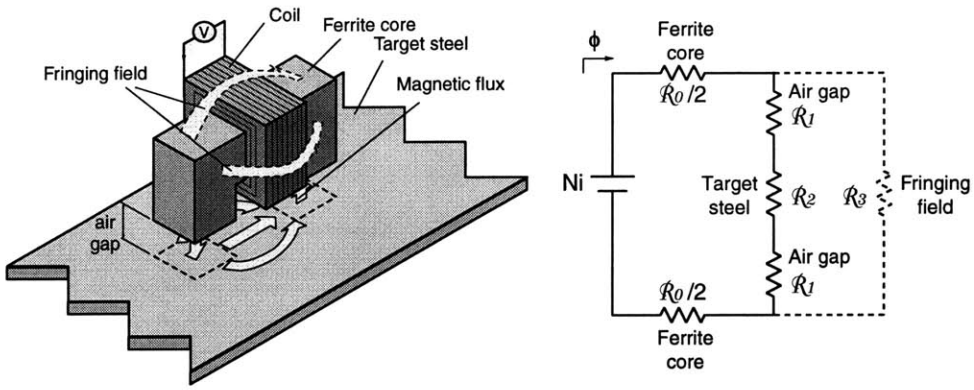

Figure 7-26: Modeling of the fringing field reluctance.

the actuator force output. However, in our experiment, we are measuring the voltage-current relation, and the fringing field contributes to the total reluctance, and affect our measurement. The fringing field can be modeled as a reluctance parallel to the air gap and target steel. By this model, we can explain the behavior of Figure 7-25 at high frequencies when the fringing field starts to dominate the total reluctance.

The second experiment uses Si-Fe laminations as the target, and the measured total reluctance is shown in Figure 7-27 compared with theoretical calculation. Since the Si-Fe laminations have lower reluctance, the parallel fringing field reluctance has less effects on our measurement, and we observe a clear 45° phase shift.

Overall, these experimental results are not completely satisfying, since we have the fringing field affecting our results, and we cannot clearly show how well this eddy-current model predicts the magnetic flux going through the air gap. A better experiment will be by measuring the magnetic flux through the air gap, or by measuring the forces applied to the target steel, hence we can avoid the fringing field from affecting the experimental results.

7.7 Summary

In this chapter, I show the conceptual designs, magnetic field analyses, force estimation, and circuit designs or our developed Dipole-Quadrupole actuator and Quad-U-Core actuator. The Dipole-Quadrupole actuator has a linear current-force relation,

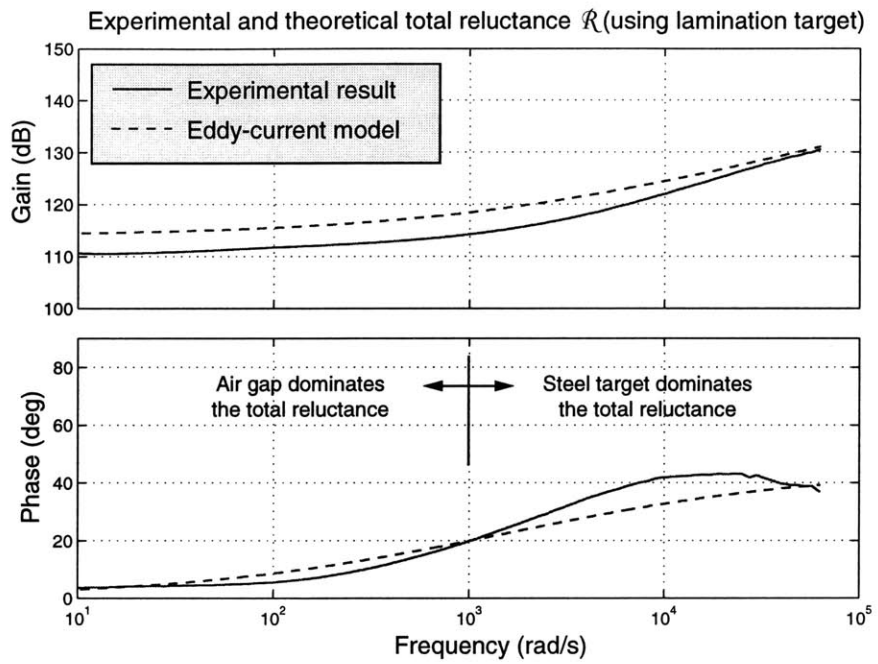

Figure 7-27: Experimental Bode Plots of total reluctance $\mathcal{R}$ by using a Si-Fe lamination target, the 45° phase change shows the effects of eddy-currents.

it also produces less axial magnetic field that can interfere with the sensor. It has the potential to be used for suspending thin tubes and strings. The Quad-U-Core actuator is easy to make, and functions as we predicted. At the end of this chapter, I further discuss the eddy-current model for actuators with small air gaps and solid steel targets.

From our experience, both the magnetic saturation in the back iron and power dissipation in the coil limit the maximum forces of our actuators. The main reason is because the actuator operates at a large air gap, it hence produces a large amount of fringing field that saturates the back iron, and it also needs a large current input to provide a sufficient magnetic field through the air gap. Although the large air gap amplifies the difficulties in magnetic saturation and thermal limit, it helps on the problem of eddy currents. Since the air gap dominates the system total reluctance, the eddy currents inside the solid steel target are insignificant within our control bandwidth.

In this thesis, we control the actuator forces by controlling the current inputs. For fast-moving target steel, the eddy currents inside the steel target can be significant,

and the current-force relation will vary with the moving speed. If the moving speed is unknown, a possible solution to control the force may be by the feedback of the magnetic flux at the air gap, since the flux-force relation is not affected by the moving speed. This topic will need further study in the future.

Chapter 8

Non-contact Sensor Design for Tubular Beams

In our experiment of tubular beam suspension, we need to use non-contact position sensors to feedback the tube positions in the two lateral dimensions. The sensors need to be robust to environmental contamination such as dust or paint for various manufacturing processes. They also need to have large air gaps, for the same reason as actuators, to allow workpiece vibration, heat insulation, and to leave room for coatings and other processes on the workpiece. Furthermore, it is desirable that sensors are compact in the axial direction, and can be placed close to the actuators to avoid possible sensor/actuator non-collocation problems.

In this project, we developed a 2-dimensional inductive position sensor to meet these criteria, as shown in Figure 8-1. This sensor was designed and built by Robert J. Ritter in our lab for his Master's thesis [93]. The mapping of the sensor outputs V_x and V_y as a nonlinear function of x and y position of the tube is shown in Figure 8-2.

I encountered various problems with using these sensors for the magnetic suspension of tubular beams, including feedthrough from the actuators and cross-coupling from other sensors. In this chapter, I summarize the operating principles of the sensor design. I also discuss the modifications that I make to solve these problems.

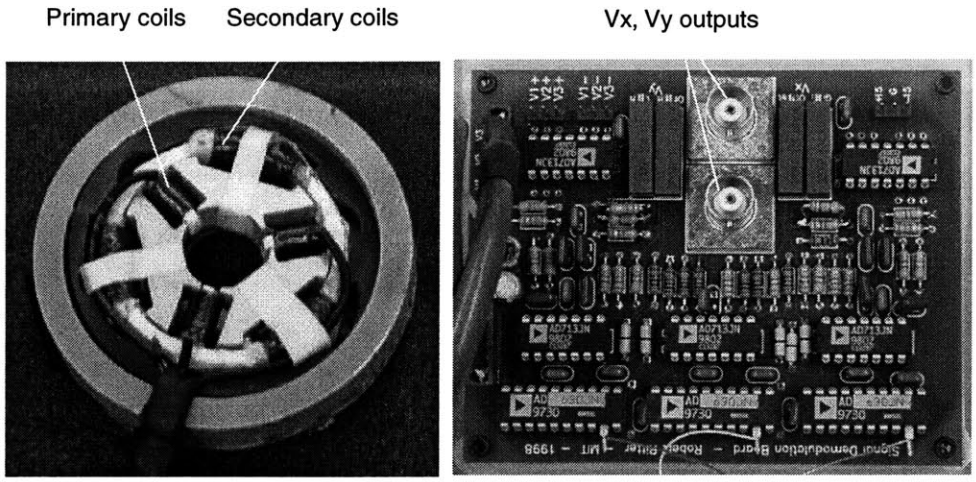

Figure 8-1: Two-dimensional position sensor for tubular beam suspension.

Table 8.1: Choices of different non-contact position sensors.

Sensor	Working Materials	Sensitive environment	Advantage
Optic	non-transparent	dust	linear
Capacitive	conductive	humidity, dust	accurate
Inductive	magnetic or conductive	-	large range
Eddy current	conductive	-	-
Hall effect	magnetic or conductive	-	-
Interferometer	mirror surface	dust, air density	accurate

8.1 Introduction to Sensor Design

For magnetic suspension of tubular structures, we can use several different types of non-contact position sensors. The comparison of different sensors are summarized in Table 8.1, the details of the comparison can be found in Sinha [97] and Usher [103].

We choose to design inductive sensors because of the following advantages:

1. It is more robust to environmental contamination such as dust or paint than capacitive or optic sensors.

2. It works for magnetic or conductive materials, and hence is compatible with magnetic suspension processes.

3. The size of the sensors can be compact in axial direction, and can be placed close

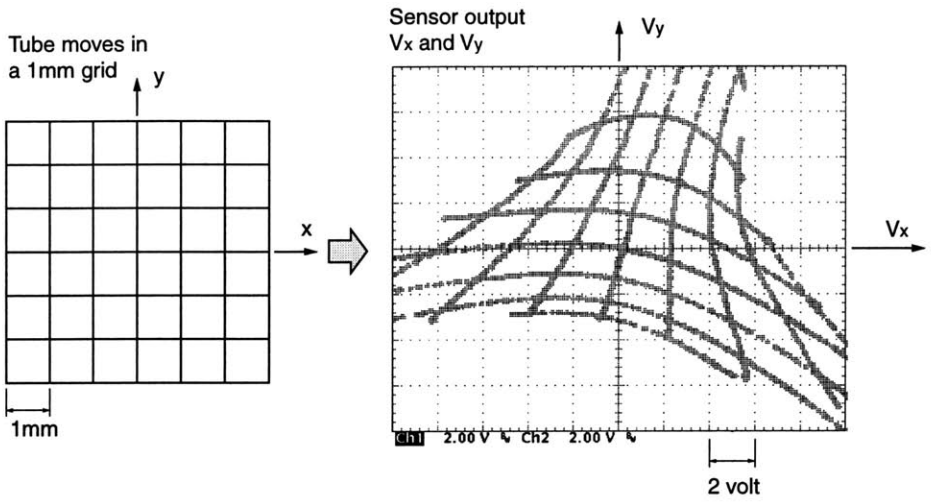

Figure 8-2: Two-dimensional position sensor output when tube is moving in a 1 mm grid in x and y.

to the actuators to avoid possible sensor/actuator non-collocation problems.

8.1.1 One-Dimensional Sensor

We designed the sensor in a similar principle to linear variable differential transformer (LVDT) [48]. Figure 8-3 illustrates the working principle of our one-dimensional sensor design. The primary coil is driven by a 6 kHz current source, the secondary coils read the time derivative of magnetic flux linkage: $V_1 = dN\phi_1/dt$ and $V_2 = dN\phi_2/dt$. By reading the amplitude of $V_1 - V_2$ by using synchronous detection, we can determine the horizontal position of the tube.

Two types of one-dimensional sensors are developed in this research. The simple E-core sensor shown in Figure 8-4(a) is designed to sense horizontal positions of tubes, but the output greatly depends on the vertical positions too. The modified E-core sensor shown in Figure 8-4(b) is designed to sense horizontal positions of tubes, and to avoid the dependence of vertical positions. Both of these sensors were built by Robert J. Ritter in his Master's thesis. The cores of the sensors are made of ferrite[1], which is ferromagnetic and non-conductive. Since ferrite is not appreciably conductive, it doesn't have a problem of phase lag due to magnetic diffusion, and is a good choice

[1]Soft ferrite was ordered from Eastern Components, Inc., (800)642-0518.

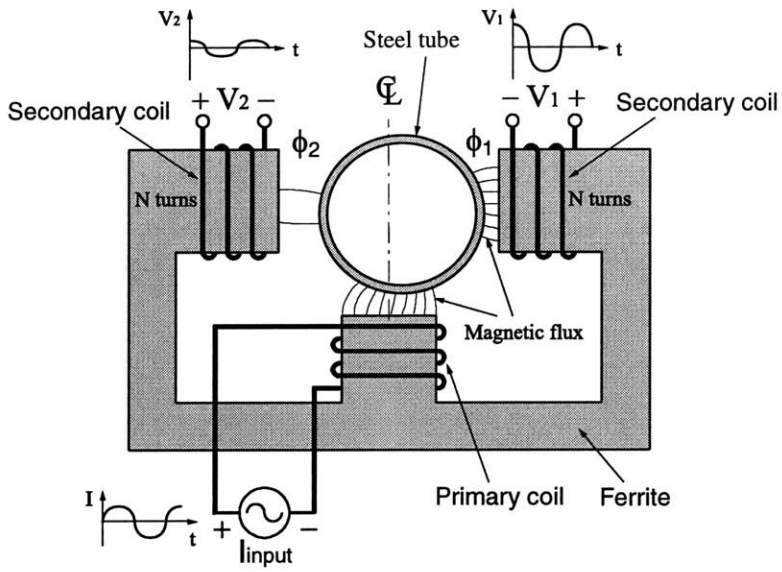

Figure 8-3: One-dimensional differential transformer position sensor.

for sensors that need high bandwidth. However, ferrite has a smaller permeability ($\mu \approx 2700\mu_o$) than silicon iron, and is difficult to machine.

This sensor design works for both ferromagnetic and conductive materials in the target. However, these two types of materials act with opposite effects. Ferromagnetic materials such as steel attract the magnetic flux, and non-magnetic conductors such as aluminum or copper repel the varying magnetic flux. Hence the sensor outputs for these two types of materials will have opposite signs with respect to displacement of the target.

8.1.2 Two-Dimensional Sensor

We really need a sensor which is active in 2 degrees of freedom ($x + y$). The design of such a 2-dimensional position sensor is illustrated in Figure 8-5. The working principle is similar to the 1-dimensional position sensor. The 3 primary coils are driven by three 6 kHz current sources with a 120° phase difference. This creates a rotating magnetic field at 6 kHz rotation frequency. We use 3 secondary coils to determine the x and y position of the tube. The original electronics in Ritter [93] uses synchronous rectification to read the amplitudes of the 3 secondary coil voltages. In this thesis, I change it to synchronous detection, and will be discussed later in this

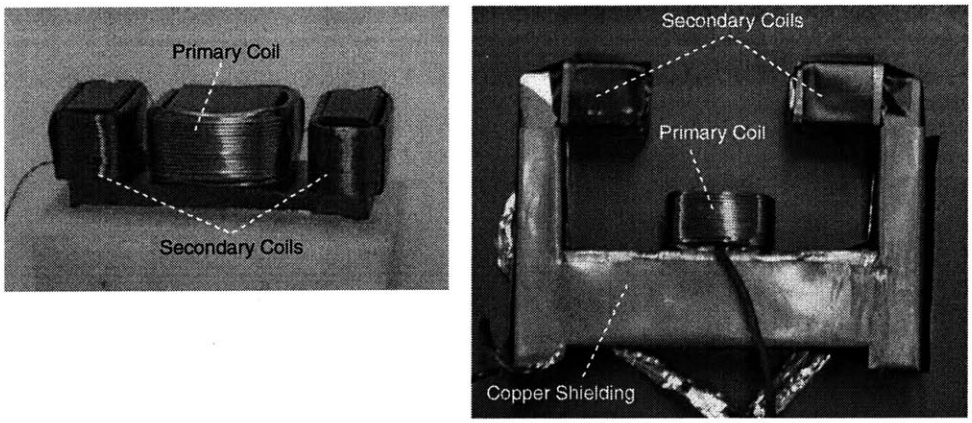

(a) (b)

Figure 8-4: One-dimensional position sensors for tubular beams: (a) a simple E-core sensor, and (b) a modified E-core sensor.

chapter. The sensor output is nonlinear to the real x and y position, and must be linearized in the software.

The core of this sensor is made of silicon iron laminations[2] with thickness of 0.007 inch. Notice the skin depth of the 6 kHz magnetic field inside the laminations will be

$$\delta = \sqrt{\frac{2}{\mu\sigma\omega}} = \sqrt{\frac{2}{(70000\mu_o)(2.1\times 10^6)(6000\times 2\pi)}} \approx 0.0007 \text{ inch.} \tag{8.1}$$

Thus only 20% of the lamination thickness is being effectively used. Since the thickness of 0.007 inch is an industrial standard, we chose them because of the lower price. Also we choose laminated steel over ferrite because: (1) it is easier to machine, and (2) the eddy current will be negligible due to the large air gap.

8.2 Modifications of the Sensor Design

In this project, I encountered several problems while using the sensors for the magnetic suspension of tubular beams. The main problems are the feedthrough caused by actuators, and the cross-coupling caused by other sensors. I also make improvements including reducing the phase lag, linearizing sensor output, and stabilizing current

[2]Laminations were ordered from Thomas & Skinner Inc., Caldwell, NJ, (973)227-2784.

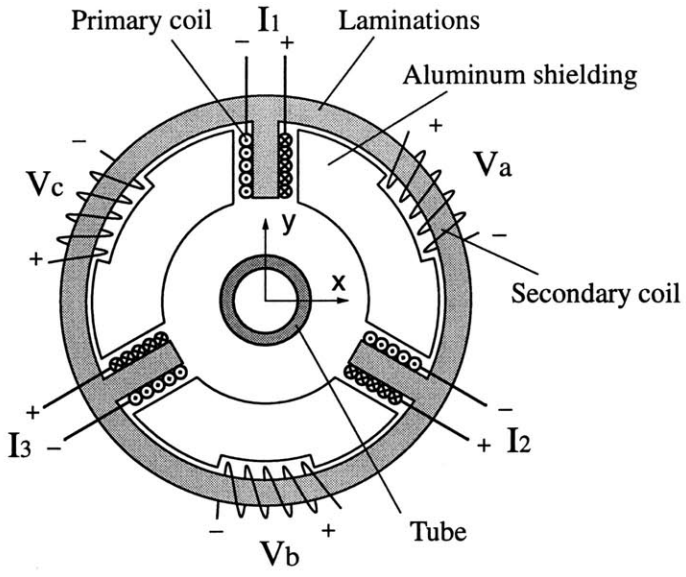

Figure 8-5: Two-dimensional differential transformer position sensor.

control loop. The original design and new modifications are illustrated in Figure 8-6. The modifications are described in the following sections.

8.3 Sensor Feedthrough Caused by Actuators

Placing the sensors close to the actuators may be desirable to avoid sensor/actuator non-collocation problems. However, the actuator generates magnetic fields that can cause feedthrough into the sensor output. We solved this problem by four steps: (1) change to synchronous detection, (2) adjust 50% duty cycle on reference signal, (3) add low-pass filters to actuator command, and (4) add magnetic shielding plates made of high-μ metal[3] outside the sensors to eliminate noise caused by the magnetic field coupling. The details are discussed in the following sections. After these efforts, the result is acceptable such that sensor and actuator can be placed right next to each other.

[3]Magnetic shielding metals were ordered from Daner-Hayes, Inc., 300 Eliot St., Ashland, MA 01712, 508-881-0400

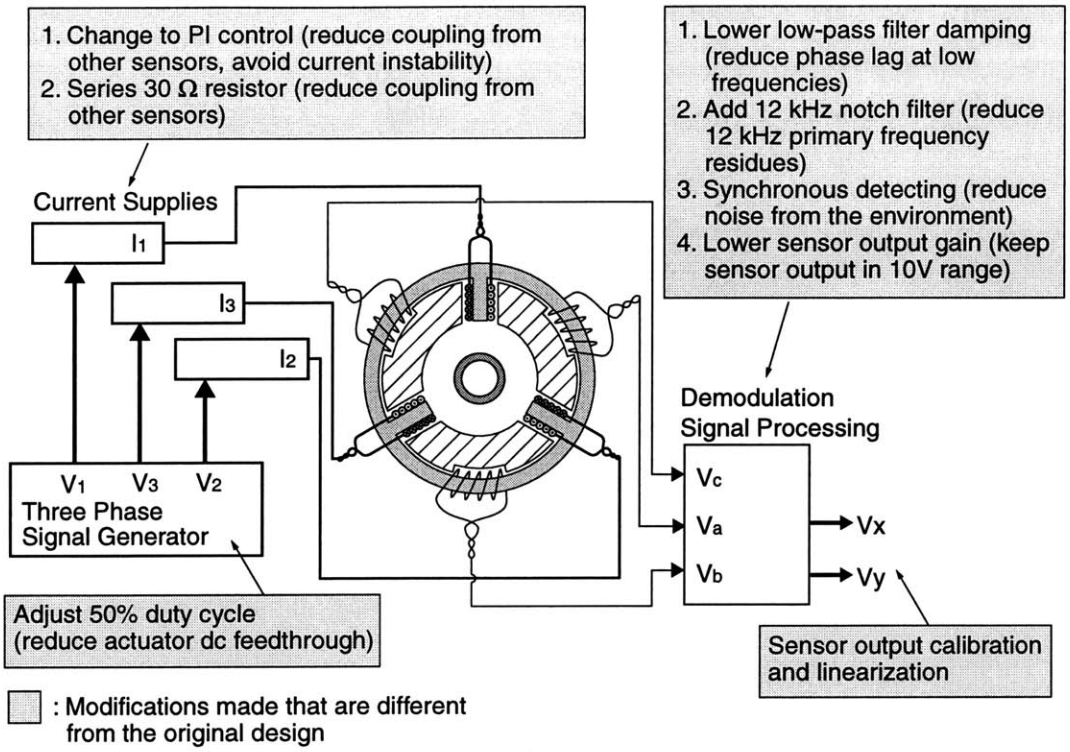

Figure 8-6: Sensor setup and modifications that are different from the original design.

8.3.1 Synchronous Detection

The first step to eliminate noise from the environment is to change the detection of sensor output from rectification to synchronous detection. The original design uses $|V| = V \cdot \mathrm{sgn}(V)$ to obtain the rectified signal. By using synchronous detection, we rectify the output by another reference signal, and we have $|V_a| = V_a \cdot \mathrm{sgn}(I_3)$, $|V_b| = V_b \cdot \mathrm{sgn}(I_1)$, and $|V_c| = V_c \cdot \mathrm{sgn}(I_2)$. By doing so, we should be able to filter out signals at other than the excitation frequency, which is 6 kHz. The circuit design is shown in Figure 8-7. Here the AD630 is an integrated circuit synchronous detector. The three phase currents I_1, I_2, and I_3 are used as the reference channels for V_b, V_c, and V_a, respectively. The output summing amplifiers yield the x and y voltages V_x and V_y, which will be low-pass filtered to get rid of the 12 kHz residual signal from synchronous detection.

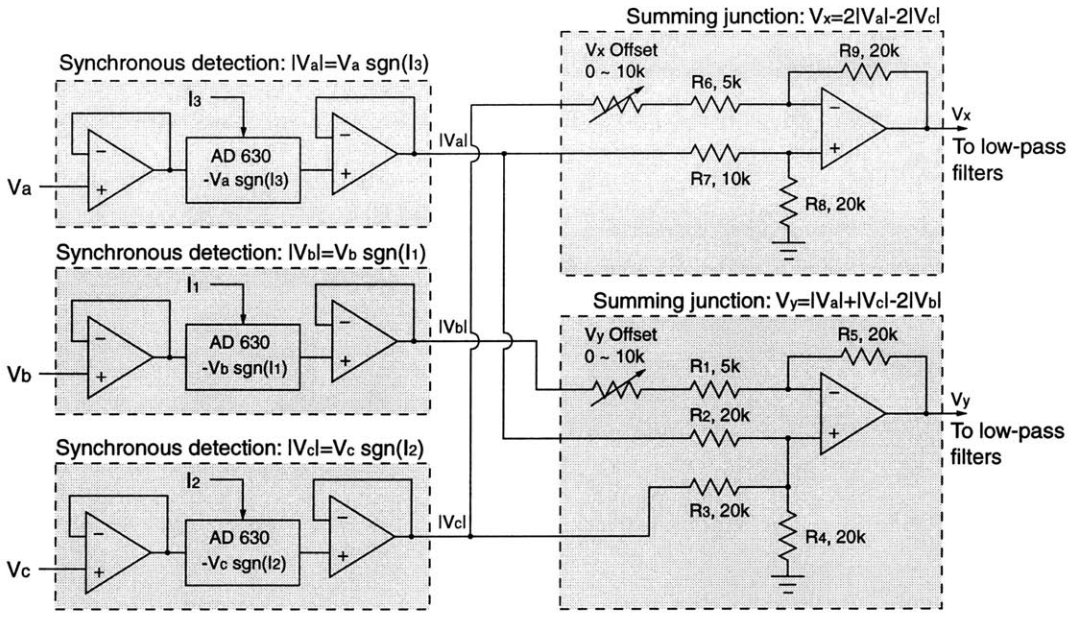

Figure 8-7: Synchronous detection on sensor outputs.

8.3.2 Sensor DC Feedthrough Caused by Actuator Current

Since we use synchronous detection to extract the 6 kHz component in the sensor output signal, any dc component in the signals V_a, V_b, and V_c should be filtered out. However, when we put sensors and actuators close together, the sensor picked up dc feedthrough from the actuator. This effect is shown in Figure 8-8. When the actuator has a linearly increasing current, the time derivative of the generated magnetic field $d\phi/dt$ is constant. This dc feedthrough should be filtered out by the synchronous detection. Although the sensor output V_y seems to work fine, the output V_x does not filter this dc component.

We figured out that it results from the 6 kHz signal generating circuit. As shown in Figure 8-9, the 6 kHz signal measured from one of the 1 Ω current sensing resistor has a duty-cycle of 53/47%. This explains why dc component was not filtered by synchronous detection.

Therefore I modified the signal generating circuit by adding a potentiometer to fine tune the signal level to obtain 50% duty cycle, as shown in Figure 8-10, After doing so, the dc feedthrough from actuators gets filtered, the results are greatly improved, as shown in Figure 8-11. There are still feedthrough due to ac magnetic flux, but the

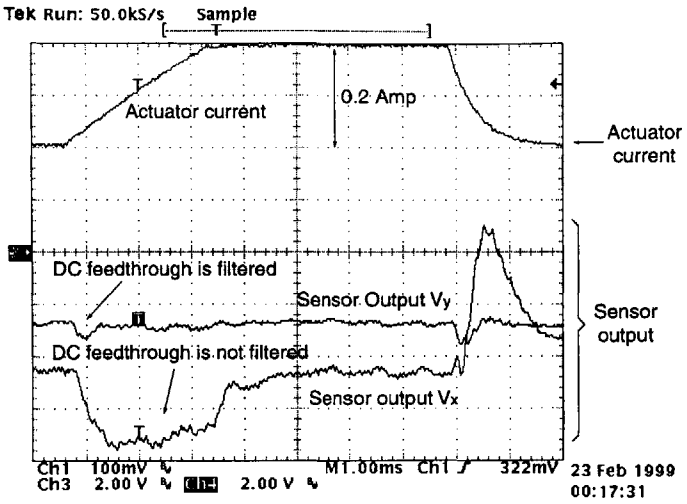

Figure 8-8: Sensor picks up dc feedthrough from the actuator: actuator has linearly increasing current, sensor output V_y is operating correctly, but V_x is not working properly.

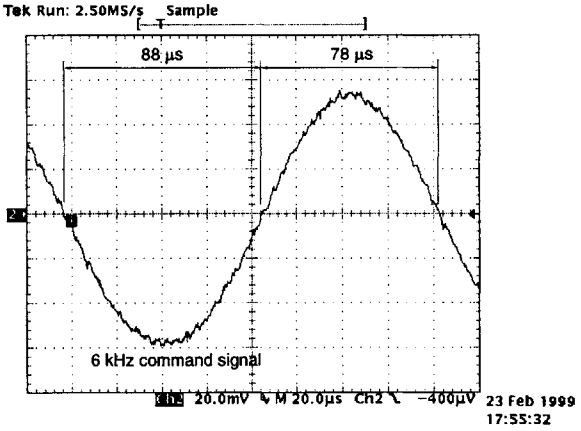

Figure 8-9: The measured 6 kHz input signal; it does not have 50% duty cycle.

dc component is effectively eliminated.

8.3.3 Sensor AC Feedthrough Caused by Actuator Current

To further reduce the feedthrough due to ac magnetic flux, I added a 2nd order low-pass filter to the actuator command. Since the sensors pick up the time derivative of the magnetic flux linkage $dN\phi/dt$, if the actuator has a step current input, the sensor will pick up the derivative of this step, which is a spike. A first-order low-pass filter added to the actuator command cannot avoid this feedthrough sufficiently. Hence I

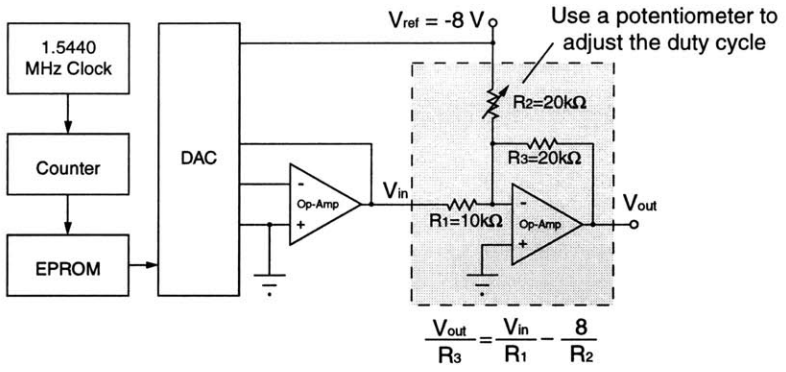

Figure 8-10: The 6 kHz signal generator, the potentiometer is added to adjust the duty cycle.

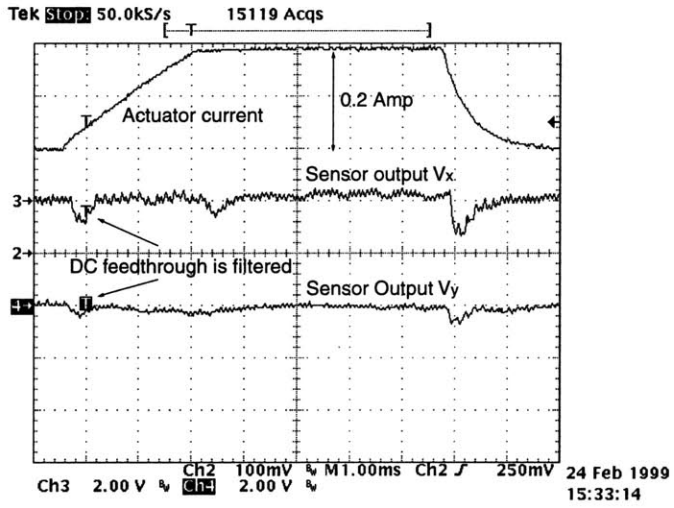

Figure 8-11: Sensor dc feedthrough caused by the actuator is filtered correctly by synchronous detection.

added a 2nd order low-pass filter to the actuator command. The details of this filter are presented in Chapter 7. The result is improved as shown in Figure 8-12.

8.4 Sensor Coupling From Other Sensors

While operating the sensor, a phenomenon is noticed that there is cross coupling between sensors. For example, if the tube moves at sensor No.1, the output of sensor No.2 will be affected too. We figured out that it is due to the change of the inductance. This is happening because we have the sensor primary coils in series, and use one current source to drive all 8 sensor coils.

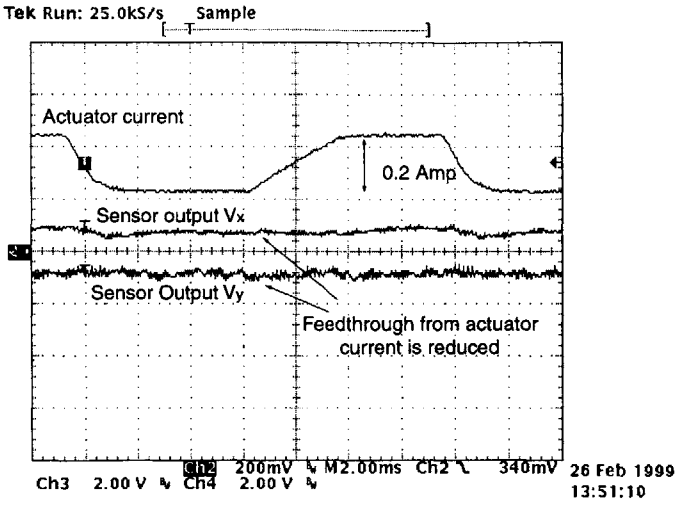

Figure 8-12: Sensor ac feedthrough caused from actuator current is reduced after actuator command is filtered by another 2nd order low-pass filter.

The model of the sensor primary coil and current control is shown in Figure 8-13. The 8 primary coils in series have a total resistance of $R_s = 2.72\ \Omega$ and a total inductance of $L_s = 304\ \mu$H. Together with the current sensing resistor of 1 Ω, the open-loop pole of this system is $(R_s + 1)/L_s \approx 2$ kHz. While tube moves toward one pole of one sensor, the inductance increases, and the gain and phase of current output change, which affects every single sensor. In the original design, we have a proportional gain of 400 for current control. This results in a bandwidth of 200 kHz, and a loop gain of 33 at 6 kHz. This gain level is insufficient to regulate the current at this frequency.

To solve this problem, we could use a current control board for each sensor, which means we will need 24 current control boards for all the 3 primary coils of 8 sensors. Another way is to improve the performance of the current control loop such that the change of the inductance will not affect the current output as much. We had 3 ideas for doing this:

1. We can increase the controller gain to improve the loop gain at 6 kHz. The disadvantage is that the closed-loop bandwidth is getting too high, and the current control loop can go unstable. Notice that the original bandwidth of 200 kHz is already too high, one of the current control board went unstable

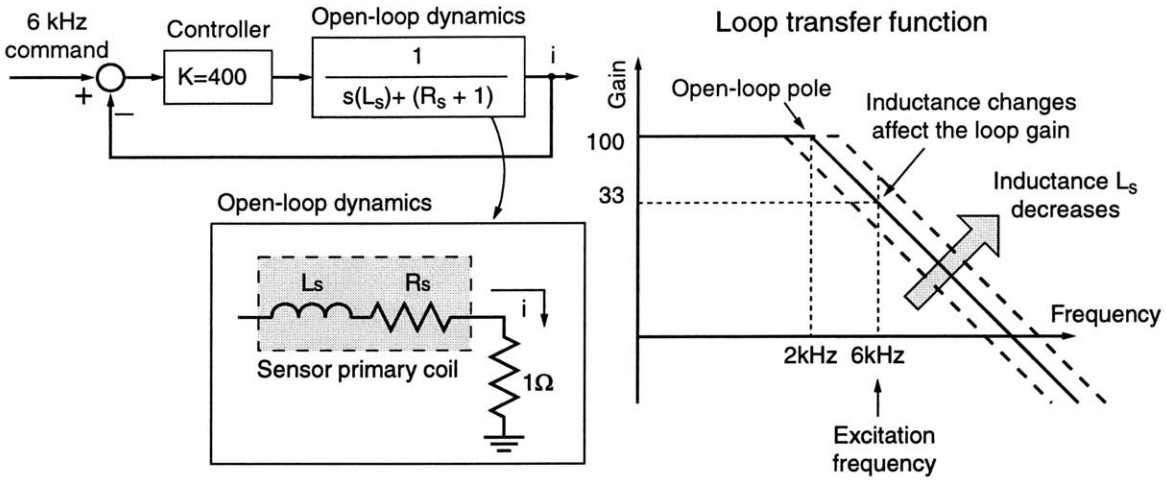

Figure 8-13: Sensor current control: the varying inductance can affect the loop gain at 6 kHz.

from time to time, especially when the chassis was touched by users and had an electrostatic discharge.

2. We can use a PI controller instead of a proportional controller, hence we can improve the loop gain at 6 kHz without increasing the closed-loop bandwidth.

3. We can use a 30 Ω resistor in series with the primary coils, which changes the open-loop dynamics, and moves the open-loop pole from 2 kHz to 18 kHz (higher than the excitation frequency at 6 kHz). By doing so, when the inductance changes, the open loop pole shifted around 18 kHz, but will not affect the loop gain at 6 kHz, as shown in Figure 8-14.

We solved the sensor-sensor coupling problem by using both (2) and (3). The final current control loop is shown in Figure 8-15. The final loop transfer function becomes:

$$\begin{aligned} L.T.(s) &= \frac{s(R_{PI}C_{PI})+1}{s(C_{PI})} \cdot 5 \cdot \frac{1}{s(L_s)+(R_s+31)} \cdot \frac{1}{R_5} \\ &= \frac{s(5\times 10^{6})+1}{s(2\times 10^{-11})} \cdot 5 \cdot \frac{1}{s(3.04\times 10^{-6})+(33.71)} \cdot \frac{1}{1\times 10^{4}}. \end{aligned} \tag{8.2}$$

This loop has a bandwidth of 70 kHz, and a loop gain of 19 at 6 kHz. The 30 Ω resistor makes the closed-loop current less sensitive to inductance changes. The PI controller

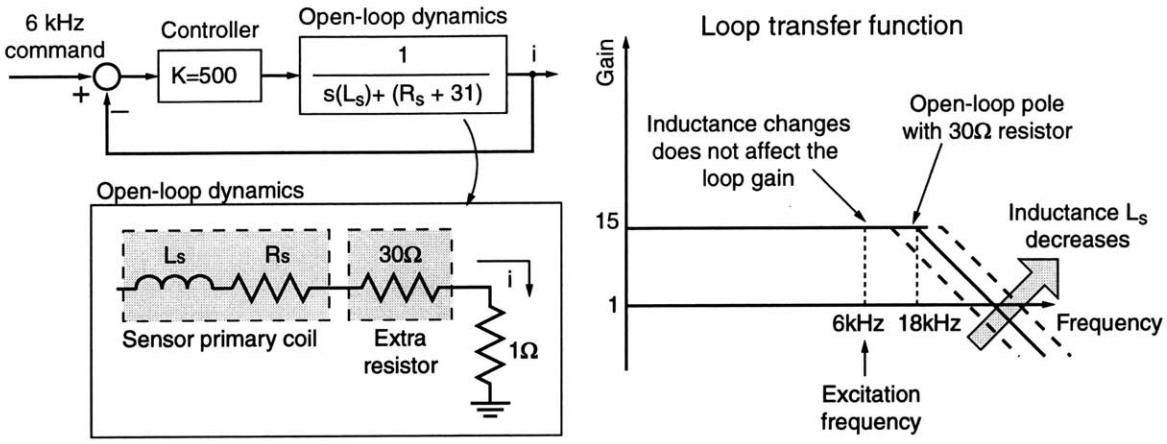

Figure 8-14: Sensor current control with 30 Ω resistor in series: the varying inductance will not significantly affect the loop gain at 6 kHz.

makes the loop gain high enough at 6 kHz without increasing the bandwidth. The loop gain at 6 kHz is lower than the original loop gain of 33, it means it has a larger steady-state error with respect to the command. However, when the inductance changes, the loop gain almost remains constant, hence the output is not varying with respect to the inductance changes. Since this approach reduced the closed-loop bandwidth from 200 kHz to 70 kHz, it also avoided the current control loop from going unstable randomly.

8.5 Reduce Phase Lag Due to Low-Pass Filters

In the original setup, we have the sensor output going through a 4th order Bessel low-pass filter with 1 kHz bandwidth [49]. This 4th order low-pass filter causes 30° phase loss at 1000 rad/sec. Actuator command has a 3rd order low-pass filter with 800 Hz bandwidth, which also causes 30° phase loss at 1000 rad/s. In addition to that, the digital control has a calculation time of $t_c = 220$ μs and a sampling time of $t_s = 250$ μs, the total time delay of $t_c + 0.5t_s$ causes 20° phase lag at 1000 rad/s. The total phase lag makes it extremely difficult to stabilize the system.

Therefore, we changed the low-pass filter to be lower damped, and added a notch filter at 12 kHz to filter the residue from synchronous detection. By doing so, we reduced the phase lag from 30° to 14° at 1000 rad/s. The new circuit diagram is

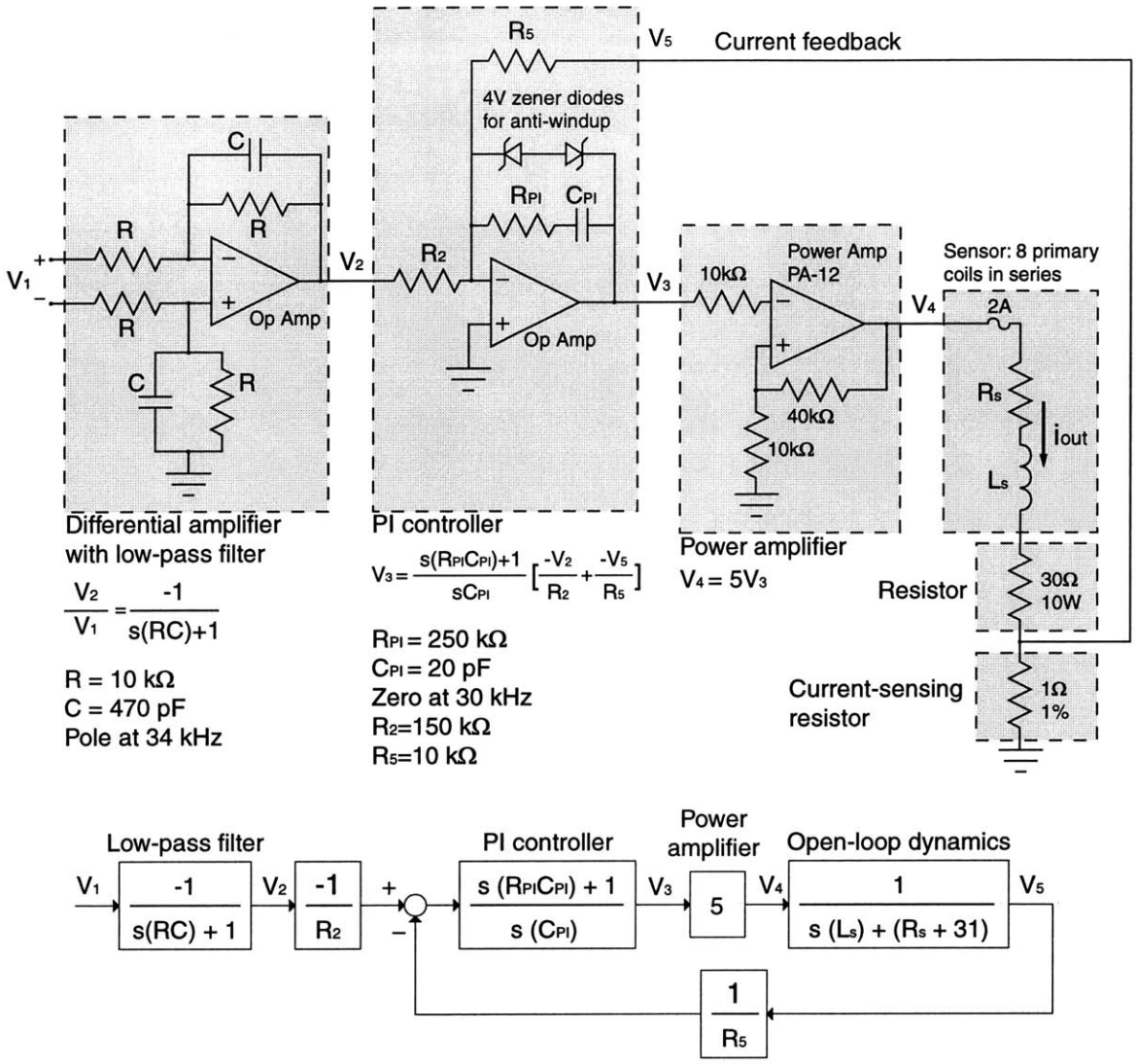

Figure 8-15: Sensor current control circuit and the corresponding block diagram.

shown in Figure 8-16. The transfer function of the 2nd order low-pass filter is:

$$\frac{V_{out}(s)}{V_{in}(s)} = \frac{K}{(R^2C^2)s^2 + (3-K)RCs + 1}. \tag{8.3}$$

The transfer function of the twin-T notch filter is:

$$\frac{V_{out}(s)}{V_{in}(s)} = \frac{R^2C^2s^2 + 1}{R^2C^2s^2 + 4RCs + 1}. \tag{8.4}$$

According to Horowitz [49, Chapter 5], in order to get a deep and stable notch, we use 1% metal film resistors and polypropylene capacitors, which have good accuracy

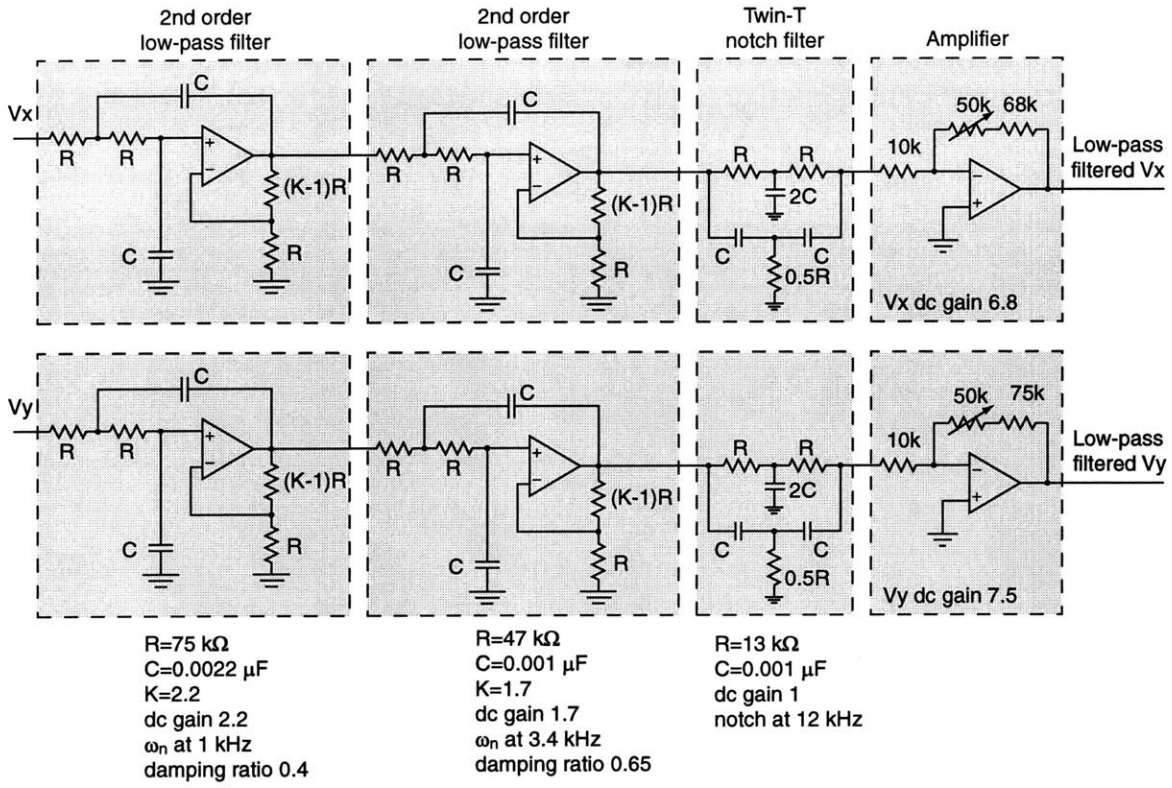

Figure 8-16: Sensor filters: low pass filters and twin-T notch filter.

and temperature stability.

8.6 Sensor Output Gain and Operating Range

The original setup of sensor output dc gain is 202 for V_x and 167 for V_y. I reduced it to 25 for V_x and 28 for V_y. The difference of dc gains between V_x and V_y is designed to have the following output:

$$V_x = 28 \cdot \sqrt{3}(|V_a| - |V_c|), \tag{8.5}$$

$$V_y = 28 \cdot (|V_a| + |V_c| - 2|V_b|). \tag{8.6}$$

The dc gain is greatly reduced from the original setup. The reason of having a dc gain of near 200 was due to originally following the wrong concept. Since sensor has very nonlinear output except near the center, we thought we could simply increase the dc gain, and only use the linear part of the sensor output. This is actually a

wrong idea. Increasing the gain does not make the system more linear, it only make the sensor output amplified, and in turn it becomes out of the ± 10 V operating range of the A/D converters, and makes the system difficult to stabilize.

8.7 Linearization of Sensor Output

To perform feedback control and feedback linearization on actuators, we need to know the positions of the tube. Since the sensor output is nonlinear, we must linearize it in the software. Hence we calibrate every sensor independently, and tried two different methods to linearize it: (1) a 2-D look-up table and (2) curve fitting. It turns out the curve fitting takes less computational time, therefore we use it to linearize the sensor output. The original sensor grids, curve fitting equations and resulting sensor outputs are given in Appendix J.

8.8 Summary

In this chapter, I briefly reviewed the designs of the non-contact position sensors. The original sensor design and field analysis can be found in Ritter [93]. I also described the modifications that I made in the circuit to solve the problems of feedthrough caused by actuators and coupling from other sensors. With these modifications, the sensors have functioned well enough to demonstrate the key experimental results of this thesis.

However, the sensors still have the following problems: At first, the nonlinear outputs of the sensor need to be improved, such as by using 4 poles to obtain a rectangular grid instead of a triangular grid. The effectiveness of linearization in software is limited. The inaccuracy of the sensor outputs are actually limiting the extension of testing model-based control methods. For example, we may need to use the information of the sensor outputs to reconstruct the vibration modal shapes. The accuracy we need for performing such task is beyond the sensors we use now. Secondly, each sensor is significantly different from each other. The calibration of

each sensor is time-consuming, which limits the possibility of mass production of such sensors. To make the sensors identical, all the parts must be made identical, such as lamination cores and coil winding.

Chapter 9

Model-Based Control Methods

Model-based control methods have been widely used in structural vibration control. This chapter reviews various model-based control methods for interested readers. Related references are listed in Chapter 2. In this chapter, I review $\mathcal{H}_2$ control, $\mathcal{H}_\infty$ control, μ analysis, and modal filter. These methods are model-based, and are not suitable for our system with varying boundary conditions. However, they do provide good performance for the closed-loop systems, and are being widely used for unvarying systems.

9.1 LQG Control ($\mathcal{H}_2$ control)

Linear Quadratic Gaussian (LQG) Control, also referred to as $\mathcal{H}_2$ control, consists of 2 parts: Linear Quadratic Regulator (LQR) and Kalman Filter. I will summarize the design method in the following subsections.

9.1.1 LQR

LQR assumes full state feedback. For a system of

$$\begin{aligned} \dot{x} &= Ax + Bu, \\ z &= Cx, \end{aligned}$$

where x is the system states, u is control input, and z is user-defined performance. LQR finds controller $u = -Fx$ to minimize the defined quadratic cost:

$$\begin{aligned} J &= \int_0^\infty [z(t)^T z(t) + u(t)^T R_{uu} u(t)] dt \\ &= \int_0^\infty [x(t)^T C^T C x(t) + u(t)^T R_{uu} u(t)] dt \\ &= \int_0^\infty [x(t)^T R_{xx} x(t) + u(t)^T R_{uu} u(t)] dt. \end{aligned} \tag{9.1}$$

Where we can tune the weighting matrix R_{uu} to reach desired performance. In general, when we put less weighting at R_{uu}, the system performance is better, but requires more control input. For example, in space structure control, we can put more weighting on the control input, and the generated controller can minimize the usage of fuel. The controller gain matrix F can be found by solving the Control Algebraic Riccati Equation:

Controller gain matrix:

$$F = R_{uu}^{-1} B^T S_c, \tag{9.2}$$

Control Algebraic Riccati Equation:

$$0 = S_c A + A^T S_c + R_{xx} - S_c B R_{uu}^{-1} B^T S_c, \tag{9.3}$$

which can be easily solved by using MATLAB.

9.1.2 Kalman Filter

Kalman Filter is an optimal observer, which minimizes the estimation error covariance in the presence of disturbance and sensor noise. For a system of

$$\dot{x} = Ax + Bu + L\xi, \tag{9.4}$$

$$y = Cx + M\theta, \tag{9.5}$$

where ξ is disturbance, y is sensor output, and θ is sensor noise. Disturbance ξ and sensor noise θ are both assumed to be zero-mean white Gaussian noise. They have

the following properties:

$$\text{Mean:} \quad E\{\xi(t)\} = 0, \tag{9.6}$$

$$\text{Correlation:} \quad E\{\xi(t)\xi'(t+\tau)\} = \Xi\delta(\tau), \tag{9.7}$$

$$\text{Mean:} \quad E\{\theta(t)\} = 0, \tag{9.8}$$

$$\text{Correlation:} \quad E\{\theta(t)\theta'(t+\tau)\} = \Theta\delta(\tau), \tag{9.9}$$

where Ξ and Θ are the intensity matrices of disturbance and sensor noise respectively. Observers use the system output y as feedback to estimate the system state by:

$$\dot{\hat{x}} = A\hat{x} + Bu + K(y - C\hat{x}), \tag{9.10}$$

where $\hat{x}$ is the estimated state. If we combine the system dynamics and the observer dynamics, we have:

$$\dot{\tilde{x}} = (A - KC)\tilde{x} + L\xi - KM\theta, \tag{9.11}$$

where $\tilde{x} = x - \hat{x}$ is the state estimate error. Kalman Filter finds the filter gain matrix K by minimizing the cost function:

$$J = E\left\{\sum_{i=1}^{n} \tilde{x}_i^2(t)\right\} = E\{\tilde{x}'(t)\tilde{x}(t)\} = tr[E\{\tilde{x}(t)\tilde{x}'(t)\}] = tr[\Sigma_{\tilde{x}}], \tag{9.12}$$

where $\Sigma_{\tilde{x}}$ is the covariance matrix of the state estimation error. The cost function J is the sum of the error variances of each state x_i. The filter gain matrix K can be found by solving the Filter Algebraic Riccati Equation, which is a dual of the Control Algebraic Riccati Equation:

Filter gain matrix:

$$K = S_o C^T R_{\theta\theta}^{-1}, \tag{9.13}$$

Filter Algebraic Riccati Equation:

$$0 = AS_o + S_o A^T + L\Xi L^T - S_o C^T (M\Theta M^T)^{-1} C S_o \tag{9.14}$$

$$\Rightarrow 0 = AS_o + S_oA^T + R_{\xi\xi} - S_oC^T R_{\theta\theta}^{-1} CS_o. \tag{9.15}$$

We can consider $R_{\xi\xi}$ and $R_{\theta\theta}$ as the weighting matrices, we can tune them based on the real disturbance and noise intensity, or we can tune them such that observer converges at required bandwidth. When we put less weighting at $R_{\theta\theta}$, the observer has higher bandwidth and converges faster, but becomes very sensitive to sensor noise.

9.1.3 LQG Control (LQR + Kalman Filter)

LQG control is simply putting LQR and Kalman Filter together. Here we represent LQG control in a more generalized form [4], including cross weighting matrices. The generalized form will make it easier to understand the similarities and differences between $\mathcal{H}_2$ control and $\mathcal{H}_\infty$ control.

System equations can be generalized as:

$$\text{System dynamics:} \quad \dot{x} = Ax + Bu + B_w w, \tag{9.16}$$

$$\text{Measurement:} \quad y = Cx + Du + D_w w, \tag{9.17}$$

$$\text{Performance:} \quad z = C_z x + D_z u, \tag{9.18}$$

where w is generalized disturbances, including disturbance ξ and sensor noise θ. Given the following assumptions:

1. $[A, B]$ and $[A, B_w]$ are controllable,

2. $[A, C]$ and $[A, C_z]$ are observable,

3. $R = \begin{bmatrix} C_z^T \\ D_z^T \end{bmatrix} \begin{bmatrix} C_z & D_z \end{bmatrix} = \begin{bmatrix} R_{xx} & R_{xu} \\ R_{xu}^T & R_{uu} \end{bmatrix} \geq 0; R_{uu} > 0,$

4. $V = \begin{bmatrix} B_w \\ D_w \end{bmatrix} \begin{bmatrix} B_w^T & D_w^T \end{bmatrix} = \begin{bmatrix} V_{xx} & V_{xy} \\ V_{xy}^T & V_{yy} \end{bmatrix} \geq 0; V_{yy} > 0,$

LQG control finds the controller by minimizing the $\mathcal{H}_2$ norm of the transfer function matrix $T_{wz}(s)$. The transfer function matrix $T_{wz}(s)$ represents the closed-loop

transfer functions from disturbance w to performance z. The $\mathcal{H}_2$ norm of $T_{wz}(s)$ is:

$$\begin{aligned} \|T_{wz}(s)\|_2 &= \left(\frac{1}{2\pi}\int_{-\infty}^{\infty} tr\left[T_{wz}(j\omega)T_{wz}^T(-j\omega)\right]d\omega\right)^{\frac{1}{2}} \\ &= \left(\frac{1}{2\pi}\int_{-\infty}^{\infty}\sum_{i=1}^{r}\sigma_i^2\left[T_{wz}(j\omega)\right]d\omega\right)^{\frac{1}{2}}, \end{aligned} \tag{9.19}$$

where σ_i is the ith singular value of T_{wz}. If the disturbance $w(t)$ is zero-mean white noise with identity intensity, then the $\mathcal{H}_2$ norm of $T_{wz}(s)$ represents the RMS of $z(t)$ in time domain:

$$\begin{aligned} \|T_{wz}(s)\|_2 &= \text{RMS of } z(t) = \sqrt{E\left\{\sum_{i=1}^{p} z_i^2(t)\right\}} \\ &= \sqrt{E\{z^T(t)z(t)\}} = \sqrt{tr[E\{z(t)z^T(t)\}]}. \end{aligned} \tag{9.20}$$

If we replace $z(t)$ by $z = C_z x + D_z u$, we have

$$\begin{aligned} \|T_{wz}(s)\|_2^2 &= E\{z^T(t)z(t)\} = \lim_{T\to\infty}\frac{1}{2T}\int_{-T}^{T}[z^T(t)z(t)]dt \\ &= \lim_{T\to\infty}\frac{1}{2T}\int_{-T}^{T}[x^T R_{xx}x + 2x^T R_{xu}u + u^T R_{uu}u]dt. \end{aligned} \tag{9.21}$$

LQG controller has the following structure:

$$\dot{\hat{x}} = (A - BF - KC + KDF)\hat{x} + Ky, \tag{9.22}$$

$$u = -F\hat{x}. \tag{9.23}$$

The controller gain F and filter gain K can be solved from the Algebraic Ricatti Equations:

Controller gain matrix:

$$F = R_{uu}^{-1}(R_{xu}^T + B^T S_c), \tag{9.24}$$

Control Algebraic Riccati Equation:

$$0 = S_c A_c + A_c^T S_c + R_{xx} - R_{xu}R_{uu}^{-1}R_{xu}^T - S_c B R_{uu}^{-1}B^T S_c, \tag{9.25}$$

with $A_c = A - BR_{uu}^{-1}R_{xu}^T$.

Filter gain matrix:

$$K = (S_o C^T + V_{xy})V_{yy}^{-1}, \tag{9.26}$$

Filter Algebraic Riccati Equation:

$$0 = A_o S_o + S_o A_o^T + V_{xx} - V_{xy}V_{yy}^{-1}V_{xy}^T - S_o C^T V_{yy}^{-1} C S_o, \tag{9.27}$$

with $A_o = A - V_{xy}V_{yy}^{-1}C$.

9.1.4 A Numerical Example of LQG Control on Beam Suspension

In this section, we use a single-input-single-output controller to demonstrate how the LQG controller works on the beam system. We neglect the cross-product penalties, by using the following MATLAB code, we can find the controller gain F and observer gain K:

```
% LQR
Rxx=C'*C;                       %state weighting
Ruu=0.01*eye(size(B,2));        %input weighting
[F,S,Ec]=lqr(A,B,Rxx,Ruu);

% Kalman Filter
Rww=B*B';                       %disturbance weighting
Rvv=0.001*eye(size(C,1));       %noise weighting
[K,P,Eo]=lqr(A',C',Rww,Rvv);
K=K';

% LQG compensator K(s): system_lqg
% loop transfer function: system_loop
A_lqg=A-B*F-K*C;
system_lqg=ss(A_lqg,K,F,zeros([size(F,1),size(K,2)]));
system_loop=series(system_beam,system_lqg);
```

Figure 9-1 shows the Bode plots of plant open-loop dynamics and the LQG controller dynamics. The plant open-loop dynamics includes dynamics of beam, sensor,

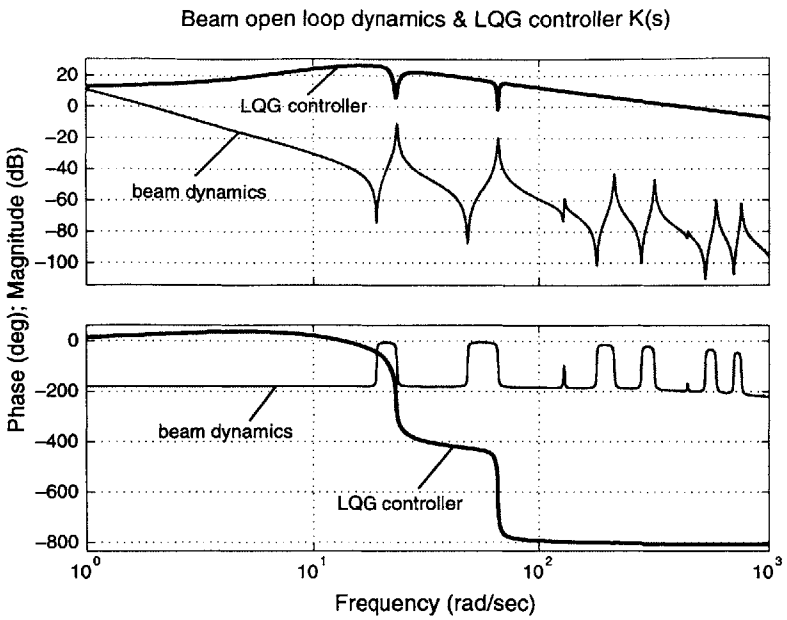

Figure 9-1: Bode plots of system open-loop dynamics and LQG controller, controller behaves as a lead compensator with notches at resonance frequencies.

actuator, and time delay. The beam dynamics is based on the beam of our experiment, where the sensor and actuator are both placed at $z = 40.5$ inches. It shows that the LQG controller is highly based on the system model, and works like a lead compensator with notch filters right at the resonance modes.

Figure 9-2 shows the associated Bode plots of the loop transfer function, and Figure 9-3 shows the Nyquist plot of the loop transfer function. It shows that LQG controller has good nominal performance, it has good phase margin and gain margin. However, we need to examine the robustness of this controller with respect to modeling errors.

Assuming the real beam has stiffness EI smaller than that of the model by 5%, and we use the previously calculated LQG controller to control the system. The Bode plots of the system open-loop dynamics and controller dynamics are shown in Figure 9-4. It shows the resonance frequencies are only slightly off the model.

The Bode plots and Nyquist plot of the resulting loop transfer function are shown in Figure 9-5 and Figure 9-6. In Nyquist plot, the loop transfer function encircles the -1 point, and shows that the closed-loop system will be unstable. This result

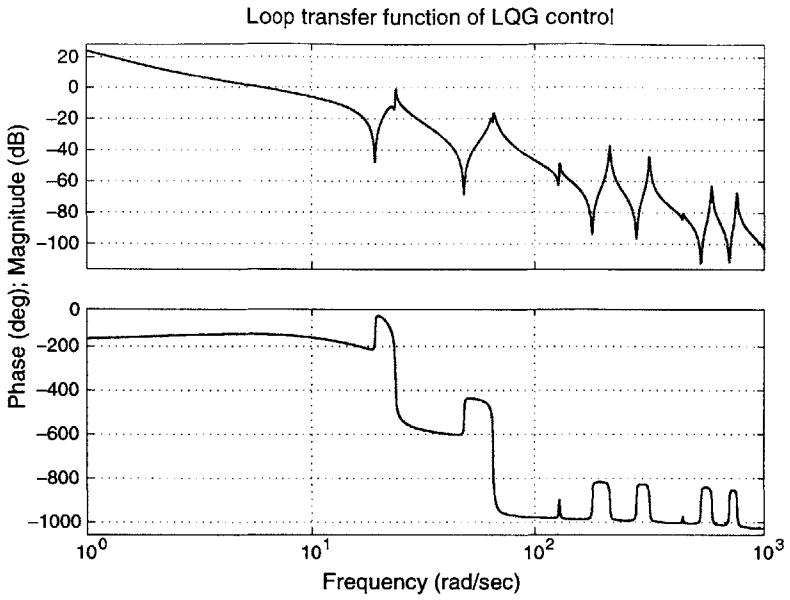

Figure 9-2: Bode plots of system loop transfer function, the resonance peaks are canceled by the controller notches.

shows that the controller has very poor stability-robustness with unmodeled errors, and a slight change of beam dynamics can make the system unstable.

LQG controllers can work on structural vibration control only when the systems are very well modeled. Stability-robustness of LQG control can be improved by adding weightings to the resonance frequencies. The weightings can make the controlled system less sensitive to parametric uncertainties. Sensitivity-Weighted LQG (SWLQG) is developed [27] for this purpose. An example of using SWLQG is shown in Appendix K. It shows that SWLQG makes the controller notches smoother. Hence by reducing the performance, it can improve the stability-robustness. However, the improvement is still limited to a small uncertainty. In our case, the controller is required to work under varying boundary conditions and tube positions, hence LQG or SWLQG control is not suitable for our design purpose.

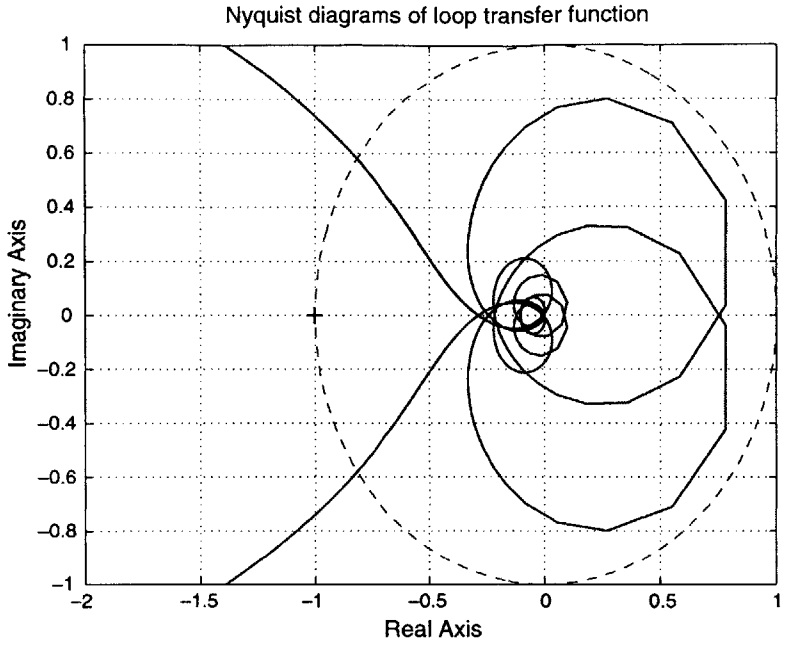

Figure 9-3: Nyquist plot of system loop transfer function, the system has good phase margin and gain margin.

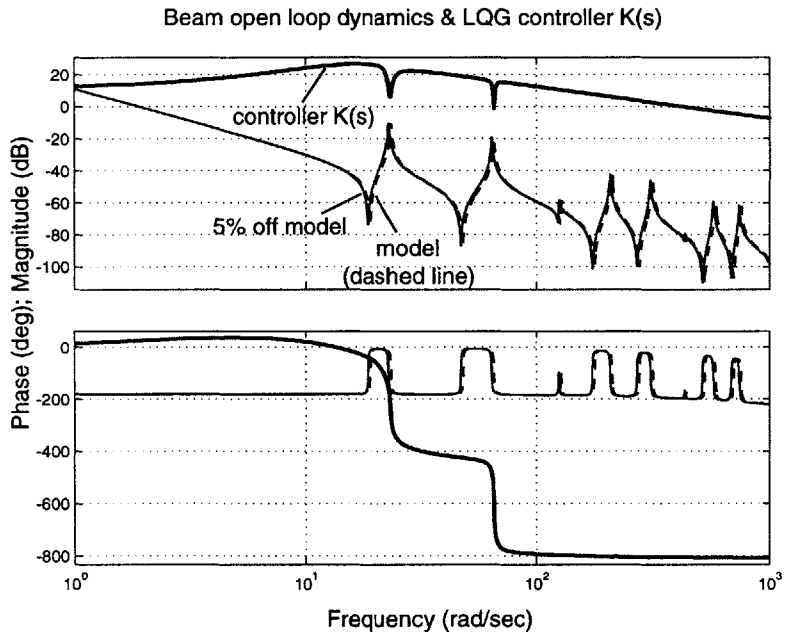

Figure 9-4: Bode plots of system open-loop dynamics and LQG controller, the controller is designed based on the model, and will be used on the 5% off model.

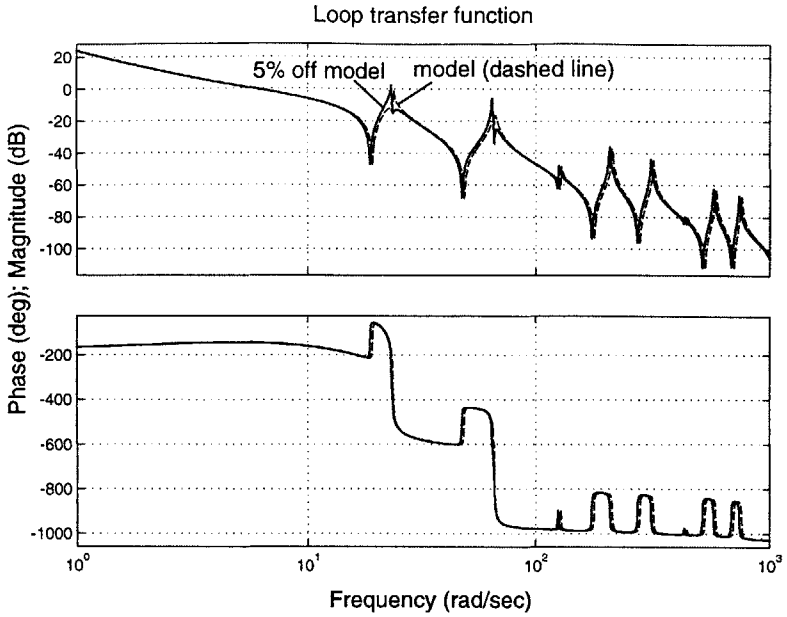

Figure 9-5: Bode plots of system loop transfer function, with 5% stiffness change, the resonance peaks cannot be exactly canceled by the controller notches.

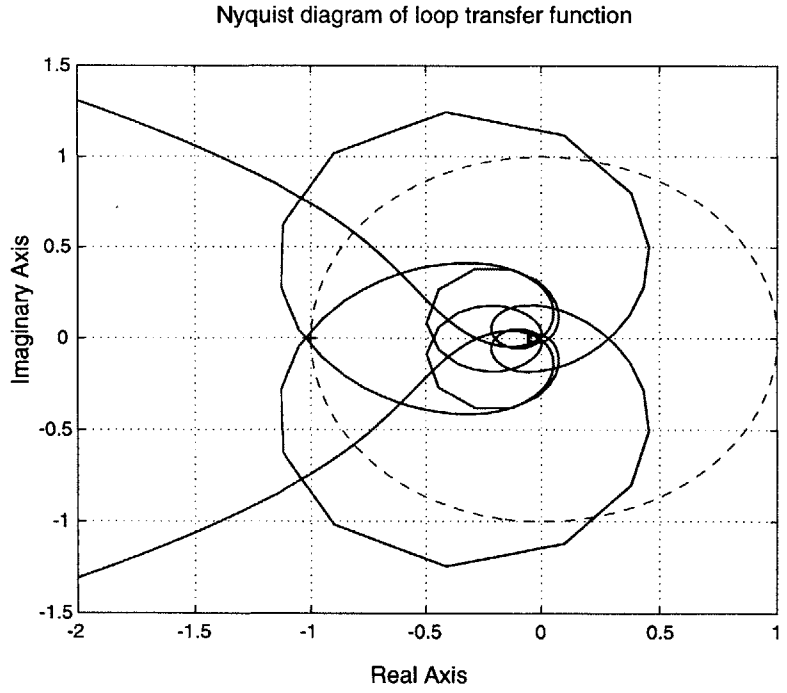

Figure 9-6: Nyquist plot of system loop transfer function, with 5% stiffness change, the closed-loop system is unstable.

9.2 $\mathcal{H}_\infty$ control

$\mathcal{H}_\infty$ control focuses on the maximum disturbances the closed-loop system can take. They are often used in the areas of buildings' vibration control in the presence of earthquakes, or airplanes' vibration control in the presence of wind gust.

In this section, we represent the $\mathcal{H}_\infty$ control by using the generalized system equations as in the previous section. $\mathcal{H}_\infty$ control finds the optimal controller to minimize the $\mathcal{H}_\infty$ norm of the transfer function matrix $T_{wz}(s)$:

$$\|T_{wz}(s)\|_\infty = \sup_\omega \overline{\sigma}[T_{wz}(j\omega)] < \gamma \tag{9.28}$$

$\mathcal{H}_\infty$ controller design is an iterative process to find γ_{min}. The control problem becomes a mini-max differential game to optimize the quadratic cost:

$$J = \inf_u \sup_w \int_{-\infty}^{\infty} [z^T z - \gamma^2 w^T w] dt \tag{9.29}$$

Notice that if $\gamma \to \infty$, it becomes the same as LQG control.

If we describe modeling uncertainty as disturbance w, we are able to use $\mathcal{H}_\infty$ control with the presence of modeling uncertainty. To do so, we have to further introduce the small gain theorem and μ analysis to combine with $\mathcal{H}_\infty$ control.

9.3 Small Gain Theorem and μ Analysis

Small gain theorem and μ analysis are tools to analyze the system stability with the presence of uncertainties. μ analysis is also called the generalized small gain theorem, and is less conservative than small gain theorem. When we combine μ analysis and $\mathcal{H}_\infty$ to design controllers by iteration, it is called μ synthesis. We will use a simple example by using small gain theorem and μ analysis, and show that they are too conservative for structural vibration control.

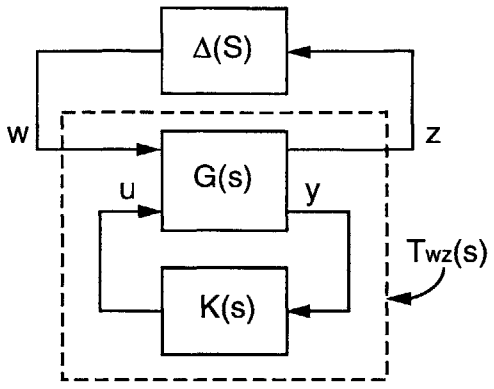

Figure 9-7: Block diagram of a controlled system $T_{wz}(s)$ with uncertainty $\triangle(s)$.

9.3.1 Small Gain Theorem

For a system as shown in Figure 9-7, $G(s)$ is the open-loop dynamics, $K(s)$ is the designed controller, $T_{wz}(s)$ is the closed-loop transfer function and $\triangle(s)$ is the uncertainty matrix. Small gain theorem states that if $T_{wz}(s)$ and $\triangle(s)$ are both stable, then the interconnected system is stable for all uncertainty $\triangle(s)$ if and only if

$$\boxed{\|\triangle(s)\|_\infty \|T_{wz}(s)\|_\infty < 1}. \tag{9.30}$$

If the uncertainty matrix $\triangle(s)$ is normalized and $\|\triangle(s)\|_\infty \leq 1$, then the system is stable for all $\triangle(s)$ if and only if $\|T_{wz}(s)\|_\infty < 1$.

Although it is a necessary and sufficient condition, small gain theorem is always considered conservative, because it is a stability requirement for ALL possible complex uncertainty matrices $\triangle(s)$. For example, if the system $T_{wz}(s)$ has $\|T_{wz}(s)\|_\infty = 1.001$, we can always find an uncertainty matrix $\triangle(s)$ which has $\mathcal{H}_\infty$ norm of 1 to destabilize the system. However, we can have the actual uncertainty matrix $\triangle(s)$ with $\mathcal{H}_\infty$ norm much larger than 1, and the system can still be stable.

By using small gain theorem as an analysis tool, we can design a controller $K(s)$ by any means, and check its stability-robustness by small gain theorem. To use small gain theorem as a synthesis tool, we can combine it with $\mathcal{H}_\infty$ control. In other words, we design the controller $K(s)$ by using $\mathcal{H}_\infty$ control to minimize $\|T_{wz}(s)\|_\infty$, and check the stability-robustness requirement of $\|T_{wz}(s)\|_\infty \|\triangle(s)\|_\infty < 1$.

However, small gain theorem is probably too conservative if $\triangle(s)$ is a diagonal matrix:

$$\triangle(s) = \triangle_d(s) = \begin{bmatrix} \triangle_1(s) & 0 & \cdots & 0 \\ 0 & \triangle_2(s) & \cdots & 0 \\ \vdots & \vdots & \ddots & \vdots \\ 0 & 0 & \cdots & \triangle_n(s) \end{bmatrix}, \tag{9.31}$$

where each diagonal component $\triangle_i(s)$ can be a matrix. For each diagonal component $\|\triangle_i(s)\|_\infty < 1$, then it is true that $\|\triangle(s)\|_\infty < 1$. From small gain theorem, the system will be stable for all diagonal $\triangle(s)$ if $\|T_{wz}(s)\|_\infty < 1$. Notice that it is only a sufficient condition now, and can be very conservative. The structured singular value μ is thus developed to handle this conservatism.

9.3.2 μ Analysis

In this section, we will introduce the definition of Structured Singular Value (SSV, μ). μ analysis is used to predict the range of diagonal uncertainties that a system can have and maintain stability.

Structured Singular Value methodology can be used to handle the unmodeled dynamics similar to the small gain theorem. It is less conservative than small gain theorem when the uncertainty matrix is diagonal. SSV is defined to provide necessary and sufficient conditions for stability-robustness to such structured perturbations.

Similar to small gain theorem, μ analysis defines $\|T_{wz}(s)\|_\mu$ such that the interconnected system $(I + \triangle_d T_{wz})^{-1}$ is stable for all diagonal uncertainty matrices $\triangle_d(s)$ if and only if

$$\boxed{\|\triangle_d(s)\|_\infty \|T_{wz}(s)\|_\mu < 1}, \tag{9.32}$$

which is also called the generalized small gain theorem. If $\triangle_d(s)$ is normalized such that each diagonal component $\|\triangle_i(s)\|_\infty < 1$, then the system is stable for all $\triangle_d(s)$ if and only if $\|T_{wz}(s)\|_\mu \leq 1$. From Equation 9.32, we define the structured singular

value μ of T_{wz} as:

$$\mu(T_{wz}(j\omega)) = \frac{1}{\min\limits_{\triangle_d}\{\sigma_{\max}(\triangle_d) : det(I + \triangle_d T_{wz}) = 0\}}, \tag{9.33}$$

unless no $\triangle_d$ makes $(I + \triangle_d T_{wz})$ singular, in which case $\mu(T_{wz}) = 0$,

and the maximum value of $\mu\left(T_{wz}(j\omega)\right)$ is:

$$\|T_{wz}(s)\|_\mu = \sup_\omega \mu\left(T_{wz}(j\omega)\right). \tag{9.34}$$

However, in general, $\mu(T_{wz}(s))$ cannot be computed. Currently, only the upper bound can be found by iteration. We take the advantage that this upper bound happens to be an $\mathcal{H}_\infty$ norm, and we can use $\mathcal{H}_\infty$ control to design the controller to minimize the upper bound. The details are shown in Appendix L, and references are listed in Chapter 2.

9.3.3 An Example of Vibration Analysis by Using Small Gain Theorem / μ Analysis

Here we will use a simple example [28] to demonstrate how small gain theorem and μ analysis work on vibration control. As shown in Figure 9-8(a), we have a simple mass-spring-damper system, it has uncertainty on the spring stiffness. The dynamics can be shown as:

$$m\ddot{x} + b\dot{x} + (k + \triangle)x = f \tag{9.35}$$

The block diagram is shown in Figure 9-8(b), and the gain of T_{wz} is shown in Figure 9-8(c).

Because the uncertainty $\triangle$ is an 1×1 matrix, μ analysis is the same as the small gain theorem, hence the system is stable for all $\triangle$ if and only if

$$\|\triangle\|_\infty \|T_{wz}(s)\|_\mu = \|\triangle\|_\infty \|T_{wz}(s)\|_\infty < 1 \tag{9.36}$$

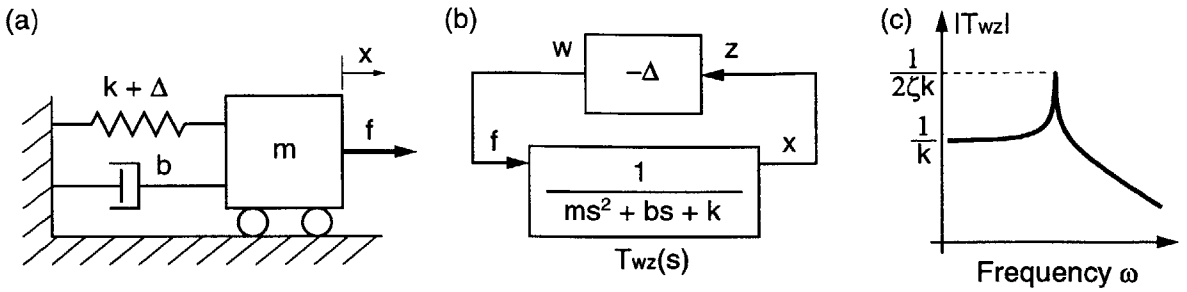

Figure 9-8: (a) A simple spring-damper-mass system, (b) the block diagram, and (c) the gain plot of $|T_{wz}|$.

In single input single output system, $\|T_{wz}(s)\|_\infty$ is simply the maximum magnitude on its Bode plot, which is

$$\|T_{wz}(s)\|_\infty = \frac{1}{2m\zeta\omega_n^2\sqrt{1-\zeta^2}} \approx \frac{1}{2m\zeta\omega_n^2} = \frac{1}{2\zeta k}. \tag{9.37}$$

From small gain theorem, for the system to be stable, the uncertainty must have:

$$\|\Delta\|_\infty < 2\zeta k. \tag{9.38}$$

A typical value of the damping ratio is $\zeta = 0.005$, which results in

$$\|\Delta\|_\infty < 0.01k. \tag{9.39}$$

The system of $m\ddot{x} + b\dot{x} + (k \pm 0.01k)x = f$ has a resonance frequency at $1.005\omega_n$ to $0.995\omega_n$. In other words, μ analysis thinks the system can be unstable when resonance frequency ω_n changes by over 0.5%. But in reality, since Δ is a real scalar, the system will be stable for $-k < \Delta < \infty$. The μ analysis is too conservative since it considers Δ to be a complex number. Figure 9-9 shows the pole plot of the system, the shaded disk shows the pole uncertainties by assuming complex Δ, and the solid line shows the actual pole variations with real Δ.

If we design a controller using μ synthesis, it will try to minimize $\|T_{wz}(s)\|_\infty$. The designed controller will move the closed-loop poles towards left-half-plane, and make sure the uncertainty disk doesn't cross to the imaginary axis. For such a simple

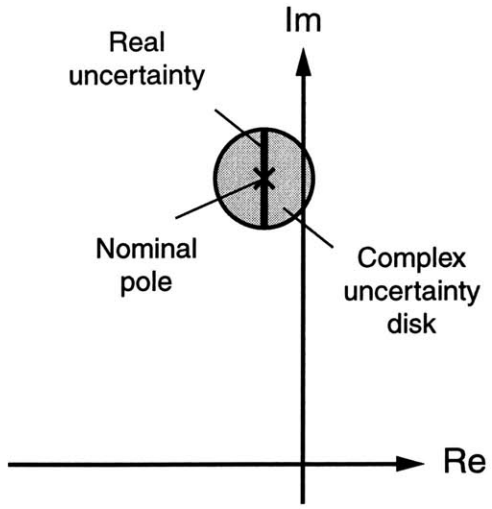

Figure 9-9: Uncertainty in a pole plot.

system, μ synthesis may work. But for systems with a large number of lightly-damped modes such as our experimental setup, μ synthesis will ask too much stability-robustness, and may generate no solution at all. Notice that it is not guaranteed that there is an existing solution. Hence the μ synthesis is almost useless in our case.

9.4 Discrete Modal Filter

In this section, we explore another model-based control strategy: Discrete Modal Filter [72]. In our system, we have 8 sensors and 8 actuators. The spatially distributed sensors make it possible to extract modal coordinates by using discrete modal filter.

9.4.1 Introduction of Discrete Modal Filter

In modal control, we can extract the modal coordinates by different methods: band-pass filter, reduced-order observer, or discrete modal filter. Band-pass filter works only when vibration frequencies are far from each other. Reduced-order observer may have observer spillover from unmodeled modes, which can make the system unstable. Discrete modal filter simply fits the sensor outputs to modal shapes to estimate the modal coordinates. It takes the advantage that resonance modes are orthogonal to each other, hence the unmodeled resonance modes will not cause observer spillover in

the estimated modal coordinates. Furthermore, the calculation is very simple. The disadvantage of using discrete modal filter is that we need a large number of sensors to avoid aliasing resonance modes with short wavelengths.

As shown before, we have beam equation:

$$EI\frac{\partial^4 u}{\partial z^4} + \rho A\frac{\partial^2 u}{\partial t^2} = f, \tag{9.40}$$

where u is the physical displacement of the beam. From expansion theorem, we can represent the physical displacement by the combination of all the modal shapes:

$$u(z,t) = \sum_{r=1}^{\infty} \xi_r(t)\phi_r(z), \tag{9.41}$$

where ξ_r is the modal coordinate, and ϕ_r is the modal shape.

By using k sensors, we can extract k modal coordinates: (notice that the symbols and normalization method are different from Meirovitch [72].)

$$\begin{bmatrix} \hat{\xi}_1(t) \\ \hat{\xi}_2(t) \\ \vdots \\ \hat{\xi}_k(t) \end{bmatrix} = \begin{bmatrix} \phi_1(x_1) & \phi_2(x_1) & \cdots & \phi_k(x_1) \\ \phi_1(x_2) & \phi_2(x_2) & \cdots & \phi_k(x_2) \\ \vdots & \vdots & \ddots & \vdots \\ \phi_1(x_k) & \phi_2(x_k) & \cdots & \phi_k(x_k) \end{bmatrix}^{-1} \begin{bmatrix} u(x_1) \\ u(x_2) \\ \vdots \\ u(x_k) \end{bmatrix}. \tag{9.42}$$

Discrete modal filter extracts the modal coordinates by fitting the modal shapes. Since each mode is decoupled, we can design controllers for each mode independently. The resulting modal forces need to be transformed back to physical coordinates. Similar to discrete sensor modal filter, with m force actuators, we can apply m modal forces:

$$N_r = \int_0^L \phi_r(x)f(x)dx = \begin{bmatrix} \phi_r(x_1) & \phi_r(x_2) & \cdots & \phi_r(x_m) \end{bmatrix} \begin{bmatrix} f(x_1) \\ f(x_2) \\ \vdots \\ f(x_m) \end{bmatrix}$$

$$\Rightarrow \begin{bmatrix} N_1 \\ N_2 \\ \vdots \\ N_m \end{bmatrix} = \begin{bmatrix} \phi_1(x_1) & \phi_1(x_2) & \cdots & \phi_1(x_m) \\ \phi_2(x_1) & \phi_2(x_2) & \cdots & \phi_2(x_m) \\ \vdots & \vdots & \ddots & \vdots \\ \phi_m(x_1) & \phi_m(x_2) & \cdots & \phi_m(x_m) \end{bmatrix} \begin{bmatrix} f(x_1) \\ f(x_2) \\ \vdots \\ f(x_m) \end{bmatrix}. \quad (9.43)$$

Therefore we can solve $f(x)$ vector by

$$\begin{bmatrix} f(x_1) \\ f(x_2) \\ \vdots \\ f(x_m) \end{bmatrix} = \begin{bmatrix} \phi_1(x_1) & \phi_1(x_2) & \cdots & \phi_1(x_m) \\ \phi_2(x_1) & \phi_2(x_2) & \cdots & \phi_2(x_m) \\ \vdots & \vdots & \ddots & \vdots \\ \phi_m(x_1) & \phi_m(x_2) & \cdots & \phi_m(x_m) \end{bmatrix}^{-1} \begin{bmatrix} N_1 \\ N_2 \\ \vdots \\ N_m \end{bmatrix}. \quad (9.44)$$

9.4.2 Controller Design

After designing the modal filter, we can design the controllers for each modes that we want to control. With 8 sensors, we are able to control at most eight modes. The modal coordinates can be obtained by using Equation 9.42, and the computed modal force can be transformed into actuator force by using Equation 9.44.

9.4.3 A Numerical Example of Modal Filter

To evaluate the discrete modal filter, we use a numerical example to show how it works. We will include modeling error in this example. For a simply supported beam with length $L = 2.95$ m, we model it as 3 m long beam. Eight sensors are located at $[0.216, 0.546, 0.864, 1.194, 1.638, 1.969, 2.477, 2.807]$ m, and eight actuators are located at $[0.381, 0.508, 10.29, 1.156, 1.803, 1.930, 2.642, 2.769]$ m. Assume the beam is vibrating, and the modal coordinates at an instant are 1, 1/4, 1/9, $\cdots$, $1/n^2$. The estimated 8 modal coordinates compared to the real modal coordinates are listed in Table 9.1. Figure 9-10 shows the real beam shape, 8 sensor outputs, and the estimated modal coordinates. Although they look very close, the estimated modal coordinates are actually contaminated by higher frequency modes.

Table 9.1: Estimation of modal coordinates by discrete modal filter.

Mode	Real modal coordinate	Estimated modal coordinate
1	1.0000	0.9828
2	0.2500	0.2681
3	0.1111	0.1071
4	0.0625	0.0724
5	0.0400	0.0363
6	0.0278	0.0306
7	0.0204	0.0253
8	0.0156	0.0222
9	0.0123	none
⋮	⋮	none

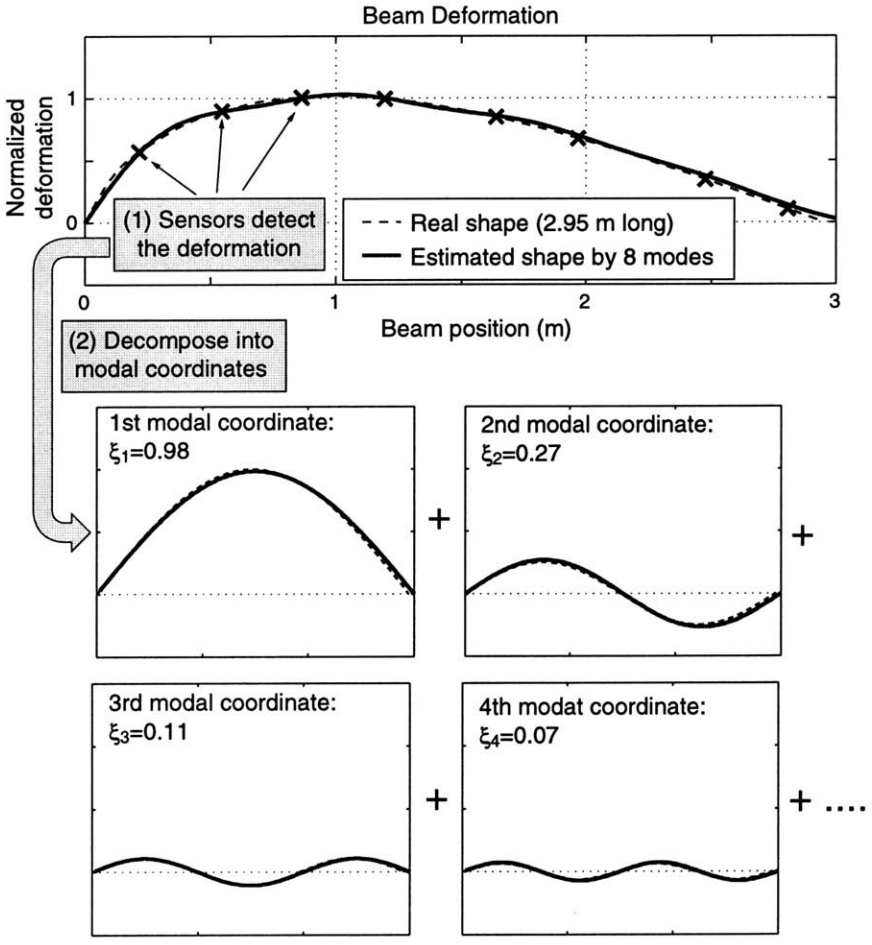

Figure 9-10: Modal filter: 8 sensor outputs are used to fit 8 modal shapes

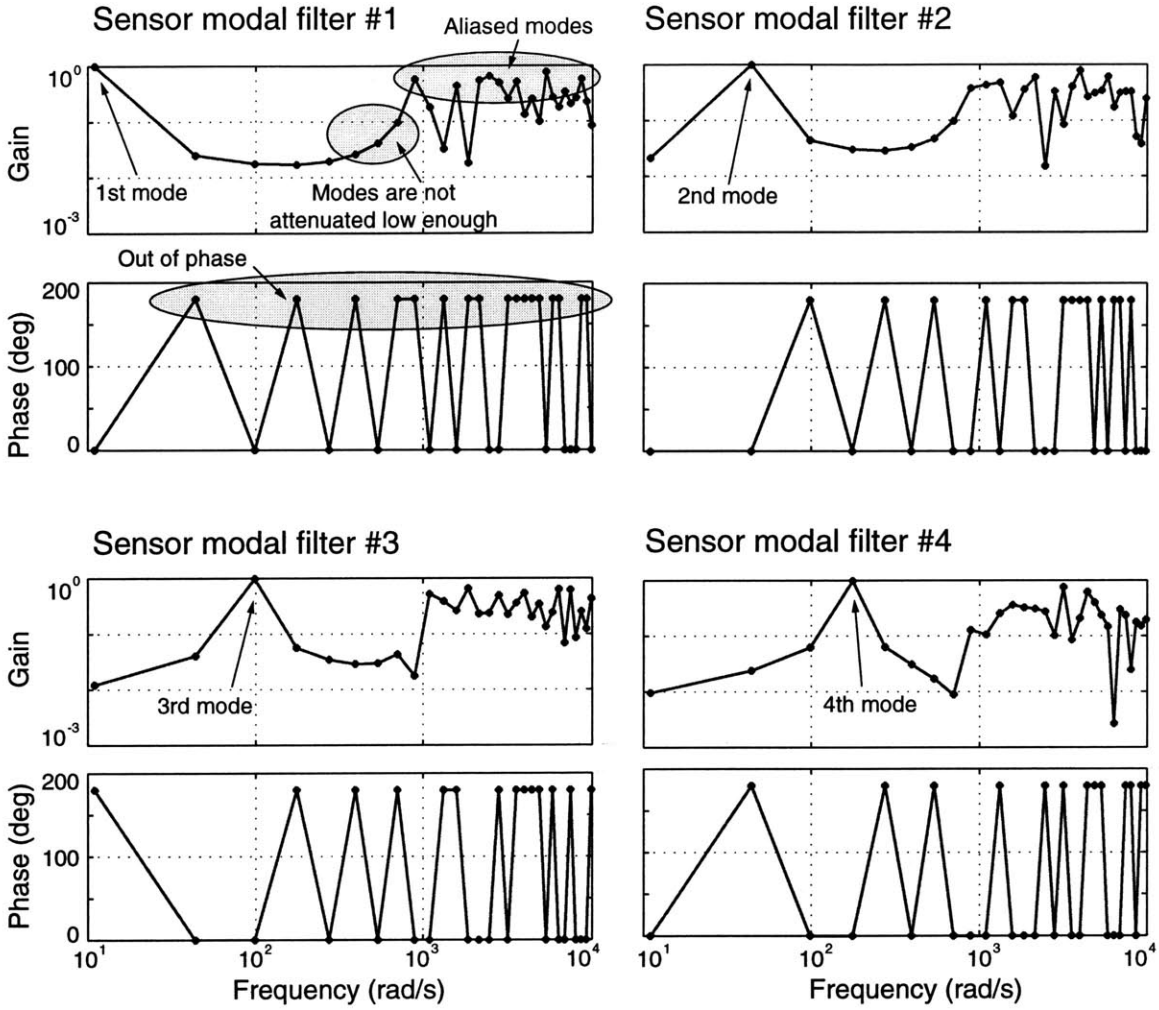

Figure 9-11: Estimated modal coordinates by 8 sensors. Each estimated modal coordinate contains contamination from other modes.

To see it more closely, we look at the modal gains in frequency domain. Assume the beam has all the modes excited, Figure 9-11 shows the components in the estimated modal coordinates. For the 1st sensor modal filter, it does attenuate the 2nd to 8th modes, but the higher frequency modes will be aliased and contaminate the estimated 1st modal coordinate. Notice that except the 1st modal coordinate, the other modal coordinates can be either in phase or out of phase and cannot be predicted.

Similar situations happen to the modal filtering by actuators. Figure 9-12 shows the components in the applied modal forces. For the 1st actuator modal filter, we apply only the 1st modal force from the 8 actuators. The 2nd to 8th modal forces are attenuated, but the higher frequency modal forces are excited. Notice that except

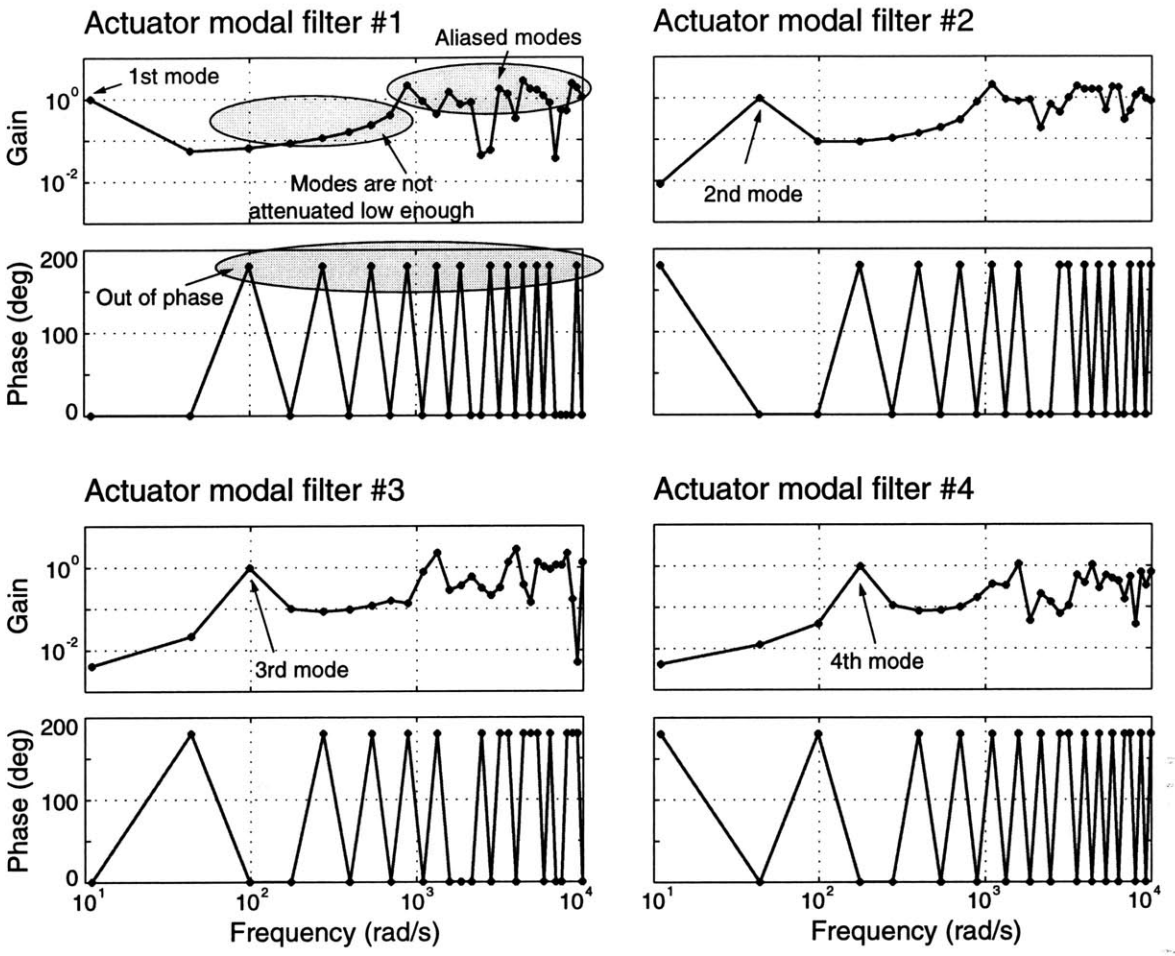

Figure 9-12: Applied modal forces by 8 actuators. Each actuator modal filter excites modal forces to other modes.

the 1st modal force, the other modal forces can be either in phase or out of phase and cannot be predicted.

9.4.4 Experimental Result

I tried using modal filter on our experimental setup in the attempt to stabilize the 10 ft long beam with free-free boundaries. However, it was never stable. It is difficult to implement the modal filter on our experimental setup due to the following two reasons. At first, the tubular beam is bent and not straight. Hence the measured sensor outputs may not be the vibrating deformation, but the original shape of the beam. Secondly, the sensors are not identical. If we use the measured sensor outputs to match the modal coordinates, the accuracy is doubtful. In order to use discrete modal filters,

we not only need a good theoretical model, we also need a good hardware: a straight beam and good identical sensors.

Although the modal filter experiment was not successful, its duality between modal sensor and modal actuator was enlightening, and that is when I realized that there can be actuator averaging that is dual to sensor averaging.

9.5 Conclusion

For our purpose of vibration control, we require the robustness associated with modeling error, varying boundary conditions, and varying tube positions. This chapter describes different model-based controllers that are being widely used. However, none of them can stabilize our experimental setup with our required stability-robustness.

The LQG control is too aggressive for our system. It offers good nominal performances (phase margin and gain margin). However, it has very poor stability-robustness with modeling errors. The LQG controller works as a lead compensator with notches at the resonance frequencies. Sensitivity Weighted LQG (SWLQG) is more robust with regard to the modeling errors. It makes the controller notches smoother, thus by sacrificing the performance, it can tolerate more modeling errors. However, it is still not enough for our required robustness.

On the contrary, μ analysis is too conservative since it considers complex uncertainties. This conservatism will ask too much for the closed-loop system, and may result in no answer at all. A possible fix is real-μ synthesis, which is still under investigation. It is known that real-μ analysis requires significant calculation time, and is not accurate for systems with order larger than 3.

Discrete modal filter has two main advantages. First, it can avoid observer spillover that happens by using observers. Secondly, it causes no phase lag, which is a common property for spatial filters. The disadvantage of using discrete modal filter is that it needs a large number of sensors. Since resonance modes with wavelengths smaller than twice the sensor distance will be aliased and contaminate the estimated modal coordinates.

Chapter 10

Dynamics of Axially Moving Structures

The suspension of fast-moving workpieces is an extension of this project. In this chapter, I review the dynamics of axially moving structures as a starting point for this extension. This chapter includes the analyses of subcritical speed behavior, and the calculation of the critical speed. In this chapter, we consider axially moving beams and strings. Dynamics of moving plates and membranes can be derived similarly. In general, the dynamics of axially moving structures becomes gyroscopic. When the moving speed approaches the critical speed, the system goes through buckling and becomes unstable. We show that the critical speed of beams and plates can be increased by increasing the magnetic bearing stiffness. At this moment, we have not fully developed the suspension technologies for fast-moving structures. The research is ongoing in our lab. Related references about dynamics of moving structures are listed in Chapter 2.

10.1 Dynamic Equations of Moving Structures

When the structures are moving and vibrating at the same time, the dynamic equations need to be modified. The dynamics can be re-derived from free body diagram of the structure element, by including the Coriolis force and centrifugal force. We can

also derive it by using convection derivative[1]:

$$\frac{\partial}{\partial t'} = \frac{\partial}{\partial t} + \vec{V} \cdot \nabla, \tag{10.1}$$

where t' is the time in moving frame, $\vec{V}$ is the moving velocity, and $\nabla = (\partial/\partial x)\hat{x} + (\partial/\partial y)\hat{y} + (\partial/\partial z)\hat{z}$.

For beams and strings moving axially with speed V, the governing equation can be obtained by rewriting beam equation in moving frame:

$$\begin{aligned} & EI\frac{\partial^4 u}{\partial z^4} - T\frac{\partial^2 u}{\partial z^2} + \rho A\frac{\partial^2 u}{\partial t'^2} = f \\ \Rightarrow \quad & EI\frac{\partial^4 u}{\partial z^4} - T\frac{\partial^2 u}{\partial z^2} + \rho A(\frac{\partial}{\partial t} + V\frac{\partial}{\partial z})^2 u = f \\ \Rightarrow \quad & \boxed{EI\frac{\partial^4 u}{\partial z^4} - T\frac{\partial^2 u}{\partial z^2} + \rho A\frac{\partial^2 u}{\partial t^2} + 2\rho AV\frac{\partial^2 u}{\partial z \partial t} + \rho AV^2\frac{\partial^2 u}{\partial z^2} = f}. \end{aligned} \tag{10.2}$$

Equation 10.2 represents a linear gyroscopic system; the last 2 terms represent Coriolis force and centrifugal force due to axial motion, respectively.

In this thesis, we focus on slow-moving or non-moving structures, and neglect the gyroscopic motion of the structure. To verify if the velocity V is negligible, we compare V with the critical speed V_c, which is the lowest speed at which divergence instability happens. For a beam with length L, the critical speed is [106]:

$$V_c = \sqrt{\frac{T}{\rho A} + \pi^2 \frac{EI}{\rho A L^2}}, \qquad \text{hinged-hinged beam,} \tag{10.3}$$

$$V_c = \sqrt{\frac{T}{\rho A} + 4\pi^2 \frac{EI}{\rho A L^2}}, \qquad \text{clamped-clamped beam.} \tag{10.4}$$

For strings, we can simply neglect the bending stiffness EI, and the critical speed will be

$$V_c = \sqrt{\frac{T}{\rho A}}, \qquad \text{strings,} \tag{10.5}$$

[1]This method is adopted from electromagnetic theories in moving frames [110].

which shows that critical speed of strings does not depend on the length of the string. Once the moving speed approaches the string propagating speed at $\sqrt{T/(\rho A)}$, it becomes unstable.

For our system with simple supports, given the tube parameters, the critical speed can be obtained as $V_c = 10.5$ m/s. If the object is moving at speed close to or higher than V_c, Equation 10.2 should be used to model the structure. The analysis of the dynamics can be solved numerically or analytically. Finite element model can be derived directly from the governing equation, and will be shown in Chapter 11. The modal analysis techniques for gyroscopic systems can be found in Meirovitch [73, 74].

10.2 Structures Moving Below Critical Speed

In this thesis, we mostly assume that the axial speed of the structure is much smaller than the critical speed, and consider the dynamics of non-moving structures for analysis. In this section, I would like to briefly discuss the effects of axial moving speed on (1) structural dynamics and (2) sensor/actuator averaging.

10.2.1 Structural Dynamics at Subcritical Speed

To demonstrate the effects on resonance frequencies due to moving speed, we use a beam example and a string example. In the following, I use my FEM program to solve for the resonance frequencies for both beams and strings. FEM modeling of moving structures is presented in Chapter 11. The results are shown in Figure 10-1. Figure 10-1(a) shows the resonance frequencies of a simply supported beam as a function of moving speed. Notice that only the 1st mode is affected significantly near the critical speed. Figure 10-1(b) shows the resonance frequencies of a moving string as a function of moving speed. Notice that all resonance modes vanish at critical speed.

For strings, the resonance frequencies can be analytically represented by the mov-

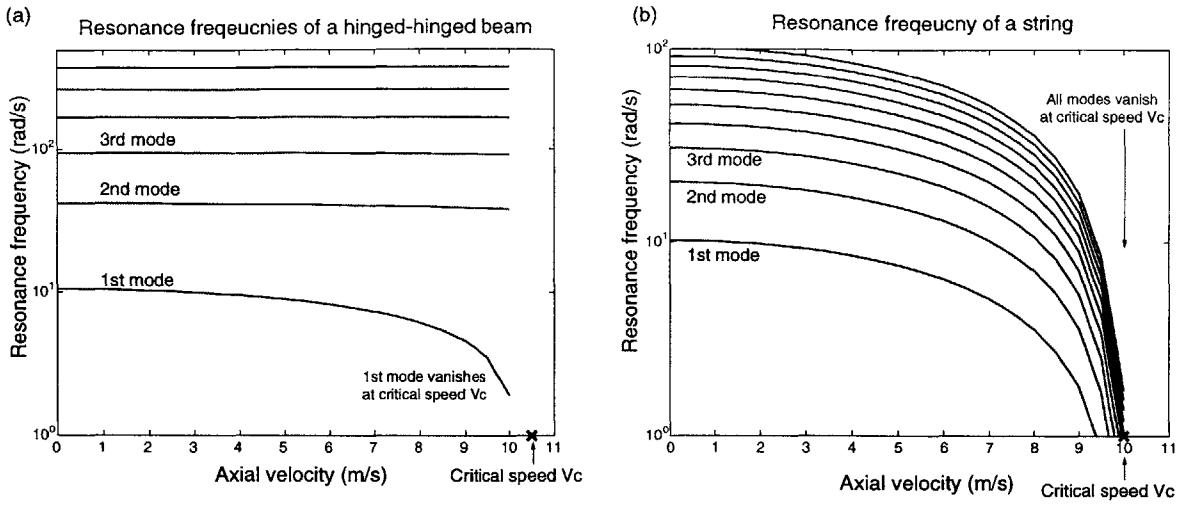

Figure 10-1: Resonance frequencies as a function of axially moving speed under critical speed V_c: (a) a beam example, and (b) a string example.

ing speed as [106]:

$$\omega_n = \frac{n\pi}{L}\left(V_c - \frac{V^2}{V_c}\right). \tag{10.6}$$

For beams, I did not find the analytical form in the literature to represent resonance frequencies as a function of moving speed.

From the viewpoint of structural vibration control, the effects of moving speed is significant. It reduces the resonance frequencies, similar to the effects of applying compressive axial load. Our control method is to design a lead compensator from the 1st resonance frequency to the control bandwidth. Therefore, the lowering of 1st resonance frequency will require us to design a lead compensator starting from lower frequencies, and the controller dc stiffness will be reduced accordingly.

10.2.2 Sensor/Actuator Averaging for Structures at Subcritical Moving Speed

As shown in Chapter 6, we use sensor/actuator averaging method to place sensors and actuators along the structures. The effectiveness of sensor/actuator averaging bases on the assumption that the vibration of the structures are dominated by sinusoidal

waveforms at high frequencies. In this section, I would like to verify if this assumption holds when the moving speed of the structure is approaching the critical speed.

Moving Beams at Subcritical Speed

For beams modeled by Equation 10.2:

$$EI\frac{\partial^4 u}{\partial z^4} - T\frac{\partial^2 u}{\partial z^2} + \rho A\frac{\partial^2 u}{\partial t^2} + 2\rho AV\frac{\partial^2 u}{\partial z \partial t} + \rho AV^2\frac{\partial^2 u}{\partial z^2} = f.$$

Assume the solution has a form of $e^{j(\omega t - kz)}$, the characteristic equation becomes:

$$EIk^4 + (T - \rho AV^2)k^2 + 2\rho AV\omega k - \rho A\omega^2 = 0. \tag{10.7}$$

For our experimental setup as an example, we have $EI = 11.68$ Nm^2, $\rho A = 0.117$ kg/m, and $T = 0$ N. Assume the beam is moving axially at 10 m/s (critical speed $V_c = 10.5$ m/s), and we check the frequency range at $\omega = 1000$ rad/s, we have solutions of

$$k = -10.52,\ 9.52,\ 0.5 + 10j,\ 0.5 - 10j. \tag{10.8}$$

If we have a resonance frequency that is $\omega_n = 1000$ rad/s, the solution of this mode will be:

$$u(z,t) = e^{j1000t}\left(C_1 e^{-j9.52z} + C_2 e^{j10.52z} + C_3 e^{(-j0.5-10)z} + C_4 e^{(-j0.5+10)z}\right), \tag{10.9}$$

where C_1 and C_2 represent the downstream and upstream propagating waves, and C_3 and C_4 represent the downstream and upstream evanescent waves. For comparison, if we have velocity $V = 0$, the solutions are:

$$u(z,t) = e^{j1000t}\left(C_1 e^{-j10z} + C_2 e^{j10z} + C_3 e^{-10z} + C_4 e^{10z}\right). \tag{10.10}$$

Hence we show that for beams, because the high frequency modes have much higher propagating speed than that of low frequency modes. When the structure moves near the critical speed, the mode shape of the 1st vibration mode may vary dramatically. However, for the high frequency modes that we are concerned for sensor/actuator averaging remain almost unchanged. Therefore, we can conclude that sensor/actuator averaging is still valid for structures such as beams and plates.

Moving Strings at Subcritical Speed

For strings with the governing equation:

$$-T\frac{\partial^2 u}{\partial z^2} + \rho A\frac{\partial^2 u}{\partial t^2} + 2\rho AV\frac{\partial^2 u}{\partial z \partial t} + \rho AV^2\frac{\partial^2 u}{\partial z^2} = f.$$

Assume the solution has a form of $e^{j(\omega t - kz)}$, the characteristic equation becomes:

$$\begin{aligned} & (T - \rho AV^2)k^2 + 2\rho AV\omega k - \rho A\omega^2 = 0 \\ \Rightarrow \quad & (Vc^2 - V^2)k^2 + 2V\omega k - \omega^2 = 0. \end{aligned} \tag{10.11}$$

The solutions of the wavenumbers are

$$k = \frac{\omega}{V_c + V},\ \frac{-\omega}{V_c - V}. \tag{10.12}$$

If we have a resonance frequency at ω_n, the homogeneous solution becomes:

$$u(z,t) = e^{j\omega_n t}\left(C_1 e^{-j\omega_n z/(V_c+V)} + C_2 e^{j\omega_n z/(V_c-V)}\right), \tag{10.13}$$

where C_1 and C_2 represent the downstream and upstream propagating waves.

If we have critical speed $V_c = 10$ m/s, and moving speed $V = 9$ m/s, a resonance modes ω_n=1000 rad/s, the original wavenumber for a non-moving string is $k = 100$ rad/m, and the resulting wavenumbers for a moving string will be $k = 52.6$ rad/m (downstream) and $k = 1000$ rad/m (upstream). In order to filter this resonance modes by using sensor/actuator averaging method, we can only attenuate half of the

waveforms: either upstream or downstream.

From Equation 10.12, we use another example of moving speed $V = 0.1V_c$, the wavenumber of k_n becomes $0.91k_n$ and $1.11k_n$. If we design sensor averaging such that $\cos k_n d = 0$, the resulting gains become $\cos(0.91k_n d) = 0.14$ for the downstream wave, and $\cos(1.11k_n d) = -0.17$ for the upstream wave. The effectiveness of the sensor averaging method is limited.

These simple examples shows that sensor/actuator averaging does not work well for moving strings, because the mode shapes of all resonance modes change significantly as the moving speed increases.

10.3 Solving Critical Speed of Moving Structures

To design a suspension system for axially moving structures. We would like to find out the critical speed that limits the axially moving speed. This section describes the techniques of solving critical speed of moving structures. We will show that the stiffness of magnetic bearing can improve the critical speed of beams and plates.

10.3.1 Analogy to Buckling

To solve for the critical speed of structures, I use beam equation to demonstrate the method. At critical speed, the system undergoes divergence instability. In other words, the poles vanish to zero. From Equation 10.2, we neglect the time derivative since the poles are zero, and we have

$$EI\frac{\partial^4 u}{\partial z^4} + (\rho AV^2 - T)\frac{\partial^2 u}{\partial z^2} = 0. \tag{10.14}$$

This analysis is analogous to classical beam buckling analysis, in which case, V is zero and T is negative (compressive axial load). Bazant [10] had a good introduction to structural buckling analysis. Assume homogeneous solution $u_h = Ce^{pz}$, the

resulting characteristic equation becomes

$$p^2(EIp^2 + (\rho AV^2 - T)) = 0. \tag{10.15}$$

The solutions of p are 0, 0, and $\pm ik$, therefore we can rewrite the homogeneous solution as

$$u_h(z) = C_1 \cos kz + C_2 \sin kz + C_3 z + C_4, \tag{10.16}$$

with

$$k = \sqrt{\frac{\rho AV^2 - T}{EI}}. \tag{10.17}$$

From another point of view, for any possible solution k_n (solved from boundary conditions), there is a critical speed V_n associated to it, and

$$V_n = \sqrt{\frac{EIk_n^2 + T}{\rho A}}. \tag{10.18}$$

To solve for k_n from boundary conditions, we use the same techniques as solving for beam dynamics. In Appendix M, I solve the critical speed for hinged-hinged beams and clamped-clamped beams, and compare them with the results from Wickert [106]. In the following subsections, I will analyze the critical speed for beams and strings with multiple supports.

10.3.2 Critical Speed for Moving Beams Supported by Magnetic Bearings

From the previous critical speed analysis, we draw the following conclusions:

1. The centrifugal force (proportional to ρAV^2) causes the beam to buckle.

2. The variables that we can control to avoid the system reaching critical speed is by increasing bending stiffness EI and tension force T, and by decreasing

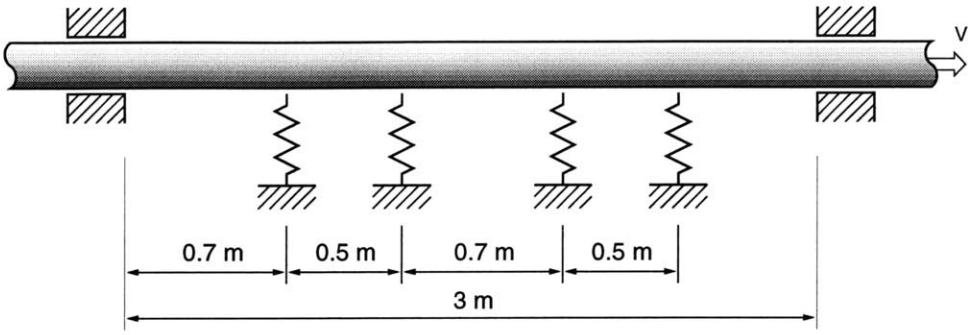

Figure 10-2: Model of a 3 m long beam with clamped-clamped ends and 4 spring supports.

distributed mass ρA and length L.

3. Since the time derivative will vanish, the damping force of the magnetic bearings will not improve the critical speed. The magnetic bearing stiffness determines the critical speed.

Hence we want to derive the relations between magnetic bearing stiffness to the critical speed. The result will help us to know the critical speed of final design. As shown in Figure 10-2, we demonstrate the method by a beam with clamped-clamped boundaries with 4 elastic supports. To calculate the critical speed, we have to solve for all the 5 spans of the beam. The deformation in these 5 spans are assigned as u_1, u_2, u_3, u_4 and u_5. Each $u_i(z)$ is assumed to be:

$$u_i(z) = C_{i1}\cos kz + C_{i2}\sin kz + C_{i3}z + C_{i4}, \tag{10.19}$$

For each interconnected boundary, it has the following relations:

$$\begin{cases} u_i = u_{i+1} & \text{deformation} \\ u_i' = u_{i+1}' & \text{angle} \\ u_i'' = u_{i+1}'' & \text{moment} \\ EI\left(u_{i+1}''' - u_i'''\right) = -Ku_i & \text{shear} \end{cases} \tag{10.20}$$

Together with the two clamped boundary conditions, we have 20 equations and 20 unknowns. Again, we set the 20 by 20 matrix to have determinant equal to zero, we

can solve for natural solutions of k_n.

I use our experimental setup as an example. The total length $L = 3$ m, mass per unit length $\rho A = 0.12$ kg/m, and the bending stiffness $EI = 12$ Nm^2. If it is clamped-clamped at both ends, the solved 1st eigenvalue and eigenvector are shown in Figure 10-3(a). The critical speed will be 20.9 m/s.

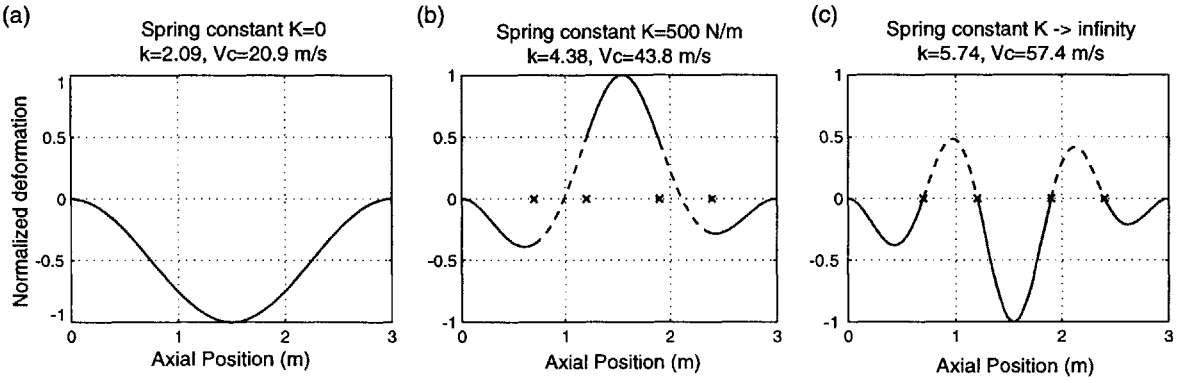

Figure 10-3: Buckling of a fixed-fixed beam by axially moving speed: (a) no intermediate support, (b) 4 intermediate supports with stiffness $K = 500$ N/m, and (c) 4 intermediate hinges.

If we add 4 supports with stiffness $K = 500$ N/m at $x = 0.7$, 1.2, 1.9 and 2.4 m, the modal shape of the first buckling mode is shown in Figure 10-3(b). The critical speed is increased to 43.9 m/s.

An extreme case is to increase the stiffness of the 4 spring supports to infinity, and they become hinged supports. The result is shown in Figure 10-3(c). The critical speed is improved to 57.4 m/s. It is obvious that the critical speed is now dominated by the longest span of the beam. In other words, we can simply approximate this critical speed by the longest span: 0.7 m. The 1st eigenvalue should be close to $k_1 \approx \pi/1.7 = 4.5$ rad/m, compared to the analytical solution of $k_1 = 5.74$ rad/m.

This simple example shows that we can improve the critical speed of beams by increasing the magnetic bearing stiffness. The idea is to decrease the natural wavelength, hence improve the critical speed.

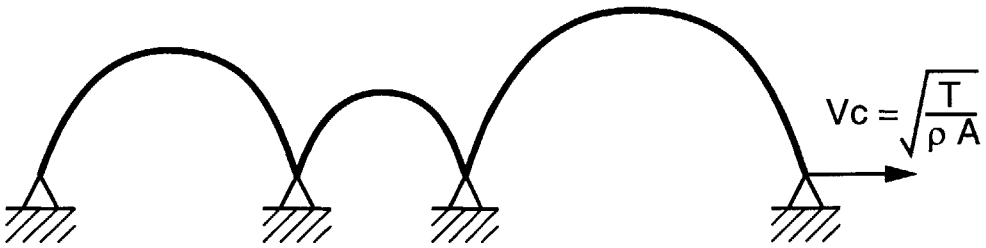

Figure 10-4: The divergence of strings when moving speed is equal to wave propagating speed.

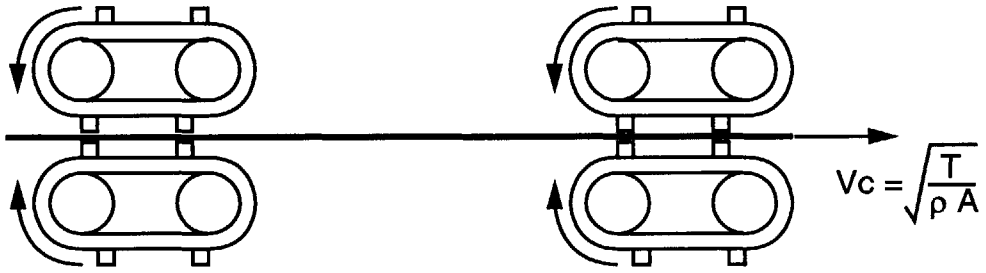

Figure 10-5: Moving boundary design may avoid critical speed of strings.

10.3.3 Critical Speed for Strings

For strings and membranes, there are less that we can do to improve the critical speed. Strings and membranes have only one critical speed: the wave propagating speed: $\sqrt{T/(\rho A)}$. The reason is that the waveforms of strings and membranes are not dispersive, all the waves have the same propagating speed. Once the moving speed reaches the wave propagating speed, all the resonance frequencies vanish to zero.

We demonstrate this in situation in Figure 10-4. No matter how stiff and how close the intermediate supports are, once the moving speed reaches wave propagating speed, each span of the strings becomes unstable. The only variables that we can change is the string tension T and the string mass per unit length ρA.

Changing the boundary condition may be able to make the critical speed increase or even disappear. By using a boundary condition as shown in Figure 10-5, we create "temporarily moving boundaries." By doing so, we can recover the moving dynamics back into non-moving strings in moving frame. This proposed method remains doubtful, and will require more careful theoretical and experimental proof.

10.4 Analysis of Moving Structures at Supercritical Speed by Nonlinear Modeling

Researchers also derive the post-buckle analysis of structures by nonlinear modeling. By linear modeling, the structure is predicted to go to infinity when it buckles. However, by nonlinear modeling, we can actually derive the post-buckle shapes of the structure, that is the new equilibrium shapes and the structure will vibrate around these new equilibria.

Without going into detail, the following equation shows the post-buckle equilibria of a simply supported beam without extra spring supports [104]:

$$\frac{w(z)}{L} = \pm\frac{2}{\pi}\sqrt{\frac{\rho}{E}}\sqrt{V^2 - V_c^2}\sin\frac{\pi z}{L}. \tag{10.21}$$

It shows that the amplitudes of the new equilibria increase with moving velocity V. For our experimental setup, the critical speed is $V_c = 10.5$ m/s for hinged-hinged boundaries. If we have $V = 13$ m/s, we will have post-buckled beam with amplitude 3.0 mm, which is about to hit the boundaries of the magnetic bearings. Therefore, we can conclude that the critical speed is a limit to our system because the amplitude of the new equilibria may be too large.

In this thesis, we only consider the first critical speed and try to stay below this speed. Further derivation of critical speed behavior is not within our interest. Interested readers can find such materials in [82, 104, 90, 89].

Chapter 11

Finite Element Modeling of Structural Dynamics

Finite element method (FEM) has been widely used for solving engineering problems. In this chapter, I review the procedures of using FEM to model structural dynamics for interested readers. The basic principles behind FEM is the principle of virtual work. In this project, I utilize it in our structural dynamics, and extend it to structures with tension and axially moving speed.

In this thesis, I use analytical modeling of structural dynamics to study the properties of the structure, and is able to derive design rules for controllers and sensor/actuator positioning. I include numerical modeling of structures by using the finite element method, since FEM is convenient and fast to solve by using computers when system parameters change, such as number of supports or boundary conditions.

In this chapter, I describe how to use FEM to model beams, strings, plates, and membranes. In order to design the controller to suspend the structures, instead of using commercial FEM software, I use Matlab to model structural dynamics by matrices of mass, stiffness, and load. I further decouple the structural dynamics matrices by similarity transformation, and then truncate the higher frequency modes. By doing so, I can reduce the order of the system model and only focus on resonance modes at lower frequencies. I also include tension forces and axially moving speed of structures into the dynamics. It provides the potential to extend to solving axially

moving structures with more complex shapes in the future.

11.1 Introduction to Finite Element Method

This introduction section of FEM mainly follows the work of Bathe [9]. By using FEM, we divide the structures into several elements, assuming that the deformation of the element can be represented by the element's nodal displacements. Finally, we can solve the structural dynamic equations in terms of the nodal displacements. The system model can then be represented in the matrix notation, which can be easily decoupled by eigenvalue problem techniques, and can be used later for controller design and simulation.

The FEM for structures can be derived from the principle of virtual work. Given an element, the principle of virtual work gives the following equation:

$$\underbrace{\int_V \bar{\epsilon}^T \tau dV}_{\text{virtual strain energy}} = \underbrace{\int_V \bar{u}^T f dV}_{\text{virtual work}}, \tag{11.1}$$

where τ is stress, $\bar{\epsilon}$ is virtual strain, $\bar{u}$ is virtual displacement, and f is force, including body force, surface force, and concentrated force. We consider linear stress-strain relationship and present it by

$$\tau = C\epsilon. \tag{11.2}$$

Generally, C is a fourth order elasticity tensor [92]. For isotropic material, C is reduced into a matrix. The C matrix can be further simplified for simple structures such as beams and plates. The list of C matrices for different structures can be found in Appendix B.

We make the FEM assumption that we can present the element displacement distribution by the nodal displacements. We can assume that

$$\boxed{u^{(m)} = H^{(m)} U}, \tag{11.3}$$

where $u^{(m)}$ is the displacement distribution of the mth element, U is the nodal displacements, and H is the displacement interpolation matrix. Notice that this is the only assumption that FEM makes. Because of this extra constraint, the simulated result will be stiffer than the analytical solutions.

Equation 11.1 to Equation 11.3 are the keys to the FEM for the structural analysis. We can further derive the strain ϵ by using nodal displacements U:

$$\epsilon^{(m)} = B^{(m)}U, \tag{11.4}$$

where $B^{(m)}$ is the strain-displacement matrix of the mth element. Combine Equation 11.1 to Equation 11.4, we can get the new equilibrium equation in the FEM version:

$$\begin{aligned} & \bar{U}^T \left(\sum_m \int_{V^{(m)}} B^T C B dV U \right) = \bar{U}^T \left(\sum_m \int_{V^{(m)}} H^T f dV \right) \\ \Rightarrow \quad & \underbrace{\sum_m \int_{V^{(m)}} B^T C B dV}_{K} U = \underbrace{\sum_m \int_{V^{(m)}} H^T f dV}_{R}, \end{aligned} \tag{11.5}$$

where K is the stiffness matrix, U is the vector of nodal displacements, and R is the vector of nodal forces. Notice that this equation represents the whole structure, and stiffness matrix K and nodal force vector R are both assembled by all the elements of the structure.

To solve the dynamics of the structures, we can include the inertia forces $\rho\ddot{u}$ into the force term f. That is, instead of using f, we will use $(f - \rho\ddot{u})$ as the force. By doing so, we can derive the dynamic equation similar to Equation 11.5:

$$\underbrace{\sum_m \int_{V^{(m)}} H^T \rho H dV}_{M} \ddot{U} + \underbrace{\sum_m \int_{V^{(m)}} B^T C B dV}_{K} U = \underbrace{\sum_m \int_{V^{(m)}} H^T f dV}_{R}, \tag{11.6}$$

where M is the assembled mass matrix. The derivation of these matrices and vectors for various structures will be shown in the following sections. In a more general case,

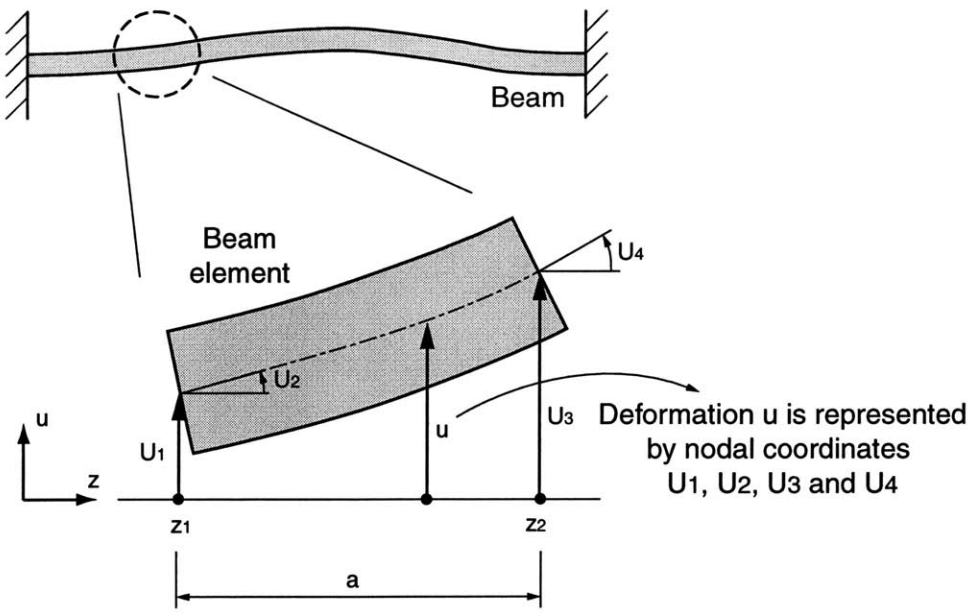

Figure 11-1: An element for Euler-Bernoulli Beam model.

the damping force can be added to the force term, and the governing equation will become

$$M\ddot{U} + D\dot{U} + KU = R. \tag{11.7}$$

Furthermore, the boundary conditions need to be applied afterwards. With the new dynamic equation, we can easily transfer it into the state-space notation:

$$\begin{bmatrix} \dot{U} \\ \ddot{U} \end{bmatrix} = \begin{bmatrix} 0 & I \\ -M^{-1}K & -M^{-1}D \end{bmatrix} \begin{bmatrix} U \\ \dot{U} \end{bmatrix} + \begin{bmatrix} 0 \\ -M^{-1} \end{bmatrix} R. \tag{11.8}$$

11.2 FEM Modeling of Beams without Tension

In this research, the beam is modeled by Euler-Bernoulli Beam element. From elasticity, the Euler-Bernoulli Beam has the stress-strain relation as:

$$\underbrace{M_{zz}}_{\tau} = \underbrace{EI}_{C} \underbrace{\frac{d^2u}{dz^2}}_{\epsilon}. \tag{11.9}$$

The beam can be divided into small elements, each element is illustrated in Figure 11-1. The displacement distribution $u(z)$ is then assumed to be a function of the

4 nodal displacements: $u(z_1)$, $\theta(z_1)$, $u(z_2)$ and $\theta(z_2)$. We define nodal displacements as U:

$$U = \begin{bmatrix} U_1 \\ U_2 \\ U_3 \\ U_4 \end{bmatrix} = \begin{bmatrix} u(z_1) \\ \theta(z_1) \\ u(z_2) \\ \theta(z_2) \end{bmatrix} = \begin{bmatrix} u(z_1) \\ \frac{du}{dz}|_{z=z_1} \\ u(z_2) \\ \frac{du}{dz}|_{z=z_2} \end{bmatrix}. \tag{11.10}$$

We make the FEM assumption that the displacement distribution $u(z)$ of the element can be represented by

$$u(z) = \alpha_1 + \alpha_2 z + \alpha_3 z^2 + \alpha_4 z^3 = HU. \tag{11.11}$$

From Equation 11.10 and Equation 11.11, we can solve the interpolation matrix H for the beam element. The details of the calculation are shown in Appendix N. The result becomes:

$$H = \begin{bmatrix} 1 - 3\frac{z^2}{a^2} + 2\frac{z^3}{a^3} & z - 2\frac{z^2}{a} + \frac{z^3}{a^2} & 3\frac{z^2}{a^2} - 2\frac{z^3}{a^3} & -\frac{z^2}{a} + \frac{z^3}{a^2} \end{bmatrix}. \tag{11.12}$$

Similarly, we can solve the strain-displacement matrix B as defined in Equation 11.4, and the result is

$$B = \begin{bmatrix} -6\frac{1}{a^2} + 12\frac{z}{a^3} & -4\frac{1}{a} + 6\frac{z}{a^2} & 6\frac{1}{a^2} - 12\frac{z}{a^3} & -2\frac{1}{a} + 6\frac{z}{a^2} \end{bmatrix}. \tag{11.13}$$

After the matrices of H and B are solved, M, K and R can be integrated along the length of the element as defined in Equation 11.6.

$$\begin{aligned} M^{(m)} &= \int_{V^{(m)}} H^T \rho H dV \text{ (assume constant } \rho) \\ &= \rho A \int_{z=0}^{a} H^T H dz \end{aligned}$$

$$= \frac{\rho A}{420}\begin{bmatrix} 156a & 22a^2 & 54a & -13a^2 \\ 22a^2 & 4a^3 & 13a^2 & -3a^3 \\ 54a & 13a^2 & 156a & -22a^2 \\ -13a^2 & -3a^3 & -22a^2 & 4a^3 \end{bmatrix}, \tag{11.14}$$

$$\begin{aligned} K^{(m)} &= \int_{V^{(m)}} B^T C B dV \text{ (assume constant } EI) \\ &= EI \int_{z=0}^{a} B^T B dz \\ &= \frac{EI}{a^3}\begin{bmatrix} 12 & 6a & -12 & 6a \\ 6a & 4a^2 & -6a & 2a^2 \\ -12 & -6a & 12 & -6a \\ 6a & 2a^2 & -6a & 4a^2 \end{bmatrix}, \end{aligned} \tag{11.15}$$

$$\begin{aligned} R^{(m)} &= \int_{V^{(m)}} H^T f dV \text{ (assume constant } f) \\ &= fA \int_{z=0}^{a} H^T dz \\ &= fA\begin{bmatrix} \frac{1}{2}a \\ \frac{1}{12}a^2 \\ \frac{1}{2}a \\ -\frac{1}{12}a^2 \end{bmatrix}, \end{aligned} \tag{11.16}$$

where A is the cross sectional area. Notice in $R^{(m)}$, the distributed force f is evenly distributed into $0.5fAa$ at each node, accompanying with bending moment $\frac{1}{12}fAa^2$. In the previous calculations, we have constant ρA, EI and fA. In more complex cases, we can simply represent these values as functions of z, follow similar steps of integration, and we can get the new FEM matrices.

The next step is to assemble the elements together to form the original structure, which is just the summation of these matrices. To demonstrate the assembly of elements, a simple example of 2 element beam is illustrated in Figure 11-2. With 2

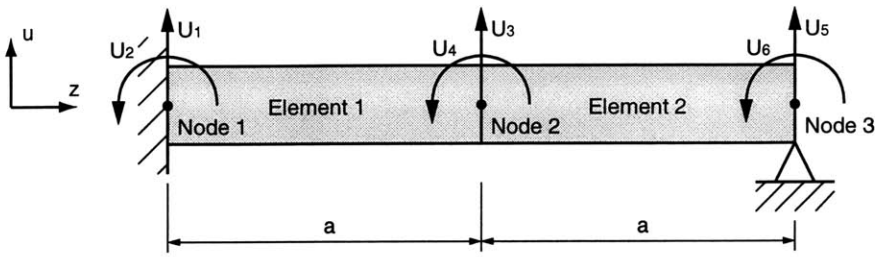

Figure 11-2: Combination of 2 beam elements.

elements, we'll have 3 nodes and 6 corresponding nodal displacements:

$$U = \begin{bmatrix} U_1 \\ U_2 \\ U_3 \\ U_4 \\ U_5 \\ U_6 \end{bmatrix} = \begin{bmatrix} u_1 \\ \theta_1 \\ u_2 \\ \theta_2 \\ u_3 \\ \theta_3 \end{bmatrix} \tag{11.17}$$

We can easily combine the matrices in the following way:

$$\begin{aligned} M &= M^{(1)} + M^{(2)} \\ &= \frac{\rho A}{420} \begin{bmatrix} 156a & 22a^2 & 54a & -13a^2 & 0 & 0 \\ 22a^2 & 4a^3 & 13a^2 & -3a^3 & 0 & 0 \\ 54a & 13a^2 & 312a & 0 & 54a & -13a^2 \\ -13a^2 & -3a^3 & 0 & 8a^3 & 13a^2 & -3a^3 \\ 0 & 0 & 54a & 13a^2 & 156a & -22a^2 \\ 0 & 0 & -13a^2 & -3a^3 & -22a^2 & 4a^3 \end{bmatrix} \begin{matrix} \cdots U_1 \\ \cdots U_2 \\ \cdots U_3 \\ \cdots U_4 \\ \cdots U_5 \\ \cdots U_6 \end{matrix} \end{aligned} \tag{11.18}$$

Similarly, we will have

$$K = K^{(1)} + K^{(2)}$$

$$= \frac{EI}{a^3}\begin{bmatrix} 12 & 6a & -12 & 6a & 0 & 0 \\ 6a & 4a^2 & -6a & 2a^2 & 0 & 0 \\ -12 & -6a & 24 & 0 & -12 & 6a \\ 6a & 2a^2 & 0 & 8a^2 & -6a & 2a^2 \\ 0 & 0 & -12 & -6a & 12 & -6a \\ 0 & 0 & 6a & 2a^2 & -6a & 4a^2 \end{bmatrix}. \tag{11.19}$$

Assume that these two elements are loaded by their own weight and the boundary supporting forces and moments F_1, M_{zz1}, F_2 and M_{zz2}, the resulting load matrix becomes:

$$R = R^{(1)} + R^{(2)} = -\rho Ag\begin{bmatrix} \frac{1}{2}a \\ \frac{1}{12}a^2 \\ a \\ 0 \\ \frac{1}{2}a \\ -\frac{1}{12}a^2 \end{bmatrix} + \begin{bmatrix} F_1 \\ M_{zz1} \\ 0 \\ 0 \\ F_2 \\ M_{zz2} \end{bmatrix}. \tag{11.20}$$

Notice that the damping of the material is not specified yet. This often happens in structural dynamics analysis due to three reasons: (1) the damping coefficient of the structure is usually very small, (2) the damping coefficient can not be easily specified at this step, and (3) if the damping is randomly assigned here, the vibration modes may not be able to be decoupled. Therefore, we will transfer it into decoupled equations first, and then add proportional damping to the system afterwards. By assuming damping coefficient to each modes independently, the system model can remain decoupled.

Before we solve the problem, the boundary conditions should be included at this step. Based on the boundary conditions, we need to reduce the degree of freedom of the model. Typical boundary conditions are:

(1) free end: $F_1 = 0$, $M_{zz1} = 0$, same degree of freedom.

(2) hinged end: $U_1 = 0$, $M_{zz1} = 0$, reduce 1 degree of freedom.

(3) cantilevered end: $U_1 = 0$, $U_2 = 0$, reduce 2 degrees of freedom.

For example, if node 1 is cantilevered and node 3 is hinged, then $U_1 = 0$, $U_2 = 0$, and U_5=0, and the governing equations can be reduced to

$$\underbrace{\frac{\rho A}{420}\begin{bmatrix} 312a & 0 & 54a \\ 0 & 8a^3 & 13a^2 \\ 54a & 13a^2 & 156a \end{bmatrix}}_{M}\begin{bmatrix} \ddot{U}_3 \\ \ddot{U}_4 \\ \ddot{U}_5 \end{bmatrix}+\underbrace{\frac{EI}{a^3}\begin{bmatrix} 24 & 0 & -12 \\ 0 & 8a^2 & -6a \\ -12 & -6a & 12 \end{bmatrix}}_{K}\begin{bmatrix} U_3 \\ U_4 \\ U_5 \end{bmatrix}=\underbrace{-\rho Ag\begin{bmatrix} a \\ 0 \\ \frac{1}{2}a \end{bmatrix}}_{R}. \tag{11.21}$$

With this new governing equation, we can further decouple it into the modal form. At first, we transfer the governing equation into state-space notation:

$$\begin{bmatrix} \dot{U} \\ \ddot{U} \end{bmatrix}=\underbrace{\begin{bmatrix} 0 & I \\ -M^{-1}K & 0 \end{bmatrix}}_{A_1}\begin{bmatrix} U \\ \dot{U} \end{bmatrix}+\underbrace{\begin{bmatrix} 0 \\ -M^{-1} \end{bmatrix}}_{B_1}R. \tag{11.22}$$

To further decouple the equation, we simply run the eigenvalue program by using Matlab, we can get the eigenvalue matrix and eigenvector matrix of the system:

$\gg$ [eigenvector, eigenvalue]=eig(A1);

We can extract the natural frequencies Ω and their corresponding modal shapes Φ from these two matrices, as shown in the MATLAB code in Appendix N:

$$\Omega = \begin{bmatrix} \omega_1 & 0 & \cdots & 0 \\ 0 & \omega_2 & \cdots & 0 \\ \vdots & \vdots & \ddots & \vdots \\ 0 & 0 & \cdots & \omega_n \end{bmatrix}, \tag{11.23}$$

$$\Phi = \begin{bmatrix} | & | & \cdots & | \\ \phi_1 & \phi_2 & \cdots & \phi_n \\ | & | & \cdots & | \end{bmatrix}, \tag{11.24}$$

where ω_n is the nth natural frequency, and ϕ_n is the corresponding modal shape.

We can decouple the governing equations by the orthogonal properties of the

modal shapes. We define modal coordinate ξ such that

$$\underbrace{\begin{bmatrix} U_1 \\ U_2 \\ \vdots \\ U_n \end{bmatrix}}_{U} = \underbrace{\begin{bmatrix} | & | & \cdots & | \\ \phi_1 & \phi_2 & \cdots & \phi_n \\ | & | & \cdots & | \end{bmatrix}}_{\Phi} \underbrace{\begin{bmatrix} \xi_1 \\ \xi_2 \\ \vdots \\ \xi_n \end{bmatrix}}_{\xi}. \tag{11.25}$$

The n decoupled equations can be shown as

$$\Phi^T M \Phi \ddot{\xi} + \Phi^T K \Phi \xi = \Phi^T R, \tag{11.26}$$

or

$$\underbrace{\begin{bmatrix} M_1 & 0 & \cdots & 0 \\ 0 & M_2 & \cdots & 0 \\ \vdots & \vdots & \ddots & \vdots \\ 0 & 0 & \cdots & M_n \end{bmatrix}}_{M_\xi} \begin{bmatrix} \ddot{\xi}_1 \\ \ddot{\xi}_2 \\ \vdots \\ \ddot{\xi}_n \end{bmatrix} + \underbrace{\begin{bmatrix} M_1\omega_1^2 & 0 & \cdots & 0 \\ 0 & M_2\omega_2^2 & \cdots & 0 \\ \vdots & \vdots & \ddots & \vdots \\ 0 & 0 & \cdots & M_n\omega_n^2 \end{bmatrix}}_{K_\xi} \begin{bmatrix} \xi_1 \\ \xi_2 \\ \vdots \\ \xi_n \end{bmatrix} = \underbrace{\begin{bmatrix} N_1 \\ N_2 \\ \vdots \\ N_n \end{bmatrix}}_{N_\xi}, \tag{11.27}$$

where M_n is the nth modal mass, and N_n is the nth modal force.

At this point, we can add proportional damping to the system, assuming

$$D_n = 2\zeta_n \omega_n M_n,$$

where ζ_n is the nth modal damping coefficient. Hence we obtain n decoupled equations

$$\begin{aligned} & M_n(\ddot{\xi}_n + 2\zeta_n\omega_n\dot{\xi}_n + \omega_n^2\xi_n) = N_n \\ \Rightarrow \quad & M_n\ddot{\xi}_n + D_n\dot{\xi}_n + K_n\xi_n = N_n. \end{aligned} \tag{11.28}$$

We can rewrite the new governing equations in the state-space notation:

$$\begin{bmatrix} \dot{\xi} \\ \ddot{\xi} \end{bmatrix} = \begin{bmatrix} 0 & I \\ -M_\xi^{-1}K_\xi & -M_\xi^{-1}D_\xi \end{bmatrix} \begin{bmatrix} \xi \\ \dot{\xi} \end{bmatrix} + \begin{bmatrix} 0 \\ -M_\xi^{-1} \end{bmatrix} N. \tag{11.29}$$

After this step, we can add in the actuator dynamics, sensor dynamics, and design the feedback controller accordingly.

11.3 FEM Modeling of Beams and Strings with Tension

The modeling method of beams with tension is very similar to modeling of beams without tension. Recall the beam dynamic equation:

$$EI\frac{\partial^4 u}{\partial z^4} = f + T\frac{\partial^2 u}{\partial z^2} - \rho A\frac{\partial^2 u}{\partial t^2} \tag{11.30}$$

Previously in Equation 11.6, we use $(f - \rho\ddot{u})$ as the force term instead of f in the FEM analysis to include the dynamics. Similarly, to include tension into the model, we use $(f - \rho\ddot{u} + T\frac{d^2u}{dz^2})$ instead of $(f - \rho\ddot{u})$, the resulting governing equation becomes:

$$\underbrace{\sum_m \int_{V^{(m)}} H^T \rho H dV}_{M} \ddot{U} + \underbrace{(\sum_m \int_{V^{(m)}} B^T C B dV - \sum_m \int_{V^{(m)}} H^T T \frac{d^2 H}{dz^2} dV)}_{K} U = \underbrace{\sum_m \int_{V^{(m)}} H^T f dV}_{R}. \tag{11.31}$$

This is a complete beam model with tension contribution.

If we neglected the bending stiffness, assuming $EI = 0$, we will get the string FEM model:

$$\underbrace{\sum_m \int_{V^{(m)}} H^T \rho H dV}_{M} \ddot{U} - \underbrace{\sum_m \int_{V^{(m)}} H^T T \frac{d^2 H}{dz^2} dV}_{-K} U = \underbrace{\sum_m \int_{V^{(m)}} H^T f dV}_{R}. \tag{11.32}$$

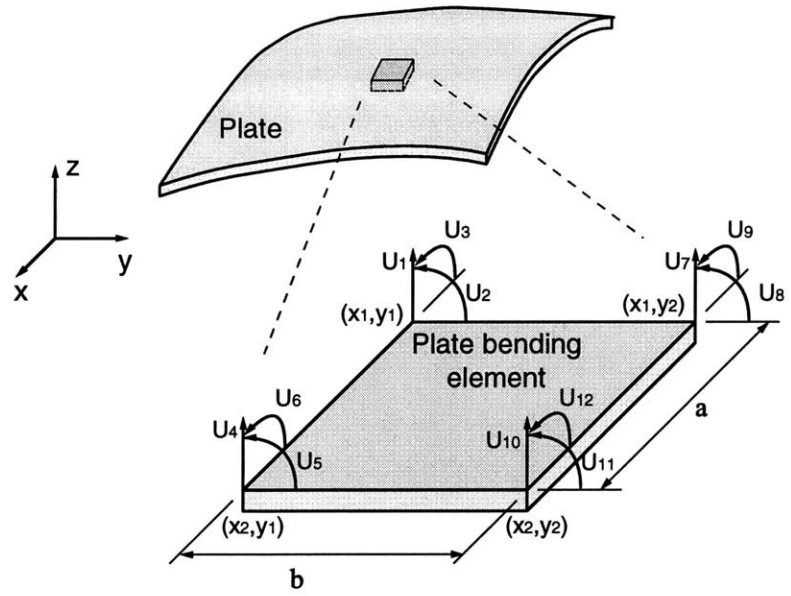

Figure 11-3: Plate element for FEM plate modeling, each element has 4 nodes, and each node has 3 nodal coordinates.

11.4 FEM Modeling of Plates without Tension

As shown in Chapter 4, classical plate dynamics can be represented by the following governing equation:

$$D\nabla^4 u = f, \tag{11.33}$$

or

$$D(\frac{\partial^4 u}{\partial x^4} + 2\frac{\partial^4 u}{\partial x^4 \partial y^2} + \frac{\partial^4 u}{\partial y^4}) = f,$$

with

$$D = \frac{Eh^3}{12(1-\nu^2)}.$$

The plate element is illustrated in Figure 11-3. To derive the FEM model of this plate bending element, we can follow similar steps in the modeling of beams. The details are shown in Appendix N. I summarize the steps in the following.

(1) Represent the stress-strain relationship:

$$\underbrace{\begin{bmatrix} M_{xx} \\ M_{yy} \\ M_{xy} \end{bmatrix}}_{\tau} = D \underbrace{\begin{bmatrix} 1 & \nu & 0 \\ \nu & 1 & 0 \\ 0 & 0 & \frac{1-\nu}{2} \end{bmatrix}}_{C_{\text{plate}}} \underbrace{\begin{bmatrix} \frac{\partial^2 u}{\partial x^2} \\ \frac{\partial^2 u}{\partial y^2} \\ 2\frac{\partial^2 u}{\partial x \partial y} \end{bmatrix}}_{\epsilon}. \tag{11.34}$$

(2) Define nodal coordinate U: In this case of plate-bending element, we have 4 nodes (x_1, y_1), (x_2, y_1), (x_1, y_2) and (x_2, y_2), and 12 corresponding nodal displacements:

$$U = \begin{bmatrix} U_1 \\ U_2 \\ U_3 \\ U_4 \\ \vdots \\ U_{12} \end{bmatrix} = \begin{bmatrix} u(x_1, y_1) \\ \theta_x(x_1, y_1) \\ \theta_y(x_1, y_1) \\ u(x_2, y_1) \\ \vdots \\ \theta_y(x_2, y_2) \end{bmatrix} = \begin{bmatrix} u(x_1, y_1) \\ \frac{\partial u}{\partial y}|_{(x_1, y_1)} \\ -\frac{\partial u}{\partial x}|_{(x_1, y_1)} \\ u(x_2, y_1) \\ \vdots \\ -\frac{\partial u}{\partial x}|_{(x_2, y_2)} \end{bmatrix}. \tag{11.35}$$

(3) Assume the displacement distribution $u(x, y)$ of the element:

$$\begin{aligned} u(x,y) &= \alpha_1 + \alpha_2 x + \alpha_3 y + \alpha_4 x^2 + \alpha_5 xy + \alpha_6 y^2 + \\ &\quad \alpha_7 x^3 + \alpha_8 x^2 y + \alpha_9 x y^2 + \alpha_{10} y^3 + \alpha_{11} x^3 y + \alpha_{12} x y^3. \end{aligned} \tag{11.36}$$

(4) Find the displacement interpolation matrix H such that $u(x, y) = HU$.

(5) Find the strain displacement matrix B such that $\epsilon = BU$.

(6) Integrate to obtain the FEM M, K and R matrices:

$$M^{(m)} = \int_{V^{(m)}} H^T \rho H dV = \int_{x=0}^{a} \int_{y=0}^{b} H^T \rho h H dy dx, \tag{11.37}$$

$$K^{(m)} = \int_{V^{(m)}} B^T C B dV = \int_{x=0}^{a} \int_{y=0}^{b} B^T C_{\text{plate}} B dy dx, \tag{11.38}$$

$$R^{(m)} = \int_{V^{(m)}} H^T f dV = \int_{x=0}^{a} \int_{y=0}^{b} H^T f h dy dx, \tag{11.39}$$

where h is the plate thickness.

11.5 FEM Modeling of Plates and Membranes with Tension

As shown earlier in this chapter, a general plate dynamics can be represented as:

$$D(\frac{\partial^4 u}{\partial x^4} + 2\frac{\partial^4 u}{\partial x^2 \partial y^2} + \frac{\partial^4 u}{\partial y^4}) = f + (T_x \frac{\partial^2 u}{\partial x^2} + T_y \frac{\partial^2 u}{\partial y^2} + 2T_{xy}\frac{\partial^2 u}{\partial x \partial y}) - \rho h \frac{\partial^2 u}{\partial t^2}. \quad (11.40)$$

Similar to Equation 11.6, we use $(f - \rho\ddot{u} + T_x \frac{\partial^2 u}{\partial x^2} + T_y \frac{\partial^2 u}{\partial y^2} + 2T_{xy}\frac{\partial^2 u}{\partial x \partial y})$ as the force term, and the resulting FEM plate model becomes:

$$\underbrace{\sum_m \int_{V^{(m)}} H^T \rho H dV}_{M} \ddot{U} +$$

$$\underbrace{(\sum_m \int_{V^{(m)}} B^T C B dV - \sum_m \int_{V^{(m)}} H^T (T_x \frac{\partial^2 H}{\partial x^2} + T_y \frac{\partial^2 H}{\partial y^2} + 2T_{xy}\frac{\partial^2 H}{\partial x \partial y}) dV)}_{K} U$$

$$= \underbrace{\sum_m \int_{V^{(m)}} H^T f dV}_{R}, \quad (11.41)$$

which is a complete plate bending model with tension contribution.

The modeling of membranes can be easily modified from the plate model. We can neglect the plate rigidity ($D = 0$), the resulting FEM membrane model becomes:

$$\underbrace{\sum_m \int_{V^{(m)}} H^T \rho H dV}_{M} \ddot{U} - \underbrace{\sum_m \int_{V^{(m)}} H^T (T_x \frac{\partial^2 H}{\partial x^2} + T_y \frac{\partial^2 H}{\partial y^2} + 2T_{xy}\frac{\partial^2 H}{\partial x \partial y}) dV}_{-K} U =$$

$$\underbrace{\sum_m \int_{V^{(m)}} H^T f dV}_{R}. \quad (11.42)$$

11.6 FEM Modeling of Moving Structures

The FEM analysis of moving structures is fairly easy. Recall the moving structure dynamics, we have convection derivative:

$$\frac{\partial}{\partial t'} = \frac{\partial}{\partial t} + V \cdot \nabla = \frac{\partial}{\partial t} + V_x \frac{\partial}{\partial x} + V_y \frac{\partial}{\partial y} + V_z \frac{\partial}{\partial z}. \tag{11.43}$$

Assume that we only have axial velocity V_z in the z direction, therefore, we replace force term f by

$$\begin{aligned} f - \rho \frac{\partial^2}{\partial t'^2} u &= f - \rho \left(\frac{\partial}{\partial t} + V_z \frac{\partial}{\partial z} \right)^2 u \\ &= f - \rho \left(\frac{\partial^2}{\partial t^2} + 2V_z \frac{\partial^2}{\partial t \partial z} + V_z^2 \frac{\partial^2}{\partial z^2} \right) u. \end{aligned} \tag{11.44}$$

Using untensioned beam as an example, the resulting FEM model becomes:

$$\begin{aligned} &\underbrace{\sum_m \int_{V^{(m)}} H^T \rho H dV}_{M} \ddot{U} + \underbrace{\sum_m \int_{V^{(m)}} 2V_z H^T \rho \frac{\partial H}{\partial z} dV}_{D} \dot{U} + \\ &\underbrace{\sum_m \int_{V^{(m)}} (B^T C B + V_z^2 H^T \rho \frac{\partial^2 H}{\partial z^2}) dV}_{K} U = \underbrace{\sum_m \int_{V^{(m)}} H^T f dV}_{R}. \end{aligned} \tag{11.45}$$

This equation has the following format:

$$M\ddot{U} + D\dot{U} + KU = R. \tag{11.46}$$

However, the D matrix does not introduce damping at all. This is a general form of a gyroscopic system, and D matrix shows the Coriolis force terms.

The FEM modeling of moving structures seems easy, however, the decoupling of the model is not as simple. We need to utilize complex modal analysis developed by Wickert [106, 107] to decouple the dynamics[1].

[1]When I first tried to decouple the system dynamics into modal coordinates, I used similarity transformation and could not get decoupled equations.

11.7 Summary

Finite Element Method provides us a convenient way of modeling complicated systems. As long as the dynamic equation can be defined, the FEM modeling can be done by following "recipes", as summarized in Appendix N.

In this thesis, I use analytic analysis to guide the modeling of uncertainties, controller design, and positioning of sensors and actuators. At the same time, I use FEM to plot all the mode shapes, bode plots of structures with different boundary conditions. The FEM modeling is programmed using Matlab.

Chapter 12

Conclusion

12.1 Primary Contributions

In this thesis, I was challenged by the task of suspending flexible structures with varying boundary conditions using magnetic forces. The scope of this thesis includes the sensor design, actuator design, structural modeling, controller design, sensor/actuator positioning, and experiment. In this thesis, I derived a peak envelope to represent the structural uncertainties with varying boundary conditions. I used a slow roll-up lead compensator to control the system. I also developed the sensor/actuator averaging method to robustly attenuate undesired resonance modes. At the end, I successfully suspend the flexible beam with varying boundary conditions and reached the design goal.

I hereby summarize the primary contributions of this thesis.

1. Developed integrated approaches for magnetic suspension and vibration control of flexible structures.

2. Developed theory to guide the designs of sensors and actuators for magnetic suspension.

3. Developed the novel sensor averaging and actuator averaging method for robust vibration control, and can be used to deal with varying boundary conditions.

4. Demonstrated the validation of the proposed ideas in a focused experiment on the magnetic suspension of tubular beams.

12.2 Future Work

In this project, due to limited time and limited hardware, we cannot finish studying all possible situations for non-contact processing. In this chapter, I would like to make a few suggestions of topics for future research, these topics may play critical roles for the extension of the suspension and vibration control technologies.

12.2.1 Force/Moment Control

In this project, we tried developing techniques of force/moment control on flexible structures. However, we have not reached satisfying results. The idea is to control a point of the structure by both force and moment. The expected advantage is that even when the sensor/actuator pair are located on a node of the vibration mode, the system is still observable/controllable.

However, it seems that it is difficult to control a system by using angle feedback and moment output. For beams, force to position will have a dereverberated transfer function with a slope of -30 dB/decade, and moment to angle will have a dereverberated transfer function with a slope of -10 dB/decade [27].

The advantage or disadvantage of using force/moment control need further studies.

12.2.2 Passive Wave-Absorbing Boundaries

In this project, we also tried to derive a passive boundary control method for beams, but we have not yet reached a solid result. In non-contact processing, it is usually possible to add damping from the boundaries of the processed elements, unless free-free boundary condition is required. If the boundaries can be added, it is possible not only to add damping, but also to design the damping coefficient such that all waves can be absorbed by the boundaries, and resonance will not exist.

Wave-absorbing boundaries had been introduced mainly for strings and membranes. The references are shown in Chapter 2. The idea is to use passive dampers on the boundaries to match the impedance of strings and membranes, such that the waves get completely dissipated by the passive damper. This boundary condition make the resonance modes completely disappear, and the Bode Plots of the strings and membranes become dereverberated transfer functions (backbones) only. As shown in Appendix O, the boundary that matches the string impedance is

$$F = -b\dot{u} = -\sqrt{\rho A T}\dot{u}. \tag{12.1}$$

I have tried to derive the boundary conditions that can match the impedance of beams, and make all the resonance modes disappear. As shown in Appendix O, our preliminary derivation show that it requires a force damper and a moment damper. The derived boundary that matches the beam impedance can be shown to be:

$$F = -b_F\dot{u} = -k\sqrt{\rho A E I}\dot{u}, \tag{12.2}$$

$$M = -b_M\dot{\theta} = -\frac{1}{k}\sqrt{\rho A E I}\dot{\theta}. \tag{12.3}$$

Both damping coefficients b_F and b_M are functions of wavenumber k, and there seems no simple solution to implement such designs. It will be valuable to further prove if there are other passive boundary designs that can match the beam impedance and make all the waves not reflecting. If such boundary conditions exist and can be implemented practically, the beam vibration control can be greatly simplified.

12.2.3 Non-contact Passive Damper Designs

For non-contact processing, it will be advantageous if we can design non-contact passive dampers, and we can place them along the structure. For non-magnetic conductive materials, it seems easy to design such magnetic dampers by just applying a dc magnetic field through the material. However, for ferromagnetic materials, there seems no good design yet to introduce damping to the material without touching it.

From the analysis of air damping, we realize that if the damping force is proportional to speed only, it will become insignificant at high frequencies. The main reason is that at high frequencies, the beam stiffness becomes much greater than the damping force. An effective non-contact damper design for steel target does not seem to exist yet.

12.2.4 Magnetic Suspension of Moving Structures

In this thesis, I evaluated the critical speed limit of suspended structures. In reality, there may be more issues that need to solved when the structure is moving at a high speed. Possible difficulties are due to:

1. Magnetic diffusion of the moving conductors.

2. Critical speed of moving structures.

In Chapter 10, I suggested the temporary moving boundary design to avoid critical speed for strings. This idea remains doubtful at this moment, and needs further theoretical and experimental proof in the future.

12.2.5 Electrostatic Suspension

Electrostatic suspension is theoretically introduced in this thesis, and ongoing research literatures are listed in Chapter 2. Topics in electrostatic suspension are separated into two categories: conductor/semiconductor suspension and dielectric suspension. The theoretical modeling of conductor/semiconductor suspension is fairly simple since the response is fast and electrostatic force can be considered static. The modeling of dielectric suspension is more complicated, and need to be further verified. The following topics will need to be studied in the future:

1. Sensor design to detect positions of dielectric materials.

2. Actuator design.

3. High-voltage amplifier circuit design

Experiments will need to be done to evaluate the robustness or the suspension, and the possibility of applying electrostatic suspension in manufacturing processes.

12.2.6 Extension to Sensor Averaging Method

In Chapter 6, we show that sensor averaging method is a non-model-based spatial filter, and show the dual properties between temporal filter and spatial filter. We can further look into this issue and see how much we can apply the theories in discrete time filtering to discrete sensor filtering. It may be advantageous to design weightings for discrete sensors to implement low-pass filters (as in Chapter 6), high-pass filters, band-pass filters, and band-stop filters. The phase should be particularly taken into considerations.

Appendix A

Material Properties

In this chapter, I summarize the properties of various materials, including elastic properties, material damping properties, and electromagnetic properties.

A.1 Elastic Properties

The elasticity properties of various materials are shown in Table A.1.

Table A.1: Elasticity properties of materials, summarized from Reismann [92]

Materials	Poisson's ratio ν	Young's modulus E (Pa)
Aluminum	0.34	6.89×10^{10}
Copper	0.34	8.96×10^{10}
Glass	0.25	6.89×10^{10}
Nylon	0.40	2.83×10^{10}
Steel	0.29	20.7×10^{10}

A.2 Material Damping Properties

The internal damping of materials can be modeled by using complex Young's modulus:

$$\hat{E} = E(1 + j\eta), \tag{A.1}$$

where $\hat{E}$ is the complex Young's modulus, E is Young's modulus, and η is the loss factor. Loss factor is a complicated function of many variables. For the same material, it varies with temperatures and vibration frequencies. Table A.2 is summarized from various references, and can only be used as an estimate.

Table A.2: Damping properties of materials, summarized from [62, 15, 29]

Materials	Processing	Loss factor η
Aluminum	alloy	$0.0004 \sim 0.001$
Aluminum	pure	$0.00002 \sim 0.002$
Cast iron		$0.003 \sim 0.03$
Copper		0.002
Glass		$0.0006 \sim 0.002$
High-Polymer		$0.8 \sim 2.0$
Steel		$0.001 \sim 0.008$

A.3 Electromagnetic Properties

The electromagnetic properties of various materials are shown in Table A.3. The dielectric and magnetic susceptibilities are defined as:

$$\epsilon = (1 + \chi_e)\epsilon_0 \qquad \epsilon_0 = 8.854 \times 10^{-12}\text{F/m} \tag{A.2}$$

$$\mu = (1 + \chi_m)\mu_0 \qquad \mu_0 = 4\pi \times 10^{-7}\text{H/m}. \tag{A.3}$$

The properties are dependent on the material components, and the list can only be used as an estimate. For any particular materials, engineers need to consult the manufacturers or do experiments to determine the real values. Also notice when the conductivity σ is small, Ohm's Law $J = \sigma E$ may not be valid.

Table A.3: Electromagnetic properties of materials, summarized from Haus [44]

Materials	Conductivity σ (mhos/m)	Dielectric Susceptibilities χ_e	Magnetic Susceptibilities χ_m
Air		0.00059	3.6×10^{-7}
Aluminum	3.5×10^7		2.2×10^{-5}
Copper	5.7×10^7		-1.0×10^{-5}
Ferrite			5000
Glass, flint		$5.6 \sim 8.9$	
Glass, ordinary	10^{-12}		
Paper		$1.0 - 1.5$	
Quartz, fused	$< 10^{-17}$	$3.7 \sim 4.1$	
Si-Fe laminations			7×10^4
Steel	$0.5 \sim 1.0 \times 10^7$		$5.5 \sim 88 \times 10^3$
Water	2×10^{-4}		-0.9×10^{-5}
Water Vapor		0.00705	

Appendix B

Elasticity Relations of Structural Elements

I will briefly go through the derivation of stress-strain relations for materials. From elasticity, we have general stress-strain relation known as Hook's Law. For different elements, we can integrate the stress-strain law and reduce it to simpler forms. The final result of this elasticity equation can be used to derive the structural dynamic equations by including Newton's Second Law $F = ma$.

B.1 Fundamentals of Elasticity

The fundamental representation of material's linear elasticity is [92]:

$$\tau_{ij} = C_{ijkl}\epsilon_{kl}, \tag{B.1}$$

where τ_{ij} is stress tensor, ϵ_{kl} is strain tensor, and C_{ijkl} is the elastic constants (81 constants). This is also known as Hook's Law, and usually takes the form of $F = kx$ for springs. For anisotropic materials, C_{ijkl} has 21 independent constants, and for isotropic materials, C_{ijkl} has only 2 independent constants. In text books, the material properties are usually represented by 5 constants:E (Young's Modulus), ν (Poisson's ratio), K (Bulk Modulus), G (Shear Modulus), and λ, and any two of them can decide the other three. If we know E and ν, then

$$K = \frac{E}{2(1-2\nu)} \qquad G = \frac{E}{2(1+\nu)} \qquad \lambda = \frac{E\nu}{(1+\nu)(1-2\nu)}. \tag{B.2}$$

The elasticity relation can be reduced for isotropic materials as:

$$\tau_{ij} = \lambda\epsilon_{kk}\delta_{ij} + 2G\epsilon_{ij}. \tag{B.3}$$

Together with the compatibility equation of displacement:

$$2\epsilon_{ij} = u_{i,j} + u_{j,i}, \tag{B.4}$$

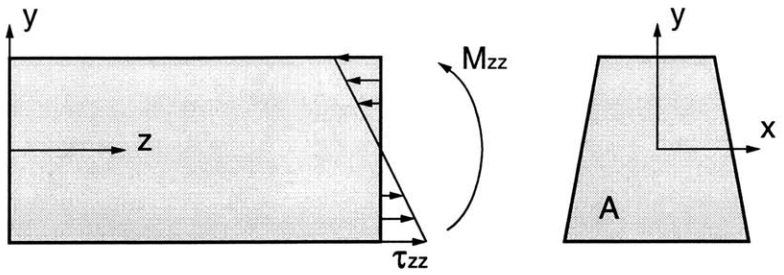

Figure B-1: A beam model: bending moment represented by the integration of stress.

we can solve the elasticity relations for a general 3D element:

$$\begin{bmatrix} \tau_{xx} \\ \tau_{yy} \\ \tau_{zz} \\ \tau_{xy} \\ \tau_{yz} \\ \tau_{zx} \end{bmatrix} = \frac{E(1-\nu)}{(1+\nu)(1-2\nu)} \begin{bmatrix} 1 & \frac{\nu}{1-\nu} & \frac{\nu}{1-\nu} & 0 & 0 & 0 \\ \frac{\nu}{1-\nu} & 1 & \frac{\nu}{1-\nu} & 0 & 0 & 0 \\ \frac{\nu}{1-\nu} & \frac{\nu}{1-\nu} & 1 & 0 & 0 & 0 \\ 0 & 0 & 0 & \frac{1-2\nu}{2(1-\nu)} & 0 & 0 \\ 0 & 0 & 0 & 0 & \frac{1-2\nu}{2(1-\nu)} & 0 \\ 0 & 0 & 0 & 0 & 0 & \frac{1-2\nu}{2(1-\nu)} \end{bmatrix} \begin{bmatrix} \frac{\partial u_x}{\partial x} \\ \frac{\partial u_y}{\partial y} \\ \frac{\partial u_z}{\partial z} \\ \frac{\partial u_x}{\partial y} + \frac{\partial u_y}{\partial x} \\ \frac{\partial u_y}{\partial z} + \frac{\partial u_z}{\partial y} \\ \frac{\partial u_z}{\partial x} + \frac{\partial u_x}{\partial z} \end{bmatrix} \tag{B.5}$$

B.2 Elasticity Relations of Different Elements

For specific elements, we can simplify the elasticity relation by integration. Use Euler-Bernoulli beam element as an example, as shown in Figure B-1. We have bending moment as an integration of stress:

$$M_{zz} = -\int_A y\tau_{zz} dA, \tag{B.6}$$

where A is the cross sectional area. We also have displacement u_z in z direction as a function of strain:

$$u_z = -y\frac{du_y}{dz}. \tag{B.7}$$

Assume $\tau_{xx} = \tau_{yy} = 0$, from Equation B.5, we can obtain the stress-strain relation:

$$\tau_{zz} = E\frac{\partial u_z}{\partial z} + \nu(\tau_{xx} + \tau_{yy}) = -Ey\frac{d^2u_y}{dz^2} + \nu(\tau_{xx} + \tau_{yy}). \tag{B.8}$$

If we neglect the stress on x and y direction: $\nu(\tau_{xx} + \tau_{yy}) = 0$, and integrate over area A to match bending moment M_{zz}, we can get:

$$\int_A y\tau_{zz} dA = \int_A -yEy\frac{d^2u_y}{dz^2} dA \Rightarrow M_{zz} = EI\frac{d^2u_y}{dz^2}. \tag{B.9}$$

Similar methods can be applied to other elements, such as Timoshenko beam element (consider both bending deformation and shear deformation) and plate bending element. The following list summarizes the elasticity relations for a few different elements [9, Chapter 4].

1. Bar element under axial load: (integrate over cross sectional area A)

$$\tau_{zz} = E\frac{du}{dz}. \tag{B.10}$$

2. Euler-Bernoulli beam element: (integrate over cross sectional area A)

$$M_{zz} = EI\frac{d^2u}{dz^2}. \tag{B.11}$$

3. Plate bending element: (reduce the 3D stress-strain relations to plane-stress element by assuming $\tau_{xz} = \tau_{yz} = \tau_{zz} = 0$, and integrate over thickness h)

$$\begin{bmatrix} M_{xx} \\ M_{yy} \\ M_{xy} \end{bmatrix} = \frac{Eh^3}{12(1-\nu^2)} \begin{bmatrix} 1 & \nu & 0 \\ \nu & 1 & 0 \\ 0 & 0 & \frac{1-\nu}{2} \end{bmatrix} \begin{bmatrix} \frac{\partial^2 u}{\partial x^2} \\ \frac{\partial^2 u}{\partial y^2} \\ 2\frac{\partial^2 u}{\partial x \partial y} \end{bmatrix}. \tag{B.12}$$

Appendix C

Orthogonality of Beam Solutions and Decoupling of Beam Equations

The beam equation is:

$$EI\frac{\partial^4 u}{\partial z^4} + \rho A\frac{\partial^2 u}{\partial t^2} = f.$$

The homogeneous solution is:

$$u(z,t) = \sum_{n=1}^{\infty} \xi_n(t)\phi_n(z), \tag{C.1}$$

where ξ_n is nth modal coordinate, and ϕ_n is nth modal shape. Replace u by mth mode and nth mode:

$$m\text{th mode:} \quad EI\frac{d^4\phi_m}{dz^4} - \omega_m^2\rho A\phi_m = 0, \quad (\times\phi_n), \quad (\int_0^L dz). \tag{C.2}$$

$$n\text{th mode:} \quad EI\frac{d^4\phi_n}{dz^4} - \omega_n^2\rho A\phi_n = 0, \quad (\times\phi_m), \quad (\int_0^L dz). \tag{C.3}$$

Then the first equation times ϕ_n and integrates over length L, and the second equation times ϕ_m and integrates over length L. Subtract the first equation from the second equation, and we got

$$\begin{aligned}
&\left(\omega_m^2 - \omega_n^2\right)\int_0^L \rho A\phi_m\phi_n dz \\
= \;& EI\int_0^L \left(\phi_n\frac{d^4\phi_m}{dz^4} - \phi_m\frac{d^4\phi_n}{dz^4}\right)dz \\
= \;& EI\left(\phi_n\frac{\partial^3\phi_m}{\partial z^3}\Big|_0^L - \frac{\partial\phi_n}{\partial z}\frac{\partial^2\phi_m}{\partial z^2}\Big|_0^L + \int_0^L \frac{\partial^2\phi_n}{\partial z^2}\frac{\partial^2\phi_m}{\partial z^2}dz - \right. \\
& \left.\phi_m\frac{\partial^3\phi_n}{\partial z^3}\Big|_0^L + \frac{\partial\phi_m}{\partial z}\frac{\partial^2\phi_n}{\partial z^2}\Big|_0^L - \int_0^L \frac{\partial^2\phi_m}{\partial z^2}\frac{\partial^2\phi_n}{\partial z^2}dz\right)
\end{aligned}$$

$$= EI\left(\phi_n\frac{d^3\phi_m}{dz^3}\Big|_0^L - \frac{d\phi_n}{dz}\frac{d^2\phi_m}{dz^2}\Big|_0^L - \phi_m\frac{d^3\phi_n}{dz^3}\Big|_0^L + \frac{d\phi_m}{dz}\frac{d^2\phi_n}{dz^2}\Big|_0^L\right). \qquad \text{(C.4)}$$

All four terms in the last part will be zero because of the geometric boundary conditions. Hence we prove that each mode is orthogonal to each other, and we conclude the orthogonality by defining the nth modal mass M_n and nth modal stiffness K_n:

$$\int_0^L \rho A\phi_m\phi_n dz = \begin{cases} 0 & \text{if m} \neq \text{n}, \\ M_n & \text{if m} = \text{n}. \end{cases} \qquad \text{(C.5)}$$

$$\int_0^L EI\phi_n\frac{d^4\phi_m}{dz^4}dz = \begin{cases} 0 & \text{if m} \neq \text{n}, \\ K_n = M_n\omega_n^2 & \text{if m} = \text{n}. \end{cases} \qquad \text{(C.6)}$$

To decouple the beam equation, we rewrite the beam equation by letting $u(z,t) = \sum \xi_n(t)\phi_n(z)$:

$$\begin{aligned} & EI\frac{\partial^4 u}{\partial z^4} + \rho A\frac{\partial^2 u}{\partial t^2} = f \\ \Rightarrow \quad & EI\sum_{n=1}^{\infty}\xi_n\frac{d^4\phi_n}{dz^4} + \rho A\sum_{n=1}^{\infty}\frac{d^2\xi_n}{dt^2}\phi_n = f \quad (\times\phi_m) \quad (\int_0^L dz) \\ \Rightarrow \quad & EI\sum_{n=1}^{\infty}\xi_n\int_0^L \phi_m\frac{d^4\phi_n}{dz^4}dz + \rho A\sum_{n=1}^{\infty}\frac{d^2\xi_n}{dt^2}\int_0^L \phi_m\phi_n dz = \int_0^L f\phi_m dz \\ \Rightarrow \quad & K_m\xi_m + M_m\frac{d^2\xi_m}{dt^2} = \int_0^L f\phi_m dz \equiv N_m, \qquad \text{m=1, 2, 3, } \cdots\infty. \end{aligned} \qquad \text{(C.7)}$$

Thereby we obtain the decoupled ordinary differential equations in modal coordinates.

Appendix D

DSP Programming by using dSPACE

This chapter describes the programming of DSP by using dSPACE. We use both dSPACE DSP board and software. The boards that we use are: DS1003 (DSP), DS 2201 (multiple I/O), and DS2103 (multiple D/A). We use total of 16 channel A/D for sensors, and 32 channels D/A for actuators. The software we use are Rti40, Trace40, and Cockpit40.

We build control block diagrams in MATLAB Simulink environment, and run the software Rti40 that compiles the code and downloads it to the DSP board. Trace40 is used to monitor variables in real time, and Cockpit40 is used to change variables in real time.

Besides using the standard dSPACE interface, we also use MATLAB code to interface with DSP board while doing real time dynamic analyzing.

D.1 Programming by using dSPACE Software

The basic operations are done by using dSPACE software, it uses MATLAB Simulink as the user interface.

D.1.1 Programming by using Simulink Block Diagram

The Simulink blocks that I build to control the system is demonstrated in Figure D-1. It is an example of using sensor averaging and actuator averaging to do beam suspension control, and only the last 2 sensors and 2 actuators are shown. We first read sensor outputs from A/D, and then linearize them into real x and y coordinates. I average the sensor outputs, and apply a lead compensator to this output. The output current is calculated by feedback linearization, and then the same current is applied to 2 actuators. The "Dynamic Signal Analyzer" block is added to do real-time dynamic analyzing, and will be discussed later.

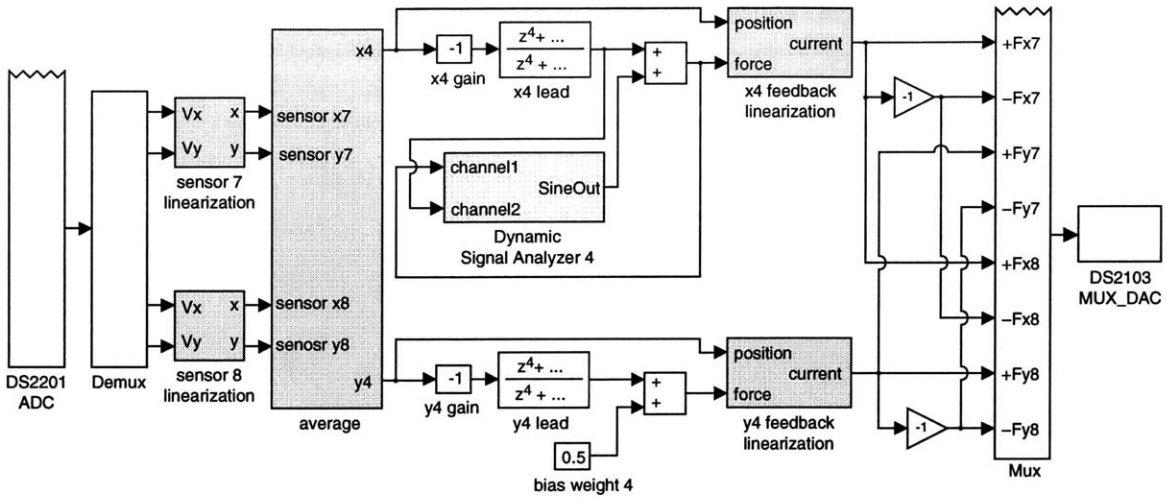

Figure D-1: Design of Simulink blocks for real-time control by using dSPACE DSP board.

D.1.2 Changing Parameters in Real-Time

We can change the parameters of the controller in real time by using dSPACE Cockpit40. A sample interface is shown in Figure D-2

D.1.3 Synchronous Output of 32 Channels of D/A Converters

To avoid making the system more complicated, we choose to output the actuator command synchronously. To output the 32 channels of D/A converters at the same time by using dSPACE DS2103 board, we specify the following commands in the file *filename.usr*:[1]

```
static void usr_initialize(void)
{
ds2103_set_outmode(DS2103_1_BASE,1,DS2103_LATCH);
ds2103_set_outmode(DS2103_1_BASE,2,DS2103_LATCH);
ds2103_set_outmode(DS2103_1_BASE,3,DS2103_LATCH);
ds2103_set_outmode(DS2103_1_BASE,4,DS2103_LATCH);
ds2103_set_outmode(DS2103_1_BASE,5,DS2103_LATCH);
ds2103_set_outmode(DS2103_1_BASE,6,DS2103_LATCH);
ds2103_set_outmode(DS2103_1_BASE,7,DS2103_LATCH);
ds2103_set_outmode(DS2103_1_BASE,8,DS2103_LATCH);
}
```

[1]This information is provided by Mr. Albert Schwarte, dSPACE GmbH, Technologiepark 25, 33100 Paderborn, Germany, Tel: +49 5251 1638 0, Fax: +49 5251 66529, Email: aschwarte@dspace.de

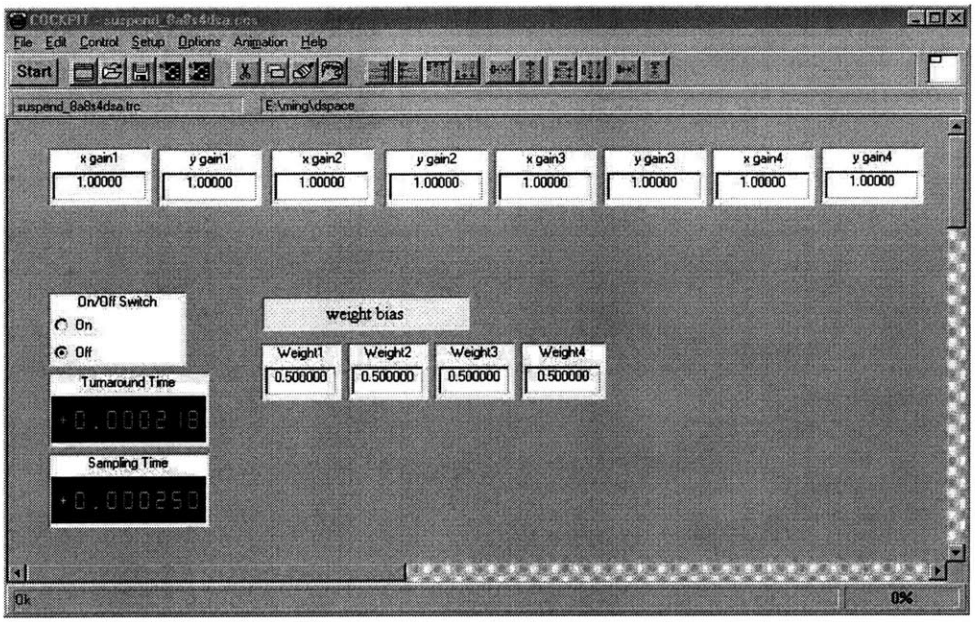

Figure D-2: PC interface to change controller parameters in real time by using dSPACE Cockpit.

D.1.4 Block Diagrams for Sensor Linearization

Sensor linearization is implemented by using curve fitting in this project. When I use the Simulink block of math function: **f(n)**, as shown in Figure D-3, the total calculation time increases by about 100 μs, which is unreasonably long. Therefore, I build the blocks to produce the sensor linearization, as shown in Figure D-4, and the total calculation time increases by only 10 μs. The reason of causing long calculation time by using **f(n)** block is still unknown.

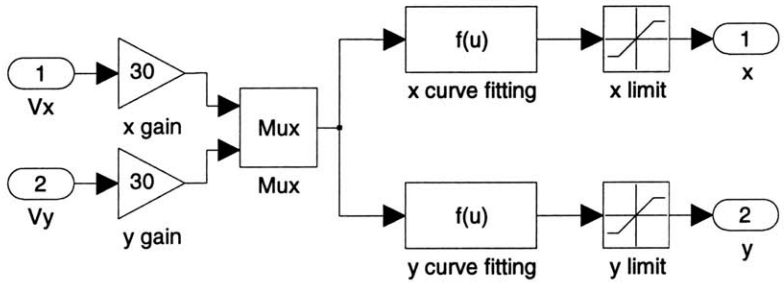

Figure D-3: Sensor linearization by using **f(n)** block.

D.2 Interfacing with DSP by using MATLAB Code

To perform the system dynamic analyzer in real time, I adopted a MATLAB code written by Ms. Lilienkamp [67] in our lab. I modified the code from SISO identification to MIMO identification, and the program can choose frequency points adaptively.

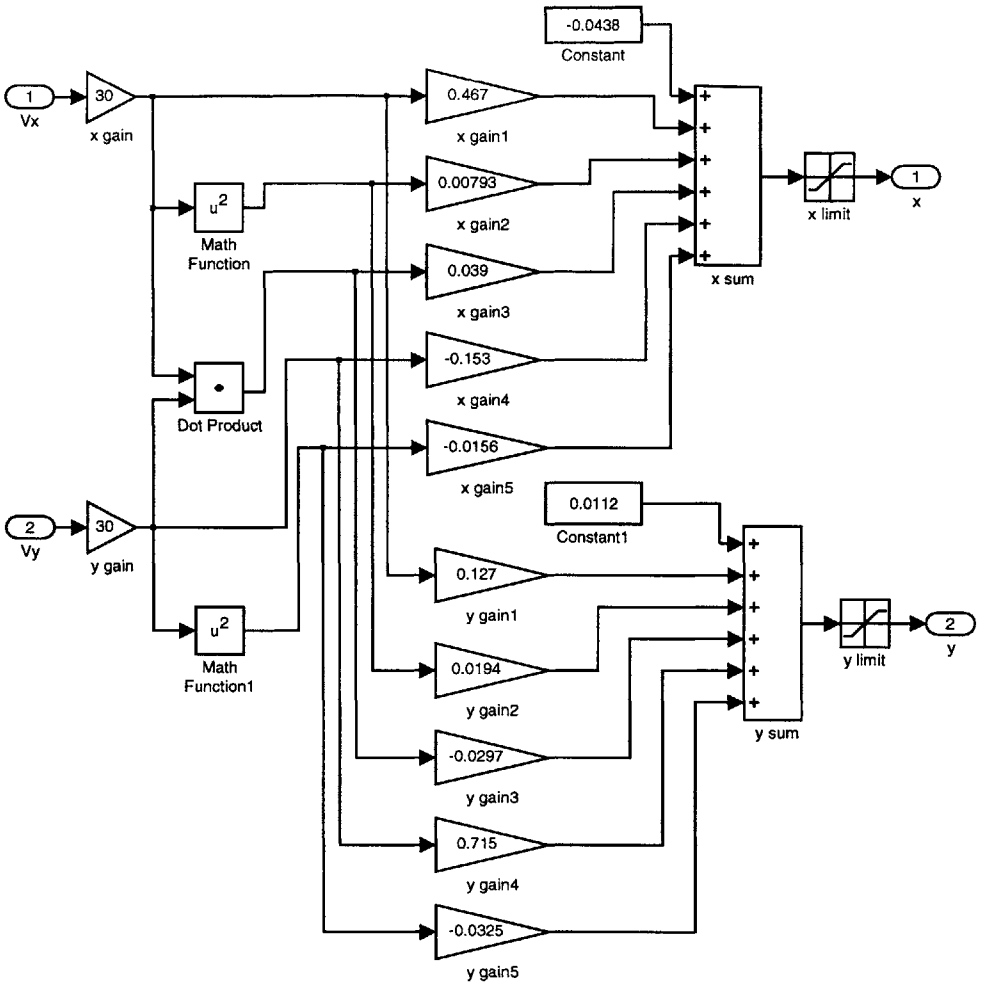

Figure D-4: Sensor linearization by building mathematical blocks.

The algorithm of this code is shown in Figure D-5 as a flow chart. It is utilizing swept sine excitation method. Users can specify the excitation frequencies and amplitudes. This code runs basically in 2 loops. The major loop finishes all specified frequency points, and the minor loop finishes all multiple inputs for each frequency point. And users can interrupt this code at anytime to change the amplitude, go back a frequency point, or to exit the program.

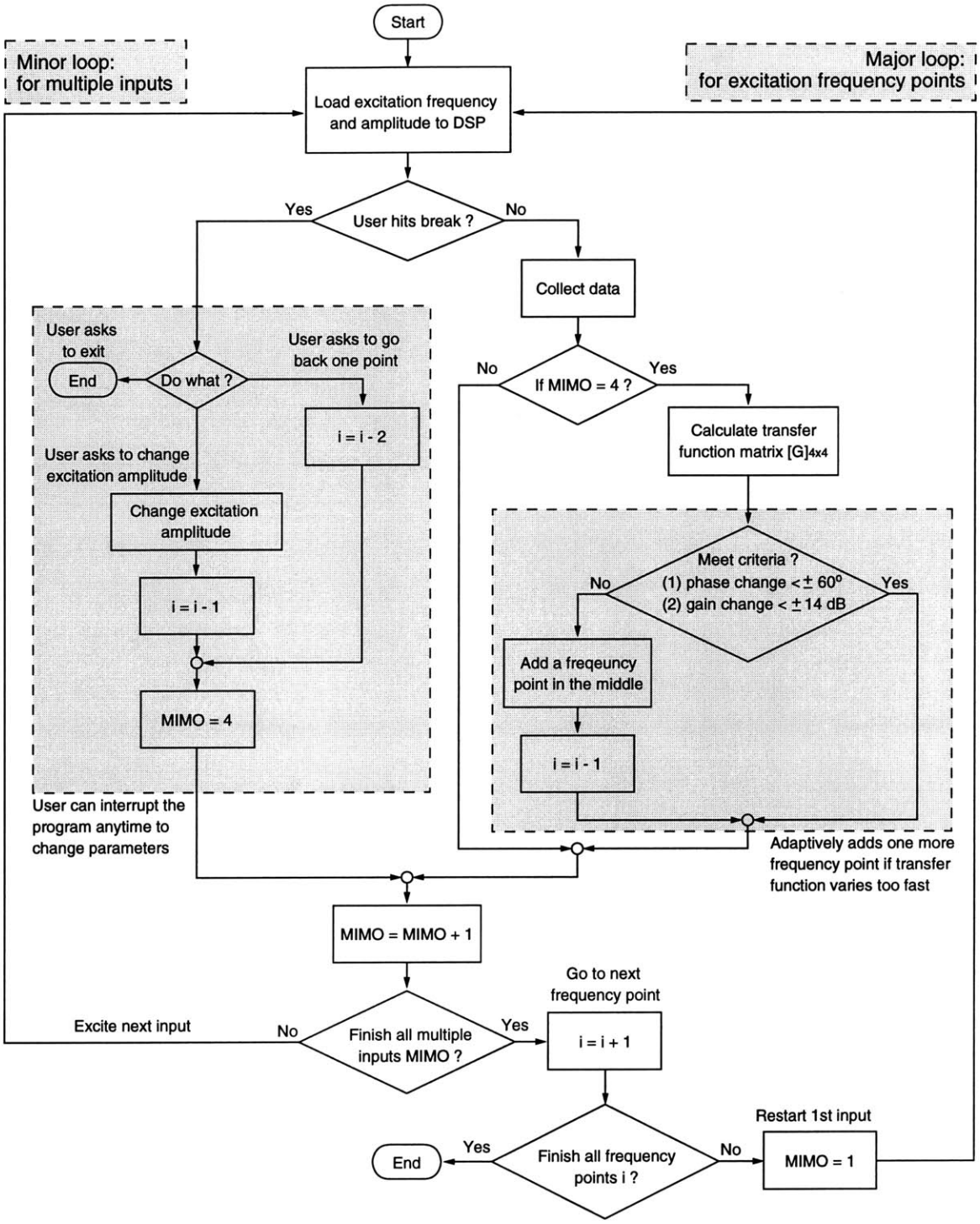

Figure D-5: Flow chart of a MATLAB code of a dynamic analyzer for MIMO systems.

Appendix E

Commonly Used Windows for FIR Filters

In Oppenheim [87, Chapter 7], it describes the following commonly used windows for FIR(Finite Impulse Response) filters:

1. Rectangular window

$$w[n] = \begin{cases} 1 & 0 \leq n \leq M \\ 0 & \text{otherwise} \end{cases} \tag{E.1}$$

2. Triangular window (Bartlett window)

$$w[n] = \begin{cases} 2n/M & 0 \leq n \leq M/2 \\ 2 - 2n/M & M/2 < n \leq M \\ 0 & \text{otherwise} \end{cases} \tag{E.2}$$

3. Hanning window

$$w[n] = \begin{cases} 0.5 - 0.5\cos(2\pi n/M) & 0 \leq n \leq M \\ 0 & \text{otherwise} \end{cases} \tag{E.3}$$

4. Hamming window

$$w[n] = \begin{cases} 0.54 - 0.46\cos(2\pi n/M) & 0 \leq n \leq M \\ 0 & \text{otherwise} \end{cases} \tag{E.4}$$

5. Blackman window

$$w[n] = \begin{cases} 0.42 - 0.5\cos(2\pi n/M) + 0.08\cos(4\pi n/M) & 0 \leq n \leq M \\ 0 & \text{otherwise} \end{cases} \tag{E.5}$$

The following figures show the shapes and frequency responses of these windows by using 9 points. The corresponding commands in Matlab to create windows are boxcar, triang, hanning, hamming, and blackman, and the command to create the frequency response is freqz. It shows that Rectangular window has the narrowest mainlobe, and Blackman window has the lowest sidelobe.

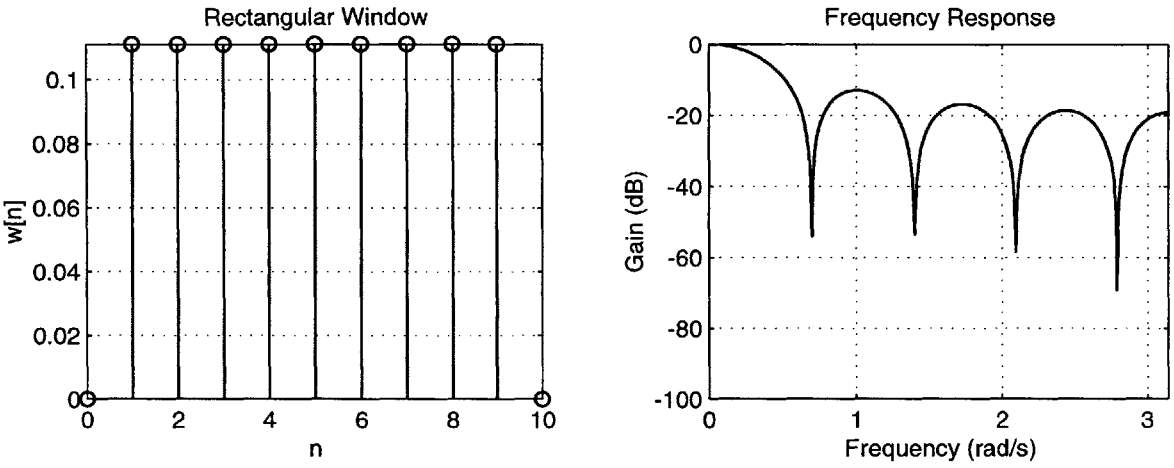

Figure E-1: Rectangular window and its frequency response.

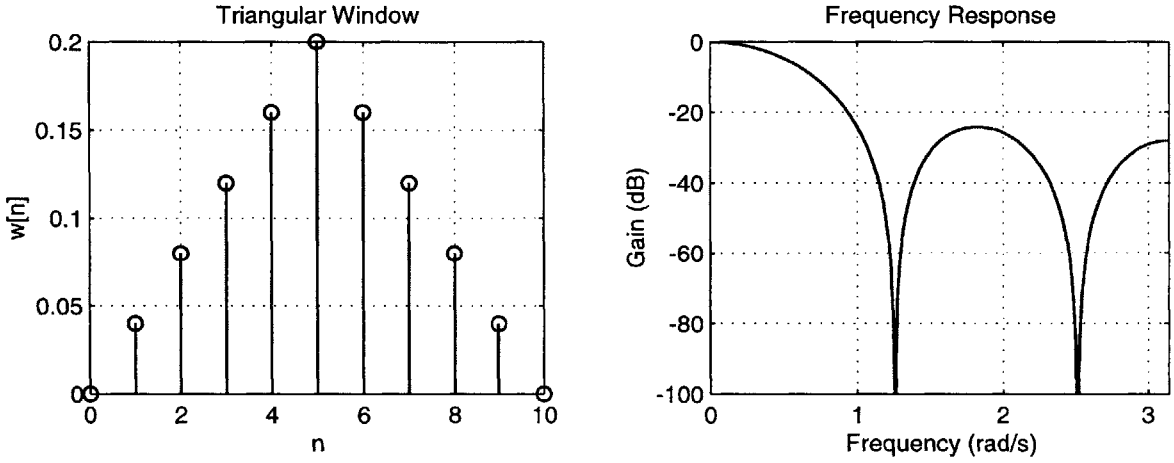

Figure E-2: Triangular window and its frequency response.

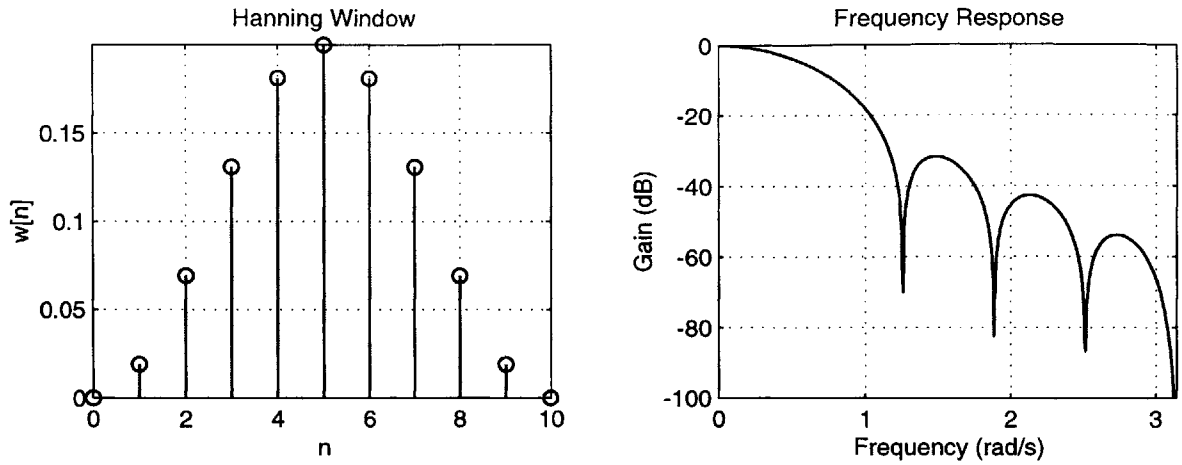

Figure E-3: Hanning window and its frequency response.

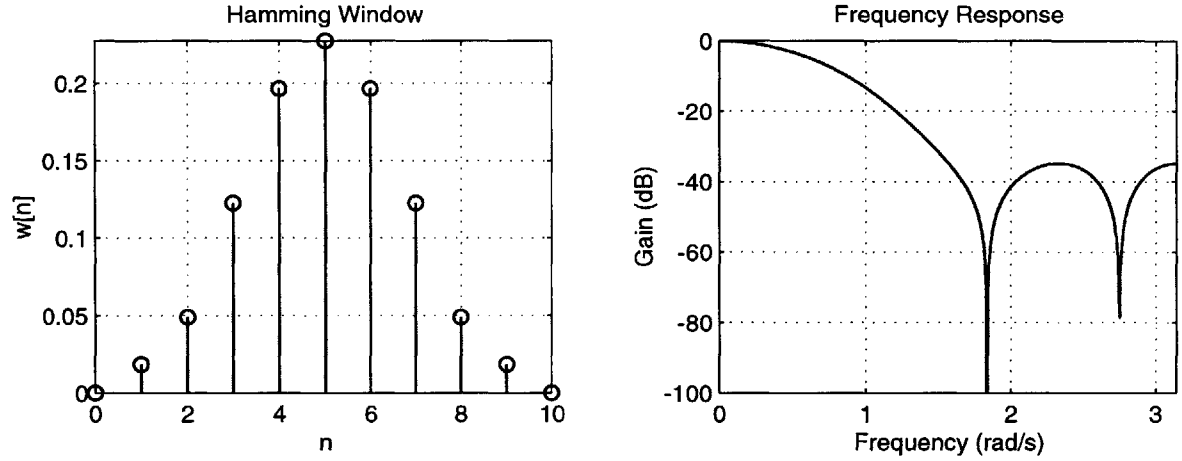

Figure E-4: Hamming window and its frequency response.

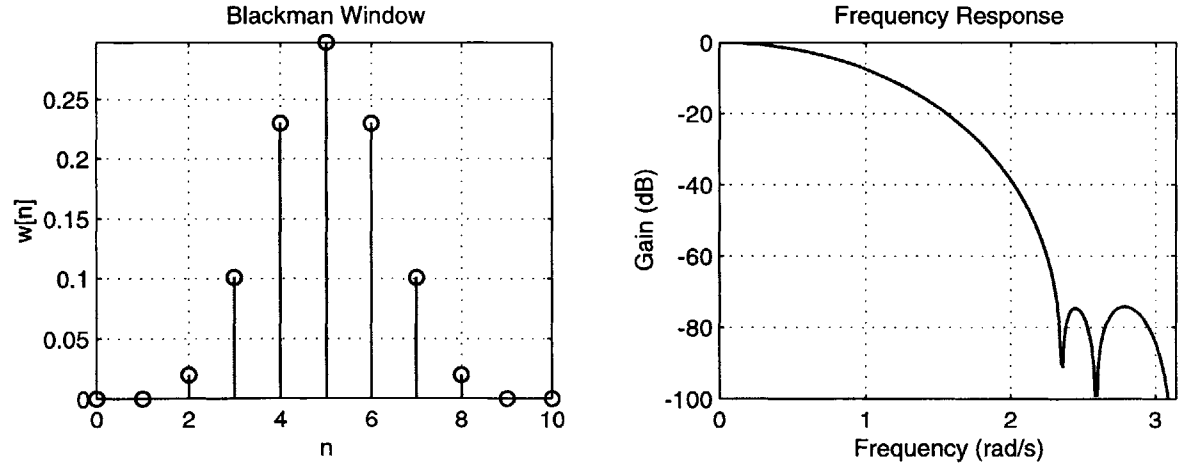

Figure E-5: Blackman window and its frequency response.

Appendix F

Proof of Circular Continuous-Sensor Averaging for Plates and Membranes

Proof of Equation 6.44 of the averaged output of a continuous circular sensing on plates and membranes. Given sinusoidal modal shape

$$\phi_n(x,y) = (C_{n1}\cos\alpha_n x + C_{n2}\sin\alpha_n x)\cdot(C_{n3}\cos\beta_n y + C_{n4}\sin\beta_n y),$$

Prove that:

$$\frac{1}{2\pi}\int_0^{2\pi}\phi_n(x_o + d\cos\theta, y_o + d\sin\theta)d\theta = \phi_n(x_o,y_o)\frac{1}{2\pi}\int_0^{2\pi}\cos(k_n d\cos\theta)d\theta,$$

where $\alpha_n^2 + \beta_n^2 = k_n^2$.

[**Proof**] Given:

$$\frac{1}{2\pi}\int_0^{2\pi}\phi_n(x_o + d\cos\theta, y_o + d\sin\theta)d\theta \tag{F.1}$$

Take the advantage of symmetry of four quadrants, as shown in Figure F-1. We average the four sensors at angles $\pm\theta$ and $\pi \pm \theta$ first, and then integrate from $\theta = 0$ to $\frac{\pi}{2}$. Average the 2 points at angles $\pm\theta$, Equation F.1 becomes

$$\frac{1}{\pi}\int_0^{\pi}\phi_n(x_o + d\cos\theta, y_o)\cdot\cos(\beta_n d\sin\theta)d\theta. \tag{F.2}$$

Average the 4 points, Equation F.2 becomes

$$\phi_n(x_o,y_o)\cdot\frac{2}{\pi}\int_0^{\frac{\pi}{2}}\cos(\alpha_n d\cos\theta)\cdot\cos(\beta_n d\sin\theta)d\theta \tag{F.3}$$

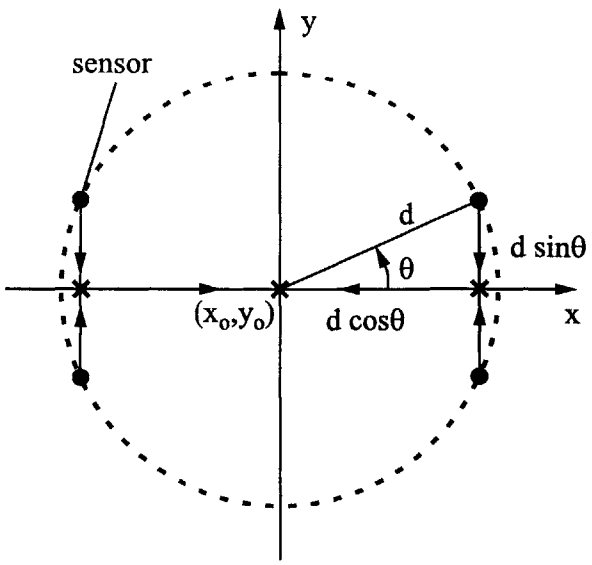

Figure F-1: Average four sensors at angles $\pm\theta$ and $\pi \pm \theta$.

We take the gain from Equation F.3 and further simplify it:

$$\begin{aligned}
& \frac{2}{\pi}\int_0^{\frac{\pi}{2}} \cos(\alpha_n d\cos\theta)\cdot\cos(\beta_n d\sin\theta)d\theta \\
= & \frac{1}{\pi}\int_0^{\frac{\pi}{2}} \cos(\alpha_n d\cos\theta+\beta_n d\sin\theta)+\cos(\alpha_n d\cos\theta-\beta_n d\sin\theta)d\theta \\
= & \frac{1}{\pi}\int_0^{\frac{\pi}{2}} \cos(k_n d\cos(\psi_n-\theta))+\cos(k_n d\cos(\psi_n+\theta))d\theta \\
= & \frac{1}{\pi}\int_{-\frac{\pi}{2}}^{\frac{\pi}{2}} \cos(k_n d\cos(\psi_n+\theta))d\theta, \qquad \text{(F.4)}
\end{aligned}$$

where $\psi_n = \tan^{-1}(\beta_n/\alpha_n)$ is the angle at which wave travels. Because the function $\cos(k\cos\theta)$ is periodic with θ of period π, Equation F.4 becomes

$$\frac{1}{\pi}\int_0^{\pi} \cos(k_n d\cos\theta)d\theta,$$

or equivalently,

$$\frac{1}{2\pi}\int_0^{2\pi} \cos(k_n d\cos\theta)d\theta.$$

Appendix G

Analytical Field Analysis of Dipole-Quadrupole Actuators

This chapter describes the analytical field analysis of the dipole-quadrupole actuator. The conceptual design of the dipole-quadrupole actuator field is shown in Figure G-1. It has 3 field components: dipole field, x-quadrupole filed, and y-quadrupole field. Their field distribution will be calculated in the following sections.

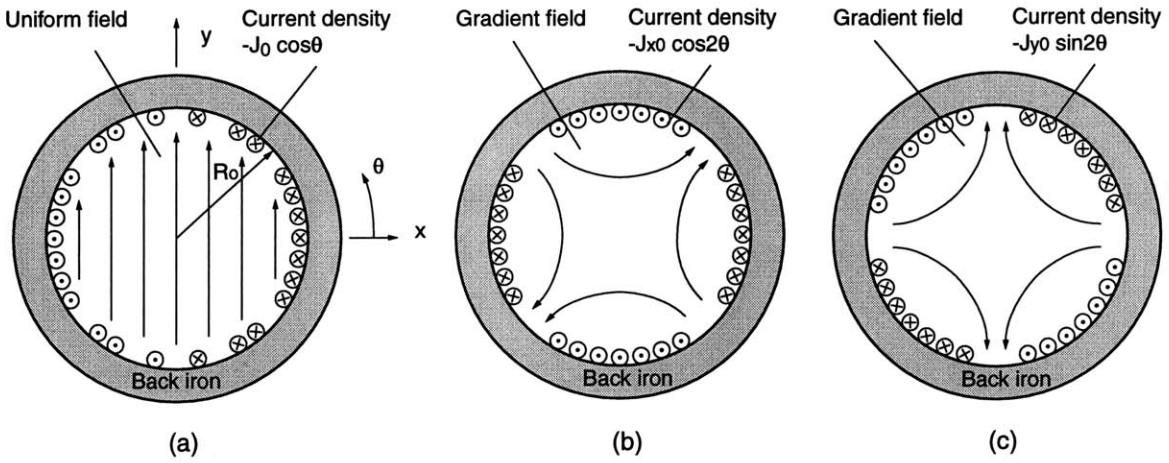

Figure G-1: Field Analysis of the Dipole-Quadrupole actuator: (a) a dipole field, (b) x-quadrupole field, and (c) y-quadrupole field.

G.1 Dipole Field

As shown in Figure G-1(a), the dipole field is driven by a current distribution of:

$$J_{dipole}(\theta) = -J_o \cos\theta. \tag{G.1}$$

Since the current distribution has a period of 2π, the associated field must be azimuthal periodic with a period or 2π. Hence we can solve the magnetic scalar potential

Ψ by choosing the solution of Laplace's Equation as:

$$\Psi = a_1 + a_3 \ln r + b_1 r\cos\theta + b_2 r\sin\theta + b_3\frac{\cos\theta}{r} + b_4\frac{\sin\theta}{r}. \tag{G.2}$$

And the magnetic field intensity $\vec{H}$ can be obtained as:

$$H_r = -\frac{\partial\Psi}{\partial r} = -a_3\frac{1}{r} - b_1\cos\theta - b_2\sin\theta + b_3\frac{\cos\theta}{r^2} + b_4\frac{\sin\theta}{r^2}, \tag{G.3}$$

$$H_\theta = -\frac{1}{r}\frac{\partial\Psi}{\partial\theta} = b_1\sin\theta - b_2\cos\theta + b_3\frac{\sin\theta}{r^2} - b_4\frac{\cos\theta}{r^2}. \tag{G.4}$$

We can now include the boundary conditions to solve the coefficients of the solution:

1. When $r \to 0$, Ψ is finite, thus $a_3 = b_3 = b_4 = 0$.

2. Assume the back iron has $\mu \gg \mu_o$, we have $H_\theta = -J_{dipole}$, thus $b_1 = 0$, $b_2 = -J_o$.

Therefore, we have $\Psi = a_1 - J_o r\sin\theta$, and the magnetic field is:

$$\begin{aligned} &\vec{H} = [H_r, H_\theta] = [J_o\sin\theta, J_o\cos\theta], \text{ in polar coordinate,} \\ \text{or} \quad &\vec{H} = [H_x, H_y] = [0, J_o], \text{ in Cartesian coordinate.} \end{aligned} \tag{G.5}$$

G.2 X-Direction Quadrupole Field

As shown in Figure G-1(b), the x-direction quadrupole field is driven by a current distribution:

$$J_x = -J_{xo}\cos 2\theta. \tag{G.6}$$

Since the current distribution has a period or π, we can assume the solution to be:

$$\Psi = a_1 + a_3 \ln r + b_1 r^2\cos 2\theta + b_2 r^2\sin 2\theta + b_3\frac{\cos 2\theta}{r^2} + b_4\frac{\sin 2\theta}{r^2}. \tag{G.7}$$

The magnetic field intensity $\vec{H}$ can be obtained as:

$$H_r = -\frac{\partial\Psi}{\partial r} = -a_3\frac{1}{r} - 2b_1 r\cos 2\theta - 2b_2 r\sin 2\theta + 2b_3\frac{\cos 2\theta}{r^3} + 2b_4\frac{\sin 2\theta}{r^3}, \tag{G.8}$$

$$H_\theta = -\frac{1}{r}\frac{\partial\Psi}{\partial\theta} = 2b_1 r\sin 2\theta - 2b_2 r\cos 2\theta + 2b_3\frac{\sin 2\theta}{r^3} - 2b_4\frac{\cos 2\theta}{r^3}. \tag{G.9}$$

We can now include the boundary conditions to solve the coefficients:

1. When $r \to 0$, Ψ is finite, thus $a_3 = b_3 = b_4 = 0$.

2. Assuming the back iron has $\mu \gg \mu_o$, hence $H_\theta = -J_x$, thus $b_1 = 0$, and $b_2 = -J_{xo}/(2R_o)$.

Therefore, we have the magnetic scalar potential:

$$\Psi = a_1 - J_{xo}\frac{r^2 \sin 2\theta}{2R_o}, \text{ in polar coordinate,}$$
$$\text{or} \quad \Psi = a_1 - J_{xo}\frac{xy}{R_o}, \text{ in Cartesian coordinate.} \tag{G.10}$$

The resulting magnetic field in Cartesian coordinate becomes:

$$\vec{H} = [H_x, H_y] = [\frac{J_{xo}}{R_o}y, \frac{J_{xo}}{R_o}x], \tag{G.11}$$

and the resulting gradients of the magnetic field become:

$$\nabla H_x = [\frac{\partial H_x}{\partial x}, \frac{\partial H_x}{\partial y}] = [0, \frac{J_{xo}}{R_o}], \tag{G.12}$$

$$\nabla H_y = [\frac{\partial H_y}{\partial x}, \frac{\partial H_y}{\partial y}] = [\frac{J_{xo}}{R_o}, 0]. \tag{G.13}$$

The result shows that the x-quadrupole current generates a magnetic field with uniform gradients.

G.3 Y-Direction Quadrupole Field

As shown in Figure G-1(c), the y-direction quadrupole field is driven by a current distribution:

$$J_y = -J_{yo}\sin 2\theta, \tag{G.14}$$

which is the same as the x-direction quadrupole field rotated by 45°. Since the current distribution has a period of π, we can rewrite the solution as:

$$\Psi = a_1 + a_3 \ln r + b_1 r^2 \cos 2\theta + b_2 r^2 \sin 2\theta + b_3\frac{\cos 2\theta}{r^2} + b_4\frac{\sin 2\theta}{r^2}. \tag{G.15}$$

The magnetic field intensity $\vec{H}$ can be obtained as:

$$H_r = -\frac{\partial \Psi}{\partial r} = -a_3\frac{1}{r} - 2b_1 r\cos 2\theta - 2b_2 r\sin 2\theta + 2b_3\frac{\cos 2\theta}{r^3} + 2b_4\frac{\sin 2\theta}{r^3}, \tag{G.16}$$

$$H_\theta = -\frac{1}{r}\frac{\partial \Psi}{\partial \theta} = 2b_1 r\sin 2\theta - 2b_2 r\cos 2\theta + 2b_3\frac{\sin 2\theta}{r^3} - 2b_4\frac{\cos 2\theta}{r^3}. \tag{G.17}$$

We can now include the boundary conditions to solve the coefficients:

1. When $r \to 0$, Ψ is finite, thus $a_3 = b_3 = b_4 = 0$.

2. Assuming the back iron has $\mu \gg \mu_o$, hence $H_\theta = -J_y$, thus $b_2 = 0$, $b_1 = J_{yo}/(2R_o)$.

Therefore, we have the magnetic scalar potential:

$$\Psi = a_1 + J_{yo}\frac{r^2}{2R_o}\cos 2\theta, \text{ in polar coordinate,}$$

$$\text{or} \quad \Psi = a_1 + \frac{1}{2R_o}J_{yo}(y^2 - x^2), \text{ in Cartesian coordinate.} \tag{G.18}$$

The resulting magnetic field in Cartesian coordinate becomes:

$$\vec{H} = [H_x, H_y] = [\frac{J_{yo}}{R_o}x, \frac{J_{yo}}{R_o}y], \tag{G.19}$$

and the resulting gradients of the magnetic field become:

$$\nabla H_x = [\frac{\partial H_x}{\partial x}, \frac{\partial H_x}{\partial y}] = [\frac{J_{yo}}{R_o}, 0], \tag{G.20}$$

$$\nabla H_y = [\frac{\partial H_y}{\partial x}, \frac{\partial H_y}{\partial y}] = [0, \frac{J_{yo}}{R_o}]. \tag{G.21}$$

The result shows that the y-quadrupole current generates a magnetic field with uniform gradients.

Appendix H

Magnetic Field Simulation of Actuators by Using MATLAB

In this chapter, we use numerical methods to solve the magnetic field distribution for both the Dipole-Quadrupole actuator and the Quad-U-Core actuator. The field distribution can be used to solve for the force as a function of current input and tube position.

H.1 MATLAB Simulation of Dipole-Quadrupole Actuators

To solve the actuator force function, we model the actuator as shown in Figure H-1. I use Matlab to solve the field distribution with the existence of the tube, and predict the force as a function of current input and the tube position.

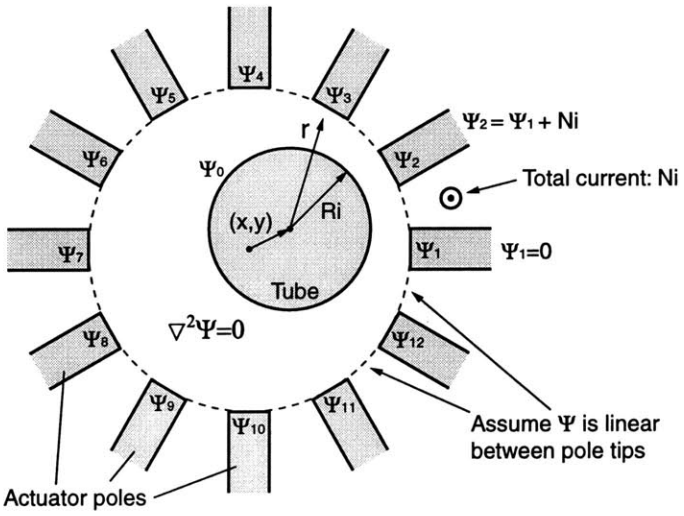

Figure H-1: Matlab simulation of the field distribution of the Dipole-Quadrupole actuator.

In this model, the magnetic scalar potential in the cavity is represented by Laplace's Equation:

$$\nabla^2\Psi = 0. \tag{H.1}$$

We solve this field problem by using the general solution and the boundary conditions. Since the dipole-quadrupole actuator is azimuthal periodic, the terms that are not periodic to θ in the general solution can be eliminated as zero, also m and p will be integers only :

$$\begin{aligned}\Psi \;=\; & a_1 + \underbrace{a_2\theta}_{0} + a_3 \ln r + \underbrace{a_4\theta \cdot \ln r}_{0} + \\ & \sum_{m=1}^{\infty}[b_{1m}r^m \cos m\theta + b_{2m}r^m \sin m\theta + b_{3m}r^{-m}\cos m\theta + b_{4m}r^{-m}\sin m\theta] + \\ & \sum_{p=1}^{\infty}[\underbrace{c_{1p}e^{p\theta}\cos(p\ln r)}_{0} + \underbrace{c_{2p}\frac{\cos(p\ln r)}{e^{p\theta}}}_{0} + \underbrace{c_{3p}e^{p\theta}\sin(p\ln r)}_{0} + \underbrace{c_{4p}\frac{\sin(p\ln r)}{e^{p\theta}}}_{0}]\end{aligned} \tag{H.2}$$

The boundary conditions are:

1. Assume that the tube has permeability $\mu \gg \mu_o$, thus we can assume the magnetic scalar potential of the tube is a constant Ψ_o.

2. The net magnetic flux going through the tube is zero, that is,

$$\int_{\theta=0}^{2\pi} H_r d\theta = 0 \tag{H.3}$$

3. The magnetic scalar potential of the 12 poles can be calculated by the current distribution. We first assume the scalar potential of the 1st pole to be $\Psi_1 = 0$. If total current between the 1st and 2nd poles is Ni, then the 2nd pole has a scalar potential of $\Psi_2 = \Psi_1 + Ni = Ni$. Similarly, we can solve $\Psi_3 \sim \Psi_{12}$.

4. Scalar potential between pole tips is assumed linear.

Since when $r \to R_i$, $\Psi = \Psi_o$, we can rewrite the solution to be:

$$\Psi = \Psi_o + C_0 \ln(\frac{r}{R_i}) + \sum_{m=1}^{\infty}(C_{1m}\cos m\theta + C_{2m}\sin m\theta)\left(\left(\frac{r}{R_i}\right)^m - \left(\frac{r}{R_i}\right)^{-m}\right). \tag{H.4}$$

$\vec{H}$ around the tube can also be calculated to be:

$$H_r|_{r=R_i} = -\frac{\partial\Psi}{\partial r}\Big|_{r=Ri} = -C_0\frac{1}{R_i} - \sum_{m=1}^{\infty}\frac{2m}{R_i}(C_{1m}\cos m\theta + C_{2m}\sin m\theta), \tag{H.5}$$

$$H_\theta|_{r=Ri} = -\frac{1}{r}\frac{\partial\Psi}{\partial\theta}\Big|_{r=Ri} = 0, \tag{H.6}$$

where $H_\theta = 0$ shows that the magnetic field is perpendicular to the tube, which complies with our assumption that the tube has $\mu \gg \mu_o$.

Another boundary condition is the magnetic flux continuity:

$$\int_{\theta=0}^{2\pi} H_r d\theta = 0 \Rightarrow C_0 \frac{2\pi}{R_i} = 0 \Rightarrow C_0 = 0.$$

In this thesis, I estimate m up to 20, and the solution can be represented by:

$$\Psi = \Psi_o + \sum_{m=1}^{20} (C_{1m} \cos m\theta + C_{2m} \sin m\theta) \left(\left(\frac{r}{R_i}\right)^m - \left(\frac{r}{R_i}\right)^{-m} \right). \tag{H.7}$$

I use 360 boundary points to estimate these 41 variables, including Ψ_o, C_{1m} and C_{2m}. A simple technique is to use pseudo-inverse to calculate the best estimate of the coefficients. When the number of algebraic equations is more than the number of variables, pseudo-inverse estimates the variables by minimizing the RMS error. The associated command in MATLAB is pinv.

H.2 MATLAB Simulation of Quad-U-Core Actuators

Similar to the Dipole-Quadrupole actuator, we can solve the magnetic field distribution for the Quad-U-Core actuator, and solve for the force as a function of current input and tube position. The model is shown in Figure H-2.

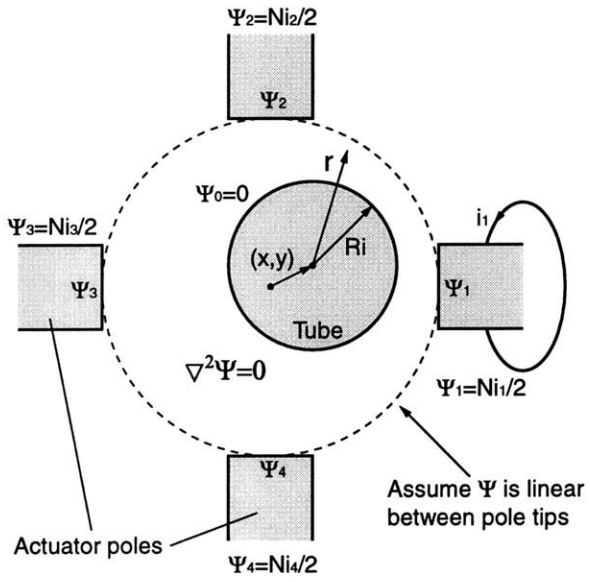

Figure H-2: Matlab simulation of the field distribution of the Quad-U-Core actuator.

Due to the azimuthal periodic condition, we have the general solution of the

magnetic scalar potential as Equation H.4:

$$\begin{aligned}\Psi &= \Psi_o + C_0 \ln\frac{r}{R_i} + \\ &\sum_{m=1}^{\infty} (C_{1m}\cos m\theta + C_{2m}\sin m\theta)\left(\left(\frac{r}{R_i}\right)^m - \left(\frac{r}{R_i}\right)^{-m}\right). \end{aligned} \tag{H.8}$$

The boundary conditions for the Quad-U-Core actuator are slightly different from the Dipole-Quadrupole actuator, they are listed in the following:

1. Assume that the tube has permeability $\mu \gg \mu_o$, thus we can assume the scalar potential of the tube is a constant Ψ_o.

2. The magnetic scalar potential of the 4 poles can be calculated by their current inputs. Since each U-core has a complete magnetic loop, thus we can assign the magnetic scalar potential of the tube to be zero ($\Psi_o = 0$), and the two poles of each U-core have magnetic potentials of $\pm Ni/2$.

3. Scalar potential between pole tips is assumed linear.

We use 360 boundary points to estimate m up to 20, the magnetic scalar potential can represented by:

$$\Psi = C_0 \ln\frac{r}{R_i} + \sum_{m=1}^{20} (C_{1m}\cos m\theta + C_{2m}\sin m\theta)\left(\left(\frac{r}{R_i}\right)^m - \left(\frac{r}{R_i}\right)^{-m}\right). \tag{H.9}$$

Appendix I

Original Power FET Circuit Designs

In this chapter, I list the original power FET current control circuit designs from Olsen [86] and Aggarwal [3]. The circuit design from Ludwick [69] is the same as that from Olsen.

Figure I-1 shows the circuit design from Olsen [86]. It uses a capacitor C_{tune} and

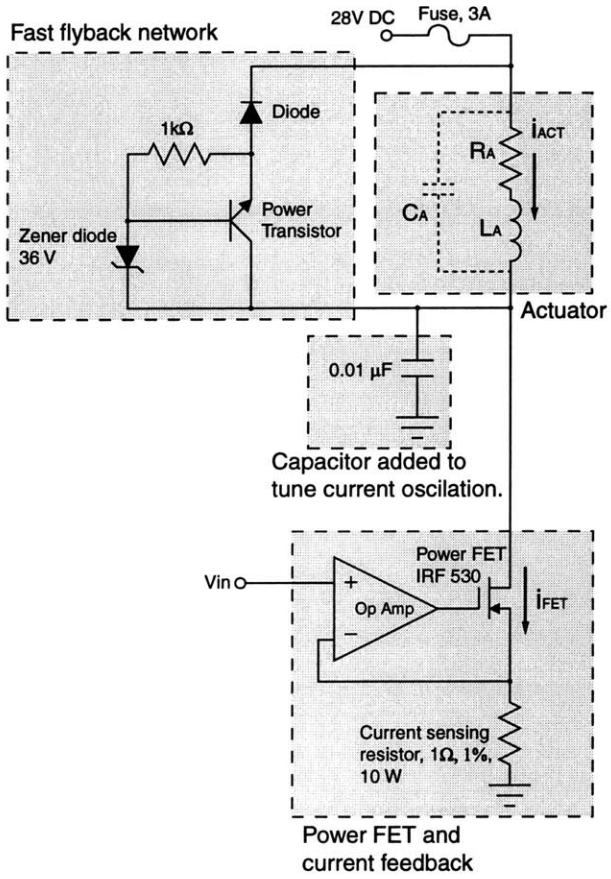

Figure I-1: Current control circuit using power FET in Olsen [86].

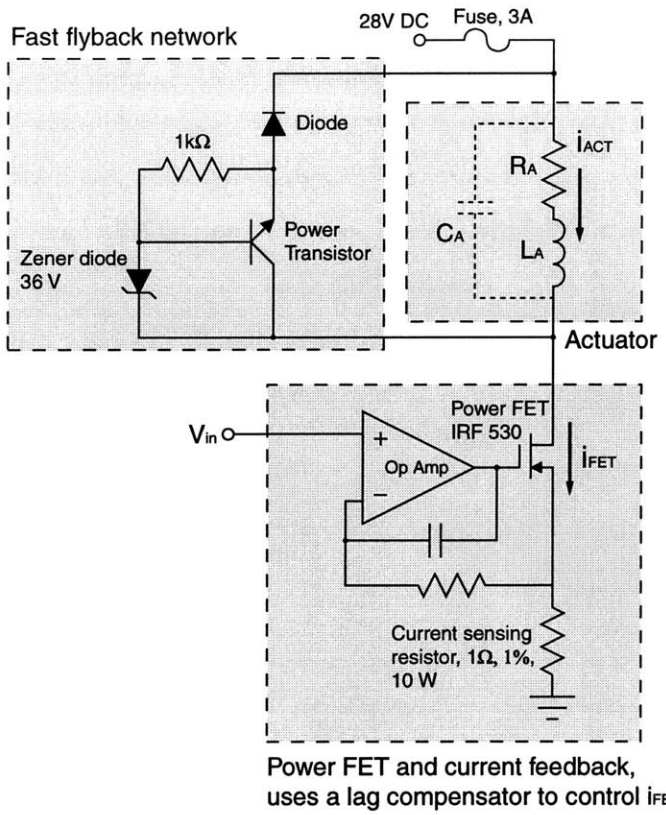

Figure I-2: Current control circuit using power FET in Aggarwal [3].

tries to eliminate loop oscillations at a frequency of 31 kHz. However, it mentions that the oscillation was never eliminated. In fact, this capacitor does not work as a damper, it moves the resonance frequency to $1/\sqrt{L_A C_{tune}}$.

Figure I-1 shows the circuit design from Aggarwal [3]. It removes the capacitor C_{tune}, and uses a lag compensator to control the power FET current i_{FET}, which reduces the high frequency components of i_{FET}. However, when I used this arrangement, I noticed that the power FET current i_{FET} was not equal to the actuator current i_{ACT}. Although i_{FET} is well controlled and smooth, the actuator current has a resonance oscillation at 4 kHz. I later used a resistor to damp out this resonance, as shown in Chapter 7.

Appendix J

Sensor Linearization

The following figures show the output of each of the 8 sensors. The x axis is V_x, and the y axis is V_y. The grids are the results of a 0.25 inch diameter steel tube moving at a 1 mm grid. The experimental results are approximated by using the following curve-fitting equations:

$$x = C_1 + C_2 V_x + C_3 V_y + C_4 V_x^2 + C_5 V_x V_y + C_6 V_y^2, \tag{J.1}$$

$$y = D_1 + D_2 V_x + D_3 V_y + D_4 V_x^2 + D_5 V_x V_y + D_6 V_y^2. \tag{J.2}$$

The curve fitting result is shown together with the measured output in the following 8 figures. And the coefficients of the curve fitting is shown in Table J.1[1].

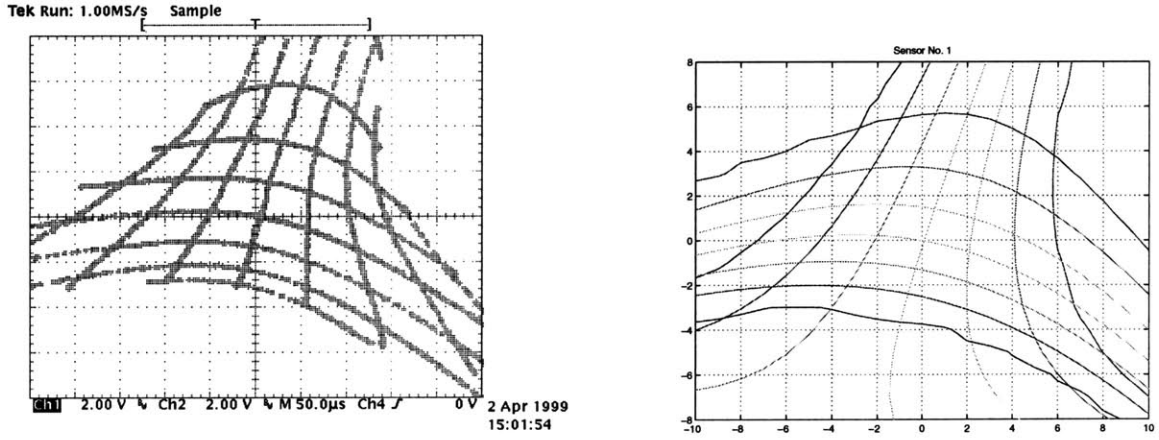

Figure J-1: Sensor No.1 linearization, left: experimental result, right: curve fitting.

[1]In dSPACE, I had to build blocks to do all the summations, as shown in Appendix D. If I use the function block $f[n]$ in Simulink, it takes extra 100 μs to finish the computation.

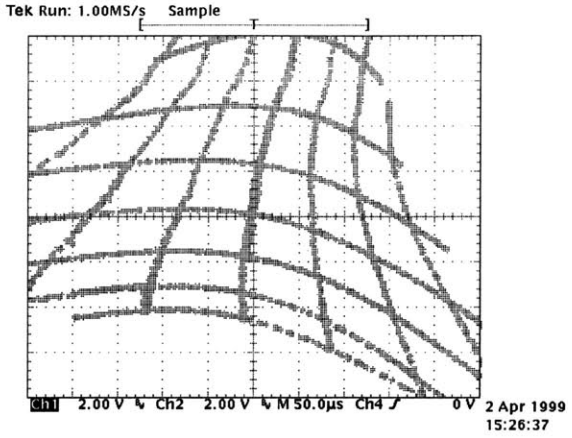

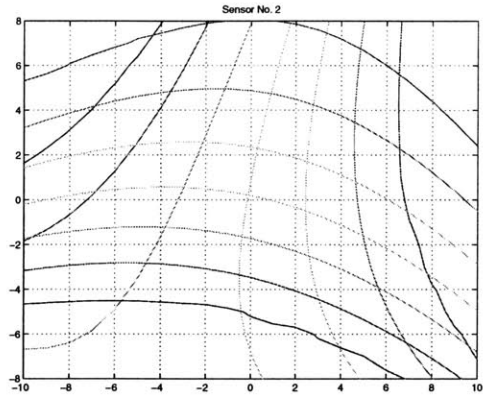

Figure J-2: Sensor No.2 linearization, left: experimental result, right: curve fitting.

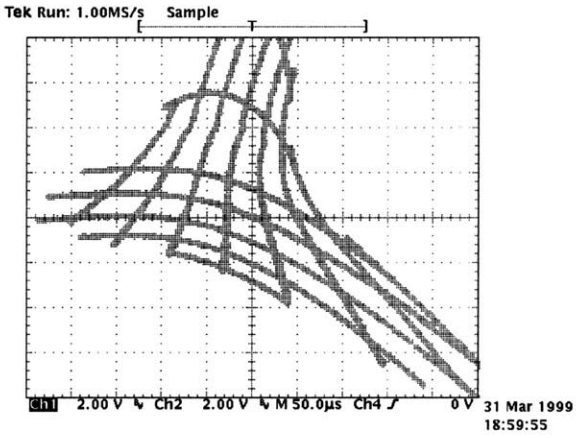

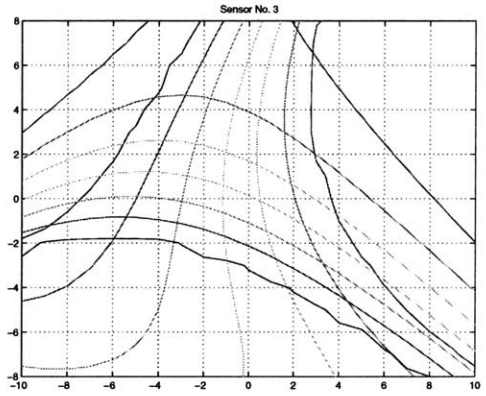

Figure J-3: Sensor No.3 linearization, left: experimental result, right: curve fitting.

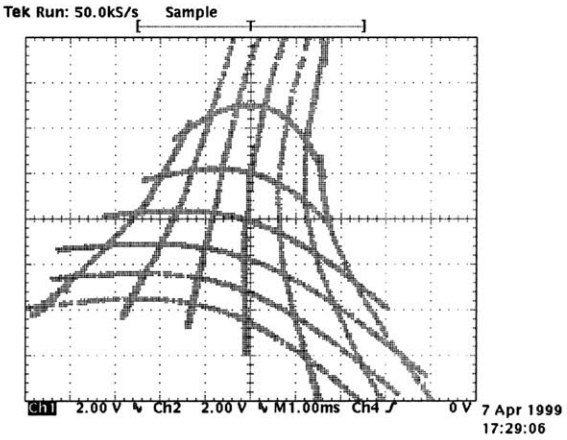

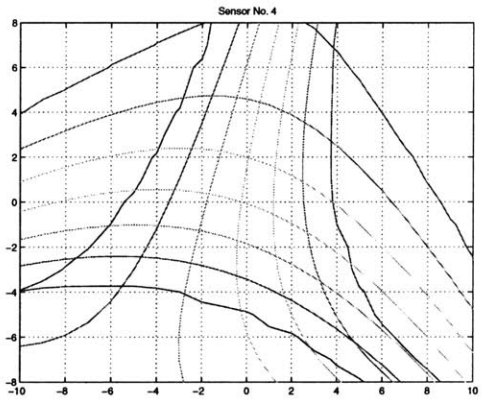

Figure J-4: Sensor No.4 linearization, left: experimental result, right: curve fitting.

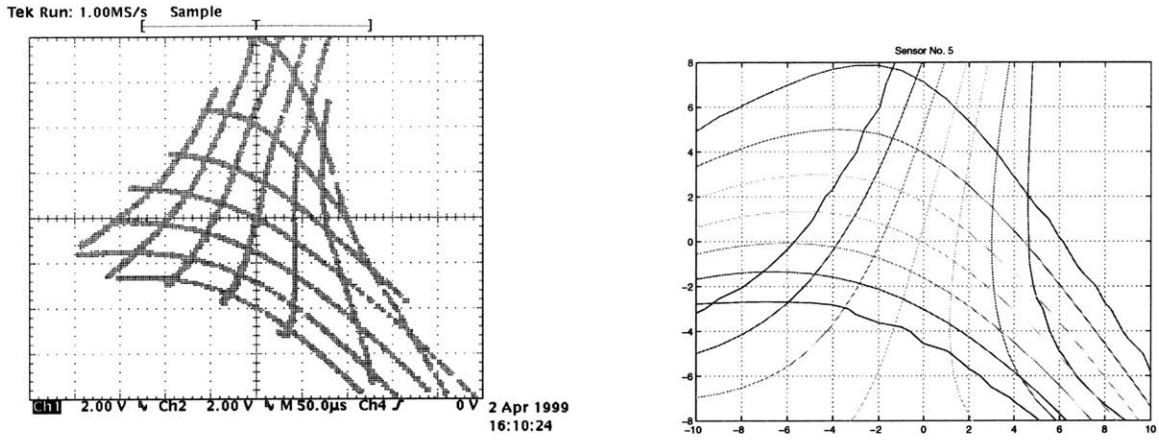

Figure J-5: Sensor No.5 linearization, left: experimental result, right: curve fitting.

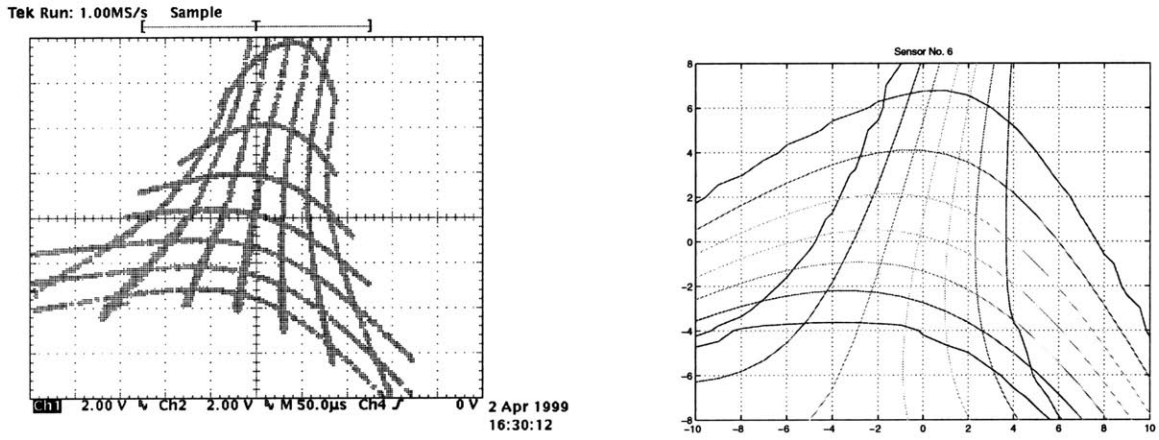

Figure J-6: Sensor No.6 linearization, left: experimental result, right: curve fitting.

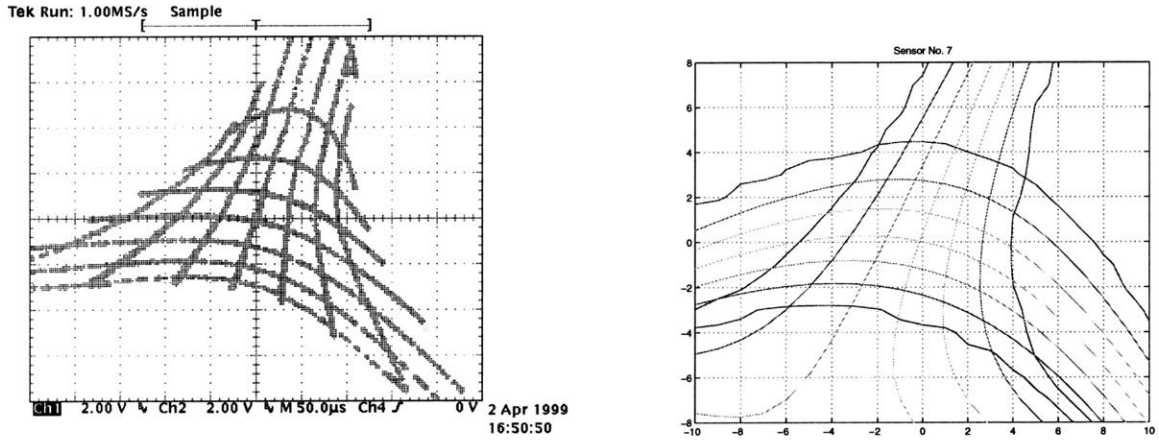

Figure J-7: Sensor No.7 linearization, left: experimental result, right: curve fitting.

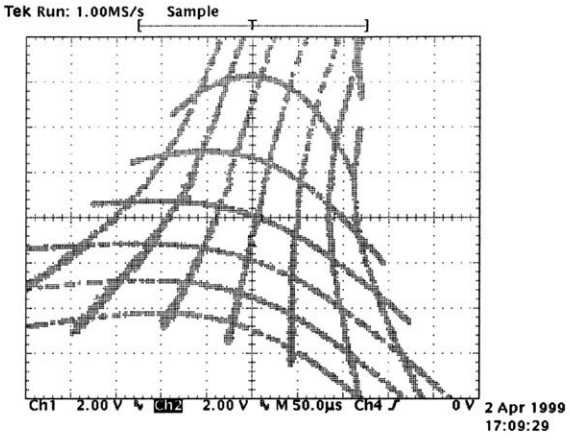

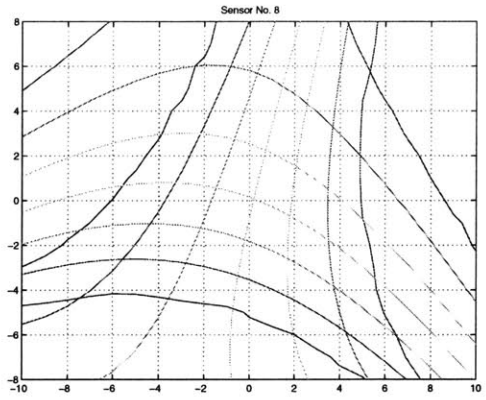

Figure J-8: Sensor No.8 linearization, left: experimental result, right: curve fitting.

Table J.1: Coefficients of curve-fitting equations for sensor linearization

Sensor	1	V_x	V_y	V_x^2	V_xV_y	V_y^2
1x	-0.043847	0.46729	-0.15319	0.0079273	0.038955	-0.015627
1y	0.011235	0.1274	0.71474	0.01942	-0.029689	-0.032486
2x	0.05803	0.36164	-0.056813	0.010592	0.023228	-0.0096095
2y	-0.092306	0.10316	0.49935	0.012558	-0.012777	-0.014355
3x	0.69207	0.61181	0.064845	0.012702	0.059637	-0.015823
3y	-0.093334	0.33676	0.75126	0.018852	-0.052586	-0.061402
4x	0.17091	0.68296	-0.075773	0.015728	0.052308	-0.018184
4y	0.039988	0.17521	0.52212	0.020383	-0.023805	-0.020588
5x	0.1146	0.59954	-0.15382	0.0091332	0.050441	-0.01266
5y	0.038691	0.32602	0.59671	0.026986	-0.024165	-0.025297
6x	0.15075	0.75589	-0.13028	0.019367	0.051827	-0.015223
6y	-0.14334	0.162	0.61413	0.032878	-0.029855	-0.021903
7x	0.095026	0.67374	-0.22482	0.017011	0.050849	-0.028012
7y	-0.011817	0.17311	0.79456	0.031287	-0.037337	-0.021257
8x	-0.096179	0.56121	-0.13537	0.013302	0.036318	-0.012284
8y	-0.066891	0.1734	0.47402	0.021386	-0.01674	-0.020254

Appendix K

Experiment of Vibration Control by Using LQG and SWLQG Control

This chapter shows an experiment of using LQG and SWLQG (Sensitivity Weighted LQG) control on beam vibration control. I did this experiment at MIT Space Systems Laboratory in the Department of Aeronautics and Astronautics in 1997, it was my final project for the MIT course 16.243 Dynamics of Controlled Structures.

The experimental setup is shown in Figure K-1. We use a motor at the hub to

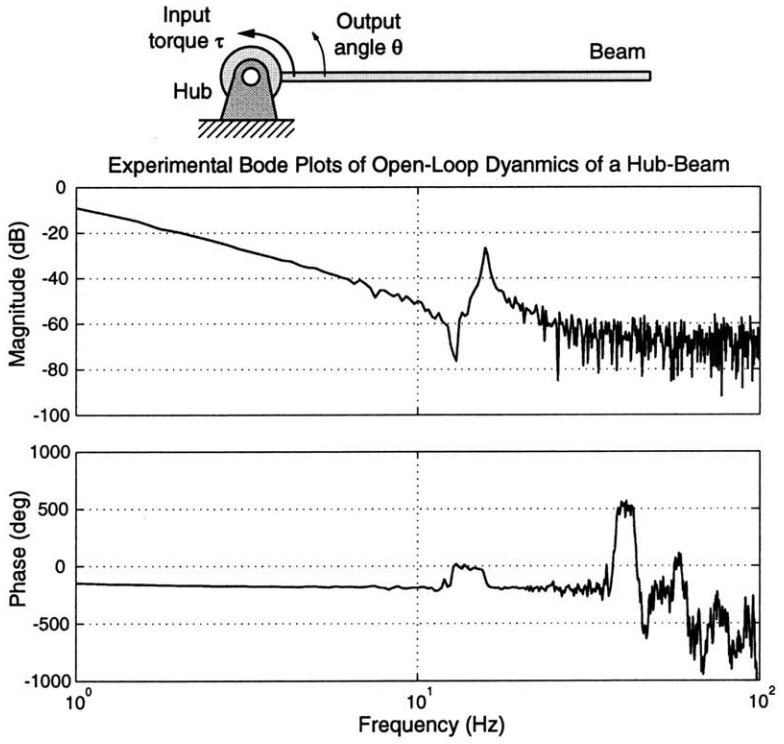

Figure K-1: Experimental Bode Plots of beam dynamics.

rotate a beam to desired angles. The experimental open-loop Bode Plots are shown in Figure K-1. The beam has the 1st vibration mode at 17 Hz.

SWLQG control is a modified version of LQG control, and is designed to improve the stability-robustness of LQG control. Figure K-2 shows the controller design by using both the LQG control and SWLQG control. LQG control creates a deep notch filter to attenuate the resonance mode, and SWLQG creates a smoother notch filter. By using a smoother notch filter, SWLQG improves stability-robustness such that it can tolerate certain uncertainties in resonance frequencies. However the smoother notch filter also make the system performance not as good as by using LQG control.

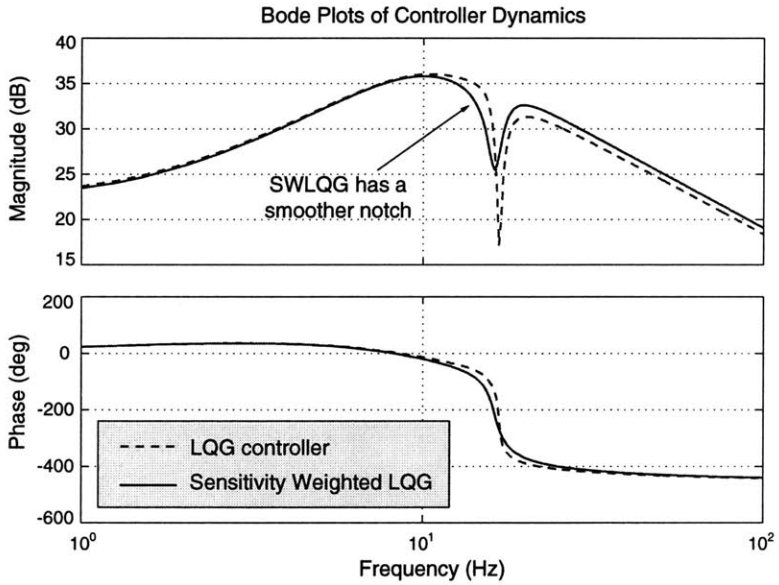

Figure K-2: Controller Design: LQG and SWLQG.

Appendix L

μ Analysis and μ Synthesis

In this chapter, we introduce μ analysis and μ synthesis. μ analysis is a generalized small gain theorem. μ synthesis is the combination of μ analysis and $\mathcal{H}_\infty$ control.

L.1 μ Analysis

For a system as shown in Figure L-1, $G(s)$ is the open-loop dynamics, $K(s)$ is the designed controller, $T_{wz}(s)$ is the closed-loop transfer function and $\triangle(s)$ is the uncertainty matrix. In μ analysis, we focus on diagonal $\triangle(s)$:

$$\triangle(s) = \triangle_d(s) = \begin{bmatrix} \triangle_1(s) & 0 & \cdots & 0 \\ 0 & \triangle_2(s) & \cdots & 0 \\ \vdots & \vdots & \ddots & \vdots \\ 0 & 0 & \cdots & \triangle_n(s) \end{bmatrix}, \tag{L.1}$$

where each diagonal component $\triangle_i(s)$ can be a matrix.

For all the diagonal uncertainty matrices $\triangle_d(s)$ with each diagonal component

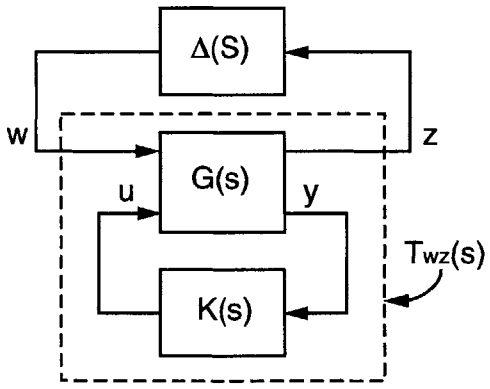

Figure L-1: Block diagram of a controlled system $T_{wz}(s)$ with uncertainty $\triangle(s)$.

$\|\triangle_i(s)\|_\infty < 1$, μ is defined as:

$$\forall \triangle_d, (I + \triangle_d T_{wz})^{-1} \text{ is stable if and only if } \mu(T_{wz}(j\omega)) \leq 1, \forall \omega, \tag{L.2}$$

and

$$\mu(T_{wz}(j\omega)) = \frac{1}{\min\limits_{\triangle_d}\{\sigma_{max}(\triangle_d) : det(I + \triangle_d T_{wz}) = 0\}}, \tag{L.3}$$

unless no $\triangle_d$ makes $(I + \triangle_d T_{wz})$ singular, in which case $\mu(T_{wz}) = 0$.

It is convenient to define the maximum value of $\mu\left(T_{wz}(j\omega)\right)$:

$$\|T_{wz}(s)\|_\mu = \sup_\omega \mu\left(T_{wz}(j\omega)\right). \tag{L.4}$$

Hence we can represent μ analysis by stating that the system will be stable for all diagonal $\triangle_d(s)$ if and only if

$$\|T_{wz}(s)\|_\mu \|\triangle_d(s)\|_\infty < 1, \tag{L.5}$$

which is also called the generalized small gain theorem.

However, in general, $\mu(T_{wz}(s))$ cannot be computed. Currently, the upper bound of $\mu(T_{wz}(s))$ is used instead. D-scale iteration is a method that iterate a D matrix to find the upper bound of $\mu(T_{wz}(s))$. This upper bound is derived to be the minimum value of $\overline{\sigma}(DT_{wz}D^{-1})$ for all possible D matrices. The D matrix has a form of:

$$D = \begin{bmatrix} d_1 I & 0 & \cdots & 0 \\ 0 & d_2 I & \cdots & 0 \\ \vdots & \vdots & \ddots & \vdots \\ 0 & 0 & \cdots & d_n I \end{bmatrix}, \tag{L.6}$$

where $d_1, d_2, ..., d_n$ are scalars. Notice that $\overline{\sigma}(DT_{wz}D^{-1})$ is a function of frequency ω, and is the upper bound of $\mu(T_{wz}(s))$. And $\|DT_{wz}D^{-1}\|_\infty$ is a scalar, and is the upper bound of $\|T_{wz}(s)\|_\mu$.

L.2 μ Synthesis

Furthermore, μ synthesis is the controller design tool that finds a stabilizing controller $K(s)$ that minimizes the cost:

$$J = \|T_{wz}(s)\|_\mu. \tag{L.7}$$

Currently, we can only find the upper bound of $\|T_{wz}(s)\|_\mu$ by $\|DT_{wz}D^{-1}\|_\infty$. We can take the advantage that this upper bound is an $\mathcal{H}_\infty$ norm, and design a controller by using $\mathcal{H}_\infty$ control to minimize $\|DT_{wz}D^{-1}\|_\infty$.

D-K iteration is a method to do this iteration, the following list shows its algo-

rithm:

1. Given $K(s)$, find the D matrix to minimize $\|DT_{wz}D^{-1}\|_\infty$.
2. Given D matrix, find $K(s)$ to minimize $\|DT_{wz}D^{-1}\|_\infty$.
3. Repeat the process until $\|DT_{wz}D^{-1}\|_\infty$ reaches a minimum.

Appendix M

Critical Speed for Moving Beams

At critical speed, the beam dynamics are reduced to:

$$EI\frac{\partial^4 u}{\partial z^4} + (\rho AV^2 - T)\frac{\partial^2 u}{\partial z^2} = 0. \tag{M.1}$$

The homogeneous solution is:

$$u_h(z) = C_1 \cos kz + C_2 \sin kz + C_3 z + C_4, \tag{M.2}$$

with

$$k = \sqrt{\frac{\rho AV^2 - T}{EI}}. \tag{M.3}$$

The critical speed V_c is

$$V_c = \sqrt{\frac{EIk_1^2 + T}{\rho A}}. \tag{M.4}$$

In the following sections, I solve the critical speed for hinged-hinged beams and clamped-clamped beams, and compare them with the results from Wickert [106]:

$$V_c = \sqrt{\frac{EI}{\rho A}\left(\frac{\pi}{L}\right)^2 + \frac{T}{\rho A}}, \text{ hinged-hinged,} \tag{M.5}$$

$$V_c = \sqrt{\frac{EI}{\rho A}\left(\frac{2\pi}{L}\right)^2 + \frac{T}{\rho A}}, \text{ clamped-clamped.} \tag{M.6}$$

M.1 Critical Speed for Moving Hinged-Hinged Beams

For a hinged-hinged beam of length L, we have boundary conditions as:

$$u\Big|_{z=0} = \frac{\partial^2 u}{\partial z^2}\Big|_{z=0} = u\Big|_{z=L} = \frac{\partial^2 u}{\partial z^2}\Big|_{z=L} = 0 \tag{M.7}$$

Replace u by the homogeneous solution, we have

$$\begin{bmatrix} 1 & 0 & 0 & 1 \\ -k^2 & 0 & 0 & 0 \\ \cos kL & \sin kL & L & 1 \\ -k^2\cos kL & -k^2\sin kL & 0 & 0 \end{bmatrix} \begin{bmatrix} C_1 \\ C_2 \\ C_3 \\ C_4 \end{bmatrix} = \begin{bmatrix} 0 \\ 0 \\ 0 \\ 0 \end{bmatrix}. \tag{M.8}$$

For C_i to be nontrivial, we set the determinant of the matrix to be zero: $|\triangle| = 0$, and it results in the following solution:

$$\sin kL = 0 \Rightarrow k = \frac{\pi}{L}, \frac{2\pi}{L}, \frac{3\pi}{L}, \cdots \tag{M.9}$$

Therefore critical speed is

$$V_c = \sqrt{\frac{EI}{\rho A}\left(\frac{\pi}{L}\right)^2 + \frac{T}{\rho A}}. \tag{M.10}$$

M.2 Critical Speed for Moving Clamped-Clamped Beams

Similarly, for clamped-clamped beam, we have boundary conditions as:

$$u\Big|_{z=0} = \frac{\partial u}{\partial z}\Big|_{z=0} = u\Big|_{z=L} = \frac{\partial u}{\partial z}\Big|_{z=L} = 0 \tag{M.11}$$

Replace u by the homogeneous solution, we have

$$\begin{bmatrix} 1 & 0 & 0 & 1 \\ 0 & k & 1 & 0 \\ \cos kL & \sin kL & L & 1 \\ -k\sin kL & k\cos kL & 1 & 0 \end{bmatrix} \begin{bmatrix} C_1 \\ C_2 \\ C_3 \\ C_4 \end{bmatrix} = \begin{bmatrix} 0 \\ 0 \\ 0 \\ 0 \end{bmatrix}. \tag{M.12}$$

For C_i to be nontrivial, we set the determinant of the matrix to be zero: $|\triangle| = 0$. It results in the following solution:[1]

$$2(\cos kL - 1) + kL\sin kL = 0 \Rightarrow k_n = \frac{2\pi}{L}, \frac{2.86\pi}{L}, \frac{4\pi}{L}, \cdots \tag{M.13}$$

Therefore, the critical speed is

$$V_c = \sqrt{\frac{EI}{\rho A}\left(\frac{2\pi}{L}\right)^2 + \frac{T}{\rho A}}. \tag{M.14}$$

[1] In the appendix of Wickert [106], it said that the solutions are $2n\pi/L$, which I believe was not completely correct.

Appendix N

Recipes for Finite Element Modeling: Beams, Strings, Plates, and Membranes

N.1 Euler-Bernoulli Beam Element

Assume the beam element has length a, mass per unit length ρA, bending stiffness EI, and tension $T = 0$.

(1)$\tau = C\epsilon$:

$$\underbrace{M_{zz}}_{\tau} = \underbrace{EI}_{C} \underbrace{\frac{d^2u}{dz^2}}_{\epsilon} \tag{N.1}$$

(2)U

$$U = \begin{bmatrix} U_1 \\ U_2 \\ U_3 \\ U_4 \end{bmatrix} = \begin{bmatrix} u(z_1) \\ \theta(z_1) \\ u(z_2) \\ \theta(z_2) \end{bmatrix} = \begin{bmatrix} u(z_1) \\ \frac{du}{dz}|_{z=z_1} \\ u(z_2) \\ \frac{du}{dz}|_{z=z_2} \end{bmatrix} \tag{N.2}$$

(3) $u = \Phi_1 \alpha$:

$$u = \underbrace{\begin{bmatrix} 1 & z & z^2 & z^3 \end{bmatrix}}_{\Phi_1} \underbrace{\begin{bmatrix} \alpha_1 \\ \alpha_2 \\ \alpha_3 \\ \alpha_4 \end{bmatrix}}_{\alpha} \tag{N.3}$$

(4) $U = A_{temp}\alpha$: where A_{temp} is a temporary matrix,

$$\begin{aligned} u(z) &= \Phi_1 \alpha \\ \theta(z) &= \frac{du}{dz} = \frac{d\Phi_1}{dz}\alpha \end{aligned}$$

Therfore, A_{temp} matrix can be found by

$$A_{temp} = \begin{bmatrix} - & \Phi_1(z_1) & - \\ - & \frac{d\Phi_1}{dz}|_{z_1} & - \\ - & \Phi_1(z_2) & - \\ - & -\frac{d\Phi_1}{dz}|_{z_2} & - \end{bmatrix} = \begin{bmatrix} 1 & 0 & 0 & 0 \\ 0 & 1 & 0 & 0 \\ 1 & a & a^2 & a^3 \\ 0 & 1 & 2a & 3a^2 \end{bmatrix} \tag{N.4}$$

(5) $u(x,y) = HU$:

$$H = \Phi_1 A_{temp}^{-1} = \begin{bmatrix} 1 - 3\frac{z^2}{a^2} + 2\frac{z^3}{a^3} & z - 2\frac{z^2}{a} + \frac{z^3}{a^2} & 3\frac{z^2}{a^2} - 2\frac{z^3}{a^3} & -\frac{z^2}{a} + \frac{z^3}{a^2} \end{bmatrix} \tag{N.5}$$

(6) $\epsilon = BU$:

$$\epsilon = \frac{d^2u}{dz^2} = \underbrace{\begin{bmatrix} 0 & 0 & 2 & 6z \end{bmatrix}}_{\Phi_2} \underbrace{\begin{bmatrix} \alpha_1 \\ \alpha_2 \\ \alpha_3 \\ \alpha_4 \end{bmatrix}}_{\alpha} = \underbrace{\Phi_2 A_{temp}^{-1}}_{B} U$$

$$\Rightarrow B = \Phi_2 A_{temp}^{-1} = \begin{bmatrix} -6\frac{1}{a^2} + 12\frac{z}{a^3} & -4\frac{1}{a} + 6\frac{z}{a^2} & 6\frac{1}{a^2} - 12\frac{z}{a^3} & -2\frac{1}{a} + 6\frac{z}{a^2} \end{bmatrix} \tag{N.6}$$

(7)M, K and R:

$$\begin{aligned} M^{(m)} &= \int_{z=0}^{a} H^T \rho A H dz \text{ (assume constant } \rho A) \\ &= \frac{\rho A}{420} \begin{bmatrix} 156a & 22a^2 & 54a & -13a^2 \\ 22a^2 & 4a^3 & 13a^2 & -3a^3 \\ 54a & 13a^2 & 156a & -22a^2 \\ -13a^2 & -3a^3 & -22a^2 & 4a^3 \end{bmatrix} \end{aligned} \tag{N.7}$$

$$\begin{aligned} K^{(m)} &= EI \int_{z=0}^{a} B^T C B dz \text{ (assume constant } C) \\ &= \frac{EI}{a^3} \begin{bmatrix} 12 & 6a & -12 & 6a \\ 6a & 4a^2 & -6a & 2a^2 \\ -12 & -6a & 12 & -6a \\ 6a & 2a^2 & -6a & 4a^2 \end{bmatrix} \end{aligned} \tag{N.8}$$

$$\begin{aligned} R^{(m)} &= fA \int_{z=0}^{a} H^T dz \text{ (assume constant volume force density } f) \\ &= fA \begin{bmatrix} \frac{1}{2}a \\ \frac{1}{12}a^2 \\ \frac{1}{2}a \\ -\frac{1}{12}a^2 \end{bmatrix} \end{aligned} \tag{N.9}$$

The commands used in Maple to generate the previous matrices are shown below:

```
> restart;
> with(linalg);
> A:=matrix(4,4,[1,0,0,0,0,1,0,0,1,a,a^2,a^3,0,1,2*a,3*a^2]);
```

```
> inverse(A);
> phi1:=matrix(1,4,[1,x,x^2,x^3]);
> H:=multiply(phi1,inverse(A));
> phi2:=matrix(1,4,[0,0,2,6*x]);
> B:=multiply(phi2,inverse(A));
> HH:=multiply(transpose(H),H);
> HHk:=map(int,HH,x=0..a);
> BB:=multiply(transpose(B),B);
> BBk:=map(int,BB,x=0..a);
> R:=map(int,transpose(H),x=0..a);
```

N.2 String Element

String element is similar to beam element, except the K matrix is different.

$$\begin{aligned} K^{(m)} &= -\int_{z=0}^{a} H^T T \frac{d^2 H}{dz^2} dz \text{ (assume constant } T) \\ &= \frac{T}{30a} \begin{bmatrix} 36 & 33a & -36 & 3a \\ 3a & 4a^2 & -3a & -a^2 \\ -36 & -3a & 36 & -33a \\ 3a & -a^2 & -3a & 4a^2 \end{bmatrix} \end{aligned} \tag{N.10}$$

The commands used in Maple to generate this matrix are shown below:

```
> restart;
> with(linalg);
> A:=matrix(4,4,[1,0,0,0,0,1,0,0,1,a,a^2,a^3,0,1,2*a,3*a^2]);
> inverse(A);
> phi1:=matrix(1,4,[1,x,x^2,x^3]);
> H:=multiply(phi1,inverse(A));
> phi2:=matrix(1,4,[0,0,2,6*x]);
> B:=multiply(phi2,inverse(A));
> HB:=multiply(transpose(H),B);
> HBa:=map(int,HB,x=0..a);
```

N.3 Plate-Bending Element

Assume the plate element has length a in x direction, length b in y direction, thickness h, density ρ, Young's modulus E, Poisson's ratio ν, and tension $T = 0$.

(1)$\tau = C\epsilon$:

$$\underbrace{\begin{bmatrix} M_{xx} \\ M_{yy} \\ M_{xy} \end{bmatrix}}_{\tau} = \underbrace{D \begin{bmatrix} 1 & \nu & 0 \\ \nu & 1 & 0 \\ 0 & 0 & \frac{1-\nu}{2} \end{bmatrix}}_{C} \underbrace{\begin{bmatrix} \frac{\partial^2 u}{\partial x^2} \\ \frac{\partial^2 u}{\partial y^2} \\ 2\frac{\partial^2 u}{\partial x \partial y} \end{bmatrix}}_{\epsilon} \tag{N.11}$$

where

$$D = \frac{Eh^3}{12(1-\nu^2)}$$

(2)U

$$U = \begin{bmatrix} U_1 \\ U_2 \\ U_3 \\ U_4 \\ \vdots \\ U_{12} \end{bmatrix} = \begin{bmatrix} u(x_1,y_1) \\ \theta_x(x_1,y_1) \\ \theta_y(x_1,y_1) \\ u(x_2,y_1) \\ \vdots \\ \theta_y(x_2,y_2) \end{bmatrix} = \begin{bmatrix} u(x_1,y_1) \\ \frac{\partial u}{\partial y}|_{(x_1,y_1)} \\ -\frac{\partial u}{\partial x}|_{(x_1,y_1)} \\ u(x_2,y_1) \\ \vdots \\ -\frac{\partial u}{\partial x}|_{(x_2,y_2)} \end{bmatrix} \tag{N.12}$$

(3) $u = \Phi_1 \alpha$:

$$u = \underbrace{\begin{bmatrix} 1 & x & y & x^2 & xy & y^2 & x^3 & x^2y & xy^2 & y^3 & x^3y & xy^3 \end{bmatrix}}_{\Phi_1} \underbrace{\begin{bmatrix} \alpha_1 \\ \alpha_2 \\ \alpha_3 \\ \vdots \\ \alpha_{12} \end{bmatrix}}_{\alpha} \tag{N.13}$$

(4) $U = A_{temp}\alpha$:

$$\begin{aligned} u(x,y) &= \Phi_1 \alpha \\ \theta_x(x,y) &= \frac{\partial u}{\partial y} = \frac{\partial \Phi_1}{\partial y}\alpha \\ \theta_y(x,y) &= -\frac{\partial u}{\partial x} = -\frac{\partial \Phi_1}{\partial x}\alpha \end{aligned}$$

Therefore, A_{temp} matrix can be found by

$$A_{temp} = \begin{bmatrix} - & \Phi_1(x_1,y_1) & - \\ - & \frac{\partial \Phi_1}{\partial y}|_{(x_1,y_1)} & - \\ - & -\frac{\partial \Phi_1}{\partial x}|_{(x_1,y_1)} & - \\ - & \Phi_1(x_2,y_1) & - \\ \vdots & \vdots & \vdots \\ - & -\frac{\partial \Phi_1}{\partial x}|_{(x_2,y_2)} & - \end{bmatrix}$$

$$= \begin{bmatrix} 1 & 0 & 0 & 0 & 0 & 0 & 0 & 0 & 0 & 0 & 0 & 0 \\ 0 & 0 & 1 & 0 & 0 & 0 & 0 & 0 & 0 & 0 & 0 & 0 \\ 0 & -1 & 0 & 0 & 0 & 0 & 0 & 0 & 0 & 0 & 0 & 0 \\ 1 & a & 0 & a^2 & 0 & 0 & a^3 & 0 & 0 & 0 & 0 & 0 \\ 0 & 0 & 1 & 0 & a & 0 & 0 & a^2 & 0 & 0 & a^3 & 0 \\ 0 & -1 & 0 & -2a & 0 & 0 & -3a^2 & 0 & 0 & 0 & 0 & 0 \\ 1 & 0 & b & 0 & 0 & b^2 & 0 & 0 & 0 & b^3 & 0 & 0 \\ 0 & 0 & 1 & 0 & 0 & 2b & 0 & 0 & 0 & 3b^2 & 0 & 0 \\ 0 & -1 & 0 & 0 & -b & 0 & 0 & 0 & -b^2 & 0 & 0 & -b^3 \\ 1 & a & b & a^2 & ab & b^2 & a^3 & a^2b & ab^2 & b^3 & a^3b & ab^3 \\ 0 & 0 & 1 & 0 & a & 2b & 0 & a^2 & 2ab & 3b^2 & a^3 & 3ab^2 \\ 0 & -1 & 0 & -2a & -b & 0 & -3a^2 & -2ab & -b^2 & 0 & -3a^2b & -b^3 \end{bmatrix} \quad \text{(N.14)}$$

(5) $u(x,y) = HU$: We don't need to calculate H until step (7).

$$H = \Phi_1 A_{temp}^{-1} \quad \text{(N.15)}$$

(6) $\epsilon = BU$: We don't need to calculate B at this moment, wait till step (7).

$$\epsilon = \begin{bmatrix} \frac{\partial^2 u}{\partial x^2} \\ \frac{\partial^2 u}{\partial y^2} \\ 2\frac{\partial^2 u}{\partial x \partial y} \end{bmatrix} = \underbrace{\begin{bmatrix} - & \frac{\partial^2 \Phi_1}{\partial x} & - \\ - & \frac{\partial^2 \Phi_1}{\partial y^2} & - \\ - & 2\frac{\partial^2 \Phi_1}{\partial x \partial y} & - \end{bmatrix}}_{\Phi_2} \underbrace{\alpha}_{A_{temp}^{-1} U}$$

$$\Rightarrow \Phi_2 = \begin{bmatrix} 0 & 0 & 0 & 2 & 0 & 0 & 6x & 2y & 0 & 0 & 6xy & 0 \\ 0 & 0 & 0 & 0 & 0 & 2 & 0 & 0 & 2x & 6y & 0 & 6xy \\ 0 & 0 & 0 & 0 & 2 & 0 & 0 & 4x & 4y & 0 & 6x^2 & 6y^2 \end{bmatrix} \quad \text{(N.16)}$$

$$\text{and } B = \Phi_2 A_{temp}^{-1} \quad \text{(N.17)}$$

(7)M, K and R:

$$\begin{aligned} M^{(m)} &= \int_{x=0}^{a} \int_{y=0}^{b} H^T \rho h H dy dx \text{ (assume constant } \rho h) \\ &= \rho h \int_{x=0}^{a} \int_{y=0}^{b} (A_{temp}^{-1})^T \Phi_1^T \Phi_1 A_{temp}^{-1} dy dx \\ &= \rho (A_{temp}^{-1})^T \int_{x=0}^{a} \int_{y=0}^{b} \Phi_1^T \Phi_1 dy dx A_{temp}^{-1} \quad \text{(N.18)} \end{aligned}$$

$$\begin{aligned} K^{(m)} &= \int_{x=0}^{l} \int_{y=0}^{h} B^T C B dy dx \\ &= \int_{x=0}^{a} \int_{y=0}^{b} (A_{temp}^{-1})^T \Phi_2^T C \Phi_2 A_{temp}^{-1} dy dx \\ &= (A_{temp}^{-1})^T \int_{x=0}^{a} \int_{y=0}^{b} \Phi_2^T C \Phi_2 dy dx A_{temp}^{-1} \quad \text{(N.19)} \end{aligned}$$

$$
\begin{aligned}
R^{(m)} &= \int_{x=0}^{l}\int_{y=0}^{h} H^T f dydx \\
&= \int_{x=0}^{a}\int_{y=0}^{b} (A_{temp}^{-1})^T \Phi_1^T f dydx \\
&= (A_{temp}^{-1})^T \int_{x=0}^{a}\int_{y=0}^{b} \Phi_1^T f dydx
\end{aligned} \tag{N.20}
$$

This part is pure algebraic calculation. It can be done easily by the software Maple. The code is shown at the end of this section. Because of the large size of the matrices, the symbolic formula is not shown in this thesis.

We use one numerical example to demonstrate the method, the variables are: $a = 1$ m, $b = 2$ m, $h = 0.001$ m, $\nu = 0.28$, $E = 2 \times 10^{11}$ Pa, $\rho = 7800$ kg/m^3, and constant volume force density f. By using the following Maple code, we get the following FEM matrices.

$$
M^{(m)} = \frac{\rho h}{12600}
\begin{bmatrix}
3454 & 922 & -461 & 1226 & 398 & 274 & 1226 & -548 & -199 & 394 & -232 & 116 \\
922 & 320 & -126 & 398 & 160 & 84 & 548 & -240 & -84 & 232 & -120 & 56 \\
-461 & -126 & 80 & -274 & -84 & -60 & -199 & 84 & 40 & -116 & 56 & -30 \\
1226 & 398 & -274 & 3454 & 922 & 461 & 394 & -232 & -116 & 1226 & -548 & 199 \\
398 & 160 & -84 & 922 & 320 & 126 & 232 & -120 & -56 & 548 & -240 & 84 \\
274 & 84 & -60 & 461 & 126 & 80 & 116 & -56 & -30 & 199 & -84 & 40 \\
1226 & 548 & -199 & 394 & 232 & 116 & 3454 & -922 & -461 & 1226 & -398 & 274 \\
-548 & -240 & 84 & -232 & -120 & -56 & -922 & 320 & 126 & -398 & 160 & -84 \\
-199 & -84 & 40 & -116 & -56 & -30 & -461 & 126 & 80 & -274 & 84 & -60 \\
394 & 232 & -116 & 1226 & 548 & 199 & 1226 & -398 & -274 & 3454 & -922 & 461 \\
-232 & -120 & 56 & -548 & -240 & -84 & -398 & 160 & 84 & -922 & 320 & -126 \\
116 & 56 & -30 & 199 & 84 & 40 & 274 & -84 & -60 & 461 & -126 & 80
\end{bmatrix}
$$

$$
K^{(m)} =
\begin{bmatrix}
177 & 16.7 & -76.2 & -163 & -3.15 & -73.6 & 40.0 & 11.6 & -32.3 & -53.6 & 1.92 & -34.9 \\
16.7 & 19.0 & -5.06 & -3.15 & -0.916 & 0 & -11.6 & 4.29 & 0 & -1.92 & 4.75 & 0 \\
-76.2 & -5.06 & 50.0 & 73.6 & 0 & 23.7 & -32.3 & 0 & 22.4 & 34.9 & 0 & 12.5 \\
-163 & -3.15 & 73.6 & 177 & 16.7 & 76.2 & -53.6 & 1.92 & 34.9 & 40.0 & 11.6 & 32.3 \\
-3.15 & -0.916 & 0 & 16.7 & 19.0 & 5.06 & -1.92 & 4.75 & 0 & -11.6 & 4.29 & 0 \\
-73.6 & 0 & 23.7 & 76.2 & 5.06 & 50.0 & -34.9 & 0 & 12.5 & 32.3 & 0 & 22.4 \\
40.0 & -11.6 & -32.3 & -53.6 & -1.92 & -34.9 & 177 & -16.7 & -76.2 & -163 & 3.15 & -73.6 \\
11.6 & 4.29 & 0 & 1.92 & 4.75 & 0 & -16.7 & 19.0 & 5.06 & 3.15 & 0.916 & 0 \\
-32.3 & 0 & 22.4 & 34.9 & 0 & 12.5 & -76.2 & 5.06 & 50.0 & 73.6 & 0 & 23.7 \\
-53.6 & -1.92 & 34.9 & 40.0 & -11.6 & 32.3 & -163 & 3.15 & 73.6 & 177 & -16.7 & 76.2 \\
1.92 & 4.75 & 0 & 11.6 & 4.29 & 0 & 3.15 & -0.916 & 0 & -16.7 & 19.0 & -5.06 \\
-34.9 & 0 & 12.5 & 32.3 & 0 & 22.4 & -73.6 & 0 & 23.7 & 76.2 & -5.06 & 50.0
\end{bmatrix}
$$

$$R^{(m)} = \frac{fh}{12}\begin{bmatrix} 6 \\ 2 \\ -1 \\ 6 \\ 2 \\ 1 \\ 6 \\ -2 \\ -1 \\ 6 \\ -2 \\ 1 \end{bmatrix}$$

The commands used in Maple to generate the previous matrices are shown below. Notice that if the variables are not specified at the beginning, the Maple commands will give the symbolic formula.

```
> restart;
> with(linalg);
> a:=1;
> b:=2;
> h:=0.001;
> rho:=7.8;
> E:=2e11;
> nu:=0.28;
> Rigidity:=E*h^3/(12*(1-nu^2));
> A:=matrix(12,12,[1,0,0,0,0,0,0,0,0,0,0,0,0,0,1,0,0,0,0,0,0,0,0,0,
> 0,-1,0,0,0,0,0,0,0,0,0,0,1,a,0,a^2,0,0,a^3,0,0,0,0,0,
> 0,0,1,0,a,0,0,a^2,0,0,a^3,0,0,-1,0,-2*a,0,0,-3*a^2,0,0,0,0,0,
> 1,0,b,0,0,b^2,0,0,0,b^3,0,0,0,0,1,0,0,2*b,0,0,0,3*b^2,0,0,
> 0,-1,0,0,-b,0,0,0,-b^2,0,0,-b^3,1,a,b,a^2,a*b,b^2,a^3,a^2*b,a*b^2,b^3,a^3*b,a*b^3,
> 0,0,1,0,a,2*b,0,a^2,2*a*b,3*b^2,a^3,3*a*b^2,0,-1,0,-2*a,-b,0,-3*a^2,-2*a*b,-b^2,0,
> -3*a^2*b,-b^3]);
> invA:=inverse(A);
> phi1:=matrix(1,12,[1,x,y,x^2,x*y,y^2,x^3,x^2*y,x*y^2,y^3,x^3*y,x*y^3]);
> phi1phi1:=multiply(transpose(phi1),phi1);
> phi1phi1a:=map(int,phi1phi1,x=0..a);
> phi1phi1ab:=map(int,phi1phi1a,y=0..b);
> M:=rho*multiply(transpose(invA),phi1phi1ab,invA);
> phi2:=matrix(3,12,[0,0,0,2,0,0,6*x,2*y,0,0,6*x*y,0,
> 0,0,0,0,0,2,0,0,2*x,6*y,0,6*x*y,
> 0,0,0,0,2,0,0,4*x,4*y,0,6*x^2,6*y^2]);
> C:=matrix(3,3,[1,nu,0,nu,1,0,0,0,(1-nu)/2]);
> phi2Cphi2:=multiply(transpose(phi2),C,phi2);
> phi2Cphi2a:=map(int,phi2Cphi2,x=0..a);
> phi2Cphi2ab:=map(int,phi2Cphi2a,y=0..b);
> K:=evalm(Rigidity*multiply(transpose(invA),phi2Cphi2ab,invA));
> phi1a:=map(int,transpose(phi1),x=0..a);
> phi1ab:=map(int,phi1a,y=0..b);
> R:=multiply(transpose(invA),phi1ab);
```

N.4 Membrane Element

Membrane element is similar to plate-bending element, except the K matrix is different.

$$\begin{aligned} K^{(m)} &= -\int_{x=0}^{a}\int_{y=0}^{b} H^T(T_x\frac{\partial^2 H}{\partial x^2}+T_y\frac{\partial^2 H}{\partial y^2})dydx \text{ (assume constant } T_x \text{ and } T_y) \\ &= -T_x(A_{temp}^{-1})^T\int_{x=0}^{a}\int_{y=0}^{b}\Phi_1^T\frac{\partial^2\Phi_1}{\partial x^2}dydxA_{temp}^{-1} \\ &\quad -T_y(A_{temp}^{-1})^T\int_{x=0}^{a}\int_{y=0}^{b}\Phi_1^T\frac{\partial^2\Phi_1}{\partial y^2}dydxA_{temp}^{-1} \end{aligned} \tag{N.21}$$

The symbolic algebraic can be done by using Maple. The code is shown at the end of this section. Because of the large size of the matrices, the symbolic formula is not shown in this thesis.

We use one numerical example to demonstrate the method, and the variables are: $a = 1$ m, $b = 2$ m, constant T_x, and constant T_y.

$$K^{(m)} = \frac{T_x}{90}\begin{bmatrix} 75 & 0 & -69 & -75 & 0 & -6 & 33 & 0 & -30 & -33 & 0 & -3 \\ 18 & 0 & -18 & -18 & 0 & 0 & 12 & 0 & -12 & -12 & 0 & 0 \\ -6 & 0 & 8 & 6 & 0 & -2 & -3 & 0 & 4 & 3 & 0 & -1 \\ -75 & 0 & 6 & 75 & 0 & 69 & -33 & 0 & 3 & 33 & 0 & 30 \\ -18 & 0 & 0 & 18 & 0 & 18 & -12 & 0 & 0 & 12 & 0 & 12 \\ -6 & 0 & -2 & 6 & 0 & 8 & -3 & 0 & -1 & 3 & 0 & 4 \\ 33 & 0 & -30 & -33 & 0 & -3 & 75 & 0 & -69 & -75 & 0 & -6 \\ -12 & 0 & 12 & 12 & 0 & 0 & -18 & 0 & 18 & 18 & 0 & 0 \\ -3 & 0 & 4 & 3 & 0 & -1 & -6 & 0 & 8 & 6 & 0 & -2 \\ -33 & 0 & 3 & 33 & 0 & 30 & -75 & 0 & 6 & 75 & 0 & 69 \\ 12 & 0 & 0 & -12 & 0 & -12 & 18 & 0 & 0 & -18 & 0 & -18 \\ -3 & 0 & -1 & 3 & 0 & 4 & -6 & 0 & -2 & 6 & 0 & 8 \end{bmatrix} + \frac{T_y}{360}\begin{bmatrix} 75 & 138 & 0 & 33 & 60 & 0 & -75 & 12 & 0 & -33 & 6 & 0 \\ 12 & 32 & 0 & 6 & 16 & 0 & -12 & -8 & 0 & -6 & -4 & 0 \\ -9 & -18 & 0 & -6 & -12 & 0 & 9 & 0 & 0 & 6 & 0 & 0 \\ 33 & 60 & 0 & 75 & 138 & 0 & -33 & 6 & 0 & -75 & 12 & 0 \\ 6 & 16 & 0 & 12 & 32 & 0 & -6 & -4 & 0 & -12 & -8 & 0 \\ 6 & 12 & 0 & 9 & 18 & 0 & -6 & 0 & 0 & -9 & 0 & 0 \\ -75 & -12 & 0 & -33 & -6 & 0 & 75 & -138 & 0 & 33 & -60 & 0 \\ 12 & -8 & 0 & 6 & -4 & 0 & -12 & 32 & 0 & -6 & 16 & 0 \\ 9 & 0 & 0 & 6 & 0 & 0 & -9 & 18 & 0 & -6 & 12 & 0 \\ -33 & -6 & 0 & -75 & -12 & 0 & 33 & -60 & 0 & 75 & -138 & 0 \\ 6 & -4 & 0 & 12 & -8 & 0 & -6 & 16 & 0 & -12 & 32 & 0 \\ -6 & 0 & 0 & -9 & 0 & 0 & 6 & -12 & 0 & 9 & -18 & 0 \end{bmatrix}$$

The commands used in Maple to generate this matrix are shown below. If the variables are not specified at the beginning, the Maple commands will give the symbolic formula.

```
> restart;
> with(linalg);
```

```
> a:=1;
> b:=2;
> A:=matrix(12,12,[1,0,0,0,0,0,0,0,0,0,0,0,0,0,1,0,0,0,0,0,0,0,0,0,
> 0,-1,0,0,0,0,0,0,0,0,0,0,0,1,a,0,a^2,0,0,a^3,0,0,0,0,0,
> 0,0,1,0,a,0,0,a^2,0,0,a^3,0,0,-1,0,-2*a,0,0,-3*a^2,0,0,0,0,0,
> 1,0,b,0,0,b^2,0,0,0,0,b^3,0,0,0,0,0,1,0,0,2*b,0,0,0,3*b^2,0,0,
> 0,-1,0,0,-b,0,0,0,0,-b^2,0,0,-b^3,1,a,b,a^2,a*b,b^2,a^3,a^2*b,a*b^2,b^3,a^3*b,a*b^3,
> 0,0,1,0,a,2*b,0,a^2,2*a*b,3*b^2,a^3,3*a*b^2,0,-1,0,-2*a,-b,0,-3*a^2,-2*a*b,-b^2,0,
> -3*a^2*b,-b^3]);
> invA:=inverse(A);
> phi1:=matrix(1,12,[1,x,y,x^2,x*y,y^2,x^3,x^2*y,x*y^2,y^3,x^3*y,x*y^3]);
> phi1xx:=matrix(1,12,[0,0,0,2,0,0,6*x,2*y,0,0,6*x*y,0]);
> phi1yy:=matrix(1,12,[0,0,0,0,0,2,0,0,2*x,6*y,0,6*x*y]);
> phi1phi1xx:=multiply(transpose(phi1),phi1xx);
> phi1phi1xxa:=map(int,phi1phi1xx,x=0..a);
> phi1phi1xxab:=map(int,phi1phi1xxa,y=0..b);
> K2:=multiply(transpose(invA),phi1phi1xxab,invA);
> evalm(K2*(-90));
> phi1phi1yy:=multiply(transpose(phi1),phi1yy);
> phi1phi1yya:=map(int,phi1phi1yy,x=0..a);
> phi1phi1yyab:=map(int,phi1phi1yya,y=0..b);
> K3:=multiply(transpose(invA),phi1phi1yyab,invA);
> evalm(K3*(-360));
```

N.5 Matlab Code of Beam Modeling

The following program is an example of FEM modeling by using MATLAB. It creates a MIMO state-space model of an Euler-Bernoulli Beam, including the decoupling and proportional damping.

```
% File: tubemode34.m
% Ming-chih Weng 12/13/99
% Finite element method
% clamped-free ends, multiple inputs, multiple outputs
% SI unit (meters, kilograms, seconds, Newtons)

clear all;

L = 120*0.0254;                      % beam length
OD = 0.25*0.0254;                    % beam diameter
thick=0.035*0.0254;                  % beam wall thickness
rho = 7800;                          % density
area = pi/4*(OD^2-(OD-2*thick)^2);   % cross sectional area
E = 2.0e11;                          % Young's Modulus
I = pi/64*(OD^4-(OD-2*thick)^4);     % bending moment of inertia

N = 24;                      % number of elements
l = L/N;                     % element length
dof = 2*N+2-2;               % N+1 nodes, 2N+2 dof, (-1) for every constraint
n=dof;                       % keep n modes, truncate the rest
state = 2*dof;               % number of states
```

```
delta = [40 100].*0.0254;      % position of the actuators
delta_s=[45 95].*0.0254;       % position of the sensors
nact=length(delta);            % number of actuators
nsensor=length(delta_s);       % number of sensors
section=round(delta/L*N);
section_s=round(delta_s/L*N);
pos=2*section+1;               % nodal coordinate of actuator
pos_s=2*section_s+1;           % nodal coordinate of sensor

% FEM matrices (4 x 4 matrix: "m4" and "k4")
m4=rho*area*l/420*[156 22*l 54 -13*l;22*l 4*l*l 13*l -3*l*l;...
      54 13*l 156 -22*l;-13*l -3*l*l -22*l 4*l*l];

k4=E*I/(l*l*l)*[12 6*l -12 6*l;6*l 4*l*l -6*l 2*l*l;...
      -12 -6*l 12 -6*l;6*l 2*l*l -6*l 4*l*l];

% Assemble elements
m_assemble=zeros(2*N+2, 2*N+2);
k_assemble=zeros(2*N+2, 2*N+2);
for count=1:N,
   c=2*count-1;
   m_assemble(c:c+3,c:c+3)=m_assemble(c:c+3,c:c+3)+m4;
   k_assemble(c:c+3,c:c+3)=k_assemble(c:c+3,c:c+3)+k4;
end

% Actuator position
f_assemble=zeros(2*N+2,nact);
for count=1:nact,
f_assemble(pos(count),count)=1;
end

% Sensor position
s_assemble=zeros(2*N+2,nsensor);
for count=1:nsensor,
s_assemble(pos_s(count),count)=1;
end

% Boundary condition for cantilever end, U1=U2=0
m_assemble=m_assemble(3:2*N+2,3:2*N+2);
k_assemble=k_assemble(3:2*N+2,3:2*N+2);
f_assemble=f_assemble(3:2*N+2,:);
s_assemble=s_assemble(3:2*N+2,:);

% Boundary condition for free end, do nothing

% State-space model #1: without damping
A1 = [zeros(dof,dof) eye(dof,dof);...
      -inv(m_assemble)*k_assemble zeros(dof,dof)];
B1 = [zeros(dof,nact); inv(m_assemble)*f_assemble];
C1 = [ s_assemble',zeros(nsensor,dof)];
D1 = zeros(nsensor,nact);
system1=ss(A1,B1,C1,D1);

% Eigenvalue problem: natural frequencies wn, and modal shapes phi
```

```
[v,d]=eig(A1);
for count=1:state,
   w(count)=abs(d(count,count));
   w_complex(count)=d(count,count);
   phi_tmp(:,count)=v(:,count)./v(1,count);
end
[wn_tmp,index]=sort(w);        % sort engenvalues (low to high)
for count=1:dof,
   c=2*count;
   wn(count)=wn_tmp(c);
   wn_complex(count)=w_complex(index(c));
   phi(1:dof,count)=real(phi_tmp(1:dof,index(c)));
   phi(1:dof,count)=phi(1:dof,count)/sqrt(sum(phi(1:dof,count).^2));
end

% Decoupling equations
M1=phi'*m_assemble*phi;        % modal mass matrix
K1=phi'*k_assemble*phi;        % modal stiffness matrix
F1=f_assemble'*phi;            % actuator
S1=s_assemble'*phi;            % sensor

% Add proportional damping
damping=0.005;                 % assume modal damping
Damp1=M1*2*damping.*diag(wn); % modal damping matrix

% Truncate higher modes (M2,Damp2,K2)
M2=M1(1:n,1:n);
K2=K1(1:n,1:n);
Damp2=Damp1(1:n,1:n);
f2=F1(1:nact,1:n);
s2=S1(1:nsensor,1:n);

% State-space model #2: decoupled, truncated, include damping
A2 = [zeros(n,n) eye(n,n); -inv(M2)*K2 -inv(M2)*Damp2];
B2 = [zeros(n,nact); inv(M2)*f2'];
C2 = [s2,zeros(nsensor,n)];
D2 = zeros(nsensor,nact);
system2=ss(A2,B2,C2,D2);
```

N.6 A Numerical Example of Plate Modeling

I also model a plate by using Matlab. Due to the length of the code, I do not include it in this section. I only demonstrate the results by the following figures, which show the first 12 mode shapes and their resonance frequencies. The variables of the plate are: 1 m long, 1 m wide, 1 mm thick, $E = 200$ GPa, $\rho = 7800\text{kg/m}^3$, $\nu = 0.28$, and tension $T = 0$. I use 7×7 elements for the modeling.

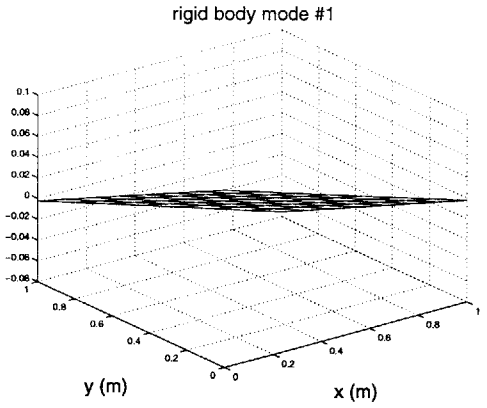

Figure N-1: Plate: 1st mode.

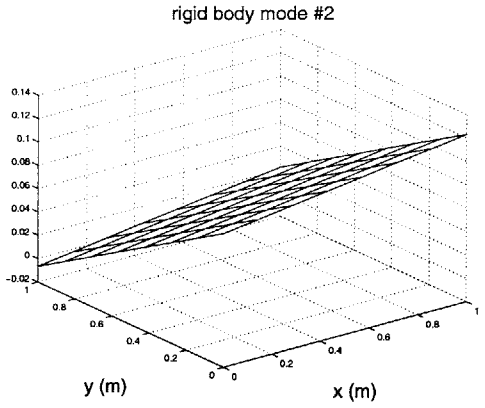

Figure N-2: Plate: 2nd mode.

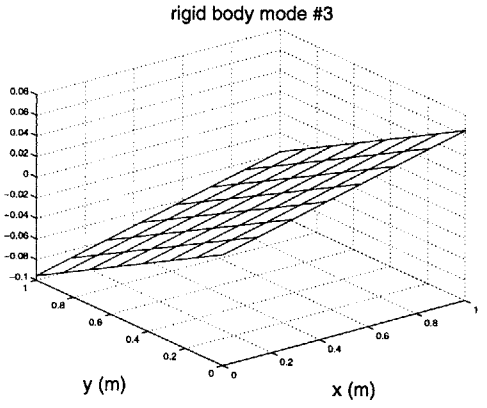

Figure N-3: Plate: 3rd mode.

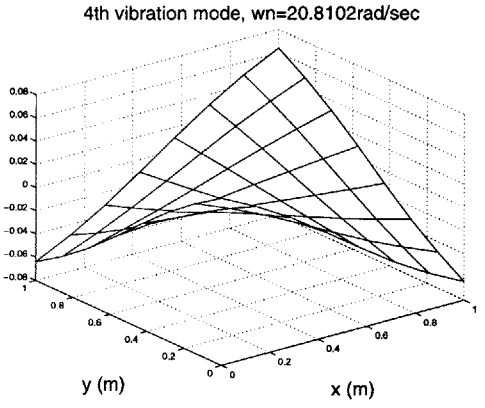

Figure N-4: Plate: 4th mode.

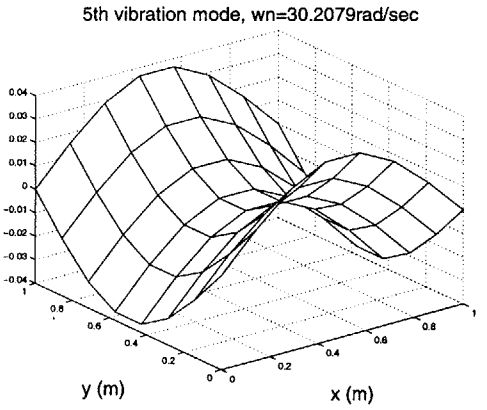

Figure N-5: Plate: 5th mode.

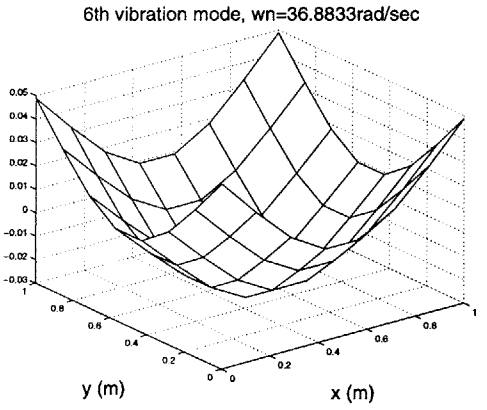

Figure N-6: Plate: 6th mode.

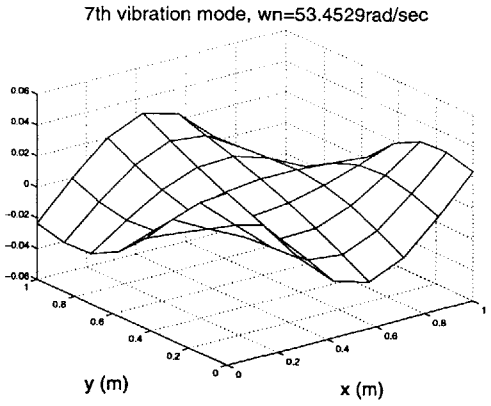

Figure N-7: Plate: 7th mode.

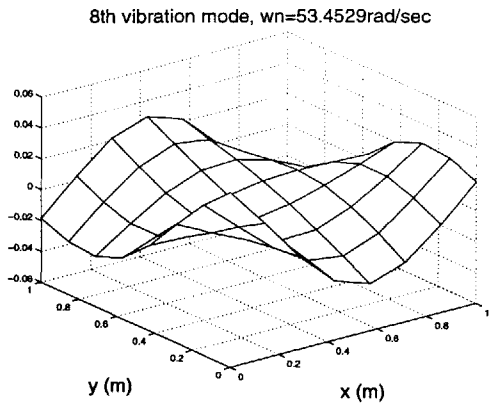

Figure N-8: Plate: 8th mode.

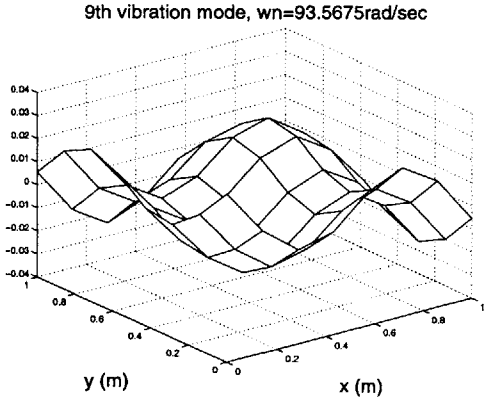

Figure N-9: Plate: 9th mode.

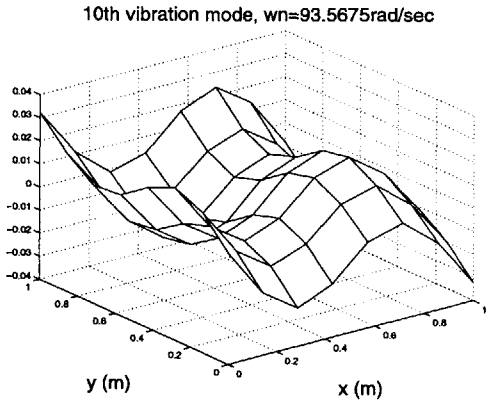

Figure N-10: Plate: 10th mode.

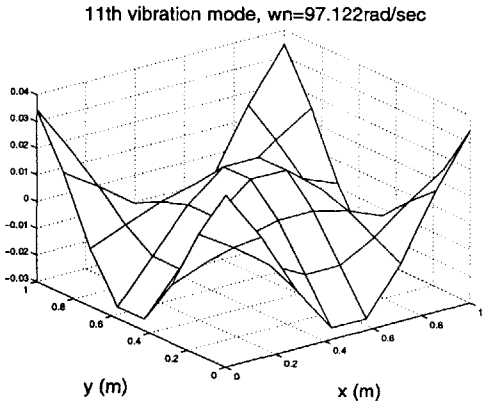

Figure N-11: Plate: 11th mode.

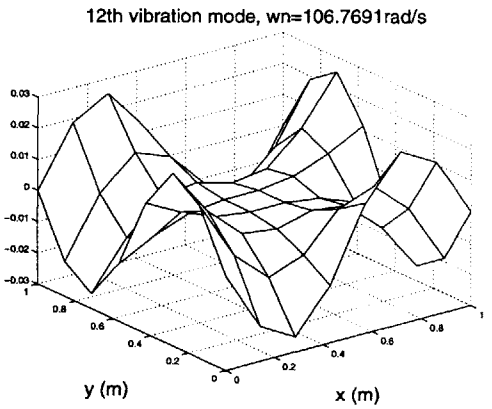

Figure N-12: Plate: 12th mode.

Appendix O

Passive Wave-Absorbing Boundaries

This chapter shows the preliminary derivation for wave-absorbing boundaries for beams without tension. The derivation for strings is well developed, and is also shown for comparison.

O.1 Passive Wave-Absorbing Boundaries for Strings

String equation is

$$-T\frac{\partial^2 u}{\partial z^2} + \rho A\frac{\partial^2 u}{\partial t^2} = f, \tag{O.1}$$

and the general solution is:

$$e^{j\omega t}\left(C_1 e^{jkz} + C_2 e^{-jkz}\right), \tag{O.2}$$

where C_1 represents upstream waves moving towards $-z$ direction, and C_2 represents downstream waves moving towards z direction. The relation between wavenumber k_n and resonance frequency ω_n is represented by

$$k_n = \sqrt{\frac{\rho A}{T}}\omega_n. \tag{O.3}$$

Assume we have a string from $z = [-L\ 0]$, and we want to find a downstream boundary at $z = 0$ such that there is no wave reflection. In other words, we want A to be zero. Assume a passive boundary condition as:

$$F = -b\dot{u} \Rightarrow T\frac{\partial u}{\partial z}\bigg|_{z=0} = -b\frac{\partial u}{\partial t}\bigg|_{z=0}. \tag{O.4}$$

We can rewrite this boundary condition by:

$$\begin{aligned} & T\frac{\partial u}{\partial z}\Big|_{z=0} = -b\frac{\partial u}{\partial t}\Big|_{z=0} \\ \Rightarrow \quad & jkT\left(C_1e^{jk0} - C_2e^{-jk0}\right) = -j\omega b\left(C_1e^{jk0} + C_2e^{-jk0}\right) \\ \Rightarrow \quad & \sqrt{\frac{\rho A}{T}}\omega T(C_1 - C_2) = \omega b(-C_1 - C_2) \\ \Rightarrow \quad & \sqrt{\rho AT}(C_1 - C_2) = b(-C_1 - C_2). \end{aligned} \tag{O.5}$$

Therefore, we can choose $b = \sqrt{\rho AT}$, and C_1 will become zero. Hence we have a perfect wave-absorbing boundary conditions for strings.

O.2 Passive Wave-Absorbing Boundaries for Beams without Tension

Beam equation is:

$$EI\frac{\partial^4 u}{\partial z^4} + \rho A\frac{\partial^2 u}{\partial t^2} = f, \tag{O.6}$$

and the general solution is:

$$e^{j\omega t}\left(C_1e^{jkz} + C_2e^{-jkz} + C_3e^{kz} + C_4e^{-kz}\right), \tag{O.7}$$

where C_1 represents upstream waves moving towards $-z$ direction, C_2 represents downstream waves moving towards z direction, C_3 and C_4 represent evanescent waves. The wavenumber-frequency relation is

$$k_n = \sqrt[4]{\frac{\rho A\omega_n^2}{EI}}. \tag{O.8}$$

Assume we have a beam at $z = [-L\ 0]$, and we want to find a right boundary at $z = 0$ such that there is no wave reflection. In other words, we want C_1 to be zero.

We use a simple damper design, and assume a passive boundary condition as:

$$F = -b_F\dot{u} \Rightarrow -EI\frac{\partial^3 u}{\partial z^3}\Big|_{z=0} = -b_F\frac{\partial u}{\partial t}\Big|_{z=0}, \tag{O.9}$$

$$M = -b_M\dot{\theta} \Rightarrow EI\frac{\partial^2 u}{\partial z^2}\Big|_{z=0} = -b_M\frac{\partial^2 u}{\partial z\partial t}\Big|_{z=0}. \tag{O.10}$$

We can rewrite the force boundary condition by:

$$\begin{aligned} & -EI\frac{\partial^3 u}{\partial z^3}\Big|_{z=0} = -b_F\frac{\partial u}{\partial t}\Big|_{z=0} \\ \Rightarrow \quad & -k^3EI(-jC_1 + jC_2 + C_3 - C_4) = -j\omega b_F(C_1 + C_2 + C_3 + C_4) \end{aligned}$$

$$\Rightarrow \quad k^3EI(-jC_1 + jC_2 + C_3 - C_4) = \omega b_F(jC_1 + jC_2 + jC_3 + jC_4) \quad \text{(O.11)}$$

We can also rewrite the moment boundary condition by:

$$\begin{aligned} & EI\frac{\partial^2 u}{\partial z^2}\Big|_{z=0} = -b_M\frac{\partial^2 u}{\partial z \partial t}\Big|_{z=0} \\ \Rightarrow \quad & k^2EI(-C_1 - C_2 + C_3 + C_4) = -j\omega k b_M(jC_1 - jC_2 + C_3 - C_4) \\ \Rightarrow \quad & kEI(-C_1 - C_2 + C_3 + C_4) = \omega b_M(C_1 - C_2 - jC_3 + jC_4) \end{aligned} \quad \text{(O.12)}$$

From Equation O.11 and Equation O.12, if we design $k^3EI = \omega b_F$ and $kEI = \omega b_M$, we will have:

$$\begin{aligned} & \begin{cases} -jC_1 + jC_2 + C_3 - C_4 = jC_1 + jC_2 + jC_3 + jC_4 \\ -C_1 - C_2 + C_3 + C_4 = C_1 - C_2 - jC_3 + jC_4 \end{cases} \\ \Rightarrow \quad & \begin{cases} j(2C_1 + C_3 + C_4) = (C_3 - C_4) \\ j(C_3 - C_4) = (2C_1 - C_3 - C_4) \end{cases} \\ \Rightarrow \quad & \begin{cases} C_1 = 0 \\ (1-j)C_3 = (1+j)C_4 \end{cases} \end{aligned} \quad \text{(O.13)}$$

Hence we make the boundary refect no waves because $C_1 = 0$. The boundary conditions can be further shown as:

$$\begin{aligned} & k^3EI = \omega b_F \\ \Rightarrow \quad & b_F = \sqrt[4]{(\rho A)^3 EI\omega^2} = k\sqrt{\rho AEI}, \end{aligned} \quad \text{(O.14)}$$

and

$$\begin{aligned} & kEI = \omega b_M \\ \Rightarrow \quad & b_M = \sqrt[4]{\frac{\rho A(EI)^3}{\omega^2}} = \frac{1}{k}\sqrt{\rho AEI}. \end{aligned} \quad \text{(O.15)}$$

Both damping coefficients b_F and b_M are functions of wavenumber k, and I do not have ideas how to realize this damper design. Practically, we can use constant b_F and b_M, and use the previous equations to calculate the damping coefficients to avoid exciting certain modes.

It will be valuable to further prove if there are other passive boundary designs that can match the beam impedance and make all the waves not reflecting. If such boundary conditions exist and can be realized practically, the beam vibration control can be greatly simplified.

Bibliography

[1] International symposium on magnetic bearings. Since 1988.

[2] International symposium on magnetic suspension technology. NASA Langley Research Center. Since 1991.

[3] Sanjay Kumar Aggarwal. Bandwidth maximization of a single degree of freedom magnetic suspension system. Bachelor's Thesis, Department of Mechanical Engineering, Massachusetts Institute of Technology, June 1995.

[4] Michael Athens. *Multivariable Control Systems.* Spring 1998. MIT course 6.245 note.

[5] Thomas Bailey and Jr. James E. Hubbard. Distributed piezoelectric-polymer active vibration control of a cantilever beam. *Journal of Guidance and Control*, 8:605–611, 1985.

[6] Mark J. Balas. Active control of flexible systems. *Journal of Optimization Theory and Applications*, 25(3):415–436, July 1978. Similar to "Feedback Control of Flexible Systems," IEEE Transactions on Automatic Control, Vol. AC-23, No.4, pp.673-679, 1978.

[7] Mark J. Balas. Trends in large space structure control theory: Fondest hopes, wildest dreams. *IEEE Transactions on Automatic Control*, AC-27(3):522–535, June 1982.

[8] V. V. Basmajian, A. B. Copeland, and T. Stephens. Studies related to the design of a magnetic suspension and balance system. Technical Report 128, Massachusetts Institute of Technology Aerophysics Laboratory, February 1966.

[9] Klaus-Jürgen Bathe. *Finite Element Procedures.* Prentice Hall, 1996.

[10] Zdeněk P. Bažant and Luigi Cedolin. *Stability of Structures - Elastic, Inelastic, Fracture, and Damage Theories.* Oxford University Press, 1991.

[11] J. W. Beams. Magnetic-suspension ultracentrifuge circuits. *Electronics*, 27(3):152–155, March 1954.

[12] J. W. Beams. Double magnetic suspension. *The Review of Scientific Instruments*, 34(10):1071–1074, October 1963.

[13] J. W. Beams, C. W. Hulburt, Jr. W. E. Lotz, and Jr. R. M. Montague. Magnetic suspension balance. *The Review of Science Instruments*, 26(12):1181–1185, December 1955.

[14] J. W. Beams, J. L. Young III, and J. W. Moore. The production of high centrifugal fields. *Journal of Applied Physics*, 17(11):886–890, November 1946.

[15] C. F. Beards. *Structural Vibration: Analysis and Damping.* Arnold, 1996.

[16] Haym Benaroya. *Mechanical Vibration.* Prentice-Hall, Inc., 1998.

[17] Robert D. Blevins. *Formulas for Natural Frequency and Mode Shape.* R. E. Krieger, 1984.

[18] W. Braunbek. Freely suspended bodies in electric and magnetic fields. *Zeitschrift für Physik*, 112:753–763, 1939. Translated from Germany.

[19] Shawn E. Burke and Jr. James E. Hubbard. Distributed transducer vibration control of thin plates. *J. Acoustical Society of America*, 90(2):937–944, August 1991.

[20] H. Canbolat, D. Dawson, C Rahn, and P. Vedagarbha. Boundary control of a cantilevered flexible beam with point-mass dynamics at the free end. *Mechatronics*, 8:163–186, 1998.

[21] G. Chen, M. C. Delfour, A. M. Krall, and G. Payre. Modeling, stabilization and control of serially connected beams. *SIAM J. Control and Optimization*, 25(3):526–546, May 1987.

[22] R. L. Clark and S. E. Burke. Practical limitations in achieving shaped modal sensors with induced strain materials. *Journal of Vibration and Acoustics, Transactions of the ASME*, 118(4):668–675, October 1996.

[23] Robert L. Clark, Chris R. Fuller, and Al Wicks. Characterization of multiple piezoelectric actuators for structural excitation. *Journal of the Acoustical Society of America*, 90(1):346–357, July 1991.

[24] Simon A. Collins, David W. Miller, and Andreas H. von Flotow. Distributed sensors as spatial filters in active structural control. *Journal of Sound and Vibration*, 173(4):471–501, 1994.

[25] Eugene E. Covert, Morton Finston, Milan Vlajinac, and Timothy Stephens. Magnetic balance and suspension systems for use with wind tunnels. *Progress in Aerospace Science*, 14:27–107, 1973.

[26] S. H. Crandall. The role of damping in vibration theory. *Journal of Sound and Vibration*, 11(1):3–18, 1970.

[27] Edward Crawley, Mark Campbell, and Steven Hall. *High Performance Structures: Dynamics and Control.* Cambridge U Press, to be published. MIT course 16.243 Dynamics of Controlled Structures text.

[28] Edward F. Crawley, Steven R. Hall, and Robert Kosut. *Robust Control I.* 1992. MIT Controlled Structures Short Course text.

[29] L. Cremer and M. Heckl. *Structure-Borne Sound.* Springer-Verlag, 1973.

[30] John Lawrence Dressler. *Video Techniques in the Feedback Control of an Electromechanical Continuum.* PhD thesis, Department of Electrical Engineering and Computer Science, Massachusetts Institute of Technology, August 1971.

[31] S. Earnshaw. On the nature of the molecular forces which regulate the constitution of the luminiferous ether. *Transactions of the Cambridge Philosophical Society*, 7:97–112, 1839. Published 1842.

[32] R. W. Ellis and Jr. C. D. Mote. A feedback vibration controller for circular saws. *Journal of Dynamic Systems, Measurement, and Control - Transactions of the ASME*, 101:44–49, March 1979.

[33] Raymond Walter Ellis. *Active Electromagnetic Vibration Control in Rotating Discs.* PhD thesis, Department of Mechanical Engineering, University of California, Berkeley, January 1977.

[34] R. L. Fittro and C. R. Knospe. μ control of a high speed spindle thrust magnetic bearing. In *Proceedings of the 1999 IEEE International Conference on Control Applications*, pages 570–575, 1999.

[35] A. E. Fitzgerald, Charles Kingsley Jr., and Stephen D. Umans. *Electric Machinery.* McGraw-Hill, Inc, fifth edition, 1992.

[36] Gene F. Franklin, J. David Powell, and Abbas Emami-Naeini. *Feedback Control of Dynamic Systems.* Addison-Wesley Publishing Company, 1986.

[37] Gene F. Franklin, J. David Powell, and Michael Workman. *Digital Control of Dynamic Systems.* Addison-Wesley Longman, Inc., third edition, 1998.

[38] Richard H. Frazier, Jr. Philip J. Gilinson, and George A. Oberbeck. *Magnetic and Electric Suspensions.* The MIT Press, 1974.

[39] C. R. Fuller, S. J. Elliott, and P. A. Nelson. *Active Control of Vibration.* Academic Press, 1996.

[40] P. J. Geary. *Magnetic and Electric Suspensions - A Survey of Their Design, Construction, and Use.* British Scientific Instrument Research Association, 1964.

[41] Andrey Geim. Everyone's magnetism. *Physics Today*, 51:36–39, September 1998.

[42] Y. Gu, R. L. Clark, and C. R. Fuller. Experiments on active control of plate vibration using piezoelectric actuators and Polyvinylidene Fluoride (PVDF) modal sensors. *Journal of Vibration and Acoustics*, 116:303–308, 1994.

[43] A. Hać and L. Liu. Sensor and actuator location in motion control of flexible structures. *Journal of Sound and Vibration*, 167(2):239–261, 1993.

[44] H. A. Haus and J. R. Melcher. *Electromagnetic Fields and Energy*. Prentice-Hall, 1989.

[45] H. Hayashiya, N. Araki, J. E. Paddison, H. Ohsaki, and E. Masada. Magnetic levitation of a flexible steel plate with a vibration suppressing magnet. *IEEE Transactions on Magnetics*, 32(5):5052–5054, September 1996.

[46] Hitoshi Hayashiya, Hiroyuki Ohsaki, and Eisuke Masada. Magnetic levitation control of elastic steel plate for steel making process. In *The International Conference on Electrical Engineering*, pages 525–528, Taejon, Korea, 1995.

[47] Hitoshi Hayashiya, Jiro Seto, Hiroyuki Ohsaki, and Eisuke Masada. Control method for switching multi supporting magnets in a magnetic levitation system of a flexible steel plate. In *LDIA '95, ML-5*, pages 115–118, Nagasaki, Japan, 1995.

[48] Edward E. Herceg. *Handbook of Measurement and Control*. Schaevitz Engineering, revised edition, 1976.

[49] Paul Horowitz and Winfield Hill. *The Art of Electronics*. Cambridge University Press, second edition, 1989.

[50] B. V. Jayawant. *Electromagnetic Levitation and Suspension Techniques*. Edward Arnold, 1981.

[51] J. U. Jeon and T. Higuchi. Electrostatic suspension of dielectrics. *IEEE Transactions on Industrial Electronics*, 45(6):938–946, December 1998.

[52] J. U. Jeon and T. Higuchi. Induction motors with electrostatic suspension. *Journal of Electrostatics*, 45:157–173, 1998.

[53] J. Jin and T. Higuchi. Direct electrostatic levitation and propulsion. *IEEE Transactions on Industry Electronics*, 44(2):234–239, April 1997.

[54] J. Jin, T. Higuchi, and M. Kanemoto. Electrostatic levitator for hard disk media. *IEEE Transactions on Industry Electronics*, 42(5):467–473, October 1995.

[55] J. Jin, T. C. Yih, T. Higuchi, and J. U. Jeon. Direct electrostatic levitation and propulsion of silicon wafer. *IEEE Transactions on Industry Applications*, 34(5):975–984, 1998.

[56] T. L. Johnson. Principles of sensor and actuator location in distributed systems. In *Advances in the Astronautical Sciences: Proceedings of NCKU/AAS International Symposium on Engineering Sciences and Mechanics*, volume 50, pages 1–14, 1983.

[57] John J. Junkins and Youdan Kim. *Introduction to Dynamics and Control of Flexible Structures.* AIAA, 1993.

[58] Suresh Kumar, Dan Cho, and William N. Carr. Experimental study of electric suspension for microbearings. *Journal of Microelectromechanical Systems*, 1(1):23–30, March 1992.

[59] H. Lamb. *Hydrodynamics.* Dover Publications, sixth edition, 1945.

[60] L. D. Landau and E. M. Lifshitz. *Fluid Mechanics.* Pergamon Press, second edition, 1987.

[61] Jeffrey Hastings Lang. *Computer Control of Stochastic Distributed Systems with Applications to Very Large Electrostatically Figured Satellite Antennas.* PhD thesis, Department of Electrical Engineering and Computer Science, Massachusetts Institute of Technology, January 1980.

[62] Benjamin J. Lazan. *Damping of Materials and Members in Structural Mechanics.* Pergamon Press, first edition, 1968.

[63] C. K. Lee and F. C. Moon. Modal sensors / actuators. *ASME Journal of Applied Mechanics*, 57:434–441, 1990.

[64] S.-Y. Lee and Jr. C. D. Mote. A generalized treatment of the energetics of translating continua, part I: Strings and second order tensioned pipes. *Journal of Sound and Vibration*, 204(5):717–734, 1997.

[65] S.-Y. Lee and Jr. C. D. Mote. A generalized treatment of the energetics of translating continua, part II: Beams and fluid conveying pipes. *Journal of Sound and Vibration*, 204(5):735–753, 1997.

[66] William S. Levine, editor. *The Control Handbook.* CRC Press, 1996.

[67] Katherine A. Lilienkamp. A Simulink-driven dynamic signal analyzer. Bachelor's Thesis, Department of Mechanical Engineering, Massachusetts Institute of Technology, February 1999.

[68] C. C. Lin. Stability and vibration characteristics of axially moving plates. *Int. J. Solids Structures*, 34(24):3179–3190, 1997.

[69] Jr. Stephen Joseph Ludwick. Modeling and control of a six degree of freedom magnetic / fluidic motion control stage. Master's thesis, Department of Mechanical Engineering, Massachusetts Institute of Technology, February 1996.

[70] D. J. Mead. Waves and modes in finite beams: Application of the phase-closure principle. *Journal of Sound and Vibration*, 171(5):695–702, 1994.

[71] L. Meirovitch and H. Baruh. On the problem of observation spillover in self-adjoint distributed-parameter systems. *Journal of Optimization Theory and Applications*, 39(2):269–291, February 1983.

[72] L. Meirovitch and H. Baruh. The implementation of modal filters for control of structures. *Journal of Guidance Control and Dynamics*, 8(6):707–716, 1985.

[73] Leonard Meirovitch. A new method of solution of the eigenvalue problem for gyroscopic systems. *AIAA Journal*, 12(10):1337–1342, October 1974.

[74] Leonard Meirovitch. A modal analysis for the response of linear gyroscopic systems. *Journal of Applied Mechanics - Transactions of the ASME*, 42(2):446–450, June 1975.

[75] Leonard Meirovitch. *Elements of Vibration Analysis*. McGraw-Hill, 2nd edition, 1986.

[76] Leonard Meirovitch. *Dynamics and Control of Structures*. John Wiley and Sons, 1990.

[77] James R. Melcher. Control of a continuum electromechanical instability. In *Proceedings of the IEEE*, volume 53, pages 460–473, May 1965.

[78] James R. Melcher. *Continuum Electromechanics*. The MIT Press, 1981.

[79] S. E. Miller and J. Hubbard. Observability of a Bernoulli-Euler beam using PVF_2 as a distributed sensor. In L. Meirovitch, editor, *Proceedings of 6th VPT and SU/AIAA Symposium on Dynamics and Control of Large Structures*, pages 375–390, Blacksburg, VA, USA, 1987.

[80] Ömer Morgül. Dynamic boundary control of a Euler-Bernoulli beam. *IEEE Transactions on Automatic Control*, 37(5):639–642, May 1992.

[81] Ömer Morgül. Dynamic boundary control of the timoshenko beam. *Automatica*, 28(6):1255–1260, November 1992.

[82] Jr. C. D. Mote. On the nonlinear oscillation of an axially moving string. *Journal of Applied Mechanics*, 33:463–464, June 1966.

[83] Jr. C. D. Mote. Dynamic stability of axially moving materials. *The Shock and Vibration Digest*, 4(4):2–11, April 1972.

[84] A. T. Nordsieck. Free-gyro systems for navigation or the like. U.S. Patent 3003356, November 1954.

[85] Yohji Okada, Takayuki Nagata, Junji Tani, and Hebing Zhang. Vibration analysis and active control of flexible-shell-structured rotor supported by magnetic bearings. *JSME International Journal, Series C*, 37(3):488–493, 1994.

[86] Sean Michael Olsen. Nonlinear compensation of a single degree of freedom magnetic suspension system. Master and Bachelor's Thesis, Department of Mechanical Engineering, Massachusetts Institute of Technology, May 1994.

[87] Alan V. Oppenheim and Ronald W. Schafer. *Discrete-Time Signal Processing.* Prentice Hall Signal Processing. Prentice Hall, Inc., 1989.

[88] Yasuo Oshinoya and Taro Shimogo. Electro-magnetic levitation control of an elastic plate. In *International Conference Maglev '89*, pages 435–440, July 1989.

[89] R. G. Parker. On the eigenvalues and critical speed stability of gyroscopic continua. *Journal of Applied Mechanics - Transactions of the ASME*, 65:134–140, 1998.

[90] R. G. Parker. Supercritical speed stability of the trivial equilibrium of an axially-moving string on an elastic foundation. *Journal of Sound and Vibration*, 221(2):205–219, 1999.

[91] Edward M. Purcell. *Electricity and Magnetism*, volume 2 of *Berkeley Physics Course.* McGraw-Hill Publishing Company, second edition, 1985.

[92] Herbert Reismann and Peter S. Pawlik. *Elasticity, Theory and Applications.* John Wiley and Sons, 1980.

[93] Robert John Ritter. Analysis and design of a two-axis noncontact position sensor. Master's thesis, Department of Mechanical Engineering, Massachusetts Institute of Technology, February 1999.

[94] James K. Roberge. *Operational Amplifiers: Theory and Practice.* John Wiley and Sons, 1975.

[95] M. Sathyamoorthy. Nonlinear vibrations of plates - a review. *The Shock and Vibration Digest*, 15:3–16, 1983.

[96] M. Sathyamoorthy. Recent research in nonlinear plate vibrations. *The Shock and Vibration Digest*, 20(5):14–20, May 1988.

[97] P. K. Sinha. Electromagnetic micrometers. In *New Developments in Automatic Testing*, number 158, pages 21–24. IEE Conf. Publn, 1977.

[98] P. K. Sinha. *Electromagnetic Suspension - Dynamics and Control.* Peter Peregrinus Ltd., 1987.

[99] Timothy Stephens. Design, construction, and evaluation of a magnetic suspension and balance system for wind tunnels. Technical Report 136, Massachusetts Institute of Technology Aerophysics Laboratory, November 1969.

[100] S. Timoshenko and S. Woinowsky-Krieger. *Theory of Plates and Shells.* McGraw-Hill Book Company, Inc., second edition, 1959.

[101] E. H. Trandt. Levitation in physics. *Science*, 243:349–355, January 1989.

[102] David L. Trumper. *Magnetic Suspension Techniques for Precision Motion Control.* PhD thesis, Department of Electrical Engineering and Computer Science, Massachusetts Institute of Technology, September 1990.

[103] M. J. Usher. *Sensors and Transducers.* MacMillan Publishers Ltd., 1985.

[104] J. A. Wickert. Non-linear vibration of a traveling tensioned beam. *International Journal of Non-Linear Mechanics*, 27(3):503–517, 1992.

[105] J. A. Wickert and Jr. C. D. Mote. Current research on the vibration and stability of axially-moving materials. *The Shock and Vibration Digest*, 20(5):3–13, May 1988.

[106] J. A. Wickert and Jr. C. D. Mote. Classical vibration analysis of axially moving continua. *Journal of Applied Mechanics - Transactions of the ASME*, 57:738–744, September 1990.

[107] J. A. Wickert and Jr. C. D. Mote. Response and discretization methods for axially moving materials. *Applied Mechanics Reviews*, 44(11):S279–S284, November 1991.

[108] Bong Wie. Active vibration control synthesis for the control of flexible structures mast flight system. *J. Guidance*, 11(3):271–277, 1988.

[109] Mark Edd Williams. *Precision Six Degree of Freedom Magnetically-Levitated Photolithography Stage.* PhD thesis, Department of Mechanical Engineering, Massachusetts Institute of Technology, October 1997.

[110] Herbert H. Woodson and James R. Melcher. *Electromechanical Dynamics, Part I: Discrete Systems.* John Wiley and Sons, 1968.

[111] Herbert H. Woodson and James R. Melcher. *Electromechanical Dynamics, Part II: Fields, Forces, and Motion.* John Wiley and Sons, 1968.

[112] Yeung Yam, Timothy L. Johnson, and Jeffrey H. Lang. Flexible system model reduction and control system design based upon actuator and sensor influence functions. *IEEE Transactions on Automatic Control*, AC-32(7):573–582, July 1987.

[113] Kemin Zhou and John C. Doyle. *Essentials of Robust Control.* Prentice-Hall, Inc., 1998.

[114] Kemin Zhou, John C. Doyle, and Keith Glover. *Robust and Optimal Control.* Prentice Hall, 1995.